Processes of cation migration in clayrocks: Final Scientific Report of the CatClay European Project

S. Altmann, M. Aertsens, T. Appelo, C. Bruggeman, Stéphane Gaboreau, M. Glaus, P. Jacquier, T. Kupcik, N. Maes, V. Montoya, et al.

CEA-R-6410

ISSN 0429 - 3460

COMMISSARIAT À L'ÉNERGIE ATOMIQUE
ET AUX ÉNERGIES ALTERNATIVES

RAPPORT FINAL DU PROJET EUROPÉEN CatClay SUR LES PROCESSUS DE MIGRATION DES CATIONS DANS LES ROCHES ARGILEUSES INDURÉES

par

Les partenaires du projet européen CatClay
(coordination S. Savoye)
Scott ALTMANN et Coll.

CEA SACLAY
DIRECTION DE L'ÉNERGIE NUCLÉAIRE
DIRECTION DES ACTIVITÉS NUCLÉAIRES DE SACLAY
DÉPARTEMENT DE PHYSICO-CHIMIE
SERVICE D'ÉTUDES DU COMPORTEMENT DES RADIONUCLÉIDES

DIRECTION DE L'ÉNERGIE NUCLÉAIRE
DIRECTION DES ACTIVITÉS NUCLÉAIRES DE SACLAY

DIRECTION DES SYSTÈMES
D'INFORMATION
CEA / SACLAY 91191 GIF-SUR-YVETTE CEDEX FRANCE

2015

RAPPORT
CEA-R-6410

- Rapport CEA-R-6410-

CEA Saclay
Direction de L'Énergie Nucléaire
Direction des Activités Nucléaires de Saclay
Département de Physico-Chimie
Service d'Étude du Comportement des Radionucléides

RAPPORT FINAL DU PROJET EUROPÉEN CatClay SUR LES PROCESSUS DE MIGRATION DES CATIONS DANS LES ROCHES ARGILEUSES INDURÉES

par

Les partenaires du projet européen CatClay (coordination S. Savoye)
Scott ALTMANN et Coll.

- Juillet 2015 -

RAPPORT CEA-R 6410 – Scott ALTMANN

« Rapport final du projet européen CatClay sur les processus de migration des cations dans les roches argileuses indurées »

Résumé – Dans le cadre des études de faisabilité d'un stockage de déchets radioactifs en couches argileuses profondes, il est maintenant bien établi que les propriétés de transport des radionucléides dans les roches argileuses sont principalement gouvernées par les surfaces chargées négativement des minéraux argileux. Tandis que le comportement diffusif des espèces non réactives neutres et anioniques est bien compris, plus d'efforts doivent être consentis pour améliorer notre compréhension des phénomènes couplés d'adsorption/diffusion pour les cations sorbés. En effet, de précédentes études ont montré que plusieurs cations connus pour former des complexes de surface très stables sur des sites de minéraux argileux migraient plus profondément dans les roches argileuses que ce qui était prévu initialement. Aussi, l'objectif général du projet Européen CatClay est d'éclaircir ces points durs, en utilisant une approche méthodologique de type « bottom-up », dans laquelle des systèmes analogues plus simples (ici une argile compactée, de type illite pure) sont étudiés expérimentalement et modélisés. Il s'agit ensuite de vérifier la possible application de ces résultats aux matériaux plus complexes que sont les roches argileuses actuellement investiguées en France, en Suisse et en Belgique pour accueillir d'éventuels sites de stockage de déchets radioactifs. Les cations d'intérêt ont été choisis pour couvrir une gamme représentative de la famille des cations : un cation se sorbant modérément, le strontium, et trois autres cations montrant de fortes affinités pour le solide, Co(II), Zn(II) et Eu(III). Pendant les 4 ans qu'a duré ce projet, un effort important a été consenti pour développer ou adapter des méthodes expérimentales nécessaires à l'acquisition de données les plus fiables possibles, et ce, pour tester in fine les différents modèles conceptuels proposés. La diffusion facilitée a ainsi été confirmée pour tous les cations d'intérêt, sauf pour Eu(III), à la fois au travers du système illite compacté, mais aussi des roches argileuses. Les premières modélisations prenant en compte la diffusion dans la double couche diffuse ont, de façon prometteuse, réussi à reproduire les données expérimentales obtenues sous des conditions variées, et ce, dans l'illite et dans les roches argileuses, même s'il reste des hypothèses implicites à vérifier dans ces modélisations. De plus, la reconstruction du réseau poreux en 3D de l'illite compactée, et avec un niveau de qualité moindre, dans les échantillons de roches argileuses, a été acquise avec succès en combinant des analyses MET et FIB sur des échantillons imprégnés avec une résine qui préserve au mieux l'état initial du réseau poreux. En se basant sur cette reconstruction 3D, des expériences de diffusion numériques ont été réalisées à l'échelle des pores d'une illite virtuelle, aidant à mieux comprendre comment s'organise la diffusion dans le réseau poreux. Finalement, le projet Européen CatClay a permis une meilleure compréhension de la migration des cations fortement sorbés à travers ces formations argileuses peu perméables, augmentant de ce fait la confiance dans notre capacité à démontrer la fiabilité de ces modèles utilisés pour prédire la migration des radionucléides à travers ces roches.

2015 – Commissariat à l'Énergie Atomique et aux Énergies Alternatives – France

RAPPORT CEA-R 6410 – Scott ALTMANN

«Processes of cation migration in clayrocks: Final Scientific Report of the CatClay European Project»

Abstract - In the framework of the feasibility studies on the radioactive waste disposal in deep argillaceous formations, it is now well established that the transport properties of solutes in clay rocks, i.e. parameter values for Fick's law, are mainly governed by the negatively charged clay mineral surface. While a good understanding of the diffusive behaviour of non-reactive anionic and neutral species is now achieved, much effort has to be placed on improving understanding of coupled sorption/diffusion phenomena for sorbing cations. Indeed, several cations known to form highly stable surface complexes with sites on mineral surfaces migrate more deeply into clay rock than expected. Therefore, the overall objective of the EC CatClay project is to address this issue, using a 'bottom-up' approach, in which simpler, analogous systems (here a compacted clay, 'pure' illite) are experimentally studied and modelled, and then the transferability of these results to more complex materials, i.e. the clay rocks under consideration in France, Switzerland and Belgium for hosting radioactive waste disposal facilities, is verified. The cations of interest were chosen for covering a representative range of cations families: from a moderately sorbing cation, the strontium, to three strongly sorbing cations, Co(II), Zn(II) and Eu(III). For the 4 years of this project, much effort was devoted to developing and applying specific experimental methods needed for acquiring the high precision, reliable data needed to test the alternative hypotheses represented by different conceptual-numerical models. The enhanced diffusion of the sorbing cations of interest was confirmed both in the simpler analogous illite system for Sr^{2+}, Co(II) and Zn(II), but also in the natural clay rocks, except for Eu(III). First modelling approach including diffusion in the diffuse double layer (DDL) promisingly succeeded in reproducing the experimental data under the various conditions both in illite and clay rocks, even though some assumptions made have to be verified. In parallel, actual 3D geometrical pore size distributions of compacted illite, and in less extent, clay rock samples, were successfully determined by combining TEM and FIB-nt analyses on materials maintained in a water-like saturation state by means of an extensive impregnation step. Based on this spatial distribution of pores, first numerical diffusion experiments were carried at the pore scale through virtual illite, enabling a better understanding of how transfer pathways are organized in the porous media. Finally, the EC CatClay project allowed a better understanding of the migration of strongly sorbing tracers through low permeability 'clay rock' formations, increasing confidence in our capacity to demonstrate that the models used to predict radionuclide migration through these rocks are scientifically sound.

2015 – Commissariat à l'Énergie Atomique et aux Énergies Alternatives – France

Processes of cation migration in clayrocks (CatClay)

(Contract Number: Grant Agreement N° 249624)

Final Scientific Report (D1.6)

Author(s): S. Altmann, M. Aertsens, T. Appelo, C. Bruggeman, S. Gaboreau, M. Glaus, P. Jacquier, T. Kupcik, N. Maes, V. Montoya, T. Rabung, J.-C. Robinet, S. Savoye, T. Schaefer, C. Tournassat, L. Van Laer, L. Van Loon.
Edited by S. Altmann & L. Van Laer

Reporting period: 01/06/10 – 31/05/14

Date of issue of this report: 31/05/14

Start date of project: 01/06/2010 Duration: 48 Months

Contents

Figures

Tables

1. Introduction

1.1 Background

Much effort has been invested over the last two decades to measure, understand and model diffusion-driven transfer of radioactive elements in saturated natural or engineered low-permeability porous materials containing large proportions of permanent negative charge swelling and/or non-swelling clay minerals, this mainly to provide support for safety cases for national radioactive waste disposal programs. The materials studied range from swelling clay- (e.g. montmorillonite) rich bentonites foreseen for constructing engineered barrier systems to sedimentary geological formations containing high proportions of illite and smectite-type minerals being studied for hosting potential disposal facilities. The underlying question driving this research can be phrased in a generalized fashion as follows: *for a given volume of saturated material under known physical-chemical conditions submitted to a gradient in dissolved concentration (always low to trace) of a given radionuclide, is it possible to predict the radionuclide's flux through the material over time?*

The main features of compacted bentonite and clayrocks influencing RN migration can be summarized as follows (cf. Figure 1):

- The porosity of highly compacted bentonites and clayrocks is dominated by pore spaces in contact with the different categories of clay mineral surfaces: edges, external basal, interlayer (smectite-type only). The pore volume dimensions and the proportioning of total pore space between the external and interlayer fractions vary as a function of bentonite dry density.
- The composition of the pore solution is determined by local (pseudo)equilibrium involving dissolved components, certain mineral phases and clay surface functional groups; the dissolved concentrations of certain components (e.g. Cl^-, Na^+) may be determined by externally imposed conditions. The dissolved speciation of diffusing trace elements is at equilibrium with the pore solution.
- Clay external and interlayer surfaces possess characteristic densities of permanent negative charge compensated in solution by equivalent amounts of positive charge in the form of cationic species. Cations compensating charge located on external basal surfaces are distributed between two populations: that in direct contact and as dissolved species present in the adjacent solution.
- Electrostatic attraction and repulsion respectively of cations and anions by external and internal surfaces determine the porosities accessible to different species; cations and neutral species can access most if not all of the total connected porosity, while anions are generally assumed to be entirely excluded from the interlayer volumes of highly compacted clay masses and more or less excluded (depending on the ionic strength) from the solution volume immediately adjacent to external basal surfaces.
- The edges of the TOT layers of smectite and illite clay minerals possess functional groups capable of sorbing cationic Me species.

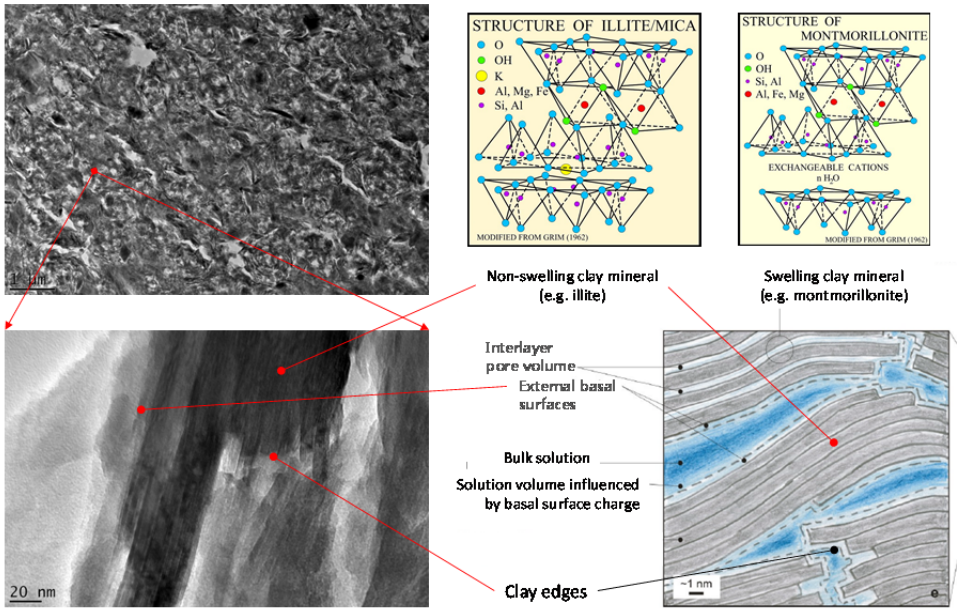

Figure 1 Conceptual model of different features influencing cation transport in compacted clay materials.

Diffusion-driven transport in porous materials is described in terms of Fick's laws, adapted to take into account the eventual effects of physical or chemical interaction of the diffusing species with the solid matrix. A common formulation for transient state conditions is:

$$\frac{\partial(Me)}{\partial t} = D_0 \cdot \delta \cdot \frac{1}{1+\frac{(S:Me)}{(Me)}} \cdot \frac{1}{\tau^2} \cdot \frac{\partial^2(Me)}{\partial x^2} \qquad (1)$$

where D_0 is the diffusion coefficient for the species 'Me' in free solution; δ is a factor ($0 < \delta \leq 1$) applied to the total porosity (ω_T) to correct for the effect of physical-chemical phenomena restricting access of Me to some fraction of the porosity; (S:Me)/(Me) represents a fixed (or variable) relationship between the concentrations of dissolved species per pore water volume (Me) and immobile species per pore water volume (S:Me) respectively, resulting from physical-chemical interaction of RN with solid matrix surfaces (if constant this ratio divided by material density / porosity is called K_d, i.e. distribution coefficient of immobile and mobile species); τ is a geometrical factor (≥ 1) representing the reduction in the effective concentration gradient (d(Me)/dx) due to the fact that diffusion paths through a porous medium will generally be greater, i.e. more tortuous, than the straight-line distance between the system boundaries, i.e. dx. The corresponding form for steady state conditions is

$$J = -D_0 \cdot \delta\omega_T \cdot \frac{1}{\tau^2} \cdot \frac{d(Me)}{dx} = -\boldsymbol{D_e}\frac{d(Me)}{dx} \qquad (2)$$

where D_e is the effective diffusion coefficient.

Experimental data regarding diffusion-driven transport in compacted clay minerals (principally bentonite) and clayrocks concern measurements of the flux, through a given volume of material under fixed physical-chemical conditions, of water molecules (HTO), halogen anions (Cl^-, I^-) and alkaline and alkaline earth cations (Cs^+, Sr^{+2}…) and show a number of common trends:

- D_e values for HTO decrease with increasing material density (bentonite) and are insensitive to solution composition (Bourg et al., 2006),
- Breakthrough times for anions are generally shorter, and the D_e values smaller, relative to HTO (Glaus et al., 2010; Van Loon et al., 2003),
- D_e values for anions generally decrease with decreasing pore solution ionic strength (van Schaik and Kemper, 1966; Muurinen et al., 1989; Van Loon et al., 2007),
- Cation breakthrough times are generally longer than for HTO (Appelo et al., 2010; Glaus et al., 2010),
- D_e values for alkaline (e.g. Na^+, Cs^+) and alkaline earth cations (Sr^{+2}, Ca^{+2}…) have been found to be significantly higher than for HTO (Glaus et al., 2007; Melkior et al., 2007; van Schaik et al., 1966).
- Diffusion-driven transport of neutral or anionic dissolved species takes place in accordance with equations 1 and 2 with (S:Me)/(Me) = 0 and appropriate δ and τ parameter values; the variation of δ as a function of solution ionic strength can be predicted qualitatively (see above), τ is (always) a fitting parameter (Ochs et al., 2001; Tournassat and Appelo, 2011).

The conceptual model for cation diffusion-driven transfer is less clear. This is exemplified by the fact that data for diffusion of alkali and alkaline earth cations generally cannot be described simply in terms of diffusion of the dissolved species (Me), i.e. using equations 1 and 2 with HTO as an analogy for the δ and τ parameter values and (S:Me) as a simple 'sink' (and source) term for immobile Me mass. For these elements, *diffusion of cation mass present in surface-associated forms (S:Me) must be considered as contributing to the global Me flux.* Diffusion of transition metals, lanthanides and actinides generally show very slow mass propagation through the material. This can be explained in terms of the high solid-solution partitioning ratios, (S:Me)/(Me), for these elements measured during studies in analogous dispersed systems. This sorption-related retardation makes it very difficult to experimentally determine the De values for such elements. (Sato et al., 1992; Torstenfelt, 1986)

The overall objective of the work described in this paper, carried out in the framework of the EC Euratom Catclay project, is to increase the understanding and predictability of how different types of 'surface-association' affect the diffusion of cationic species in compacted clay systems, in particular for elements of interest to performance assessment other than alkaline and alkaline earths (transition metals, lanthanides/actinides…).

1.2 Modelling approaches: an overview

Various approaches have been proposed for interpreting/conceptualizing cation diffusion in compacted clay materials, differing mainly in two aspects:

- how total Me mass is to proportioned among one or more possible 'surface-associated' forms, and consequently located in the different pore spaces shown in Figure 1, and
- how the diffusion behaviour of each form is described in terms compatible with Fick's laws.

Note that these aspects also correspond to the two computation steps generally used when numerically modelling couples speciation-diffusion processes: a speciation calculation for each volume element wherein the total mass brought in from adjacent cells during the previous transport step is redistributed among all surface and dissolved species, followed by a transport step wherein the mass present in the various dissolved or surface species forms is moved independently to adjacent volume elements in accordance with species-specific Fick's laws.

1.2.1 Surface speciation models

A correct representation of the phenomena governing how Me total mass is proportioned among surface species is primordial since, as will be seen below, it is the basis of hypotheses as to how each surface species contributes to overall diffusive flux. In general more or less sophisticated chemical speciation models are used to calculate the local equilibrium between dissolved species (Me) and a set of surface species, $(S:Me)_i$ in systems containing a clay-rich material in contact with a solution of known composition. A wide range of such models have been proposed for interpreting experimental results for metal cation solid-solution partitioning on different clay mineral-containing materials (e.g. montmorillonite, illite, bentonites, clayrocks (Opalinus (CH), Callovo-Oxfordian (FR)…) over a range of chemical conditions (pH, ionic strength, sorbing metal concentration…). They can be classified based (i) on how the clay surface is described in terms of specific molecular entities interacting/reacting differently with dissolved metal cations, (ii) on the stoichiometry and stability of the metal-surface species and (iii) on whether or not the effect of the electrostatic field associated with charged clay surfaces is explicitly considered.

The simplest models do not consider metal-surface interaction mechanisms at all, relying simply on a (S:Me)/(Me) term to represent experimentally determined partitioning of total metal mass between solid phase associated mass and dissolved mass under given solution composition conditions. The term can be a constant, the so-called K_d, or variable as a function of total metal concentration, e.g. Langmuir or other isotherms. This representation can offer a mathematically concise, and perhaps adequate, means of calculating (S:Me) for systems characterized by otherwise invariant geochemical conditions.

All of the other models are based on conceptualisations of clay mineral surfaces as hosts for physical or chemical moieties which can interact electrostatically or react chemically with dissolved cations to form different types of S:Me 'surface species', the formation of which can be described by mass action laws. These models are commonly termed thermodynamic sorption models (TSM) (cf. OECD, 2012). As indicated above and illustrated in Figure 1, two main types of sites are generally recognized as present on illite and smectite type minerals: (i) permanent negative charge localisations on the basal external surfaces and interlayer surfaces (smectite only) and (ii) functional groups at the TOT layer edges. Work carried out over the past several decades on the equilibrium speciation of systems containing single clay minerals or complex clay-rich materials dispersed in solutions of differing background electrolyte, pH and sorbing trace metal element concentrations has yielded an extensive published experimental database, principally in the form of isotherms and pH sorption edges as a function of system composition (ionic strength, competing cation and ligand concentrations…), but also in certain cases including spectroscopic information on surface species molecular structure, for a variety of major and trace metal cations (e.g. Na(I), Cs(I), Sr(II), Mn(II), Co(II), Ni(II), Zn(II), Eu(III), Am(III), U(VI, IV)) (Brouwer et al., 1983; Maes and Cremers, 1986; Bradbury and Baeyens, 2005b; 2009; Dahn et al., 2003). This effort

has been accompanied by a correspondingly intense effort to develop TSM model interpretations with a general objective of having, for a specific clay mineral (montmorillonite, illite…), a chemically and physically coherent description of its equilibria with all dissolved components, the experimental and modelling work of Bradbury and Baeyens on cation sorption in illite and montmorillonite minerals certainly constituting a reference in the field. Tournassat et al. (2013) provides an incisive critical overview of TSM models for pH-dependent sorption of divalent cations on montmorillonite.

The essential characteristics of TSM models for cation sorption on illite and smectite type minerals of interest for coupling with diffusion behaviour can be summarized by the following points:

- Sorption of alkali element cations (Cs(I), K(I), Rb(I)…) and alkaline earth divalent cations (Sr(II), Ca(II)…) is determined by interactions with structural negative charge localisations on basal and interlayer surfaces. Three site types have been identified for alkali cation sorption on illite: abundant but low energy 'planar' sites (PS), lower abundance but higher energy 'type II' sites (T2) and low abundance, high specificity 'frayed-edge' sites (FES). PS and T2 sites should be present in montmorillonite basal and interlayer surfaces. Surface complexation on edge sites (see below) may also contribute slightly to alkaline earth cation fixation. (Bradbury and Baeyens, 2000;Bradbury and Baeyens, 2005a; Brouwer et al., 1983)

- Sorption of transition metal, lanthanide and actinide cations involves at least two surface complexation type sites located on the edges; a low concentration, high energy 'strong' site (SS) and a higher abundance, lower energy 'weak' site (WS). In addition, at least one cation exchange site (PS), possibly also 'T2', is needed at low pH.

A variety of mass action laws for both basal and edge site species have been proposed representing different hypotheses regarding the stoichiometry, molecular scale 'geometry' and the contribution of electrostatic forces to the stability of each type of surface site – cation species association. They reflect different compromises across the spectrum of TSM modelling objectives extending from efficient representation of sorption datasets for evaluating and defending K_d values used in performance assessment to capturing as closely as possible available knowledge regarding surface species fine structure and bond energetics. The main model differences of interest in the context of coupling surface speciation to diffusion are (i) whether or not the totality of the surface charge associated with external basal surfaces is considered to be compensated by S:Me species, and (ii) the stoichiometry and stability (also reversibility) of edge site surface complexes. These are addressed below.

Basal surface sites

Two formalisms are used for mass action laws for cation reactions with basal surface sites (PL, T2, FES), cation exchange and surface complexation, differing essentially in that the second allows existence of a negatively charged surface site component, $S{:}^-$, while the first does not. An example of the differences is illustrated by the following equilibria involving surface sites with Na^+ and Co^{2+}, the first being the cation exchange formalism and the following, surface complexation.

$$2S{:}Na + Co^{+2} \leftrightarrow S_2{:}Co + 2Na^+ \qquad K_{Na/Co}$$

$$S{:}^- + Na^+ \leftrightarrow S{:}Na \qquad K_{S:Na}$$
$$2S{:}^- + Co^{+2} \leftrightarrow S_2{:}Co \qquad K_{S_2:Co}$$
$$2S{:}Na + Co^{+2} \leftrightarrow S_2{:}Co + 2Na^+ \qquad K_{S_2:Co}/(K_{S:Na})^2$$

The fraction of surface sites present in the charged $S{:}^-$ speciation in the surface complex formulation will depend on the surface complexation constants, $K_{S:Na}$ and $K_{S2:Co}$, with very high values corresponding to effectively zero $S{:}^-$ concentration, i.e. a cation exchange equivalent model. Low to moderate values of $K_{S:Na}$ and $K_{S2:Co}$ lead to significant $S{:}^-$ concentrations, therefore corresponding residual surface charge density, i.e. moles $S{:}^-$ per m^2 surface. This capacity of surface complexation representation to allow existence of free S:- sites on external basal surfaces is essential in order for the model to accord with data on net particle charge such as given by zeta potential measurements or by indirect information such as anion accessible porosity in compacted materials.

The residual surface charge density possible in surface complexation representations must be compensated by a corresponding cation excess in the adjacent solution. Two types of models exist for representing the ion distributions in an extension of this zone, electrical double layer (EDL) models and the Donnan equilibrium. EDL models, while originally developed for describing complexation with metal oxides (see ref for overview: Dzombak and Morel, 1990), are also appropriate for permanent charge external basal surfaces of clays since these models are based on (i) considering a mineral surface as 'planar', (ii) the positioning of charged solution components at specific distances from the charged reference plane depending on the type of S:Me complex formed (ligand exchange (inner sphere) or not (outer sphere)) and (iii) taking into account how electrostatic forces affect sorbing component activity as a function of distance from the surface. Figure 2 shows the essential features of one such model, the Stern-Gouy-Chapman double

layer model, being the Stern layer comprising a population of cation charge located in close proximity to the negative charge localisations in the TOT layer (outer sphere complexes), a residual charge σ_0 representing the proportion of total surface charge density uncompensated by ions in the Stern layer and a zone wherein σ_0 is compensated by an excess of cation charge (and correspondingly increasing anionic charge) exponentially decreasing (anion increasing) towards the electrostatically neutral bulk solution reference composition. The Donnan approximation for this same system simply replaces the diffuse zone by a fixed thickness layer having a constant electrostatic potential and homogeneous cation – anion composition consistent with counterbalancing σ_0 relative to the bulk solution composition.

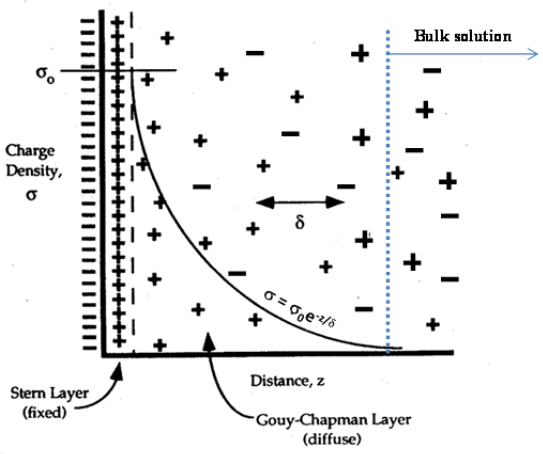

Figure 2 Essential features of Stern-Gouy-Chapman double layer model.

While surface complexation models with EDL and Donnan volumes have been used for describing equilibria in clay interlayer solutions this does not seem to be conceptually correct for the simple reason that distinction between site associated and site un-associated charge compensating cations, respectively S:Me and Me^+, does not seem reasonable in confined, two to three water layer thick interlayer spaces delimited by two charged surfaces given that the interlayer spacing in a two-layer hydrate observed for Na-montmorillonite at density's above 1400 kg/m^3 (Kozaki et al., 1997) is ~ 0.6 nm and the hydrated radii of mono- and divalent cations is generally of the order of 0.2 to 0.3 nm (Ohtaki and Radnai, 1993). The cation exchange formalism therefore is considered most appropriate for interlayer site equilibria. While total charge compensation can be achieved using non EDL surface complexation mass action laws with very high K values, these high values are considered less appropriate from a conceptual point of view because they are in contradiction with the relatively low stability of non-ligand exchange, outer sphere type bonds.

Edge sites

The TOT edges of illite and smectite particles possess oxygen atoms capable of undergoing ligand exchange reactions with solution components, in particular H^+ and hydrolysable multivalent cations, and can gain or lose protons as a function of solution pH resulting in a pH dependent edge charge and electrostatic potential. Spectroscopic studies show that these elements form inner sphere complexes with TOT edges and that the mechanism depends on the cation (electronic structure) and pH (competition of H^+ for O coordination and cation hydrolysis). Virtually all surface complexation models for clays distinguish at least two classes of surface complexation sites reacting with divalent cations, high stability (energy) (HES) and low stability (energy) (LES), with HES being present at much smaller densities (mol/kg clay) than LES. Note that these sites are distinct from the so-called 'frayed edge sites' of illites which react preferentially with alkali metal cations: Cs^+ and K^+.

Cation reaction with edge sites has generally been modelled using surface complexation models similar to those developed for metal oxyhydroxides, with or without electrostatic activity correction terms based on one of the various electrical double layer models. The model having one of the most extensive databases for cation-clay equilibria, that of Bradbury and Baeyens (1997, 1999, 2005), does not have an electrostatic correction term.

Tournassat et al. (2013) offers an in-depth, critical review of surface complexation modelling divalent transition metal cations (Co, Zn, Ni…) reactivity with montmorillonite, in particular as a function of pH. These authors conclude that, while non-electrostatic mass action laws for HES reactivity (e.g. B&B) are quite efficient in representing pH and ionic strength dependent sorption data, they are at odds with the fact that the electrostatics of clay surfaces should play a role in sorption, and therefore should ideally be present in the sorption model formalism, and that existing electrostatic models based on oxide-analogy stoichiometry's and a mean field representation of edge surface potential cannot model observed sorption dependence on pH (the range > 8 in particular) and ionic strength. An alternative

electrostatic model for HES equilibria is proposed incorporating cation substitution for structural Mg in the octahedral sheet. Sorption on the LES is treated in terms of surface complexation with aluminol sites.

Some evidence exists indicating progressive, long-term incorporation of the metal cation into the TOT structure which would necessitate a kinetic, and non-equilibrium, representation of cation binding.

1.2.2 Diffusion models for surface associated Me (S:Me)

A variety of models have been proposed for representing the hypothesized contribution of surface associated Me to overall Me flux through porous clay rich materials. They differ in how Me mass is proportioned among one or more surface-associated states (DL, SL, IL, ES) as described in the previous section and in the values for Fick's law parameters assigned to each state. This is schematized in Figure 3 in terms of a time-space discretization of Fick's laws constrained by local equilibrium and electro-neutrality in each cell (i.e. the fluxes associated with the different Me forms are not independent, but coupled).

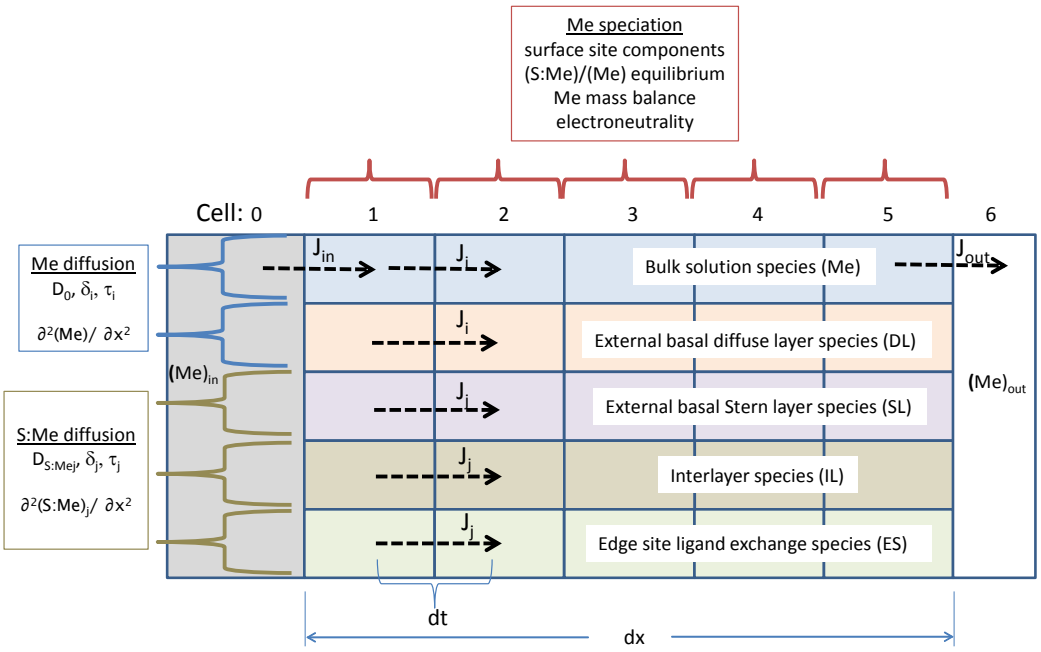

Figure 3 Time-space discretized representation of the variety of models proposed for cation diffusion-sorption in clays (see below).

Examples of the types of conceptual models proposed for coupling cation speciation on clay surfaces with diffusion are:

- All Me mass present as surface species, DL+SL+IL+ES (i.e. that determined by K_d measurements), is immobile; only bulk solution species (Me) diffuse with pore mobilities proportional to their mobilities in free solution, D_0. As mentioned above, this hypothesis is incoherent with measured D_e for alkali and alkaline earth (and certain other element) cations if porosity and geometrical factors (τ, δ) for HTO are assumed to hold for dissolved cations – the corresponding intrinsic mobilities, i.e. 'D_0', are too high. While slight differences could be explained in terms of $\tau_{cation} < \tau_{HTO}$, the roughly ten-fold factors observed for certain cations, e.g. Cs, cannot be justified in terms of physically rational τ values.

- A fraction of the surface-associated Me mass is mobile and contributes along with free solution cation species to overall flux. The fraction, f*(SL+DL+IL+SC), varies depending on the nature of the cation-surface interaction (outer sphere, surface complex formation). If the same parameter values (D_0, δ, τ, d(Me)/dx) are assumed to apply to both free and the mobile fraction of surface species, the corresponding Fick's 2nd law form is:

$$J = -D_0 \cdot \delta\omega_T \cdot \frac{1}{\tau^2} \cdot \frac{(\omega_T + fK_d\rho)}{(\omega_T + K_d\rho)} \cdot \frac{d(Me)}{dx} \qquad (3)$$

  Molera 2002, Molera and Eriksen (2002) consider f to be the time-averaged fraction of surface associated Me mass which is present in a mobile form. They fit this type of model to data for diffusion through bentonite at varying densities and ionic strengths and found: Na: f~100% (all conditions), Sr: f~10 – 50 % depending on density and ionic strength, Cs (trace levels): f~0.5 – 5% depending on density, Co: f~ 0% (all conditions). The most likely candidate for the mobile fraction is diffuse layer (DL) species.

- Gimmi and Kosakowski (2011) arrive at a similar result but expressed differently in terms of an average surface mobility factor, $\mu_s = D_s\tau_s/D_0$, applied to the surface-associated Me mass. The μ_s factors in illite are roughly $Na^+ = 0.4$, $Sr^{+2} = 0.2$, $K^+ = 0.07$, $Cs^+ = 0.0003$ (at trace concentration).

$$J = D_0 \times \nabla C \times \left[\frac{\varepsilon}{\tau_p} + \left(\frac{\rho K_d}{\tau_s}\right)\mu_s\right] \quad (4)$$

- Bourg et al (2006, 2007, 2008) introduce the idea of describing alkali and alkaline earth cation (as well as anion, HTO) diffusion in swelling clays in terms of parallel fluxes taking place in two porosity domains: interlayer and macro pore, contributing to overall flux quantified in terms of apparent diffusion coefficients. A mobility reduction factor is applied to the interlayer diffusion. Cation speciation is not considered other than to assume mass is divided into dissolved (macropore) and interlayer fractions.

$$\frac{(D_a/D_0)_{cation}}{(D_a/D_0)_{neutre}} = \frac{\delta_{cation}}{(1-f)+f\delta_{neutre}} = \frac{\varepsilon+\rho K_d\left(\frac{D_S}{D_0}\right)_{cation}}{\varepsilon+\rho K_d} \cong \left(\frac{D_S}{D_0}\right)_{cation} \quad (5)$$

- Glaus et al (2007) interpreted results of trace cation (Na^+ and Sr^{2+}) diffusion in montmorillonite at variable ionic strength in terms of summed fluxes potentially taking place in two porosities (solution, interlayer), cation mass distribution between solution (Me) and interlayer (IL) being determined by a cation exchange model. The corresponding interlayer flux for trace concentration [B] in electrolyte cation concentration [A] is given by:

$$J_{IL} = -D_{IL}{}^{B}_{A}K\frac{CEC\cdot\gamma_B}{y\cdot z_B(\gamma_A)^{z_B}}[A]^{-z_B}\cdot\frac{d[B]}{dx} \quad (6)$$

with D_{IL} being cation diffusivity in the interlayer, K the conditional B/A exchange coefficient, γ the solution activity coefficients, z ion charge. Glaus et al. (2010) invoke the possibility of diffuse layer cation flux:

$$-J = D_0\cdot\delta_{free}\cdot\omega\cdot\nabla[B]_{free} + D_{IL}\cdot\delta_{IL}\cdot\omega\cdot\nabla[B]_{IL} + D_{DL}\cdot\delta_{DL}\cdot\omega\cdot\nabla[B]_{DL} \quad (7)$$

with specific concentration gradients, $\nabla[B]$, and diffusivities, D, and geometry correction factors, δ. In reality, the model is closer to a two compartment representation for cation flux, i.e. (Me) and (IL+DL), since there is no specific treatment of the diffuse layer associated with external surfaces, either for cations or anions.

- Ochs et al. (1998, 2001) explicitly consider the effects of charged surfaces in compacted bentonite on the porosity accessible to cations and anions by means of an electrical double layer constrictivity factor, $\delta_{el,i} = \frac{1}{n_{0,i}d}\int_0^d n_i(x)\,dx$, where $n_i(x)$ is calculated by a Stern-Gouy EDL relationship. The corresponding Fick's law D_a parameter becomes:

$$D_a = \frac{\omega}{\omega+\rho K_d}\frac{\delta_g\cdot\delta_{el}}{\tau^2}D_0 \quad (8)$$

δ_g/τ^2 being the geometrical factor determined for HTO and K_d the distribution coefficient calculated using a cation exchange model. The model distinguishes between cation mass present in the Stern (f_{SL}.CEC), assumed immobile, and that in the diffuse layer (f_{DL}.CEC), assumed to have the same mobility as free species. The fraction of cation i present in the Stern layer determined by iterative optimisation to diffusion data obtained at one bentonite density (f_{SL} = 0.67 for 400 kg m^{-3}) was validated by predicting D_a for other densities. This model does not distinguish between cations interacting with interlayer and external basal charge, assuming that a Stern-Gouy model is applicable for all surfaces. As indicated above, while use of an EDL description for cations compensating external surface charge seems reasonable, such a model seems less defendable for interlayer volumes given the characteristic surface separation distances (~ 0.5 nm) and radii of hydrated cations (~0.2 – 0.3 nm).

- Appelo and Wersin (2007) and Appelo et al. (2008, 2010) bring together all of the above concepts in the PhreeqC multicomponent diffusion (MCD) module. Alkali and alkaline earth cations are assumed to interact with three types of surface sites (frayed edge, intermediate, planar ~ CEC) through surface complexation equilibria, the constants for frayed edge and intermediate type site complexes assuring complete compensation of these type sites. On the other hand, the constants for the planar sites are such that charge compensation in the Stern layer is incomplete. The pore volume is consequently divided into three fractions (free (δ_{free}), diffuse or Donnan layer (δ_{DL}), interlayer (δ_{IL})), with the total flux of a given cation being determined by its particular characteristics in each volume fraction as given in:

$$J = -\left\{\frac{\omega}{\tau^2}\left(\delta_{free} + \delta_{DL}\frac{c_{DL}}{c_{free}}\frac{n_{H2O}}{n_{DL}}\right) + \frac{\delta_{IL}\omega}{\tau^2{}_{IL}}\left(\frac{c_{IL,CEC}}{|z|}\right)\frac{d\beta}{dc_{free}}\right\}D_0\frac{dc_{free}}{dx} \quad (9)$$

where n_{H2O}/n_{DL} is a 'viscosity ratio' factor to account for potential lower mobility of DL species relative to their free solution mobility and β is the molar or equivalent fraction of the cation expressed relative to the CEC.

This formulation effectively groups basal Stern layer (SL) mass with interlayer (IL) mass, $c_{IL,CEC}$, and applies the same geometric factors and gradient, $d\beta/dx$. $1/\tau^2_{IL}$ is used as a fitting parameter. The integration of interlayer and Stern layer diffusion in the expression of the flux allows taking into account the specificity of cations

having the same charge. Interlayer and Stern layer species are considered to have the same mobility as in free solution, i.e. no viscosity ratio or other factor is applied as was done for DL species, the authors preferring to incorporate this aspect in the tortuosity parameter, $1/\tau^2_{IL}$.

This last 'MCD' model, coupled with an appropriate cation speciation model, will be considered as the reference framework and working hypothesis for interpreting data obtained within Catclay.

1.3 The EC Euratom (FP7) CatClay project

The CatClay (Processes of cation migration in clayrocks) Project, a small-scale focused collaborative EURATOM project[1] has the overall objective of providing a scientifically well grounded answer to the following question: Can the migration of actinides and other strongly sorbing radionuclides in clayrock be predicted by coupling models of (i) their sorption equilibria on representative clay minerals and (ii) the diffusion-driven mass transport of radionuclide sorbed and dissolved species in compacted masses of these clay minerals?

Assuming that speciation models for cation sorption on clay materials (illite, clayrock) developed based on the results of measurements in dispersed material systems are valid for the corresponding compacted material, the CatClay project has the following specific objectives:

- Extending, consolidating and testing against experimental data, of theoretical and numerical models for linking the thermodynamic states of *electrostatically interacting cations* (monovalent, bivalent, trivalent) relative to charged clay surfaces with their corresponding diffusion-driven mobility.
- Evaluation of whether or not the above model framework, after inclusion of appropriate representations of surface complexation reactions for Zn^{2+} and Eu^{3+} with illite edge sites (based on available literature data, results of specific measurements), is appropriate for modeling diffusion driven transport of these species. This will be done by comparing model predictions with experimental data on diffusion in compacted illite systems under different conditions. The target question is whether or not translational displacement of covalently bound cations is capable of contributing significantly to RN flux, as is the case for electrostatically interacting cations present in the Stern layer.
- Determination / modelling of the effects of compacted clay and clayrock structure (mineral-porosity-discontinuities, spatial heterogeneity) at the mesoscopic scale (<mm) on diffusion driven transport of strongly sorbing cations.

In order to advance along these lines, the project was guided by the following strategy:

- Selection of illite de Puy as a model clay mineral and several test cations based on known differences in speciation with clay mineral basal and edge sites: Sr^{2+}, Co^{2+}, Zn^{2+} and Eu^{3+}.
- Development / adaptation of conceptual and numerical models (the PhreeqC MCD code) capable of representing the diffusion-driven transport of the above (and other) cations explicitly in terms of their different surface speciation forms with illite, i.e. basal surface species in both Stern layer and diffuse layer forms, ligand exchange complexes with edge sites.
- Use appropriate surface complexation models to calculate the speciation of test cations in illite-containing systems over a range of chemical conditions (pH, competing cations, complexing ligands) selected to modify significantly the relative contributions of basal and edge site species to overall solid-solution partitioning. If necessary, develop an illite de Puy specific model for the cation based on experimental results (batch sorption, spectroscopic…).
- Carry out diffusion measurements for each cation in highly compacted illite equilibrated with different solution compositions (principally pH and ionic strength, but also carbonate ligand) selected to favour one or the other of the two main types of surface species (edge site complexes; basal plane charge compensation, especially the fraction in diffuse layer).
- Calibrate model for bivalent cation diffusion along basal surfaces (diffuse + solution + Stern?) using data for Sr^{2+} (low pH, low and high ionic strength) and HTO. -->Interpret/improve model.

[1] Grant n° FP7 249624 under Fission 2009 – 1.1.2: Actions in support of the safety case and license applications for geological repositories.

- Predict Co^{2+} and Zn^{2+} diffusion at low (~5) and high pH (~ 9) and low and high ionic strength (1M), assuming behaviour identical to Sr^{2+} for basal and immobility of edge complexes. Compare with data, interpret, conclusions regarding Sr^{2+} / Co^{2+} / Zn^{2+} analogy, immobility of edge site species…
- Modify nature of illite surface sites: The negative surface charge on the planar surfaces of clay minerals can be effectively blocked by high selective transition metal-organic ligand complexes such as copper-ethylenediamine $Cu(en)_2^{2+}$, leading to a reduced access of alkaline and alkaline-earth metals to these exchange sites (Maes et al., 1979). As the concentration of Stern and/or diffuse layer species should be significantly reduced in $Cu(en)_2^{2+}$-illite: --> is the observed diffusion coherent with model predictions based solely on free species diffusion?
- Modify Me solution speciation (CO_3 complexes) --> is observed diffusion coherent with model predictions?
- Characterize compacted illite structure (co-organisation of particles and porosity in oriented samples) plus random walk particle tracking in real sample porosity --> constraints on certain diffusion parameters (ω, τ, δ)
- Carry out, and model, analogous diffusion measurements for each cation in three different clayrocks (Opalinus, Callovo-Oxfordian, Boom Clay).
- Compare the illite and clayrock system results.

The principal results are described in the following sections.

2. Illite de Puy system

2.1 Illite de Puy preparation and characterisation

All experiments reported in the present study were performed on illite collected in the region of le Puy-en-Velay, from the Massif Central region in France. The composition of this illite was first described by Gabis (1963) . Because of its natural origin, the clay-rich Puy-en-Velay formation also contains background impurities such as carbonates, feldspars and quartz. As a consequence, this illite was pretreated using a multistep process and saturated in sodium using the method of Baeyens and Bradbury (1997). High purity Na-Form illite du Puy was used for all of the following experiments.

Samples of purified Na-illite were powdered in a mortar and the <100 µm fraction was separated by sieving. X-ray diffraction data of the Na conditioned illite showed the composition to be ~80-90 wt.% illite and ~5-12 wt.% K-feldspar and ~1-5 wt.% micas. X-ray diffraction performed on oriented preparation have also highlighted the presence of illite/smectite mixed layer (~20 to 30 % of the clay fraction) with a low content of smectite layer (< 20%). The chemical analysis of the major elements was carried at BRGM for Na conditioned purified illite. The results are given in (Table 1). There is good agreement between the chemical composition in Table 1 and that given for illite du Puy in Van Olphen and Fripiat (1979). The mean structural formula of the conditioned Na-illite deduced from EPMA analyses and bulk analyses results is given as:

$$Na_{0.08}K_{0.69}Ca_{0.06}(Si_{3.51}Al_{0.49})(Al_{1.20}Mg_{0.39}Fe^{3+}_{0.36})O_{10}(OH)_2$$

Table 1 Chemical composition in wt% of Na-illite

Na-illite	Na_2O	K_2O	CaO	MgO	MnO	Al_2O_3	Fe_2O_3	SiO_2	TiO_2	P_2O_5	S (total)	C (total)	L.O.I.
Wt %	0.60	7.75	0.40	3.70	0.05	20.50	6.80	50.20	0.71	0.27	<L.Q.	<L.Q.	8.41

The total specific surface area of the powdered Na-illite sample was determined from the nitrogen adsorption/desorption isotherm at 77K according to the BET method (Brunauer et al., 1938) using a Micromeritics Tristar 3000 surface area analyser. Prior to the measurements, the samples were outgassed at 110 °C for 72 h. The measured value was 110 m^2g^{-1}. Grain or real density (ρ_{gr}) was determined in a micromeritics Accupix 1330 helium pycnometer. A mean value of 2.79 ± 0.001 g cm^{-3} was measured for the Na-form of the purified illite.

Zeta potential was determined from the measurement of the electrophoretic mobility with a zetameter Malvern Zetasizer IV. The measurements were made on two different NaCl electrolytes background (0.1 and 1 M) and at two pHs (5 and 9) (cf. Table 2).

Table 2 Zeta potential of Na-illite (in mV)

	NaCl	
pH	0.1 M	1 M
5	-24.4 ± 3.2	-4.9 ± 2.7
9	-32.9 ± 3.2	-9.7 ± 3.2

Cation exchange capacity measurements were performed on Na-form illite using the cobalt hexamine method (Remy and Orsini, 1976) with a reagent/solid ratio of 20 and a reaction time of 30 minutes. CEC yielded a value of 190 ± 10 mmolc kg^{-1} (Table 3).

Table 3 CEC values obtained for the purified Na-form illite

Sample	Cation exchange population (mmolc kg^{-1})				CEC_Σ (mmolc kg^{-1})
	Na^+	K^+	Ca^{2+}	Mg^{2+}	
Sample 1	164.8	3.5	20.3	2	190.5 ± 10
Sample 2	162.7	3.2	20.4	2	188.3 ± 10

Dry clay samples were compressed to a target dry bulk density of 1700 kgm^{-3}. The compaction density was selected in order to mimic the specific porosity (ϕ_i) of claystone (Callovo-Oxfordian) clay matrix (Robinet et al., 2012). A specific method of resin impregnation (Gaboreau et al., 2014) was applied on some compressed samples for the characterization of the microstructure in a water-like saturation state. Electron Transmission microscopy (TEM) was used to measure the size of the illite particles from compressed Na-illite. An average length of 56 ± 20 nm and a

thickness of 18 ± 6 nm were measured. These results are in good agreement with previous studies (Hassan et al., 2006; Rajec et al., 1999). From the ultra-thin section, illite is in the form of particles with a face-to-face stacking of several crystallites (Figure 4). According to Rajec et al. (1999), the lateral surfaces of the particles are not regular due to the stacking of layers of varying sizes. This morphology is called "barrel" (i.e., stacking of elementary layers with a hexagonal base and decreasing size from the center toward the top and bottom of the particle).

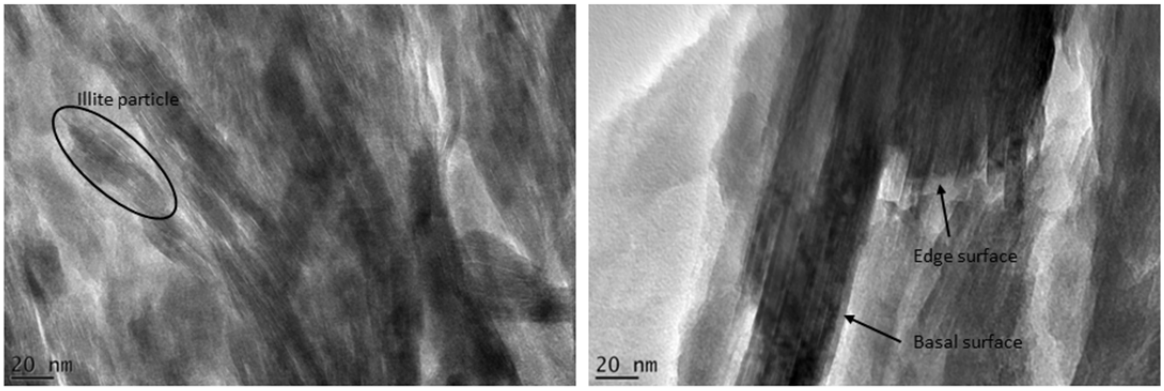

Figure 4 High resolution TEM images of the compressed illite microstructure.

2.2 Particle and porosity organisation in compacted illite

2.2.1 Method

Dry crushed powder of purified illite was first sieved at 100 µm and then compacted, using an hydraulic press at dry density of 1.7 g cm^{-3}. The size of the sample was fixed at a diameter of 35 mm with a thickness of 10 mm. The compaction density was selected in order to mimic the specific porosity (ϕ) of claystone clay matrix (Robinet et al., 2012). The samples were then placed in cells to ensure a mechanical confinement and work at a constant volume for the rehydration and impregnation processes. Some compacted samples, dedicated to bulk macroscopic measurement were freeze-dried and placed under vacuum before measurements as described hereafter. No special method (Keller et al., 2013) was employed in the present work. The compacted samples were immersed in solid nitrogen (melting point inferior than liquid nitrogen), to avoid the precipitation of ice crystals. Lyophilization was applied to sublime the water (Pret, 2003).

Resin impregnation is conventionally used to sample preparation for imagery application and the method used must preserve the texture in a water-like saturation state without losing the clay confinement and modifying the pore space geometry during the manipulation of the samples (sectioning, image acquisition). The works of Sammartino et al. (2002) and (2003) have shown that the specific qualities methylmethacrylate (MMA) monomer (low viscosity, dipole moment similar to water, small size molecules) make it the most suitable resin for impregnating clayey materials. Details about this technique can be found in (Gaboreau et al., 2012; Gaboreau et al., 2011; Pret, 2003; Pret et al., 2004; Pret et al., 2010; Sammartino et al., 2002; Sardini et al., 2009). MMA impregnation was applied to the freeze-dried, lyophilized samples described above. The samples were then place in container under vacuum for 24h. The vacuum was broken by introducing a small amount of MMA (vapor) and then saturated with liquid MMA for 2 months. After this period, MMA was polymerized (solidification into poly-MMA) by heating at 60°C. The impregnated IDP samples in a water-like saturation state and can be handled without damaging the microstructure. These samples were used to prepare specimens for multi-techniques images acquisition.

2.2.2 Results

2.2.2.1 Bulk macroscopic characterization

The pore volume and the pore size distribution (PSD) were determined by N_2 adsorption and Mercury Intrusion Porosimetry (MIP) measurement. Figure 5 shows that more than 90% of the theoretical pore volume was analyzed by N_2 adsorption with pore size diameters ranging from 2 to 100 nm. The pore volume investigated by MIP measurement only reaches 80% of the total pore volume.

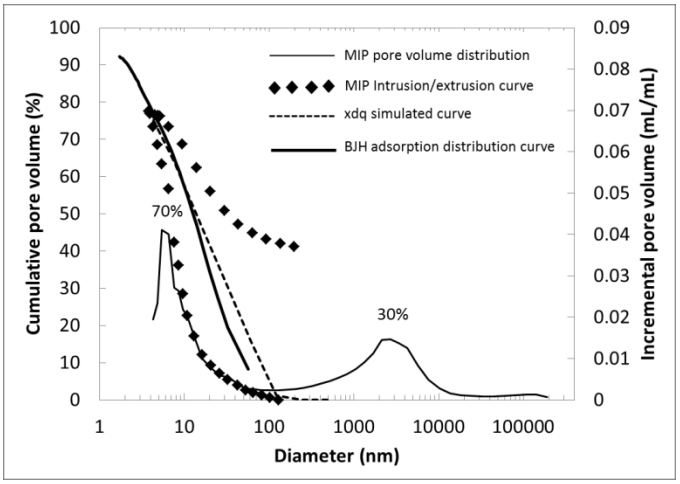

Figure 5 Pore size distributions which were determined with N_2 adsorption and MIP analyses. MIP pore size distribution was calculated with the xdq program. MIP incremental distribution is presented to illustrate the different sizes of pore analyzed.

The cumulative PSD of the connected pore was modeled by simulating the intrusion and extrusion curves using *XDQ* software (Xu et al., 1997a; b). The pore size diameter was affined according the shape of the pore with the modified Washburn equation:

$$d_p = f\frac{\gamma cos\alpha}{P} \qquad (10)$$

where d_p is the pore diameter and *f* the shape factor. The shape factor for various types of pores range from 2 for slit (parallel walls) to 4 for cylindrical pore of circular cross section (Cook and Hover, 1999). The shape factor used to calculate the PSD assumes a 'slit' pore shape. The adjustment made with the shape factor reveals that the PSD calculated with the N_2 adsorption and the MIP are reasonably similar, the only difference being the total pore volume detected with each technique where the pore size limit detection of the MIP is approximately 7 nm.

2.2.2.2 2D microscopic spatial distribution of pores

Microstructure of compacted IDP were analysed through image analysis performed on a upscaling approach from 2D transmission electron microscopy (TEM) and 3D Focus ion Beam nanoTomography (FIB-nT) microscopy images. From the 2D TEM images, semi-variograms were computed for 4 directions (0°, 45°, 90° and 135°) on 3 TEM images acquired with increasing magnifications. Computed semi-variograms are relatively similar for a given direction indicating a coherent microstructure regardless of image magnification. The asymptote is reached around 100 nm indicating that the IDP microstructure is composed of objects, pores or particles, having a size around this value. Semi-variograms computed in the four directions for the same image show microstructure anisotropy. An analytical adjustment of the semi-variograms using an exponential law (the most suitable for the present case in comparison to Gaussian or spherical models) (Woodcock et al., 1988):

$$\gamma(h) = C \times \left(1 - exp\left(-\frac{3h}{a}\right)\right) \qquad (11)$$

with C being the asymptote value and 'a' the correlation length. Adjusting the 'a' parameter provides a direct comparison of the semi-variograms computed in several directions allowing texture anisotropy to be assessed (Figure 6). As an example, a correlation length of about 110 nm is obtained for these 3 TEM images in the 0° direction. The evolution of 'a' as a function of direction is given for the 3 analysed images in a rose diagram (Figure 6). Anisotropic behavior is clearly shown for these three images with the highest and the lowest correlation lengths differing by a factor of around two. Note here that maximum and minimum correlation lengths cannot be directly compared due to a slight tilting between these 3 images and the discrepancy between analyzed directions and the real maximum and minimum orientations. For the 3 images the lowest correlation length is orthogonal to the highest and seems to correspond to the compaction axis (Figure 6). This behavior indicates a preferential orientation of the clay particles and the associated pore space during the compaction procedure.

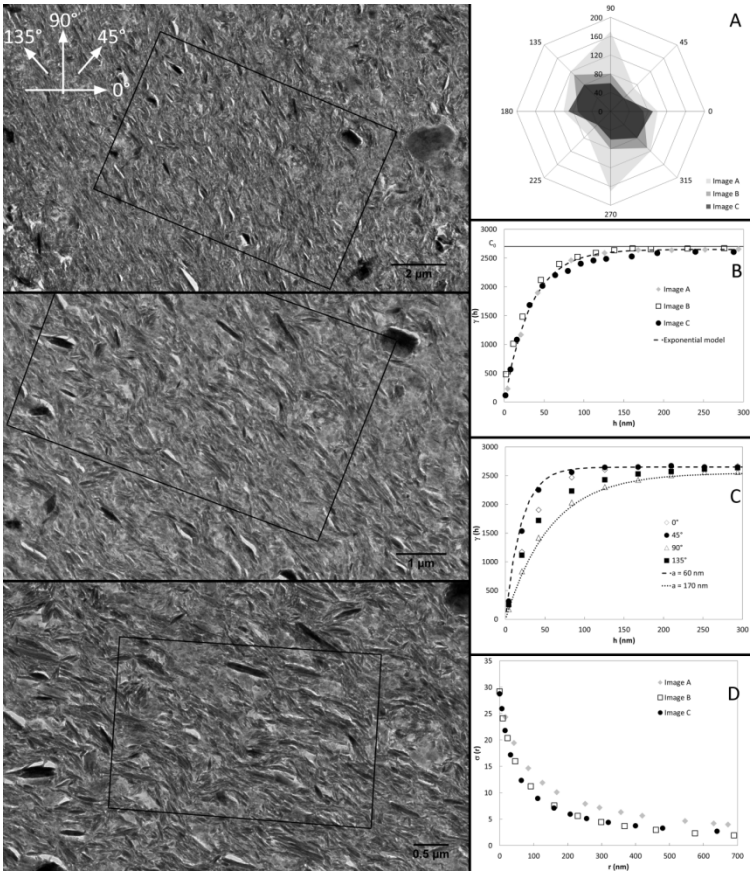

Figure 6 TEM images at different field of view. The orientation grid indicates the sens of totation of the different angle measurment. Orientation (A), variograms (B, C) and covariance (D) calculated on the TEM images.

The representative volume element (RVE) (or Representative Surface Element for 2D application) is defined by Drugan and Willis (1996) as 'the smallest material volume element of the composite for which the usual spatially constant macroscopic representation is a sufficiently accurate model to represent mean constitutive response'. In order to estimate the RVE, a method inspired by that of Galli et al. (2012) was used based on the spatial variability of grey level mean values computed for various window sizes. For a given window size, r, the standard deviation is calculated as follows:

$$\sigma^2(r) = \frac{1}{N}\sum_{x=1}^{N}(Z(r)_x - \bar{Z}(r))^2 \qquad (12)$$

with $Z(r)_x$ the grey level mean of a window of size 'r' centered on pixel x and $\bar{Z}(r)$ the mean grey level of all the windows of size r (which is roughly equivalent to the mean grey level of the image). In order to optimize the computation of the grey level mean values of windows having different sizes, we have applied a 'local mean filter' (spherical filter) of different sizes to the image. The local mean filter transforms the grey level of each pixel into the mean grey level of the pixels in a surrounding disc of radius r. The standard deviation is then computed for each filtered image. For the three analyzed TEM, the standard deviation $\sigma^2(r)$ according to the evolution of the window size images is relatively similar, in agreement with results obtained from semi-variograms (Figure 6). Standard deviations reach an asymptote at a radius of around 500-600 nm; this corresponds to a surface area of 1 µm². The characteristic lengths needed to reach the Representative Surface Element (diameter of 1-1.2 µm) is larger by an order of magnitude than the correlation lengths determined from semi-variograms and in a good agreement with the notion of 'size of object' and the 'size of spatial arrangements of objects'.

2.2.2.3 3D microscopic spatial distribution of pores

Image stacks obtained either by secondary electron (SE) or Energy selective backscaterred (EsB) detection with FIB-nT allow distinguishing porosity (pure black to dark grey levels) from the surrounding clay matrix (grey level). A method was developed to detect the pores close to the voxel resolution (5 nm³). These pores are composed of pixels with grey levels mixed between pure black and the clay matrix grey value. To separate these pores from the surrounding clay matrix, the gradient magnitude, which is equivalent to inflecion point in the intensity profile, was increased by exaggerating the light and dark edges of the transition in order to determine the optimal transition between pores and clay grains. This sharpening effect does not transform the edge of the object but improves sharpness by increasing the acutance, although resolution remains the same (Figure 7).

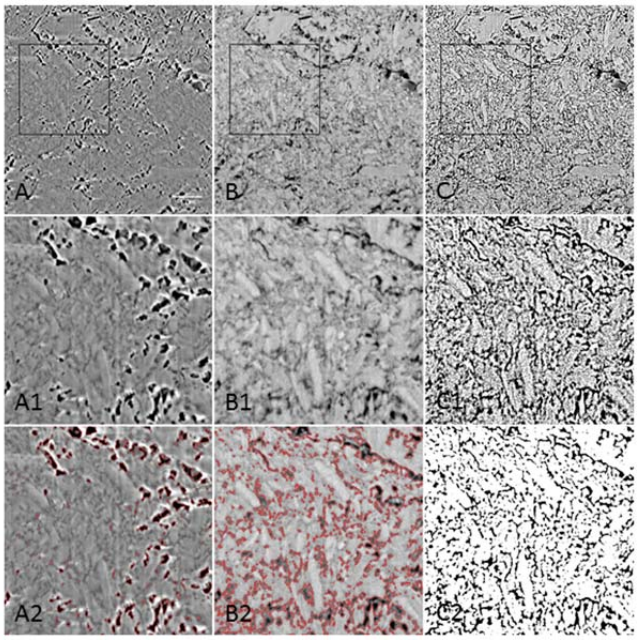

Figure 7 Secondary Electron Microscopy (SEM) images of the compacted Illite de Puy with the same x,y coordinates. A and B are SE and BSE images. The red outlines represent the automatic detection of the pores with the multi-level Ostu thresholding according the type of images (SE or BSE). C images represent the method proposed in the present work to imrove the segmentation of the smallest pores. C3 Illustrates the binarization of the BSE images after the segmentation (black are pores).

The pores were then segmented using a watershed algorithm (Vincent and Soille, 1991). This segmentation procedure was applied to the stack of BSE images. Figure 8 shows a 3D visualization of the volume obtained from FIB-nt (A). The porosity segmented from the previous method was superimposed on the volume (in yellow, B) and the pore volume is illustrated in the Figure 8c. Otsu thresholding (blue pores) was applied on the same volume to illustrate the difference of pore volume segmented according to the 2 methods. A region of interest (ROI) points out this difference. Otsu thresholding only allows showing individualized big pores (blue) while, with the method developed here, the same pores are detected and, in addition, a majority of the smaller ones.

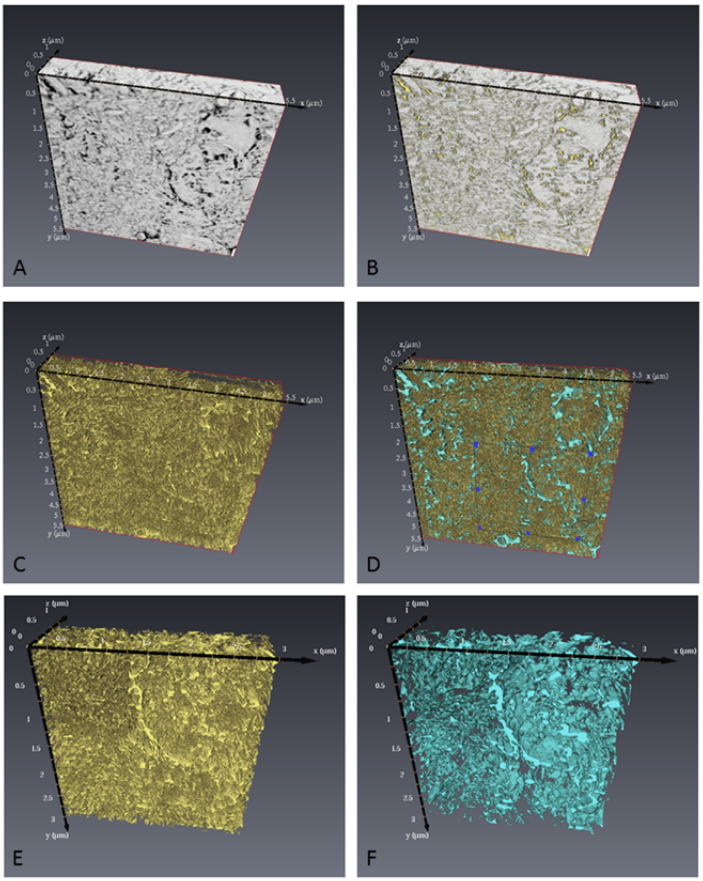

Figure 8 *3D visualization of the BSE FIB-nt stack images (A). (B) segmentation of the porosity (yellow). (C) Pore volume segmented from the method developed in the present work. (D) Superimposition of the porosity segmented with Otsu thresholding (blue). A region of interest (ROI) is placed on the volume to illustrate the difference between the two approaches. (E and F) ROI 3D visualization of the pore volume according the method of segmentation, the present work (yellow) and Otsu thresholding (blue).*

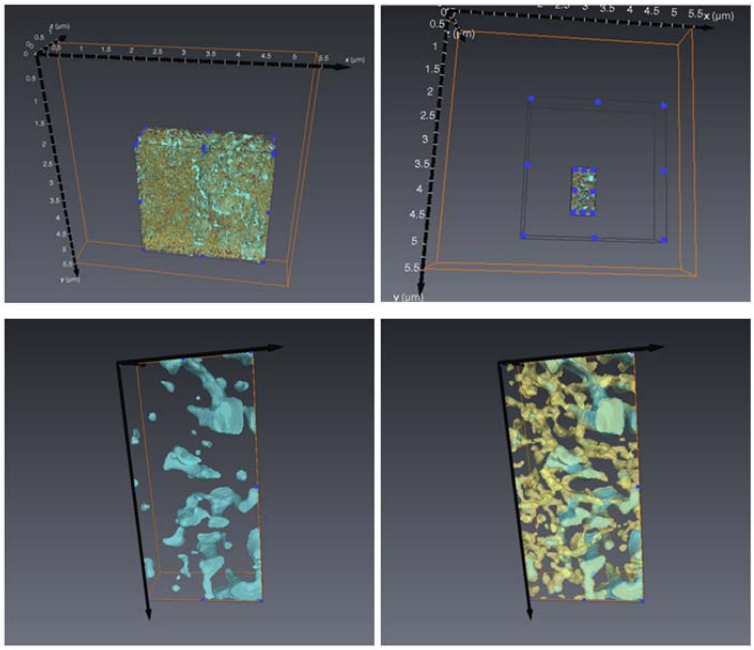

Figure 9 *Region of interest (ROI) illustrating the pores segmented from (1) Otsu thresholding (light blue) and (2) the method developed in the present work (yellow). The yellow pores mainly represent 'throats'.*

Figure 9 focalizes on a ROI where only some big pores are localized in order to illustrate the importance of detecting the smallest pores. The yellow pore network represents, in addition to the big blue pores, detection of the throats assuming the connectivity between the biggest pores.

The void volume segmented from the overlapping area of the BSE images stack allows calculation of a porosity of 28 %, which represent 70 % of the total porosity of the sample (Figure 10). The porosity obtained on the same BSE images stack by using the multi thresholding Otsu method is ~30 % of the total porosity (Figure 10). The main difference between the two previous methods is the connectivity of the pore network. With the classic Otsu method, only isolated pores objects are segmented as mentioned in previous studies (Keller et al., 2011), while with the method developed here, more than 90 % of the segmented pores are connected. The majority of the pores have pore radii ranging from 5 to 50 nm. 30 % of the remaining total porosity could not be reached with FIB-nT owing to the fact that pore radii are below the 5 nm pixel resolution limit.

Pore size distribution (PSD) was retrieved by determining the aperture diameter map (Delerue et al., 1999) on pore volumes segmented with the classic Otsu method and the method developed here. There is good agreement between the PSD obtained with the pore volume extracted from the FIB-nt volume and those calculated from the bulk macroscopic characterization (N_2 adsorption and MIP) (Figure 10). The pore diameters detected range from 5 to 100 nm and the most frequent pore diameter is around 10 nm. The main difference is the limitation on the pore diameters which can be detected. The pore diameter below the pixel size detection limit (< 5nm) could not be segmented and the method used to separate the pore network from surrounding matrix is also of importance. The PSD, obtained from the pore volume segmented with the multi-level threshold method based on Otsu thresholding, shows that only macropores are detected, not the smallest pores. The main mesoscopic pore network is not segmented with such automatic methods. The pore network is mainly composed of individual pores not interconnected where only 10 % of the porosity is connected. Such pore networks do not allow 3D geometrical characterization to be carried out in order to evaluate the anisotropy of the porous compacted clay sample. With the method derived here the PSD display a continuum between the largest and the smallest pores ranging from 5 to ~100 nm in which ~90% of the segmented pore volume is connected. The main difference with the classic Otsu thresholding described in many recent works (Keller et al., 2011; Keller et al., 2013) is that the present method gives access to the class of pores assuring the connectivity of the pore network, the throats between macropores.

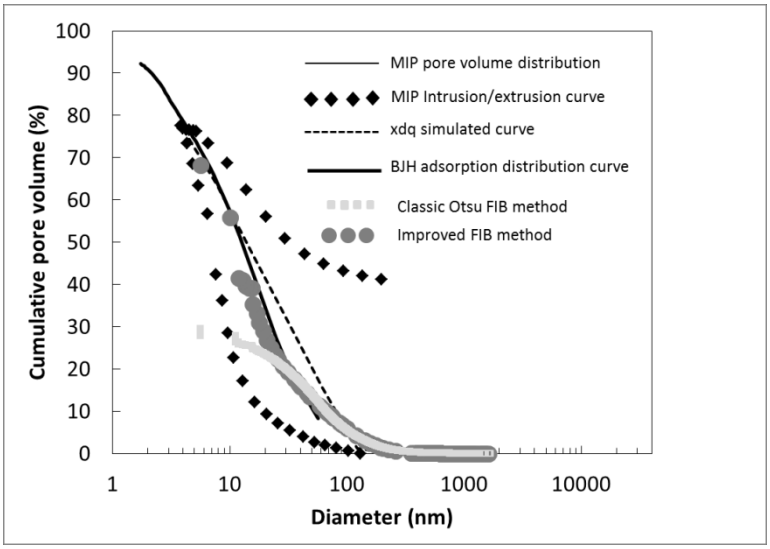

Figure 10 Pore size distribution (PSD) of the compacted Illite de Puy. PSD calculated with the different methods (bulk and microscopic) are illustrating. The PSD calculated from the 3D FIB-nt volume is given according the the two discussed methods (the present work and Otsu thresholding).

In addition to the characterization of the 3D pore network (pore volume, connectivity, PSD), a 3D geometrical characterization of the compacted clay materials from FIB-nt images was performed to evaluate the anisotropy of the compacted clay plug. All the geometrical parameters were extracted using the public-domain software i-morph (http://imorph.fr/). The 3D geometrical characterization of the pore network was performed on a ROI (Figure 11). The calculations were done on the pore volumes segmented from (1) the Otsu thresholding and (2) the method proposed here. The 3D visualization of the components constituting the pore volume displays several individualized pores (one color represents a pore) in the case of Otsu pore network while in the present work a continuum is observed with some small isolated pores. The Mean Intercept Length (MIL) method (Vicente et al., 2012) was used to measure isotropy. If the volume is isotropic, a line passing through the volume at any 3D direction will make a similar number of intercepts

through the pore volume. The MIL calculated for the three main directions X, Y, Z is given in Table 4. The mean length along the Z direction, which correspond to the axis perperpendicular the compaction direction, is higher than for the two others directions.

Table 4 Macroscopic and morphologic description of the compacted IDP determined by image analysis.

Pore Volume characteristics	
Porosity (-)	0.28
Specific surface (m^2/m^3)	3.5×10^{-7}
Cell mean aperture diameter (nm)	78
Throat mean aperture diameter (nm)	19
Half axis length of the equivalent ellipsoid (nm)	
a	14
b	5
c	35
Mean Interception length (nm)	
X	6.1
Y	5.3
Z	6.9

The particle shape analysis (Figure 11c) combined with the orientations in the media confirms these observations. The mean orientation of the main principal axis of the pores is a vector (14, 5, 35), this confirms the anisotropy obtained with the MIL method. The 3D visualization of the shape of the pore (Figure 11c) indicates also that the pore volume is mainly composed of pores with flattened shape and throat. The mean aperture diameter of each class of pore is given in Table 4.

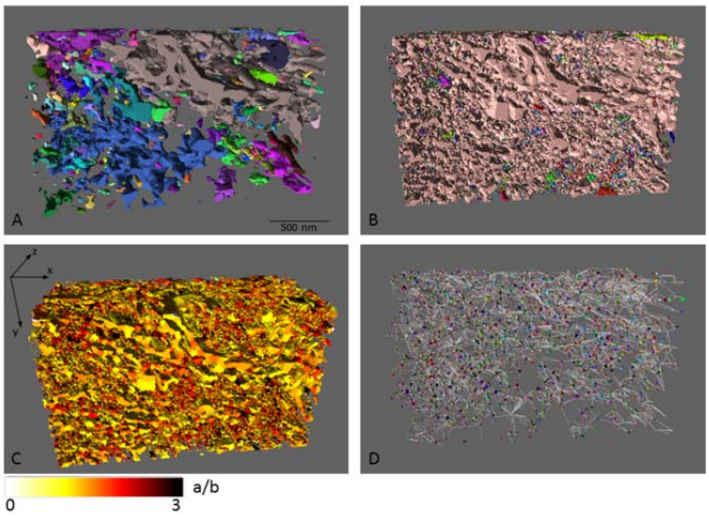

Figure 11 3D visualization of a ROI of 400 x 240 x 180 pixels. (A) Pore components segmented from Otsu thresholding. Each color represents a non-connected pore. (B) Pore components segemented from the present work. (C) Local shape classification, half axis lenght are computed. The color palette indicates the a/b values. (D) Skeleton representation of the pore volume

The tortuosity of the pore volume was calculated from a 3D skeleton obtained by Distance Ordered Homotopic Thinning combined with a fast machine method (Sethian, 1999). The results show that tortuosities depend on direction, with tortuosity being close to 1 in the X, Z directions and around 1.2 in the Y direction (parallel to the axis of compaction). These results confirm that the pore volume organization is slightly anisotropic with a preferential organization of the clay particles perpendicular to the axis of compaction.

2.2.3 Diffusion simulation in 3D pore network

2.2.3.1 Random walk particle tracking and information on G factor

Numerical diffusion simulations were performed by Andra at the pore scale for compacted illite material based on the spatial distribution of pores extracted from 3D FIB/SEM images in partnership with BRGM (cf. §2.2.1). The diffusion equation in heterogeneous porous media is solved for a heterogeneous discretized media using a specifically

developed method called *Time Domain Diffusion* (TDD) (Delay et al., 2002; Delay and Porel, 2003). The TDD algorithm is a particle tracking method defining the rules of particle displacement for 2-D or 3-D grids where each cell is characterized by a specific porosity and an apparent diffusion coefficient. Diffusion modelling can be directly performed on the binarised (pores and solid) image sequence. For our purpose, pores constitute the unique diffusion-accessible phase (porosity is equivalent to 100 %) whereas the solid (the minerals) is assumed to be non-porous.

We have modeled numeric ''in-diffusion'' tracer diffusion experiments from the 3-D digitized volume of the spatial distribution of pores and minerals (spatial resolution: 5 nm). This method is briefly described below; details on it can be found in Robinet et al. (2012). The main steps of the modelling are the following: (i) a constant concentration of particles is imposed on one surface of a cubic volume, (ii) the particles diffuse through using the TDD algorithm, (iii) after a diffusion period the position of each particle is recorded allowing them to be visualized in the 3D volume (Figure 12 b) and the particle concentration profile from the entrance surface to be plotted (Figure 12c); (iv) the macroscopic diffusion coefficient (apparent diffusion coefficient D_a) is finally determined from the diffusion profile by adjusting an analytical solution assuming an homogeneous media. From the diffusion coefficient, a geometry factor can be computed ($G = D_a / D_0$ where D_0 is the diffusion coefficient applied in the pores). The diffusion anisotropy is evaluated by modeling diffusion in various diffusion directions imposed by the boundaries at the sample surface.

Here three sub-volumes of 250×250×180 voxels (named Vol. A, Vol. B and Vol. C) (1.25 µm × 1.25 µm x 900 µm) were used to support in-diffusion modelling (Figure 12a). Diffusion in directions parallel and perpendicular to the compaction axis were successively analyzed for the same volume respectively for these three sub-samples. Several preliminary tests were performed to optimize simulation times. For each simulation, we finally worked with 100 000 particles and a diffusion time of 0.08 ms. Figure 12b illustrates the diffusion of particles thought the virtual sample. As shown in Figure 12c, particle profiles are well-fitted using the analytical solution assuming a homogenous media. This tends to demonstrate that at the scale of few hundred of nanometers the sample can be considered as homogenous.

The computed geometry factors (G) in directions parallel and perpendicular to the compaction axis are given in Table 5. The geometry factor varies according to the compaction axis with $G_\perp$ ranging from 0.329 ±0.01 (Vol. B) to 0.286±0.047 (Vol. A) for diffusion perpendicular to the compaction axis and $G_{//}$ ranging from 0.211±0.014 (Vol. C) to 0.157±0.065 (Vol. A) for diffusion parallel to the compaction axis. This means that the diffusion coefficient is higher in the direction perpendicular to the compaction axis, the diffusion anisotropy is ($G_\perp / G_{//}$) ranges between 1.45 and 2.1. HTO being considered as a non-reactive species, its diffusion behavior is controlled by its mobility through the pore network, consequently our modelling results can be directly compared against HTO diffusion experiments. HTO diffusion experiments through compacted illite (parallel to the compaction axis) performed by SCK-CEN lead to an apparent diffusion coefficient $D_a = 4.5\ (\pm 1.1)\times 10^{-10} m^2/s$ (cf. Table 5). From diffusion modelling, we have obtained a mean $G_{//}$ values of 0.188 involving a D_a for HTO equal to $4.38\times 10^{-10} m^2/s$. This value is in a good agreement with the mean apparent diffusion obtained from diffusion experiments. This good agreement can be explained as follows: (i) almost all the pore space was extracted from the FIB/SEM images (thanks to an important work to pre and post processing of images) and (ii) modelling was carried out on volumes having sizes compatible with the Representative Element Volume (~ 1 μm^3).

Table 5 Results of diffusion modeling and comparison with experimental result obtained by SCK-CEN for HTO.

		Direction of diffusion	Porosity (-)	Geometry factor G (-)	Ecart-type	Equivalent D_a (HTO) ($10^{-10} m^2/s$)	Anisotropy (-)
Diffusion modelling	Vol. A	⊥	0.296	0.286	0.047	6.66	1.45
		//		0.197	0.011	4.59	
	Vol. B	⊥	0.258	0.329	0.01	7.67	2.10
		//		0.157	0.065	3.66	
	Vol. C	⊥	0.324	0.311	0.073	7.25	1.47
		//		0.211	0.014	4.92	
	Mean	⊥	0.2927	0.309	0.071	7.20	1.64
		//		**0.188**	**0.039**	**4.38**	
Experimental HTO diffusion	SCK-CEN	//	0.36	**0.193**	-	**4.5 (±1.1)**	-

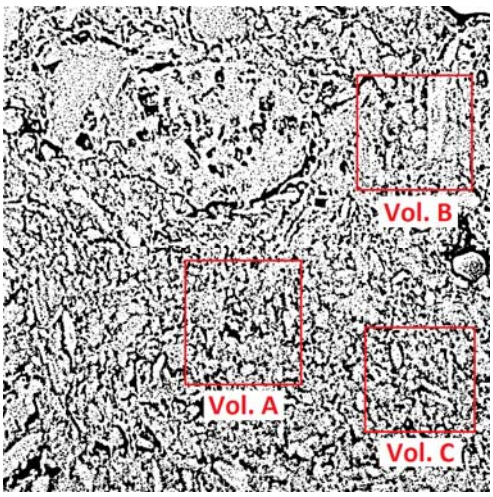

(a)

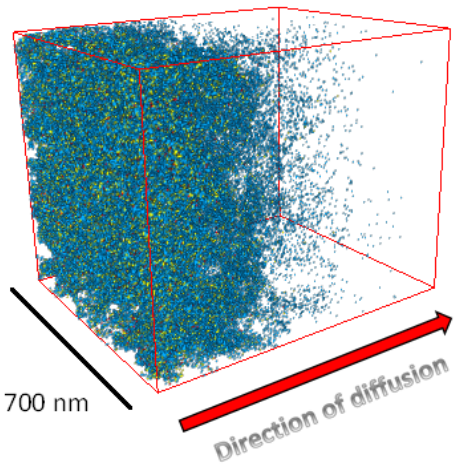

(b)

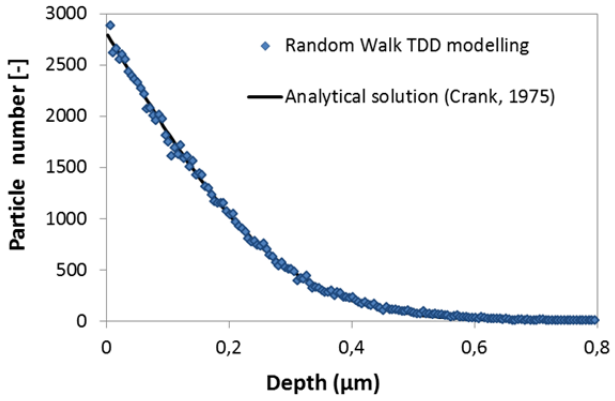

(c)

Figure 12 Diffusion modelling based on the 3D spatial distribution of pores extracted from FIB/SEM images (a) selected areas used to model diffusion; (b) result of an in-diffusion simulation of 400 000 particles through Volume A; (c) example of a diffusion profile fitted using an homogenous analytical solution.

2.2.3.2 Observation concerning the relation of surface-related diffusion to clay particle organisation

All of the foregoing models hypothesize that diffusion of cation species within the interlayer spaces (in expanding clays, smectites) and in the diffuse layer associated with external basal surfaces contribute to net element flux during diffusion-driven transport. The driving force for such diffusion parallel to charged clay surfaces is a surface activity gradient which can be expressed in terms of the molar or equivalent fraction for cation i, β_i, as $d\beta_i/dx_s$, with x_s designating distance along the clay particle surface. The relationship of β_i to the corresponding bulk solution activity, c_i, is given by thermodynamic equilibrium (e.g. cation exchange mass action laws for interlayer, surface complexation for external basal) which means that $d\beta_i/dx_s = d\beta_i/dc_i \cdot dc_i/dx_s$. The gradient dc_i/dx_s will be determined by the difference in c_i at the borders of a given clay particle, which in turn means that dc_i/dx_s will depend on particle orientation relative to the gradient of c_i in the surrounding solution phase, i.e. $1/\tau^2 \cdot dc_i/dx$. As a consequence (cf. Figure 13), particles whose surface planes x and y axes are oriented perpendicular to the local dc_i/dx vector orientation will experience a null surface activity gradient, while those x and/or y axes are oriented at other z-relative angles will experience surface activity gradients proportional to dc_i/dx but weighted by the cosine of the smaller z-relative angle (x or y).

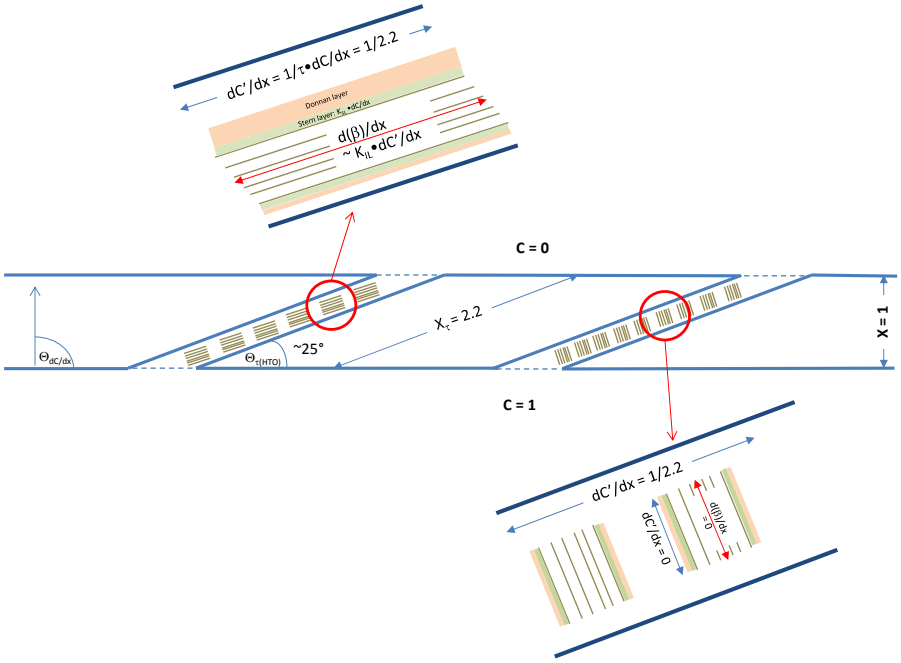

Figure 13 Schematic representation of the relationship between particle orientation, the macroscopic gradient and the surface diffusion gradient.

The implication of the foregoing as regards modelling diffusion in saturated compacted clay material systems is that the distribution of particle orientations in the material will influence the contribution of surface diffusion to overall flux and that the fraction of particles oriented at (or close) to 90° relative to the dc/dx gradient will act as simple sink-source terms. This can be illustrated by the example illustrated in Figure 14 which shows particle orientations in Illite de Puy compacted along the axis indicated by dC/dx in the left hand side image to a dry density of ~1.7 g/cm^3 (Robinet and Gaboreau, 2012). The right hand top figure shows the probability distribution for particle orientations relative to the dC/dx axis; As expected, the most frequent orientation is at 90° to the compaction axis. If the diffusion gradient coincides with the compaction axis, and if the tortuosity (τ=2.2) calculated for HTO diffusion in illite at this density based on measured D_e (~2x10^{-10} m^2 s^{-1}) and porosity (~0.4) (more details in 2.5.1.2) can be used to estimate the mean gradient orientation, dc_i/dx, at the local (particle) scale (~65° relative to dC/dx, e.g. dashed line Figure 14 left), the orientation distribution would be as indicated on the right hand bottom figure.

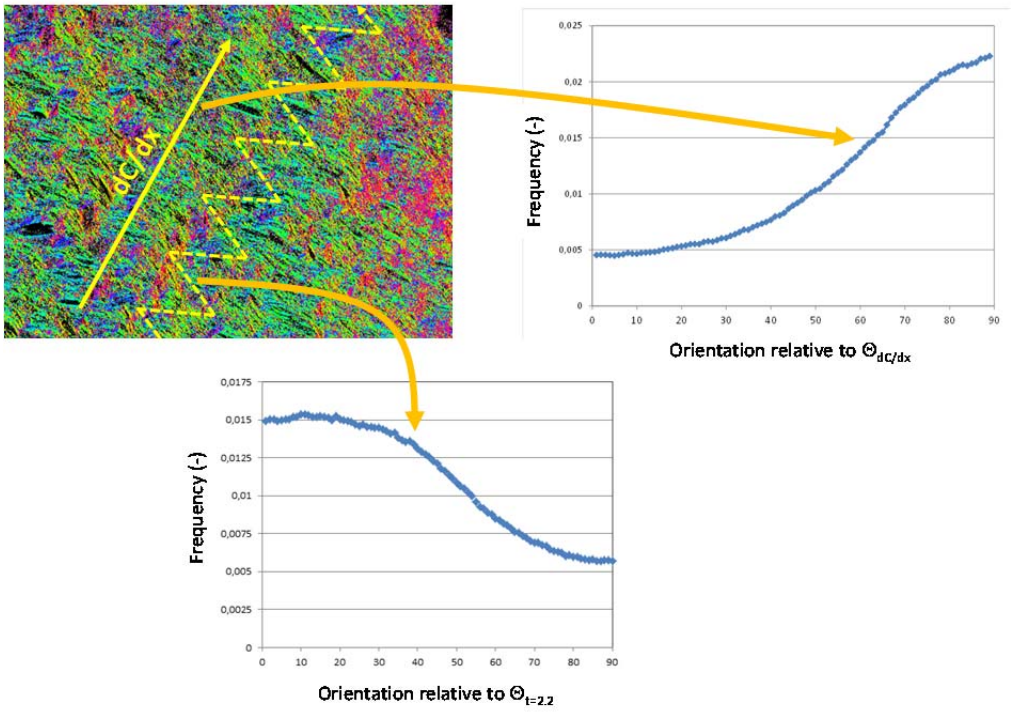

Figure 14 Example of distribution of clay particle orientations in illite de Puy compacted to 1700 kg m³ relative (i) to a macroscopic diffusion gradient oriented along the compaction axis (upper right) or (ii) to an average gradient orientation corresponding to HTO-inferred tortuosity (lower right). Robinet and Gaboreau (2011)

2.3 Speciation of test cations in illite de Puy systems

2.3.1 Solution chemistry in sorption experiments

Knowledge on the composition of the solution in contact with the clay mineral is crucial for sorption studies and surface complexation modelling, as the uptake of a (radio)nuclide, usually present at trace concentrations, can be altered when stable isotopes of the given nuclide are present in solution (thus increasing the total element concentration) or when different ions compete for the same sorption sites (potentially decreasing the uptake) (Soltermann et al, 2013). Clay minerals such as illite are prompt to release elements into solution (Si, Al, Fe, Mg, among others). Those elements are part of the illite structure or originate from mineral impurities in the sample. The elements contained in the illite structure (Figure 1) can be divided in three sub-groups:

- elements present in the TOT (tetrahedral-octahedral-tetrahedral) layers (mostly Si, Al, Mg, Fe);
- elements present in the interlayers of illite (mostly K). Those elements balance most of the negative TOT layer charge that originates from isomorphic substitutions in the tetrahedral and octahedral sheets;
- elements present at the external edge and basal surfaces of the particles that compensate a small part of the total negative charge of the TOT layers (most of the charge is compensated by non-exchangeable interlayer K): those elements are mostly Na because of the sample conditioning process, but also K (cannot be avoided due to the dissolution of the clay) and remaining Ca, Mg and Sr (not removed completely in the purification process or originating from dissolution of impurities and re-adsorption during the conditioning step).

Every cation can potentially compete for cation exchange and surface complexation sites. It is thus important to take all the cations into account that were released into solution during a sorption experiment. As an example, in Table 6 the chemical analysis of a supernatant solution in 0.1 M NaCl at pH 5 and a solid-to-liquid (S:L) ratio of 2 g L^{-1} is shown (equilibration time 7 days). To account for K^+ release, 1×10^{-4} M KCl were added, while the pH was kept constant by using 2×10^{-3} M MES buffer. As such, this solution composition can be regarded as a "typical" background solution in sorption experiments with illite. In addition, Table 6 also shows the respective concentrations for severe acid treatment together with literature data (Poinssot et al., 1999). These data represent the total amount of metal ions, which can be released from the illite material under the respective conditions. As expected, values after acid treatment are higher than for pH 5. As described above, the metal ion levels measured for Si, Al and Mg are related to a (partial) dissolution of the solid, while the other elements originate from (i) elements associated with the illite surfaces and (ii) minor mineral impurities still present despite the conditioning process (a more thorough discussion concerning the impurities can be found below).

Table 6 Chemical analysis of the supernatant solutions for a 0.1M NaCl solution at pH 5 (equilibration time 7 days) and from the severe acid extraction (Δt=1d) at S:L = 2 g L^{-1}. Data from Poinssot (1999) at S:L=8.7 g L^{-1}. For the error estimation four different samples were prepared and analysed separately.

Element	Sorption solution pH 5 (NaCl 0.1 M)	Acid extraction	Acid extraction Literature data (Poinssot (1999))
	mmol kg^{-1} (clay)	mmol kg^{-1}	mmol kg^{-1}
Mg	4.7±2.9	19.2±0.1	39
Al	6.6±5.1	56±0.3	146
Si	*74.6**	131.7±1.3	210
K	23.9±13.2[#]	80.1±0.7[#]	36
Cr	0.047±0.004	n.m.	n.r.
Mn	0.08±0.08	0.23±0.02	1
Fe	n.d.	5.8±0.2	21
Co	0.002±0.001	n.m.	n.r.
Ni	0.02±0.01	0.02±0.01	0.03
Cu	0.17±0.31	0.08±0.002	0.07
Zn	0.24±0.21	0.08±0.01	0.4
Rb	0.024±0.003	0.24±0.001	0.2
Sr	0.20±0.04	0.16±0.002	0.1
Cs	0.005±0.001	n.m.	n.r.
Ba	0.030±0.007	0.08±0.004	0.1
Pb	0.005±0.006	0.02±0.006	0.02

* value calculated based on Figure 15e, as ICP-MS measurement were not reliable
[#] 10^{-4} M KCl was added to account for K^+ release in a "typical" sorption solution
n.d. not detected in solution
n.m. not measured
n.r. value not reported

The amount of background cations released in solution during a sorption experiment is, strictly speaking, only valid for the given experimental conditions. Different parameters such as pH and ionic strength but also experiment duration and the S:L ratio can alter cation concentrations in solution, because some of the processes (e.g. dissolution) are driven by kinetics rather than by thermodynamic equilibrium considerations. As an example, Al^{3+} concentrations in a 0.1M $NaClO_4$ solution for a solid to liquid ratio of 2.4 g L^{-1} are reported to be higher in the pH range between 3-4 than the ones determined for S:L=0.9 g L^{-1}, while the apparent release of Al is lower for 0.01M compared to 0.1M $NaClO_4$ for similar solid to liquid ratios (Poinssot et al., 1999). The former result is logical because at higher S:L ratios a higher surface area is in contact with the solution and hence a larger concentration of Al results from particle dissolution. The latter could be due to a change in dissolution kinetics as a function of ionic strength (unlikely), or can be related to an increase in Al^{3+} uptake by cation exchange processes at low ionic strength. Consequently, the Al concentrations measured at given experimental conditions cannot be considered as representative of the concentration of Al that can release in total or under different experimental conditions (Bradbury & Baeyens, 2005). This statement is also true for other elements such as Ca, Mg or naturally released Sr. Experimental data on the composition of the solution in contact with Na-illite (or in general: clay minerals) in a large range of conditions can serve as a basis to understand these processes. A range of processes to be taken into account have already been pointed out and are available in the literature (Baeyens and Bradbury, 2004; Bradbury and Baeyens, 2005; Poinssot et al., 1999).

- *Cation exchange:* at low pH, cations originating from the dissolution of the clay structure compete with Na^+ for the adsorption on cation exchange sites, including Al^{3+}. H^+ is also part of the competing cations, as the cation exchange capacity (CEC) decreases with decreasing pH (Poinssot et al., 1999);
- *Cation exchange/specific adsorption*: the total CEC of illite is divided in at least three types of sites, i.e. planar sites, type II sites and frayed edge sites. The planar sites seem to be very similar to cation exchange sites present on the montmorillonite basal surfaces. The type II sites are perhaps the most intriguing ones. This subset of surface sites is necessary to model cation exchange processes for Cs^+, K^+ (Poinssot et al., 1999) and Ca^{2+} (Baeyens & Bradbury, 2004). Their structural origin is however unclear.
- *Clay dissolution*: clay dissolution is reported to be fast during the first hours of an experiment and then decreasing with time (Poinssot et al., 1999). The initially rapid dissolution can be tentatively attributed to the dissolution of part of the surface sites, but the stoichiometry of this dissolution process is not necessarily the same as the stoichiometry of the phase. Moreover impurities present in the sample (e.g. kaolinite) can also contribute to the mass balance and change the stoichiometry.

Since the above processes are expected to be dependent on pH, the release of several elements was determined as a function of pH under conditions similar to those in the sorption experiments (for details see below). Briefly, Na-illite was suspended in 0.1 and 0.5 M NaCl at a solid-to-liquid ratio of 2 g L^{-1}. Buffers were added at 2×10^{-3}M (for detailed information on the buffers used see Baeyens & Bradbury, 1997) and the pH was adjusted between 2.5 < pH < 11.5. After an interaction time of 7 days the samples were centrifuged at 600000*g* and the supernatant solutions analysed by ICP-MS for Al, Si, Mg, Ca and Sr. The results are shown in Figure 15a-e (together with data from literature) and are discussed below by element:

- *Ca:* High Ca concentrations are observed at low pH values (i.e. ~2×10^{-4} M a pH 5) for both ionic strengths (Figure 15a). Despite the fact that a careful conditioning process was carried out, this result can be related to the presence of Ca-bearing (mineral) "impurities" in the illite sample as indicated by the work of Poinssot et al. 1999, where similar Ca levels were observed at low pH under similar experimental conditions (e.g. S:L ratio). In addition, the significantly lower [Ca] values reported by Bradbury et al. (2009) are also in line with this hypothesis, as the authors applied a more severe acidic treatment in their conditioning procedure to remove a "Ca-silicate phase" (in detail: several equilibration steps at pH ~ 3.5 for 3-4 h). Apart from accessory mineral dissolution, the high Ca levels at low pH can be due to a (complete) desorption of a Ca stock initially present on a solid surface. Baeyens and Bradbury (2004) have shown that Ca is present on Na-illite and undergoes cation exchange with Na or Cs, and that Ca present on the conditioned material has a very high affinity for the type II sorption site. Thus the hypothesis can be made that Ca can sorb on a deprotonated type II sorption site (indicated by a decreasing Ca concentration at increasing pH values in Figure 15a) while it desorbs when this site undergoes protonation (indicated by the present results and (Poinssot et al. 1999):

$$> SOH \leftrightarrow > SO^- + H^+$$

$$> SO^- + Ca^{2+} \leftrightarrow > SO \cdots Ca^{2+}$$

  The amount of Ca released by this reaction can be calculated to 22.5 mmol kg^{-1} according to Baeyens (2004), which is considerably smaller than the amount of Ca observed in the supernatant (100 mmol kg^{-1} at pH 5) and supports the presence of an accessory Ca-containing mineral phase.

- *Mg and Sr:* Mg and Sr levels at low pH values (pH 5) are smaller than found for Ca by a factor of 20 and 200 i.e. 5 mmol kg^{-1} for Mg and 0.5 mmol kg-1 for Sr respectively. (Table 6). While the latter (low) concentration can be related to Sr associated with the clay matrix, the high Mg concentrations be attributed to clay dissolution. For these elements, similar pH dependence as for Ca, i.e. a decreasing metal ion concentration with increasing pH, is observed (Figure 15b and c). Bradbury et al. (2005) proposed a sorption model for Sr considering two surface complexation sites: one being effective at low (weak site 1: $\equiv S^{W1}OH$), the other at high pH values (weak site 2: $\equiv S^{W2}OH$), with pK_a values of 4.0 and 8.5,. Due to similar chemical properties of Sr, Ca and Mg, sorption processes for Ca, Mg and Sr are attributed to take place on the weak sites 1 and 2. For cation interaction by cation exchange, a dependence on the background electrolyte concentration would be expected. However, the respective effect (i.e. a decrease in concentration) is not evident in our data when the ionic strength is increased from 0.1 to 0.5 M NaCl.

- *Si and Al:* Si and Al are present in the clay structure and their release into solution due to dissolution reactions must be taken into account. For Al, the metal ion concentration in solution is strongly dependent on the pH, with an essentially constant concentration between 5 < pH < 9 (more pronounced for the experiments in 0.5 M NaCl), and high Al levels in the more acidic and basic regions (Figure 15d). The dashed line presented in Figure 15d represents the solubility plot for aluminium hydroxide (bayerite) calculated using the computer code ECOSAT. As observed, the Al concentrations at intermediate pH (5 < pH < 9) follow this solubility curve (also, the data in 0.5 M NaCl are in better agreement compared to the lower background electrolyte concentration) indicating that the amount of Al in solution most likely arises from precipitation of $Al(OH)_3$. At low pH values, the Al levels are likely to originate from clay dissolution, and, due to the high concentrations, may compete efficiently with other cations for cation exchange sites. In contrast to Al, the Si concentration is constant and independent of the pH (Figure 15e). The measured aqueous Si levels (~1.5×10^{-4} M) follow reasonably well the solubility curve of quartz, which is taken as a representative for Si secondary minerals and has a solubility on the lower range of possible solids. This result suggests that Si containing secondary phases control the Si concentrations in solution rather than clay dissolution. This is in line with the lower Si levels reported by Bradbury and Baeyens (2009), where the authors used a more severe conditioning procedure targeting on the removal on a "Ca-silicate phase" (see also the discussion for Ca; note that lower Si concentrations are found despite a higher S:L ratio (9 g L^{-1}) and the shorter contact time (1 day) compared to the present results). A respective mineral phase was, however, not detected in our XRD results (detection limit XRD < 1%). As discussed for Al, the higher Si concentrations observed at high and low pH values indicate a partial dissolution of the clay solid, although a thermodynamically expected complete dissolution of the clay at these extreme pH values does not occur (results not shown). However, due to the high Si levels found in solution, minor

secondary Si containing mineral phases (e.g. the unknown "Ca-silicate phase") may affect metal ion sorption at trace concentrations, as will be discussed below.

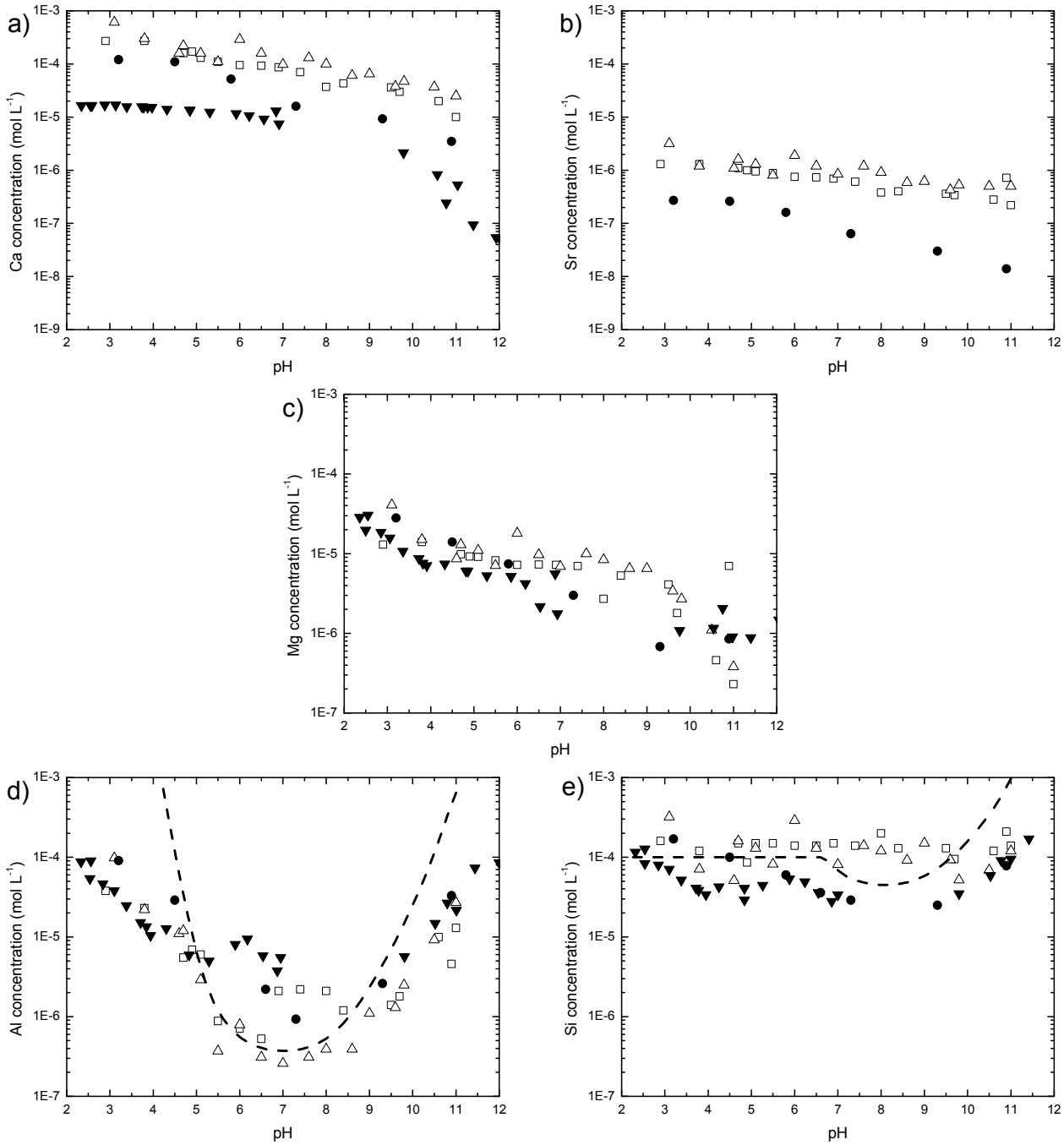

Figure 15 Chemical analyses of the supernatants of a Na-illite suspension as a function of pH for Ca (a), Sr (b), Mg (c), Al (d) and Si (e) in 0.1 and 0.5 M NaCl after 1 day (S:L = 2 g L^{-1}). Data from this work (□: 0.1 M NaCl; Δ: 0.5 M NaCl), Poinssot et al. (1999) (●: S:L = 2.4 g L^{-1}, 0.1 M $NaClO_4$, Δt = 7 d) and Bradbury et al. (2009 (▼:S:L = 9.0 g L^{-1}, 0.1 M $NaClO_4$, Δt = 1 d). The solid lines represent solubility data for aluminium hydroxide (bayerite) and quartz.

2.3.2 Aqueous speciation of Sr, Co, Zn and Eu

In order to study strontium, cobalt, zinc and europium sorption on Na-illite it is essential to determine the aqueous speciation of these elements under the groundwater conditions expected in the studied system (see Table 6 and Figure 15). Aqueous speciation and solubility calculations have been done with Phreeqc v3.1.2. code (Parkhurst and Appelo, 2013) and the thermodynamic data used in the calculations is specified in each section for each element. The background electrolytes that have been used for the sorption experiments have been NaCl (i.e Sr, Zn and Eu) or $NaClO_4$ (i.e Co, Zn). Perchlorate is known to be a non-coordination anion, not affecting the aqueous speciation of the studied cations. In the case of chloride, it has been observed that this anion can form weak complexes with divalent and

trivalent cations, only relevant under very saline conditions. In the following section, it will be discussed when chloride complexation can play a role in the aqueous speciation.

2.3.2.1 Strontium

Strontium exists in natural environment solely in the +2 oxidation state. Thermodynamic data for the strontium aqueous species are listed in Table 7.

Table 7 Thermodynamic data for the aqueous species of strontium.

Reaction	logK	Reference
$Sr^{2+} + H_2O = Sr(OH)^+ + H^+$	-13.29	Baes, 1976
$Sr^{2+} + Cl^- = SrCl^+$	0.23	Bourbon, 1996

The left-hand plot of Figure 16 shows the influence of pH in the aqueous speciation of strontium. Calculations have been done at 0.1 M NaCl taking into account, the water composition listed in Table 7. The fraction diagram shows that the dominant species of aqueous strontium is mainly the Sr^{2+} cation in the pH range between 2-12. Only 8% of the complex $SrCl^+$ will be observed at the higher ionic strength used in the sorption experiments (0.1 M NaCl).

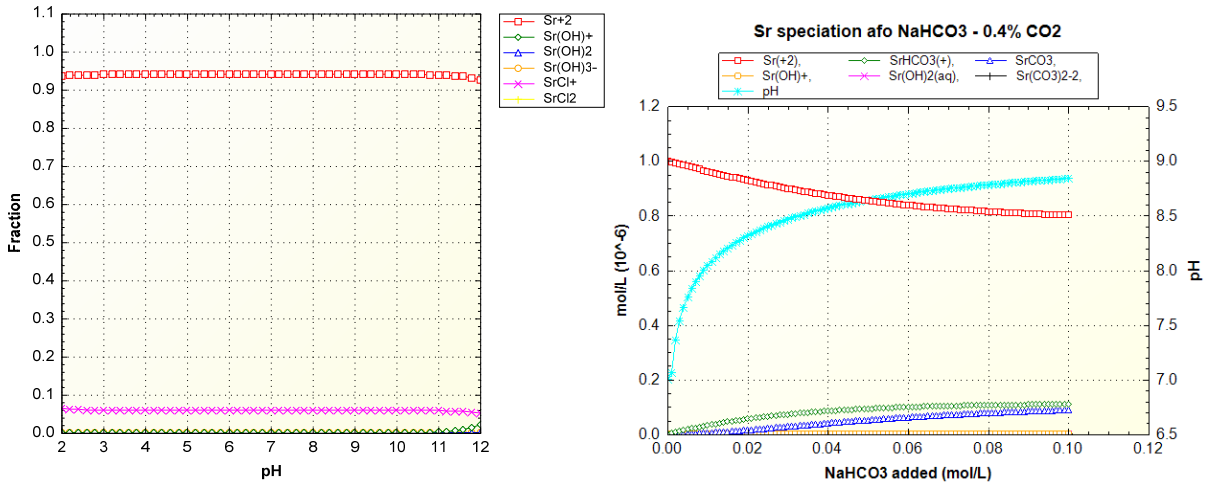

Figure 16 Left-hand plot: Aqueous speciation calculations of strontium as a function of pH at 0.1 M NaCl. Right-hand plot: Aqueous speciation calculations as a function of $NaHCO_3$ concentration at 0.4 % pCO_2 (MOLDATA TDB). Initial ionic strength is set at 0.1 M $NaClO_4$, so conditions should be identical to the left-hand plot at pH 7. While adding $NaHCO_3$, no attempt is made to keep IS constant, so in the end it amounts to 0.203, which should not make that much difference (running the programme with 0.2 M $NaClO_4$ initial IS does not alter outcome significantly).

The right-hand plot of Figure 16 shows the aqueous speciation of Sr as a function of the total inorganic carbonate (TIC) concentration under 0.4% pCO_2, using the Thermodynamic database (TDB) MOLDATA R2v1, the TDB developed at SCK·CEN, which incorporates data from different literature sources (Wang *et al.*, 2011). Thermodynamic data for strontium carbonates are shown in Table 8. At 0.4% CO_2(g), and upon adding additional $NaHCO_3$ to the system, Sr carbonate complexes are formed ($SrHCO_3^+$ and $SrCO_3$) to a maximum of 20% at 0.1 M $NaHCO_3$. At a concentration of 0.016 M $NaHCO_3$ (representative for the Boom Clay), which are used in the diffusion experiments with illite, only <10% of Sr is complexed with carbonate.

Table 8 Thermodynamic data for the aqueous species of strontium carbonates.

Reaction	logK	Reference
$Sr^{2+} + HCO_3^- = Sr(CO_3) + H^+$	-7.53	MOLDATA R2v1
$Sr^{2+} + HCO_3^- = Sr(HCO_3)^+$	1.18	MOLDATA R2v1

2.3.2.2 Cobalt

Cobalt can be found at several valence states, although Co(II) is the most common redox state in aqueous media. Cobalt thermodynamic data for aqueous species are listed in Table 9. As the sorption experiments were performed

solely in $NaClO_4$ and under Ar (exclusion of CO_2), carbonate or chloride complexations are neglected and only hydrolysis species are included and discussed as neither carbonate nor chloride were used in the sorption experiments.

Table 9 Thermodynamic data for the aqueous species of cobalt.

Reaction	logK	Reference
$Co^{2+} + H_2O = Co(OH)^+ + H^+$	-9.23	Plyasunova (1998)
$Co^{2+} + 2H_2O = Co(OH)_2 + 2H^+$	-18.6	Idem
$Co^{2+} + 3H_2O = Co(OH)_3^- + 3H^+$	-31.7	idem
$Co^{2+} + 4H_2O = Co(OH)_4^{2-} + 4H^+$	-46.42	idem

Figure 17 shows the influence of pH in the aqueous speciation of cobalt. Calculations have been done at 0.1 M $NaClO_4$ taking into account, the water composition listed in Table 6. It can be seen that different hydrolysis species appear depending on the pH range. Co is mainly present as Co^{2+} ion at acid-to-near-neutral conditions (pH 2 - 8), at pH 7 cobalt starts to hydrolyse to form the complex $CoOH^+$ and in the pH range between 9.5 – 12 the main aqueous species is $Co(OH)_2$.

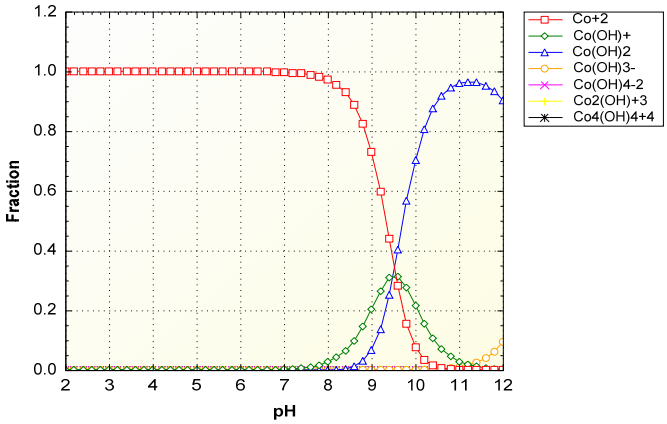

Figure 17 Aqueous speciation of cobalt as a function of pH at 0.1 M $NaClO_4$.

2.3.2.3 Zinc

Zn is not a redox sensitive element and is only present in aqueous solution as Zn(II). Thermodynamic data for zinc aqueous species are listed in Table 10.

Table 10 Thermodynamic data for the aqueous species of zinc.

Reaction	logK	Reference
$Zn^{2+} + H_2O = Zn(OH)^{2+} + H^+$	-9.0	Baes and Mesmer (1976)
$Zn^{2+} + 2H_2O = Zn(OH)_2^+ + 2H^+$	-16.9	Idem
$Zn^{2+} + 3H_2O = Zn(OH)_3 + 3H^+$	-28.4	Idem

Zinc mainly takes the form of Zn^{2+} ions at pH levels up to 8. At higher pH Zn will start to form Zn hydroxide complexes with $Zn(OH)_2$ being the predominant species between pH 9 and 11.5. The negatively charged $Zn(OH)_3^-$ copmplex is only observed at extreme pH values (i.e. > 11.5), while $ZnOH^+$ is only of minor importance between pH 8 and 9 (Figure 18).

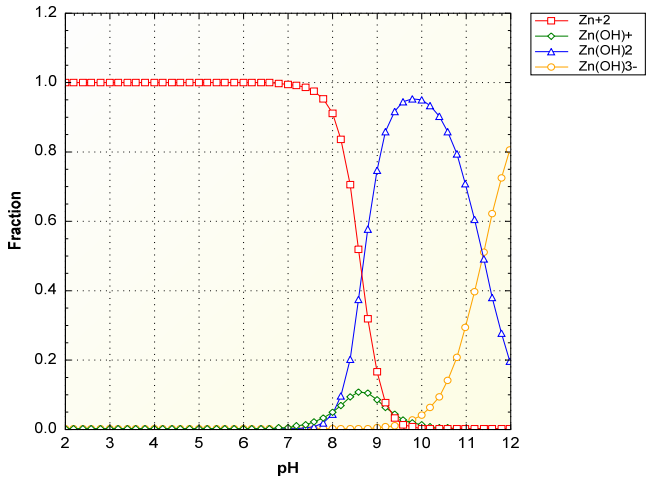

Figure 18 Aqueous speciation of zinc as a function of pH at 0.1 M $NaClO_4$.

The graphs in Figure 19 show the aqueous speciation of Zn under different pCO_2 and total inorganic carbonate (TIC) conditions. At high pCO_2, and upon adding additional $NaHCO_3$ to the system, significant amounts of Zn carbonate complexes are formed. Figure 19a and b represent the Zn speciation under these conditions, calculated with two different thermodynamic databases (TDB): MOLDATA R2v1 (Figure 19a), (Wang et al., 2011), and phreeqc.dat (Figure 19b), the TDB accompanying the Phreeqc geochemical modelling code (Parkhust and Appelo, 2013).

Table 11 Thermodynamic data for the aqueous species of zinc carbonates.

Reaction	logK	Reference
$Zn^{2+} + HCO_3^- = ZnCO_3 + H^+$	-6.40	MOLDATA R2v1
$Zn^{2+} + HCO_3^- = ZnHCO_3^+$	1.45	MOLDATA R2v1

At 0.4% CO_2(g), speciation calculations using MOLDATA TDB predict that the $ZnCO_3$(aq) complex will dominate the aqueous Zn speciation above 0.06 M $NaHCO_3$ (pH 8.7) (Figure 19a). For the conditions representative for the Boom Clay (0.016 M $NaHCO_3$) 25% of Zn is complexed, mainly with carbonate, but also hydrolysis species are formed. By contrast, under the same conditions the aqueous Zn speciation predicted using Phreeqc.dat TDB would be dominated by $Zn(CO_3)_2^{2-}$, already at quite low $NaHCO_3$ concentration (Figure 19b). This latter species is not present in the MOLDATA TDB. At 10% CO_2(g), Zn^{2+} would be the dominant species with smaller amounts of $ZnHCO_3^+$ and $ZnCO_3$(aq), whatever the $NaHCO_3$ concentration (up to 0.1 M), according to MOLDATA TDB. At 0.1 M $NaHCO_3$ (pH 7.7), almost 50% of aqueous Zn forms carbonate complexes (Figure 19c).

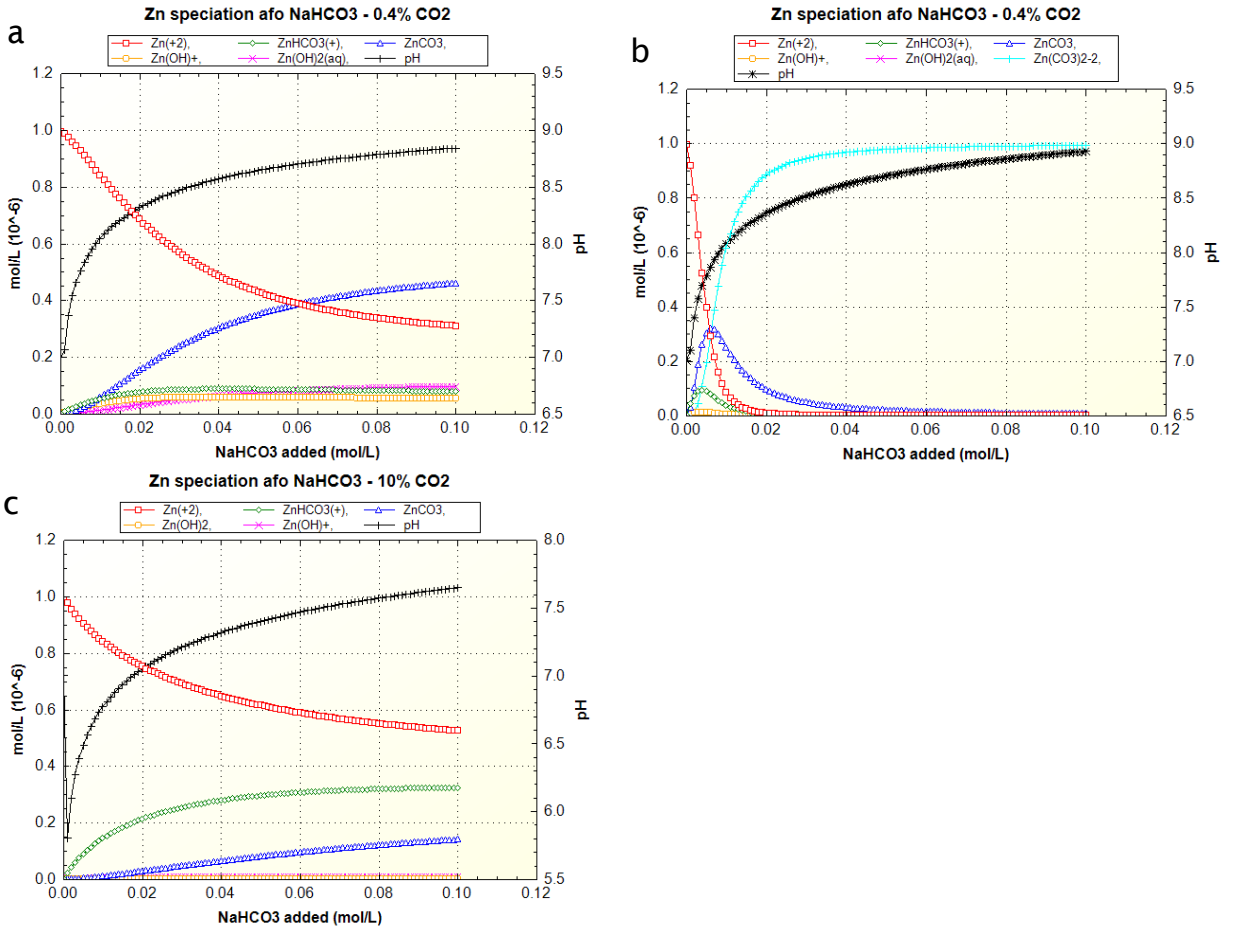

Figure 19 (a-c) Speciation calculations for Zn under different CO_2 conditions as a function of $NaHCO_3$ concentration: (a) 0.4 % CO_2 (MOLDATA TDB); (b) 0.4 % CO_2 (phreeqc.dat TDB) and (c) 10% CO_2 (MOLDATA TDB). The hydrolysis constants for Zn in these calculations differ slightly with these of the speciation calculations without CO_2. The most prominent difference is the appearance of a 4th Zn hydrolysis species at pH > 11, which is outside the experimental scope for most of the experiments (isotherms, diffusion). For pH below 11, it hardly makes a difference.

2.3.2.4 Europium

Europium generally forms compounds with an oxidation state of +III, although it can also exist in the redox state (+II) at very reducing redox conditions, not expected in this work. Eu aqueous speciation can be affected by pH and by the groundwater carbonate and chloride concentration. Silicates have also been identified to form strong aqueous complexes with Eu(III) (Guillaumont (2003)). Speciation calculations have been made in this work using the thermodynamic data listed in Table 12 and the ionic strength correction SIT. Carbonate influence will be not discussed, as no carbonates have been used in the sorption experiments.

Table 12 Thermodynamic data for europium aqueous species and solid phases.

Reaction	logK	Reference
$Eu^{3+} + H_2O = EuOH^{2+} + H^+$	-7.8	Spahiu & Bruno, 1995
$Eu^{3+} + 2H_2O = Eu(OH)_2^+ + 2\,H^+$	-15.7	Neck et al., 2007
$Eu^{3+} + 3H_2O = Eu(OH)_3 + 3H^+$	-26.2	Idem
$Eu^{3+} + 4H_2O = Eu(OH)_4^- + 4H^+$	-40.7	Idem
$Eu^{3+} + 3H_2O = Eu(OH)_3\,(am) + 3H^+$	-17.6	Diakonov et al., 1998
$Eu^{3+} + Cl^- = EuCl^{2+}$	0.76	Luo & Byrne 2001, 2007
$Eu^{3+} + 2Cl^- = EuCl_2^+$	-0.05	Spahiu & Bruno, 1995
$Eu^{3+} + H_4(SiO_4) = EuSiO(OH)_3^{2+} + H^+$	-2.62	Jensen & Chopin, 1996; Thakur et al. 2007

Figure 20 shows the influence of pH in the aqueous speciation of europium. Calculations have been done at the two different ionic strengths used in the sorption experiments (0.1 and 0.5 M NaCl) and with the water composition listed in Table 6. If silicon complexation it is not taken into account, it can be seen that different hydrolysis species appear

depending on the pH range. Eu is mainly present as the free Eu^{3+} ion at acid-to-near-neutral conditions (pH 2 - 7), at pH 7 europium starts to hydrolyse to form the complex $EuOH^{2+}$ and in the pH range between 8 – 11 the main aqueous species is $Eu(OH)_2^+$. Only a pH higher than 11 Eu is present as $Eu(OH)_3$. Chloride complex $EuCl^{2+}$ is only present as minor species in the pH range between 2 – 7, (12%) at I = 0.1 M NaCl and at 30% at I = 0.5M NaCl. If silicon content is taken into account ($1x10^{-4}$ M) it can be observed that the complex $EuOSi(OH)_3^{2+}$ appears at pH between 5 and 10 being the main aqueous species in solution at pH 7 - 9.5 (see Figure 20c). When working with europium at tracer level, it is very important to work at low concentrations as it can be seen in Figure 20d, as the solubility of $Eu(OH)_3$ (am) in the pH range between 8 and 12 can be very low (10^{-6} M and 10^{-9} M, respectively).

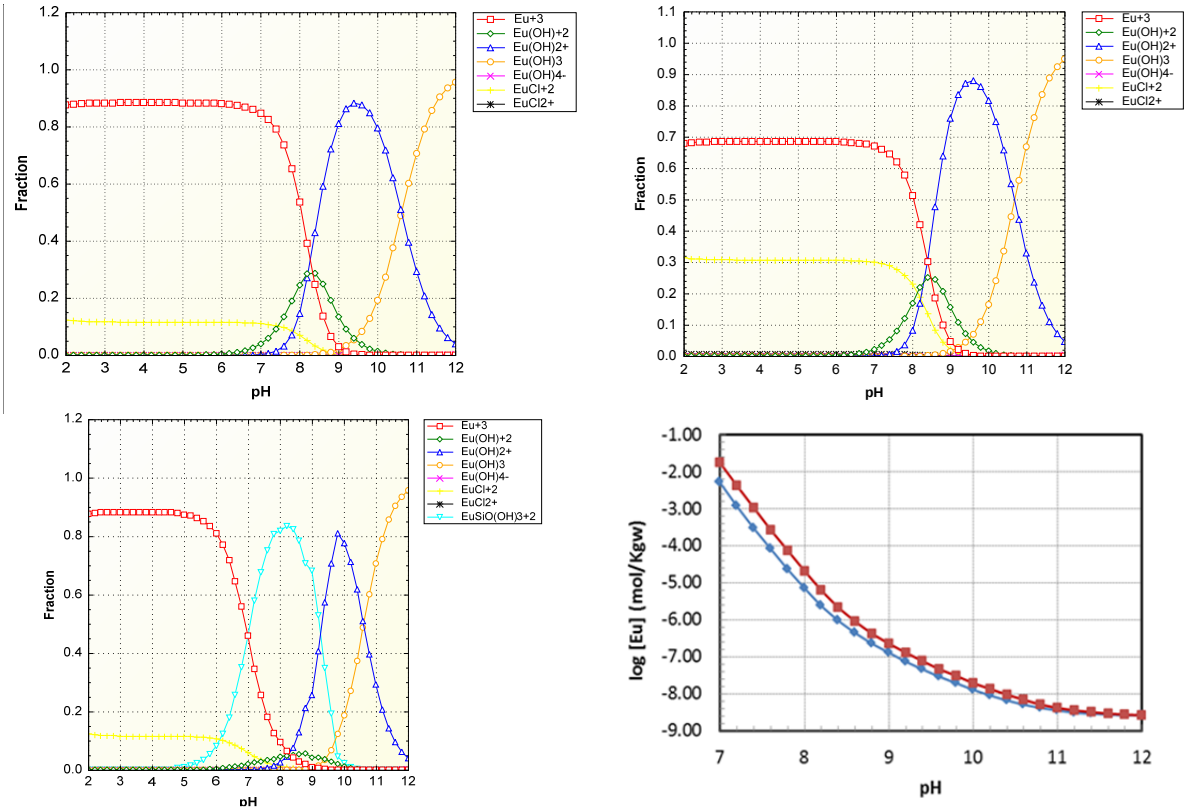

Figure 20 Aqueous speciation of europium as a function of pH at a) 0.1 M NaCl, b) 0.5 M NaCl and taking into account the water composition listed in Table 12 without silicon c) 0.1 M NaCl taking into account the water composition listed in Table 12; d) solubility of $Eu(OH)_3$ (am) as a function of pH at 0.1 M NaCl (blue line), 0.5 M NaCl (red line).

2.4 Sorption of test cations on illite de Puy

2.4.1 State of the art

The state of the art at the beginning of the Catclay project regarding sorption of Sr^{2+}, Zn^{2+} and Eu^{III} on illite and on analogous mineral surfaces is described in project deliverable D1-2b « Technical report on complete dataset regarding the known properties of selected clay minerals and input requirements for macroscopic models. Database regarding sorption of Sr^{2+}, Zn^{2+} and Eu^{III} on illite and on analogous mineral surfaces ».

2.4.2 Overall methodology for measuring sorption

Batch sorption experiments were designed to study the sorption as a function of sorbate (Sr^{2+}, Co^{2+}, Zn^{2+}, Eu^{3+}) concentration at constant pH and ionic strength (*"sorption isotherm"*) and as a function of pH at trace (radio)nuclide concentrations and a fixed ionic strength (*"sorption edge"*). The sorption isotherm experiments were carried out by three EC CatClay partners (SCK·CEN, KIT-INE and PSI-LES) in an inter-laboratory programme, covering a variety of experimental conditions (pH, ionic strength, inorganic (IC) and organic carbon (OC; present as dissolved organic matter). While the detailed experimental conditions were varied by each laboratory, some experimental procedures were standardized for better comparison of the results:

- All experiments were performed in glove boxes under N_2 atmosphere (O_2 < 0.1 ppm) to (i) prevent a possible influence of CO_2 or (ii) to sustain a fixed CO_2 atmosphere (e.g. 0.4% CO_2).

- Radiotracer solutions used in the different laboratories were purchased from different commercial sources. When a non-carrier free solution was used the concentration of active and inactive isotopes were measured by ICP-MS prior to the experiments, giving a total concentration of the respective metal ion in the (radioactive) stock solutions.

- Buffers were used in the pH range 4-10 to ensure the pH stability during the experiments (2×10^{-3} to 1×10^{-2} M). For strongly acidic (pH< 4) and alkaline conditions (pH > 9), the suspensions were titrated to the target pH with $HClO_4$ or NaOH (SCK·CEN), or aliquots of 1M HNO_3 or 0.1M NaOH were added and the solution pH was allowed to evolve with time (PSI-LES). For a detailed description and the effect of the buffers on metal ion sorption see Bradbury & Baeyens (2009a) and Perrin & Dempsey (1974). A modification to this protocol was carried out for the Eu^{3+} sorption edge, where no buffer material was used, for a better comparability to literature data and time resolved laser fluorescence spectroscopy (TRLFS) results (see 2.3.2.4).

- The amount of solid in the tracer containing suspensions, i.e. the solid-to-liquid ratio (S:L ratio) was (mostly) fixed at 1 and 2 g L^{-1} for the experiments performed by SCK·CEN and KIT-INE, respectively. In the experimental protocol followed by PSI-LES, S:L was varied between 0.25 and 2.0 g L^{-1}. While the former ratio was applied to experimental conditions where a high metal ion uptake was expected (i.e. high pH, low ionic strength), the latter was used at low pH and high ionic strength (i.e. low uptake). This procedure should thus increase the concentration/activity of the radiotracer in solution.

- The contact time of the tracer solutions with Na-illite was at least 7 days.

- Phase separation was carried out by ultracentrifugation. Due to the different instrumentation, the centrifugation speed (i.e. the *g*-value) varied between the different laboratories (600000*g*, 180800*g* and 15000*g* for KIT-INE, PSI-LES and SCK·CEN, respectively). In case of Co(II) and Zn(II), sorption edge data (K_d values) were observed to scatter significantly for similar experimental conditions between 4 < pH < 7, when the phase separation was done at lower separation speed (up to 1.7 log units for experiments performed at similar pH and a phase separation at 180800*g*). One possible explanation is the presence of small (colloidal?) clay particles with bound radionuclides remaining in the supernatant (due to incomplete phase separation or resuspension during sample transport), which would increase the experimentally determined activity in solution, decrease the log K_d values and lead to scatter in the sorption data. Due to a lack of a better phase separation, a different experimental protocol was used by PSI-LES for additional batch-type experiments ("membrane approach").

- The activities in the supernatant were measured by γ- or liquid scintillation counting (LSC). Labelled standard solutions were counted simultaneously with the supernatant solutions from the batch sorption tests.

- A formal estimation of the maximum absolute error performed by Bradbury and Baeyens (1997) yielded an uncertainty in log K_d of ~0.15 log units. However, for conditions where the sorption is very high (i.e. high pH values; > 99% of the radiotracer sorbed), higher uncertainties of ±0.5 log units were used (Bradbury & Baeyens, 2005).

2.4.3 Detailed experimental protocols

2.4.3.1 Sr and Zn sorption by SCK·CEN

Zn and Sr *sorption edges* were measured at trace radionuclide concentrations at different ionic strengths in a controlled N_2 atmosphere glovebox (no CO_2). The indifferent electrolyte $NaClO_4$ was used for ionic strength control. Initially, $NaClO_4$ solutions were prepared and buffer solutions were added to a concentration of 5×10^{-3} M to ensure the pH stability during the experiments. For more acidic (pH< 4.5) and alkaline conditions (pH >10) the solutions were titrated to the target pH with $HClO_4$ or NaOH. For the Sr sorption edges, aliquots of radiotracer ^{85}Sr (carrier concentration 5×10^{-9} – 1×10^{-8} M) were added to the $NaClO_4$/buffer solutions. Experiments were performed at two ionic strengths (0.1 and 0.01 M $NaClO_4$). After 1 day of equilibration, subsamples were taken to determine the initial Sr activity (A_{init}). Afterwards, aliquots of conditioned Na-illite suspensions (at the same ionic strength) were pipetted into the centrifuge tubes to achieve a final solid/liquid ratio of 1, 2 or 5 g L^{-1} (depending on the degree of sorption). The suspensions were shaken for 7 days, followed by phase separation at ~ 15000*g* (2h) and filtration (0.45 µm). The initial Sr activity (A_{init}) and the activity in the supernatant after equilibration (A_{eq}) were determined by γ-counting (Canberra Packard Cobra). For the Zn sorption edges, carrier-free ^{65}Zn was added to the $NaClO_4$/buffer solutions. Experiments were performed at two different ionic strengths (0.1 and 0.5 M $NaClO_4$) and at S:L from 1 to 5 g L^{-1}. The rest of the experiment was similar to the method for Sr.

The *sorption isotherm* investigations at SCK·CEN focused on the effect of dissolved inorganic (IC) and organic carbon (OC) on the sorption of Zn on illite. The experiments were performed at pH 8.4 and at different concentrations of dissolved inorganic carbon (IC) (CO_2-free conditions, atmospheric CO_2 (0.04%), 0.4% CO_2 and 10% CO_2) and dissolved

organic carbon (DOC) (15 and 60 mg C L^{-1}) in 0.1 M $NaClO_4$. The DOC was added as purified humic acids extracted from pore water of the Boom Clay (a potential host rock investigated within the Belgian waste disposal programme). The experiments without CO_2 and with 0.4% CO_2 were carried out in controlled atmosphere gloveboxes. The solution of the experiments performed at 0.4% CO_2 consisted of 0.084 M $NaClO_4$ and 0.016 M $NaHCO_3$ with a final ionic strength of 0.1 M, representative of the conditions in Boom Clay. The experiment with 10% CO_2 was performed in a glove box, with an illite suspension in 0.1 M $NaHCO_3$ that was bubbled with a 10% CO_2 gas mixture. A series of Zn solutions covering a Zn concentration range from 1×10^{-7} to 5×10^{-4} M was labelled with ^{65}Zn. For the isotherms without $NaHCO_3$, TRIS buffer (1×10^{-2} M) was added to maintain a constant pH. After one day equilibration, subsamples were taken giving the initial Zn activity (A_{init}). Thereafter, aliquots of conditioned Na-illite suspensions were pipetted into the centrifuge tubes to a final solid/liquid ratio of 1 g L^{-1}. The suspensions were shaken for 7 days, followed by phase separation at ~ 15000*g* (2h) and filtration (0.45 µm). Both A_{init} and the activity in the supernatant after equilibration (A_{eq}) were determined by γ-counting and the total Zn concentration by ICP-MS.

Table 13 Overview of the batch sorption experiments performed by SCK·CEN.

Element	Type of experiment	[M] initial (M)	Ionic strength (M)	S:L (g L^{-1})	pH	Inorganic carbon (%CO_2)	Organic carbon (mg C L^{-1})
Sr	Edge	5×10^{-9} – 10^{-8}	$NaClO_4$ 0.01 M	1-5	3-11	/	/
Sr	Edge	5×10^{-9} – 10^{-8}	$NaClO_4$ 0.1 M	1-5	3-11	/	/
Zn	Isotherm	10^{-7} – 5×10^{-4}	$NaClO_4$ 0.1 M	1	8.4±0.2	/	/
Zn	Isotherm	10^{-7} – 5×10^{-4}	$NaClO_4$ 0.1 M	1	8.4±0.2	/	± 15
Zn	Isotherm	10^{-7} – 5×10^{-4}	$NaClO_4$ 0.1 M	1	8.4±0.2	/	± 60
Zn	Isotherm	10^{-7} – 5×10^{-4}	$NaClO_4$ 84 mM+ $NaHCO_3$ 16 mM	1	8.4±0.2	0.4%	/
Zn	Isotherm	10^{-7} – 5×10^{-4}	$NaClO_4$ 84 mM + $NaHCO_3$ 16 mM	1	8.4±0.2	0.4%	± 15
Zn	Isotherm	10^{-7} – 5×10^{-4}	$NaClO_4$ 84 mM + $NaHCO_3$ 16 mM	1	8.4±0.2	0.4%	± 60
Zn	Isotherm	10^{-7} – 1×10^{-5}*	$NaHCO_3$ 0.1M	1	8.1±0.2	10%	/
Zn	Edge	~10^{-6}	$NaClO_4$ 0.1 M	1-5	3-11	/	/
Zn	Edge	~10^{-6}	$NaClO_4$ 0.5 M	1-5	3-11	/	/

*: concentrations are not yet confirmed by ICP-MS analysis.

2.4.3.2 Co and Zn sorption by PSI-LES

PSI-LES focused on Co and Zn sorption investigations (both sorption edges and -isotherms) at variable ionic strengths (0.01, 0.03, 0.1 and 1.0 M $NaClO_4$). Sorption isotherm experiments were carried out at fixed pH values of pH 5 (Co and Zn) and pH 9 (only Zn). The experimental setup for the *sorption edge* measurements followed a protocol described by Bradbury and Baeyens (2009a). Aliquots of the standard labelled $NaClO_4$ solutions were pipetted into 40 mL polypropylene centrifuge tubes with a total metal ion concentration (active + inactive) of $\times10^{-7}$ M (Zn) and 1×10^{-6} M (Co). Subsequently, buffer (MES and CHES) was added (2×10^{-3} M) and aliquots of the Na-illite suspension were pipetted from the vigorously stirred stock suspension. With regard to the experimental conditions, the solid-to-liquid ratio was varied between 0.42 (high pH, low ionic strength) and 2.0 g L^{-1} (low pH, high ionic strength).

For the *sorption isotherm* experiments, a series of salt concentrations ($ZnCl_2$ and $Co(NO_3)_2{\cdot}6H_2O$) covering the concentration range between 1×10^{-3} and 1×10^{-8} M at the desired ionic strength was labelled with the desired radioactive tracer. Aliquots of this solution were pipetted into centrifuge tubes, followed by addition of buffer (MES for pH 5 and CHES for pH 9; 2×10^{-3} M) and an aliquot of the Na-illite stock suspension. The solid-to-liquid ratio was varied between 0.25 and 1.3 g L^{-1}. After a contact time of at least 7 days (end-over-end shaking), the solid phase was separated (180800*g*) and the pH of the supernatant solution was checked and the supernatant sampled for γ-counting (Canberra Packard Cobra Quantum). All experiments were performed in duplicates.

As mentioned above, highly scattered K_d values in the sorption edge experiments were observed under similar experimental conditions. An example is shown for Zn(II) in 0.1M $NaClO_4$ in Figure 21. One possible explanation is the presence of small clay particles remaining in the supernatant due to insufficient phase separation. Therefore, a different approach was followed for the sorption edge experiments for Co(II) and Zn(II). In a "membrane approach" (Kalis et al., 2007; Marang et al., 2006), the solid phase and the tracer solution are separated by a permeable membrane, preventing the presence of colloids in the outer solution. The decrease in tracer concentration (activity) in the latter is monitored as a function of pH.

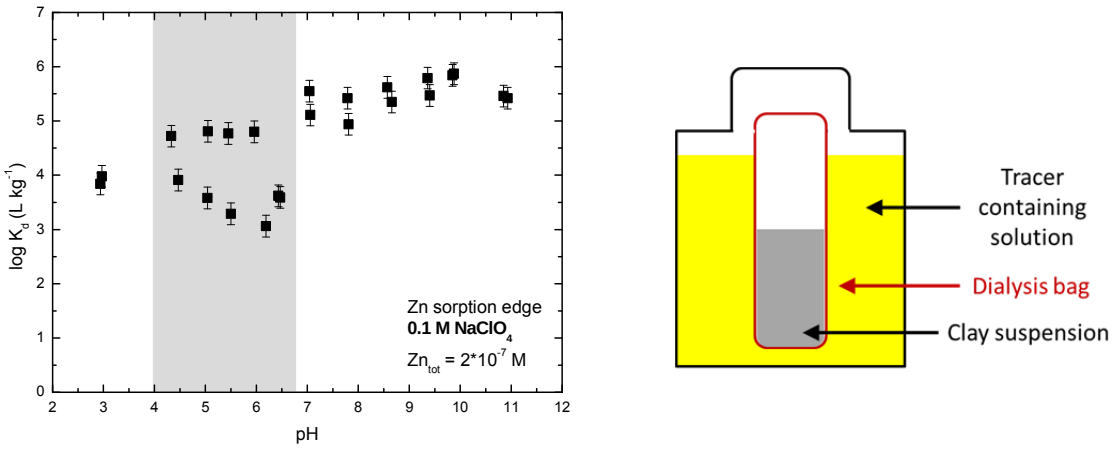

Figure 21 (a) Zn(II) sorption edge measurements at trace Zn concentration on Na-illite in 0.1 M $NaClO_4$. Scattered K_d values are indicated by the grey area. (b) Schematic representation of the "membrane dialysis" setup.

Dialysis bags (Medicell Int., size 9, molecular weight cut-off (MWCO) 12-14 kDa, ~2nm) were rinsed several times with MilliQ water in order to remove impurities. After drying, one side was sealed and 10 mg of Na-illite were suspended in 20 mL of $NaClO_4$ (0.01, 0.03 and 0.1 and 1.0 M). In a polyethylene bottle, 180 mL of a $NaClO_4$ solution (at same ionic strength as the Na-illite suspension) were spiked with ^{65}Zn or ^{60}Co (total metal ion concentration 9×10^{-7} M and 3×10^{-6} M for Zn and Co, respectively) and the pH was adjusted to pH 3.0 (no buffer added). Subsequently, an aliquot was taken (=A_0) and the dialysis bag placed in the bottle. After shaking end-over-end overnight, the bag was removed from the bottle and samples were taken for γ-analysis. After γ-counting the samples were backfilled into the initial reservoir, the pH was increased (ΔpH ~ 0.5) and the procedure repeated. For pH > 4.5, 2×10^{-3} M MES buffer was added to prevent a drift in pH. As the dialysis membranes are expected to degrade at high pH, the experiments were terminated at pH ~9.

The exchange between the outside solution (therefore also for the radionuclide) and the solution inside the dialysis bag is expected to be fast (Δt = 3 h for a complete replacement; personal communication B. Baeyens). However, Kalis et al. (2007) as well as Marang et al. (2006) reported longer times (typically in the order of a few days) for divalent metal ions to reach equilibrium between the donor (containing the metal ion) and the acceptor solution (containing only the background solution) using (negatively) charged cation exchange membranes. Similar equilibration times (~4 days) were reported by Majone et al. (1998) by using cellulose ester membranes. Therefore, an additional study was performed to investigate the sorption kinetics for the "membrane approach".

The setup was similar to the one mentioned above, but MES buffer was used (2×10^{-3} M) to sustain a constant pH. The tracer activities were measured by liquid scintillation counting (LSC) due to the short sampling intervals in the early stages of the experiment (analysis by γ-counting would have lasted at least 30 minutes). As the amount of sorbed tracer is calculated by comparing the activities (A_t) to the one determined at the beginning (A_0), A_0 was corrected for decay. As for all the sorption experiments described in this chapter, the experiments in the "membrane dialysis" approach were performed in duplicate. The results for Zn and Co are shown in Figure 22. As indicated, a steep increase in the distribution coefficient is visible for t < 1d for both Zn and Co. With increasing time, the slope decreases but the K_d seems to increase steadily. The difference in log K_d is Δ = 1 L kg^{-1} for Zn (Δt ~ 80d) and 0.4 L kg^{-1} for Co after ~40d. In the latter case, the experiments were terminated thererafter due to a limited amount of experimental time. When comparing these results to the timeline of the "standard" batch type sorption experiments, i.e. Δt = 7d, K_d increases by ~0.3 and ~0.2 log units for Zn and Co, respectively. Consequently, the K_d values calculated in the "membrane approach" type sorption experiments were corrected for these factors.

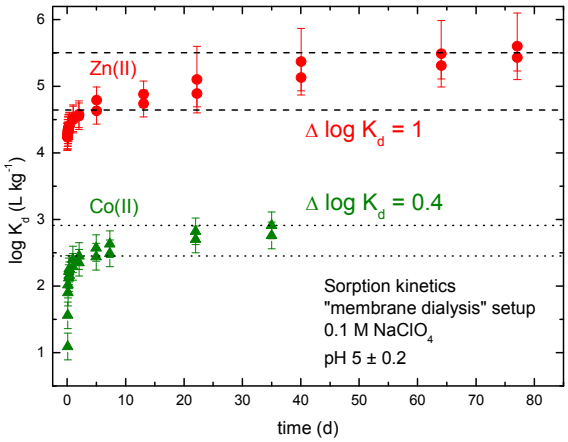

Figure 22 Time dependent evolution of K_d for Zn(II) and Co(II) in Na-illite for the "membrane dialysis" setup at pH 5. Experiments were performed in 0.1 M $NaClO_4$.

Table 14 Overview of the batch sorption experiments performed by PSI-LES.

Element	Type of experiment	[M] initial (M)	$NaClO_4$ (M)	S:L ratio (g L^{-1})	pH	Remark
Co	Edge	1×10^{-6}	0.01, 0.03, 0.1, 1	0.3 – 1.8	2.5-11	/
Co	Edge	3×10^{-6}	0.01, 0.03, 0.1, 1	0.5	2.5-9	Dialysis membrane setup
Co	Isotherm	1×10^{-7} – 8×10^{-4}	0.01, 0.1, 1	0.3 – 1	5	/
Zn	Edge	2×10^{-7}	0.01, 0.03, 0.1, 1	0.3 – 1.8	3-11	/
Zn	Edge	9×10^{-7}	0.01, 0.03, 0.1, 1	0.5	3-9	Dialysis membrane setup
Zn	Isotherm	1×10^{-7} – 8×10^{-4}	0.01, 0.1, 1	0.2 – 0.6	5, 9	/

2.4.3.3 Sr, Zn and Eu (Cm) sorption by KIT-INE

Batch sorption studies: KIT-INE performed batch-type sorption experiments with Sr^{+2}, Zn^{+2} and Eu^{+3} as a function of background electrolyte concentration and pH (Table 15) focusing on experiments under variable metal ion concentration (sorption isotherms). The experimental setup differed slightly from the ones mentioned before: 30 mg of dry Na-illite was suspended in 15 mL of the desired NaCl solution (S:L = 2 g L^{-1}). In case of the *sorption isotherm* experiments, aliquots of three different solutions with the respective non-radioactive element ([M] = 1.5×10^{-6} , 1.5×10^{-4} and 1.5×10^{-2} M), as well as an aliquot of the active isotope were pipetted into 20 mL PE bottles (Zinsser Analytics), giving a total metal ion concentrations of 1×10^{-9} to 4×10^{-4} M. While for ^{85}Sr a carrier-free stock solution was used, the concentration of the inactive isotope(s) has to be accounted for in case of ^{65}Zn and ^{152}Eu. For Sr and Zn the total metal ion concentration in solution (Table 15) was determined by taking into account the stable Zn/Sr inventory associated with the conditioned Na-illite (i.e. 8×10^{-5} mol kg^{-1} for Zn and 2×10^{-4} mol kg^{-1} for Sr). Buffers were added to fix the experimental pH at the desired values of 5.5, 7.0 and 8.3 (these values differ with respect to the ones used by PSI-LES). The experimental protocol on the Eu^{3+} *sorption edge* in 0.1 and 0.5 M NaCl also differed. No buffer materials were used for a better comparison with TRLFS data. The suspensions were shaken for at least 7 days, followed by phase separation at ~ 600000*g*. The activity in the supernatant was determined by γ- and liquid scintillation counting (LSC). In addition, the metal ion concentration in the supernatant was frequently checked by ICP-MS.

TRLFS study: In a glove box, three parallel samples were prepared containing Na-illite at a S:L ratio of 0.25 g L^{-1} and 2×10^{-7} M Cm(III) in 5 mL 0.1 M NaCl. The isotopic composition of the Cm solution is dominated by ^{248}Cm (89.0 %). ^{246}Cm (9.4 %) and other isotopes (< 1 %) are of minor relevance. The pH was increased from 3 to 11 in small steps (ΔpH~0.25) by addition of CO_2-free NaOH (0.01, 0.1 and 1 M, respectively). To keep the system as simple as possible, no buffer was added. The samples were shaken for 2-3 days to reach equilibrium. Subsequently the pH was measured and 3 mL were transferred into quartz cuvettes. During TRLFS experiments, the suspensions were continuously stirred. Prior to each measurement, the emission spectrum of an acidic Cm standard solution (pH ~ 1) was recorded as a reference. The TRLFS measurements were performed with a Nd:YAG pumped dye laser setup at an excitation wavelength of λ_{ex} = 396.6 nm (dye: Exalite 398). The fluorescence emissions at a given laser energy were detected using an optical multichannel

analyser consisting of a polychromator with a 1200 lines/mm grating. To filter out light scattering and background fluorescence, the emission spectra were recorded in the range 580 – 620 nm 1 µs after the exciting laser pulse in a time window of 1 ms. For lifetime measurements, the time delay between the laser pulse and the camera gating was scanned with time intervals of 5 and 10 µs.

Table 15 Overview of the batch sorption experiments performed by KIT-INE.

Element	Type of experiment	[M] initial (M)	NaCl (M)	S:L ratio (g L^{-1})	pH	Remark
Sr	Isotherm	3×10^{-7} – 4×10^{-4} [a]	0.1, 0.5	2	5.5, 8.3	b, c
Zn	Isotherm	2×10^{-7} – 5×10^{-4} [a]	0.1, 0.5	2	5, 9	b, c
Eu	Isotherm	2×10^{-9} – 2×10^{-4}	0.1, 0.5	2	5.5, 7.0, 8.3	b
Eu	Edge	2×10^{-9}; 4×10^{-7}	1 – 4	2	3-11	b
Cm	TRLFS	2×10^{-7}	0.1	0.25	3-11	no buffer

a: Inventory associated with the purified Na-illite was accounted for.
b: 1×10^{-4} M KCl added.
c: Initial concentration determined by the chemical analysis of the supernatant in the equilibrium sorption solution

2.4.4 Results and Discussion

The sorption results for the different elements will be described independently in the following sections.

2.4.4.1 Strontium

Sorption edges for Sr on Na-illite were determined at trace metal ion concentrations ($1x10^{-7}$ – $1x10^{-9}$ M) in 0.01 and 0.1 M $NaClO_4$ in the pH range between 3-11, while two sorption isotherms were measured in 0.1 and 0.5 M NaCl at pH 5.5 and 8.3, respectively. The results are presented in Figure 23 (the corresponding experimental conditions can be found in Table 15.). The principal cations in solution in an equilibrated Na-illite suspension affecting Sr uptake are K, Mg, Ca and Al (note that other cations are also present (Table 6). Due to the similar chemistry of Sr, Mg and Ca regarding selectivity coefficients and sorption behaviour (Bradbury 2005), the latter elements compete with Sr for the available exchange sites. In addition, the dissolved aluminium will also compete with the bivalent cations for these sites. The selectivity of illite for K^+ decreases, when cations with greater charge density, such as Ca, Mg or Al are present. However, the constant background concentration of 10^{-4} M of KCl (as was used in the sorption experiments to account for K^+ release from the clay solid) may have an influence in the availability of sorption sites for Sr.

Sr sorption edges show clearly that the uptake of Sr is a function of the background electrolyte concentration, as $\log K_d$ is approximately 1 to 1.5 orders of magnitude higher for the lower ionic strength (0.01 M), thus indicating that cation exchange is the dominating sorption mechanism for Sr on Na-illite. While the decrease in K_d for pH values < 5.5 can be related to competitive effects from cations released into solution from the illite itself (see section 2.3.1), the increase in sorption for pH ≥ 9 is correlated to surface complexation (Bradbury and Baeyens (2005b). This result is in line with the sorption isotherms, where $\log K_d$ is observed to be affected by an increase in background electrolyte concentration (0.1 to 0.5 M) rather than by an increase in pH (pH 5.5 to 8.3). In addition, constant $\log K_d$ values are detected with increasing Sr equilibrium concentration, thus indicating an uptake solely by cation exchange. The results at 0.5 M NaCl tend to increase at higher $[Sr]_{equilibrium}$, though this effect might only be an experimental artefact. As the sorption of a bivalent cation in a bivalent-monovalent cation exchange system decreases as the square of the monovalent cation concentration (Bradbury and Baeyens, 2005), K_d should decrease due to competition by a factor of 25 (~1.4 in log units) in 0.5 M NaCl compared to 0.1 M background electrolyte solution. However, such a distinct decrease is not indicated by the present results, where $\log K_d$ drops only by ~0.8 log units. The reason for this behaviour is not understood in detail at the moment.

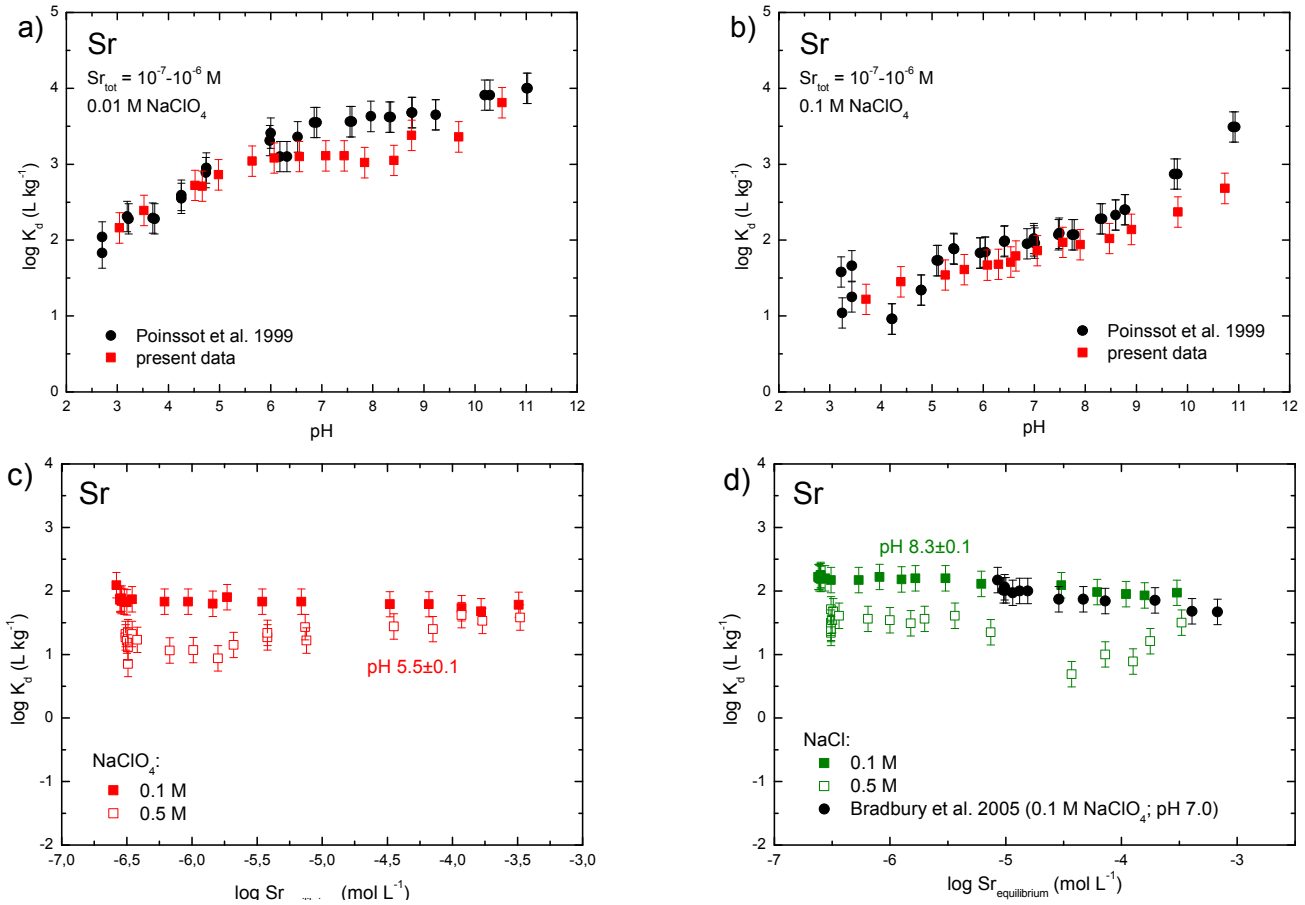

Figure 23 Sr sorption edge measurements on Na-illite in 0.01 M (a) and 0.1 M $NaClO_4$ (b) at low Sr concentrations together with literature data (S:L=1.5-1.9 g·L^{-1}; $[Sr]_{initial}$= 1x10^{-9} M) (Poinssot et al., 1999). Sr sorption isotherms at different NaCl concentrations at pH 5.5 (c) and 8.3 (d) together with literature data measured at pH 7 (S:L=1.8 g·L^{-1}; 0.1M $NaClO_4$; (Bradbury & Baeyens, 2005). For experimental details see Table 13 and Table 15.

Bradbury & Baeyens (2005) were able to model Sr sorption edges onto Na-illite with the same origin (Poinssot et al, (1999) by taking into account cation exchange and the surface complexation reactions at a single site (≡S^{W2}OH), the latter process dominant only at high pH (pH ≥ 9). Despite some uncertainties, i.e. scattered data at I = 0.5 M for the sorption isotherms, lower K_d values at intermediate and high pH (sorption edge data in 0.01 and 0.1 M $NaClO_4$, respectively), the present results are in good agreement with the data given by Poinssot et al. (1999) and Bradbury and Baeyens (2005) (Figure 23a, b and d), thus indicating a similar sorption behaviour for Sr on the Na-illite used in this work.

2.4.4.2 Zinc

<u>In absence of inorganic and dissolved organic carbon</u>

Experiments on Zn uptake onto Na-illite were performed by three laboratories (PSI-LES, KIT-INE and SCK·CEN) as a function of pH (*sorption edges*) and metal ion concentration (*sorption isotherms*) between 0.01 and 1M NaCl and $NaClO_4$. Zn uptake in 0.1M $NaClO_4$ is presented in Figure 24 as both sorption edges and sorption isotherms. For both datasets, the results obtained in the different laboratories are in good agreement. However, scattered K_d values are observed for the conventional setup experiments at 4 < pH < 7 for the experiments performed at PSI-LES and may be related to an insufficient phase separation (see discussion above). This is supported by comparable logK_d values for the "conventional sorption setup" and the "dialysis membrane approach" over the whole pH range (Figure 24a). Excluding the scattering data for the conventional setup, the sorption edge data show an increase in Zn(II) uptake with increasing pH up to pH ~7, while at higher pH the distribution ratios are similar (note that the errors in this pH range are higher). A typical "edge" shape is however not observed, as the logK_d varies roughly about 2 log units (3.7 to 5.7). The flat shape of the sorption edge is quite remarkable and differs significantly from measured Zn sorption edges on Na-montmorillonite (Baeyens & Bradbury (1997); Bradbury & Baeyens (1997)), where logK_d varies over four orders of magnitude (with log K_d from ~2 to 6) with a sharp edge situated between 5 < pH < 8 (Figure 24a). A good agreement between the different laboratories is also observed for the sorption isotherms results, where the experiments were performed only in the conventional sorption setup. The distribution coefficients at trace Zn concentrations are in line with the values determined by sorption edge measurements. For low Zn equilibrium concentrations, the K_d is constant

up to ~ $1x10^{-8}$ M, after which a gradual decrease is detected with increasing $Zn_{equilibrium}$. This effect is more pronounced at pH 5 compared to pH 9, with a change in K_d of ~4 and ~1 log units, respectively.

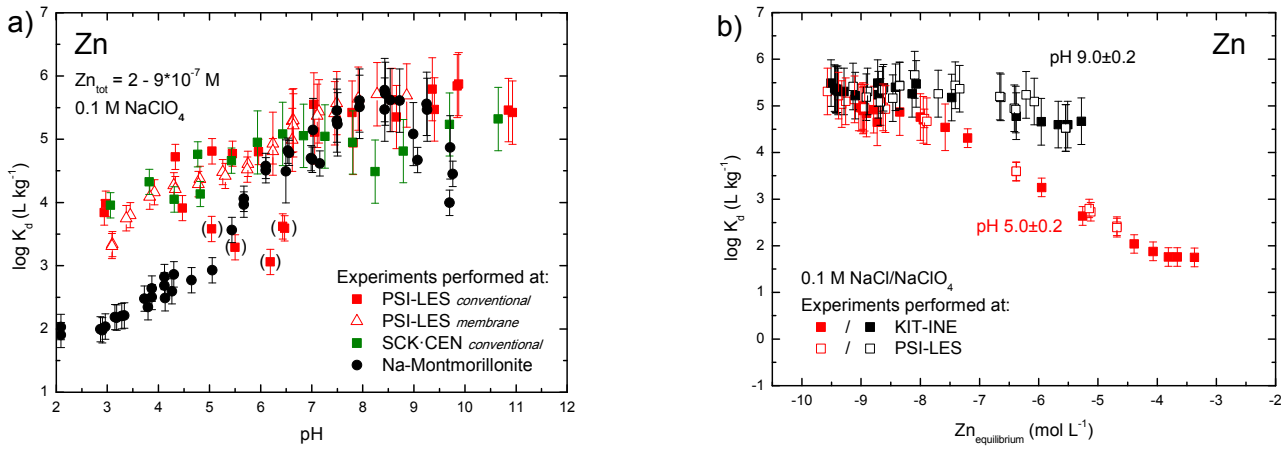

Figure 24 pH dependent Zn(II) sorption onto conditioned Na-illite at trace Zn levels in 0.1M $NaClO_4$ determined by conventional setup and the dialysis membrane approach together with literature data on Zn sorption onto Na-montmorillonite ([Zn]<5 $x10^{-8}$ M; S:L = 1.2 g L^{-1}; 0.1 M $NaClO_4$; Bradbury and Baeyens, 1997) (a). Zn sorption isotherms at pH ~5 and ~9 in 0.1M NaCl and $NaClO_4$ (b; conventional setup only). The experiments were performed by the CatClay partners in three different laboratories. For experimental details see Table 13 and Table 15.

The pH dependent Zn sorption onto Na-illite at various ionic strengths (0.01, 0.03, 0.1, 0.5 and 1M $NaClO_4$) is shown in Figure 25. An effect of the background electrolyte concentration on the Zn uptake at trace Zn levels was not observed by SCK·CEN (Figure 25a) and was neither detected by PSI-LES using the conventional sorption setup method (results not shown). However, $logK_d$ values for the latter experiments were observed to scatter strongly, hampering a conclusive interpretation. Consequently, the setup was modified and the sorption experiments were performed in the "dialysis membrane" approach. The results are shown in Figure 25b. By this method an ionic strength dependence is apparent, with an increase in Zn sorption for decreasing $NaClO_4$ concentration at pH < 7 (data in 0.03M $NaClO_4$ are also available but omitted due to a better visibility). Above pH 7, distribution coefficients for all $NaClO_4$ concentrations are observed to be more or less similar. Note that this result is not in contradiction to the results obtained by SCK·CEN (Figure 25a)), as the change in $logK_d$ between 0.1 and 1M $NaClO_4$ is only ~0.5, i.e. it lies within the analytical uncertainty. However, questions still remain, if the data for the "conventional setup" and the "dialysis membrane approach" can be compared without restrictions, as sorption equilibrium is apparently not achieved for the latter (Figure 22). In the case of the sorption isotherms (Figure 25c and d) no ionic strength dependence is visible for pH 5 and 9. In summary, the following can be deduced from the present results:

- inner-sphere complexation is the dominant sorption mechanism for pH > 7.
- non-specific ion exchange reactions seem to be absent in the Zn/IdP system, indicating that surface complexation mechanism is the dominant sorption process over the whole pH range. This result is in contradiction with the results for Zn(II) sorption onto Fithian Na-illite (Vermilion County, Illinois) (Gu and Evans 2007), as well as Zn sorption onto Na-montmorillonite (Figure 24a; Baeyens & Bradbury (1997); Bradbury & Baeyens (1997)). In addition, cation exchange mechanisms on Na-IdP were reported for Ni as trace cation (Bradbury and Baeyens, 2009a). A clear expalantion for this discrepancy cannot be given here. The data may point to the presence of an accessory mineral with a high affinity towards Zn in the acid-to-neutral pH range or a Zn selective sorption site, responsible for Zn uptake at trace concentrations. Both assumptions remain to be confirmed experimentally.

The sorption edge at I = 0.1 M $NaClO_4$ was modelled (Figure 26) using a non electrostatic model similar to the one described in the literature for other divalent cations (Bradbury & Baeyens, 2009a). Information on the reactions and site densities can be found in Table 16 and Table 17. Only experimental data from the conventional setup have been used in the modeling (in this model, no competition with the cations of the porewater is taken into account). Cation exchange and strong and weak sites have been used for the surface complexation model. As can be seen a high sorption under acidic conditions has been measured in all the experiments. This is an unexpected observation that can still not be explained. For modeling this high sorption, a very high selectivity constant needs to be used which is not in agreement with the sorption behavior of other divalent cations in Na-illite.

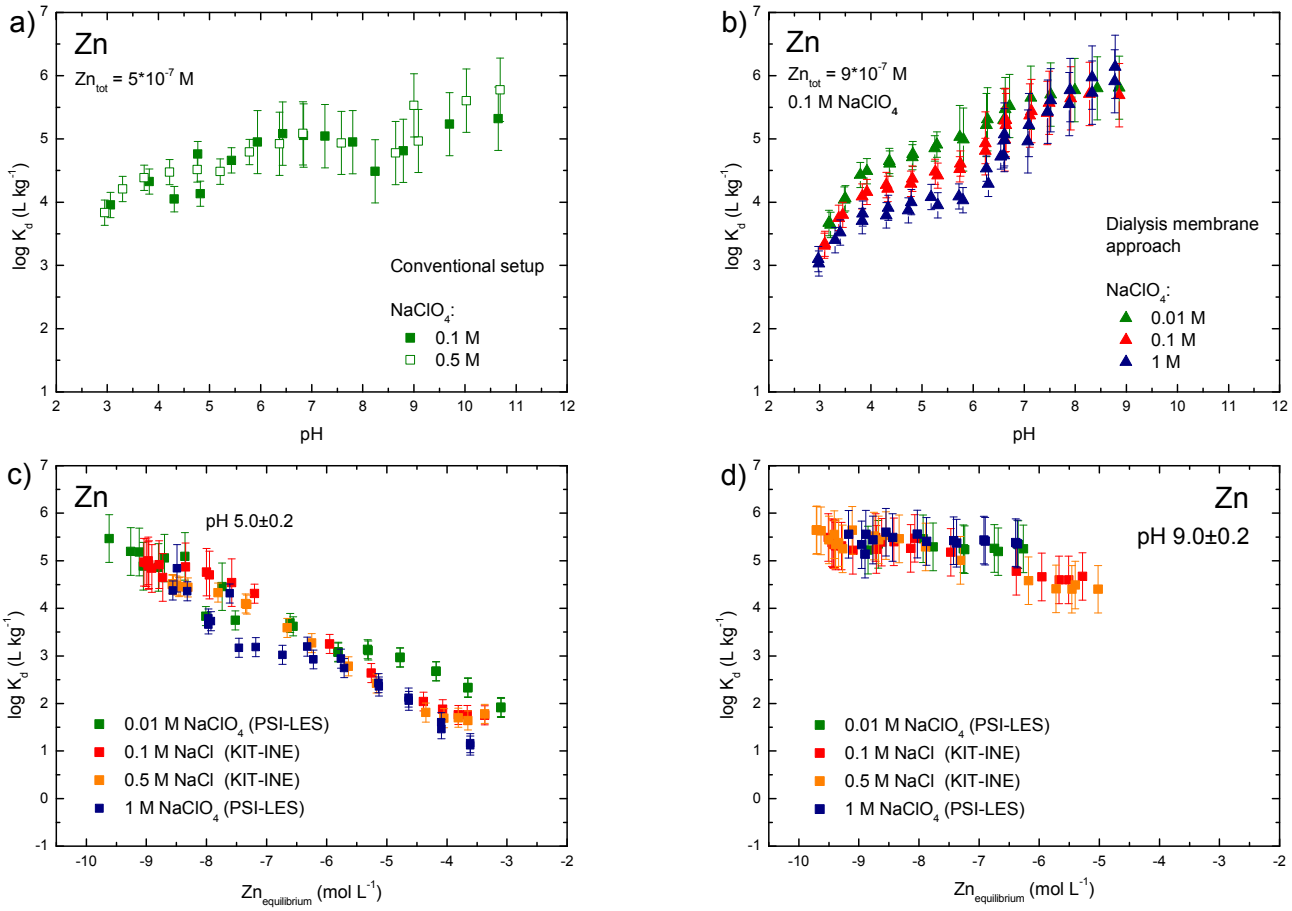

Figure 25 Zn (II) sorption onto conditioned Na-illite at different $NaClO_4$ concentrations as a function of pH trace Zn levels (a and b) and as a function of Zn equilibrium concentration at pH 5 and 9 (c and d). The sorption edge experiments were performed by the dialysis membrane approach (a, experiments performed at PSI-LES) and by the conventional setup (b, experiments performed at SCK·CEN), while for the sorption isotherms (c and d)only the conventional setup was used (experiments performed at PSI-LES and KIT-INE). For experimental details see Table 14 and Table 15.

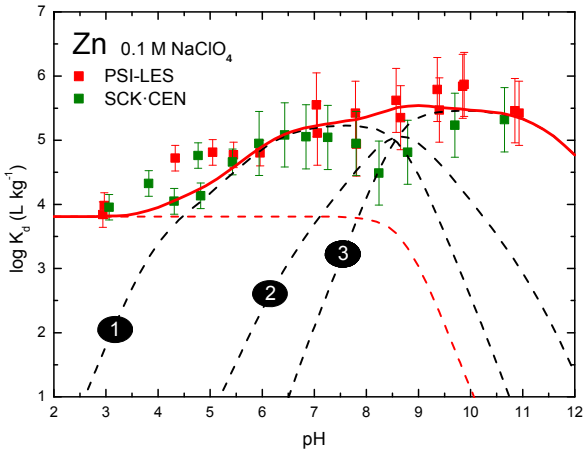

Figure 26 Sorption edges for Zn on Na-illite in 0.1M $NaClO_4$, The continuous curves were calculated using the 2SPNE SC/CE model and the parameters given in Table 16 and Table 17.

The sorption isotherm was also modelled at I = 0.1 M NaCl/$NaClO_4$ at pH = 5.0 and pH = 9.0 (Figure 27). Information on the reactions and site densities can be found in Table 16 and Table 17. A change in the $logK_c$ for the cation exchange reaction needed to be incorporated in order to model the isotherm, decreasing it from 3.0 to 2.2.

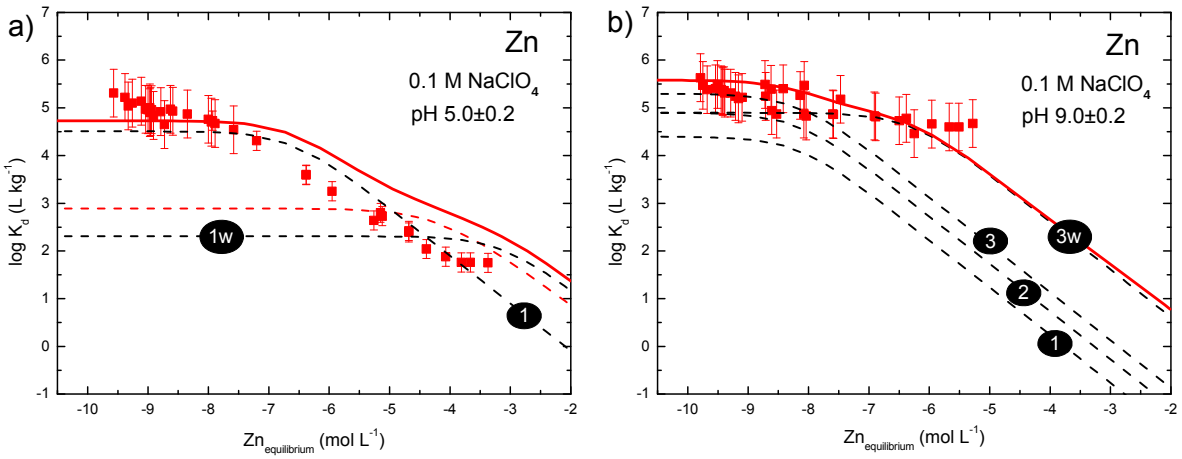

*Figure 27 Sorption isotherms for Zn on Na-illite in 0.1M $NaClO_4$ at pH = 5 and pH = 9. The continuous curves were calculated using the 2SPNE SC/CE model and the parameters given in Table 16 and Table 17, symbols represent experimental data. The contributions to the overall sorption of the individual Zn surface species are shown by the different curves (black dashed lines): **1**:S^sOZn^+; **2:** S^sOZnOH; **3:** $S^sOZn(OH)_2^-$;**1w:** $S^{w1}OZn^+$;**3w:** $S^{w1}OZn(OH)_2^-$; and cation exchange reaction (red dashed line).*

Table 16 Summary of site types, site capacities and protolysis constants determined for Na-illite (Bradbury and Baeyens, 2009) and used as non-adjustable parameters in the model calculations of the sorption edges on Na-illite.

Edge sites		**site capacity (mol kg^{-1})**	
$\equiv S^sOH$		2.0×10^{-3}	
$\equiv S^{w1}OH$		4.0×10^{-2}	
$\equiv S^{w2}OH$		4.0×10^{-2}	
Protolysis reaction	**logK** $\equiv S^sOH$	**logK** $\equiv S^{w1}OH$	**logK** $\equiv S^{w2}OH$
$\equiv SOH + H^+ \Leftrightarrow \equiv SOH_2^+$	4.0	4.0	8.5
$\equiv SOH \Leftrightarrow \equiv SO^- + H^+$	-6.2	-6.2	-10.5

Table 17 Cation exchange reactions and selectivity coefficients on Na-illite and summary of surface complexation reactions and stability constants for Zn(II) on the strong and weak sites of Na-illite.

Surface complexation reaction	**Surface complexation (logK)**	**Reference**
$\equiv S^sOH + Zn^{2+} \Leftrightarrow \equiv S^sOZn^+ + H^+$	2.1	This work
$\equiv S^sOH + Zn^{2+} + H_2O \Leftrightarrow \equiv S^sOZnOH^0 + 2H^+$	-6.4	This work
$\equiv S^sOH + Zn^{2+} + 2H_2O \Leftrightarrow \equiv S^sOZn(OH)_2^- + 3H^+$	-15.0	This work
$\equiv S^{w1}OH + Zn^{2+} \Leftrightarrow \equiv S^{w1}OZn^+ + H^+$	-1.4	This work
$\equiv S^{w1}OH + Zn^{2+} + 2H_2O \Leftrightarrow \equiv S^{w1}OZn(OH)_2^- +$	-16.7	This work
Cation exchange reaction	**Selectivity coefficient (logK$_c$)[a]**	**Reference**
$2Na-clay + Zn^{2+} \Leftrightarrow Zn-clay + 2Na^+$	3.0	This work (sorption edge)
$2Na-clay + Zn^{2+} \Leftrightarrow Zn-clay + 2Na^+$	2.2	This work (sorption isotherm)

[a] The high value of K_c is indicative that the underlying uptake reaction may be different from cation-exchange. It may thus be speculated that other binding sites present at relatively low concentrations may be responsible for the high K_c values measured at the trace Zn concentrations applied in the present experiments.

In presence of inorganic and dissolved organic carbon

SCK·CEN studied the effect of carbonate ion and organic matter complexation on the sorption of Zn. Figure 28 shows Zn sorption isotherms at pH 8.2-8.4 under different carbonate conditions. In the absence of carbonate, log K_d values amount to 4.5-4.7, which is in line with results from sorption edge data (Figure 25). Log K_d tends to decrease with increasing Zn, pointing to a saturation of high affinity sorption sites. Under higher pCO_2 conditions, the sorption isotherms appear to decrease slightly, but only just a little. There is no clear difference between the sorption isotherms under CO_2 free conditions or at 0.4% CO_2 (10x atm) at pH 8.4 (0.016 M $NaHCO_3$). At even higher CO_2 conditions (10% CO_2, 0.1 M $NaHCO_3$), a small difference is observed (maximum factor 2). The results thus suggest that the influence of carbonate complexation on Zn sorption under relevant Boom Clay conditions is relatively low, in line with speciation calculations using MOLDATA TDB. The dominance of $Zn(CO_3)_2^{2-}$ species, as predicted using phreeqc.dat TDB, is unlikely.

In contrast with inorganic carbon, dissolved organic carbon has a much more pronounced effect on the Zn sorption on illite at trace and intermediate Zn concentrations (Figure 28). At 60 mg C L^{-1} the Zn sorption decreases by two orders of magnitude (log K_d ~ 4.5 to log K_d ~ 2.5). This effect can be attributed to the formation of soluble organic carbon-Zn complexes, decreasing the amount of Zn available for sorption.

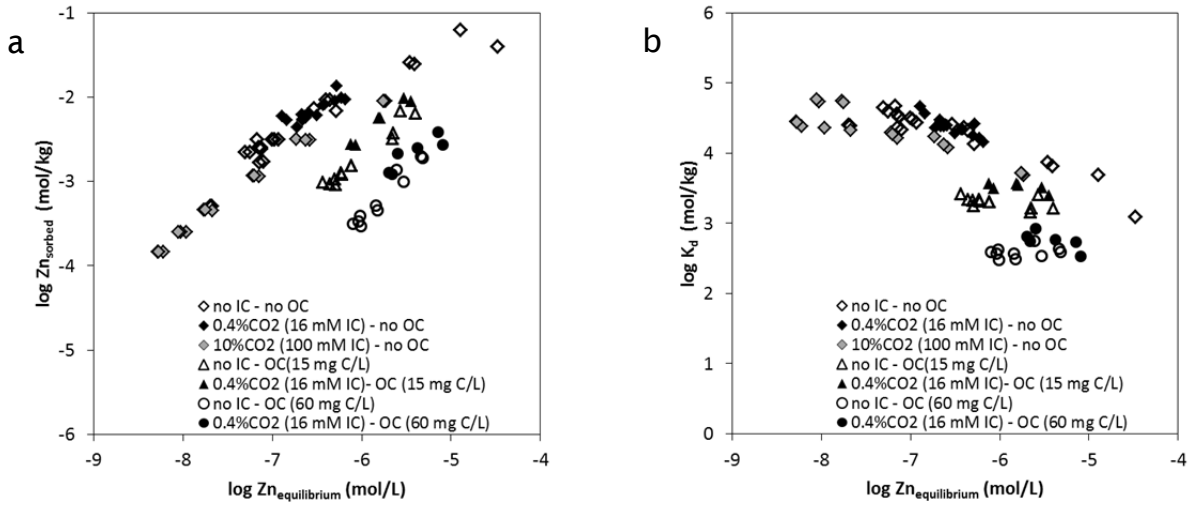

Figure 28 Sorption Isotherms (a) and logK_d (b) as function of pH for Zn on Na-Illite at pH 8.2-8.4 at different dissolved inorganic and organic carbon concentrations.

2.4.4.3 Cobalt

Co sorption edges and isotherms were performed by PSI-LES and recorded in four different background electrolyte concentrations, i.e. 0.01, 0.03, 0.1 and 1.0 M $NaClO_4$. As the logK_d values for the sorption edges scattered at low pH by using the conventional setup, also the "dialysis membrane" approach was followed (only for the sorption edges). The results are shown in Figure 29a together with literature data on Co(II) sorption onto Na-illite of the same origin (Bradbury & Baeyens, 2009).

Two distinct pH regions can be deduced: (i) constant logK_d values at low pH (pH ≤ 6) and (ii) increasing logK_d at higher pH, thus indicating Co uptake by cation exchange and surface complexation. While the present data show slightly higher K_d values compared to the data of Bradbury & Baeyens (2009), the general sorption behaviour is reproduced quite well. Following the discussion for Zn, the higher Co uptake at low-to-neutral pH may be due to an accessory mineral phase, although this hypothesis is highly speculative. While for the conventional setup no effect of the background $NaClO_4$ concentration on the Co uptake was observed (results not shown), this effect is evident in the "dialysis membrane" approach although the difference in logK_d between 0.1 and 1M is quite small (Figure 29b; note that the data for the "conventional setup" and the "dialysis membrane approach" cannot be compared without restrictions). This result is in line with the sorption isotherms at pH 5, where the data indicate a higher Co uptake in 0.01M $NaClO_4$, while similar K_d values are found for 0.1 and 1 M $NaClO_4$ (Figure 29c and d). At low Co equilibrium concentrations K_d is high and independent of concentration (indicating a linear sorption behaviour), while its value decreases with increasing Co concentration.

To summarize, the sorption behaviour of Co(II) onto Na-illite can thus be explained by cation exchange and surface complexation mechanisms, the former being dominant at low pH (≤ 6) and low background electrolyte concentrations (0.01 M), while the latter is responsible for metal ion uptake at higher ionic strengths (≥0.1 M) and higher pH values (pH > 6).

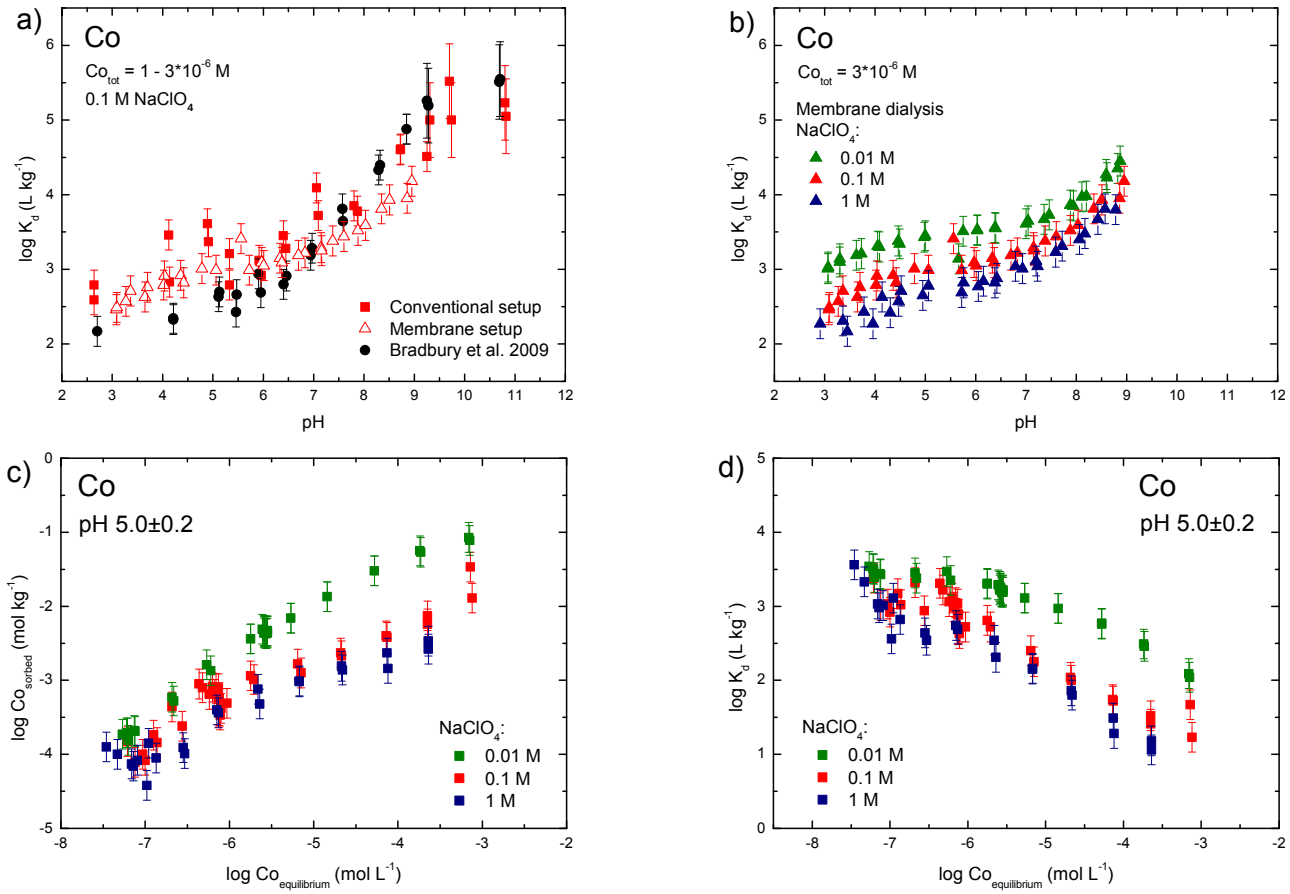

Figure 29 pH dependent Co(II) sorption onto conditioned Na-illite at trace Co levels in 0.1M $NaClO_4$ determined by conventional setup and the dialysis membrane approach together with data from Bradbury & Baeyens (2009) (a) $Co_{initial}$=1x10^{-10}; S:L=1.6 g L^{-1}). Zn sorption edges measured in the membrane approach at different $NaClO_4$ concentrations (b). Co sorption isotherms at pH 5 in $NaClO_4$ concentrations presented as Co sorbed (c) and as logK_d (d) vs. Co equilibrium concentration. For experimental details see Table 14 and Table 15.

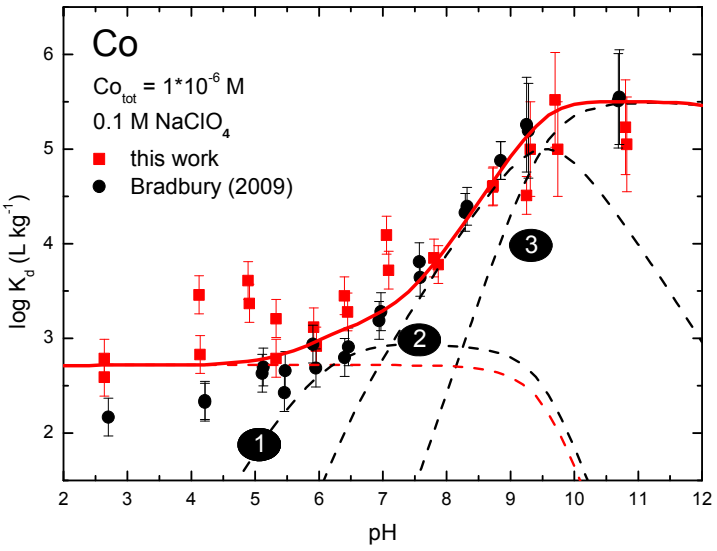

Figure 30 Sorption edges for Co on Na-illite in 0.1 M $NaClO_4$. The continuous and discontinuous curves were calculated using the 2SPNE SC/CE model and the parameters given in Table 16 and The sorption edge at I = 0.1 M NaClO4 was modelled (Figure 30) using a non electrostatic model similar to the one described in the literature (Bradbury & Baeyens, 2009). Information on the reactions and site densities can be found in Table 16 and Table 18. Only experimental data for the conventional setup has been used (in this model, no competition with the cations of the porewater is taken into account). Cation exchange and only strong sites have been used for the surface complexation model.

*Table 18. Symbols represent experimental data. The contributions to the overall sorption of the individual Co surface species are shown by the different curves (black dashed lines): **1**:S^sOCo^+; **2:** S^sOCoOH; **3:** $S^sOCo(OH)_2^-$ and cation exchange reaction (red dashed line).*

The sorption edge at I = 0.1 M $NaClO_4$ was modelled (Figure 30) using a non electrostatic model similar to the one described in the literature (Bradbury & Baeyens, 2009). Information on the reactions and site densities can be found in Table 16 and Table 18. Only experimental data for the conventional setup has been used (in this model, no competition with the cations of the porewater is taken into account). Cation exchange and only strong sites have been used for the surface complexation model.

Table 18 Cation exchange reactions and selectivity coefficients on Na-illite and summary of surface complexation reactions and stability constants for Co(II) on the strong sites of Na-illite.

Surface complexation reaction	**Surface complexation (logK)**	**Reference**
$\equiv S^sOH + Co^{2+} \Leftrightarrow \equiv S^sOCo^+ + H^+$	0.5	This work
$\equiv S^sOH + Co^{2+} + H_2O \Leftrightarrow \equiv S^sOCoOH^0 + 2H^+$	-7.0	Bradbury & Baeyens (2009)
$\equiv S^sOH + Co^{2+} + 2H_2O \Leftrightarrow \equiv S^sOCo(OH)_2^- + 3H^+$	-16.5	Bradbury & Baeyens (2009)
Cation exchange reaction	**Selectivity coefficient (logK$_c$)**	**Reference**
$2Na-clay + Co^{2+} \Leftrightarrow Co-clay + 2Na^+$	1.8	This work (sorption edge)
$2Na-clay + Co^{2+} \Leftrightarrow Co-clay + 2Na^+$	1.0	This work (sorption isotherm)

The sorption isotherm was also modelled at I = 0.1 M $NaClO_4$ at pH = 5.0 (Figure 31). Information on the reactions and site densities can be found in Table 16 and Table 18. Similar to Zn, a change in the $logK_c$ for the cation exchange reaction had to be introduced in order to model the isotherm, decreasing it from 1.8 to 1.0.

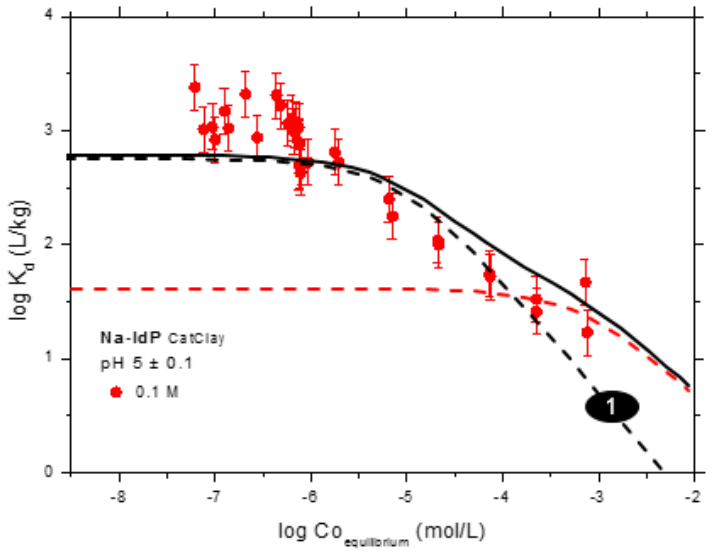

*Figure 31 Sorption isotherm for Co on Na-illite in 0.1M $NaClO_4$ at pH = 5. The continuous curves were calculated using the 2SPNE SC/CE model and the parameters given in Table 16 and Table 18. Symbols represent experimental data. The contributions to the overall sorption of the individual Co surface species are shown by the different curves (black dashed lines): **1**:S^sOCo^+ and cation exchange reaction (red dashed line).*

2.4.4.4 Europium and Curium

The pH dependent Eu sorption at trace metal ion concentrations ($2x10^{-9}$ M) was investigated as a function of ionic strength in 0.1 and 0.5 M NaCl (Figure 32a). Two distinct areas can roughly be deduced from this figure: (i) an increasing $logK_d$ for pH < 7 and (ii) constant $logK_d$ above this value. When the background electrolyte concentration is increased to 0.5 M, $logK_d$ decreases for pH < 5, whereas it is not changing thereafter. Thus an Eu uptake onto illite is affected by both cation exchange processes (at low pH and ionic strengths) and surface complexation reactions (higher pH values).

In line with these results, similar sorption isotherms are observed at pH 5.5, 7.0 and 8.3 (Figure 32b-d). Up to Eu equilibrium concentration of ~$1x10^{-7}$ M a linear sorption behaviour is observed, while $logK_d$ decreases by a further increase of the metal ion concentration. Both the sorption edge and isotherm results are in good agreement with published results (Poinssot et al. 1999; Bradbury & Baeyens 2005) on the same Na-illite material (Figure 32a-c).

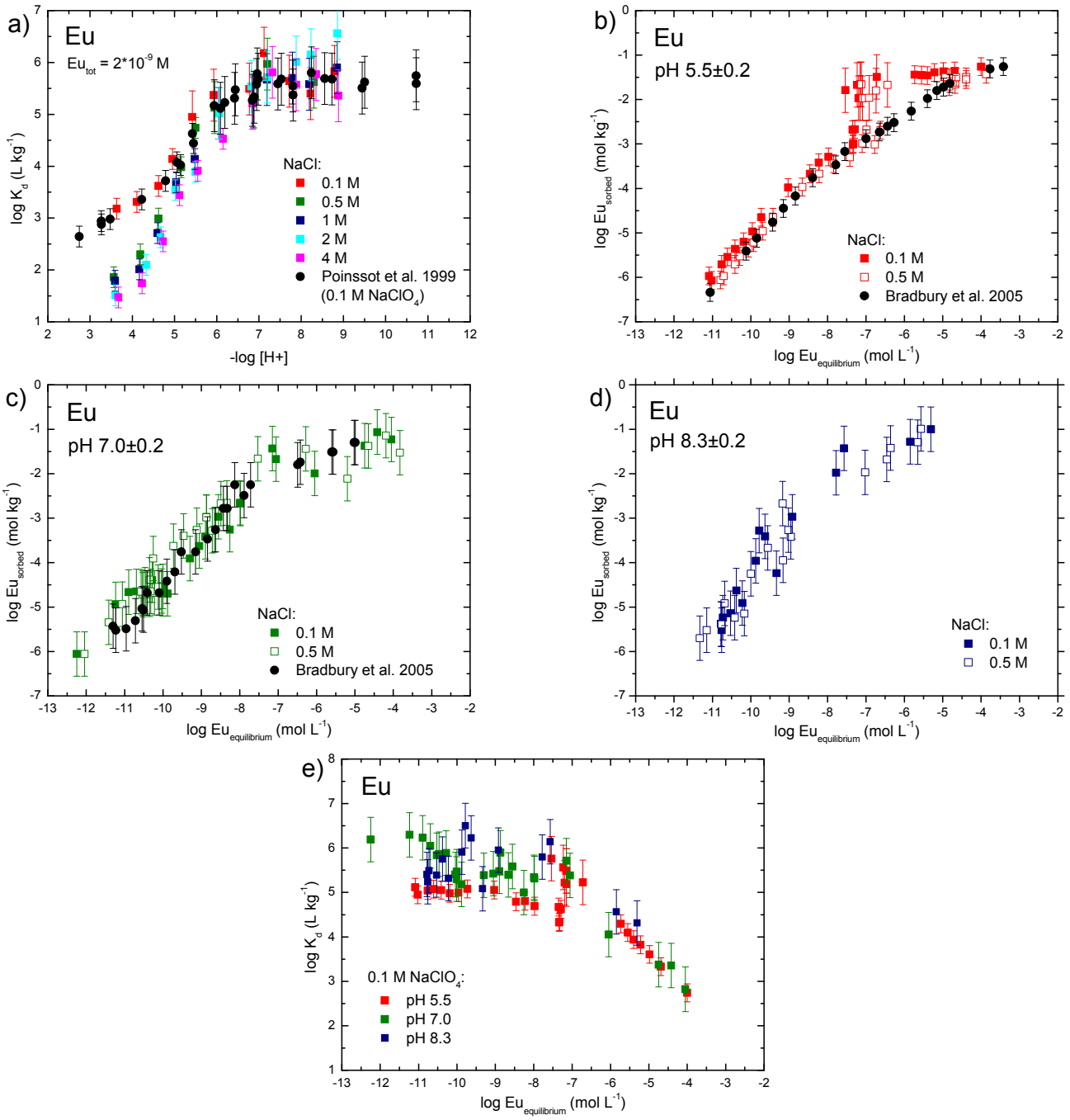

Figure 32 Eu sorption edge on Na-illite at trace Eu levels in various NaCl concentrations together with literature data (S:L=1.8 g L^{-1}; $[Eu]_{initial}$= 3x10^{-9}M) (Poinssot 1999) (a). Eu sorption isotherms in 0.1 and 0.5 M NaCl at pH 5.5 (b), 7.0 (c) and 8.3 (d) together with literature data Bradbury & Baeyens 2005 (pH 7; S:L=1.2 – 1.8 g L^{-1}; 0.1M $NaClO_4$). (e) Comparison of sorption isotherms at different pH in 0.1M NaCl. For experimental details see Table 15.

However, discrepancies are visible for the isotherm recorded at pH 5.5 at intermediate Eu equilibrium concentrations (~1x10^{-7} M). At these conditions, an increased Eu uptake is observed (as lower activities in solution are detected, the uncertainties for these data points are higher). The reason for this behaviour is not completely understood at the moment, but a minor accessory mineral phase, which was not removed by the conditioning process, can be responsible for the higher Eu uptake [personal communication B. Baeyens]. In fact, a Ca-containing solid phase may be present based on our solution chemistry data (see Table 6 and the discussion in chapter 1b) and was also discussed to be associated with the conditioned Na-illite Bradbury & Baeyens (2005) used within their work. The calculated Ca inventory in the latter work was ~50-60 mmol kg^{-1}, which is in excellent agreement with the Ca inventory released at pH 5.5 according to our Ca solubility data (Table 6). Following the interpretation of Bradbury & Baeyens (2005), Eu sorption on Na-illite uptake is described by sorption onto two types of amphoteric surface sites: (i) a "strong site" ($\equiv S^{s}OH$) with a high affinity but low capacity (2 mmol kg^{-1}) is responsible for the Eu uptake at trace metal ion concentrations, while (ii) two additional sites ("weak sites" $\equiv S^{w1}OH$ and $\equiv S^{w2}OH$ with low affinities but high capacities of 40 mmol kg^{-1}) are responsible for Eu uptake at higher Eu equilibrium concentrations (as $\equiv S^{s}OH$ is saturated above Eu_{sorbed} ~2 mmol kg^{-1}; Figure 32b).

Apart from information on the macroscopic sorption behaviour (i.e. determination of distribution coefficients), information on the microscopic scale (i.e. metal ion speciation) is needed for a thorough understanding of the sorption processes occurring on clay surfaces. In addition, these speciation data are needed for being incorporated in a complete conceptual model, describing migration processes of (radio)nuclides in compacted clay systems. In a first step, the pH dependency on the speciation of a trivalent metal ion (Cm) in a Na-illite suspension is investigated experimentally by time resolved laser fluorescence spectroscopy (TRLFS). In a subsequent step, these results can be compared to speciation data derived in compacted systems (i.e. from diffusion experiments with trivalent metal ions used as tracers).

In Figure 33a the evolution of the fluorescence emission spectra for the interaction of Cm with a Na-illite suspension (0.25 g L^{-1}) in 0.1 M NaCl between pH 4 and 11 is shown. At pH ≤ 5 the emission spectra resemble the one for the Cm aquo ion with an emission peak maximum at 593.8 nm. This result is in accordance with the results of the batch sorption experiments, where a metal ion uptake by cation exchange is expected under the given experimental condition. In this coordination, Cm is electrostatically bound in an outer sphere attachment onto the clay surface and retains its hydration sphere ($Cm(H_2O)_9^{3+}$). Hence, the Cm fluorescence decay at low pH (pH ≤ 5) follows the one for the Cm aquo ion (Figure 33b).

When increasing the pH, a shoulder appears at higher wavelengths, indicating a change in the first coordination sphere of the Cm ion and the formation of an inner-sphere sorbed Cm(III) complex. In accordance, the decay of the fluorescence intensity with an increasing delay time changes compared to the free Cm ion, as H_2O quenchers in the first coordination sphere are being removed (Figure 33b). The fraction of this surface sorbed Cm species increases as the pH is increased further.

Increasing the pH further (pH>6) leads to a slight shift in the emission peak maxima, indicating an additional change in the first coordination sphere of the inner-spherically bound Cm. Three single component emission spectra with λ_{max} = 589.5, 603.5 and 606.8 nm can be derived by peak deconvolution, occurring in the pH range 4 < pH < 11 (Figure 33c). The positions of the emission peak maxima are consistent with the emission bands observed by Rabung et al. (2005).

Further, a pH-dependent curium species distribution can be calculated, by using the single component emission spectra and the spectrum for the curium aquo ion (Figure 33d). At pH~4 only the Cm aquo ion is present in solution. Its fraction decreases when the pH is increased, while the first Cm surface complex (Cm species 1) is being formed. The latter species dominates the speciation only in a narrow pH range, given that the second Cm species appears already at pH > 5. Its contribution is increasing with a steep initial rise and dominating the species distribution up to pH ~8, after which the third surface sorbed Cm species becomes prevalent, its fraction increasing up to pH 11.5.

It should be mentioned, that a low fluorescence intensity and thus a low signal-to-noise ratio was detected for the Cm emission spectra above pH 6 (i.e. for inner-spherically bound Cm). The decrease in fluorescence intensity by inner sphere complexation can hereby be related to a (i) a shift of the absorption maximum for surface sorbed Cm compared to the free Cm ion in aqueous solution when the exciting wavelength is kept constant (Wang 2004) and (ii) energy transfer processes from the excited Cm electronic states to the solid, e.g. structural Fe. Thus, fluorescence intensity factors (FI_i) for the different surface sorbed Cm species *I* (required for an accurate calculation (Fanghanel 1998) are observed to be low, i.e. 0.34, 0.07 and 0.04 for the Cm species 1 to 3, respectively (in line with literature data on the same system (Rabung, 2005): FI_i = 0.19, 0.09 and 0.08) and the uncertainties in the given speciation plot are thought

to be as high as ±10%. In addition, the described processes as well as a loss in fluorescence intensity due to light scattering lead to a very low signal-to-noise ratio hampering a determination of a fluorescence lifetime τ. The latter can be related to the number of H_2O/OH^- molecules in the first Cm coordination sphere (Kimura, 1994, 1996), as these entities act as luminescence quenchers via an energy transfer from the excited Cm to OH vibronic states.

However, due to the similar results (single component emission spectra and a comparable pH dependent speciation) compared to literature data on Na-illite (Rabung, 2005, Bradbury & Baeyens 2005), the observed surface sorbed Cm species can be assigned to the complexes *clay*···$Cm(OH)_x(H_2O)_{5-x}$ with x = 0, 1, 2 appearing subsequently with increasing pH.

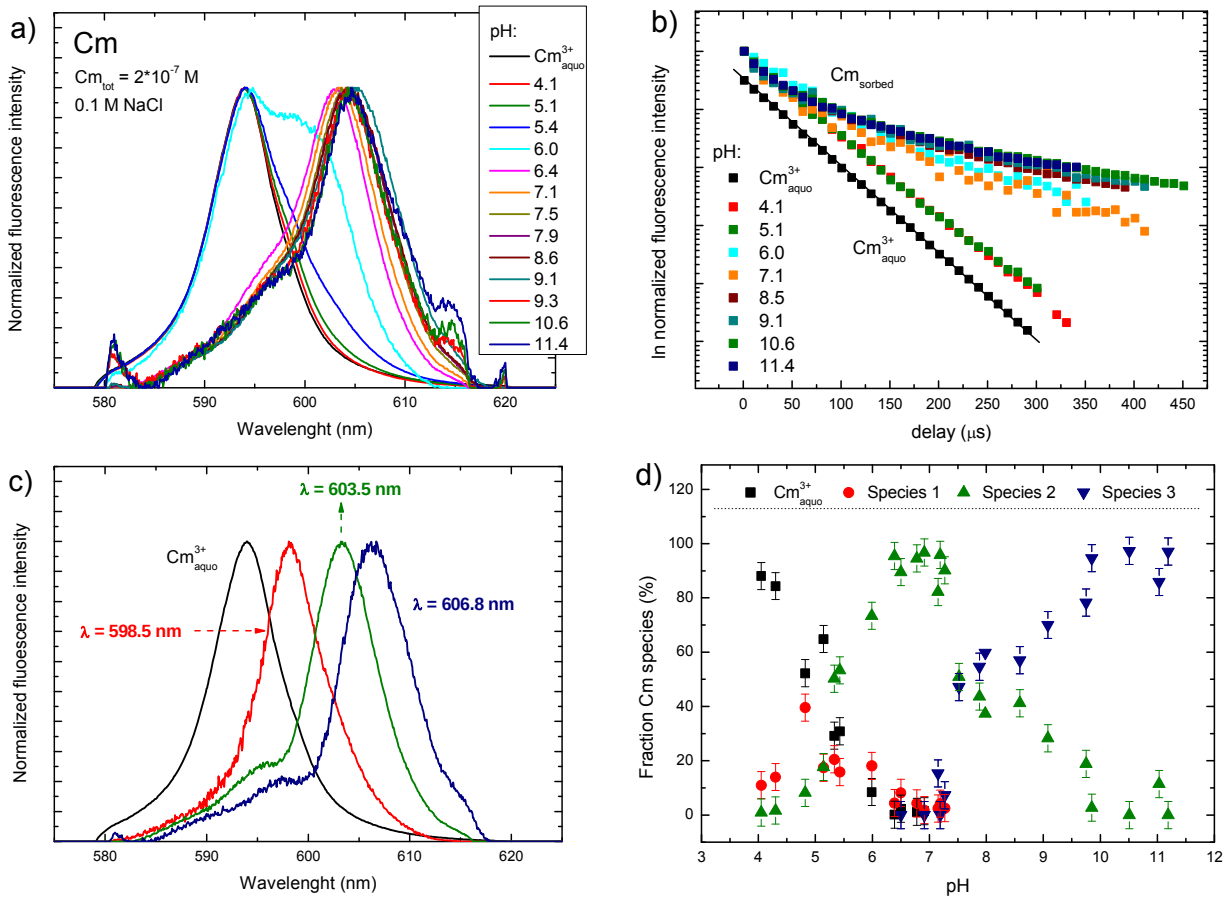

Figure 33 Cm fluorescence emission spectra in an aqueous Na-illite suspension at various pH together with the spectrum of the Cm_{aquo} ion (a) and the single component emission spectra calculated by peak deconvolution (c). All spectra are scaled to the same peak height. Cm species distribution derived by peak deconvolution of the TRLFS emission spectra (d). The delay dependent decrease in Cm fluorescence intensity at various pH is shown in (b). The measurement were performed in 0.1M NaCl at S:L=0.25 g L^{-1} and $[Cm]_{initial}$= 2x10^{-7}M. For experimental details see Table 15.

2.4.5 Comparison of sorption on compact and suspended illite

Figure 34 and Figure 35 compare the results of Sr^{2+} and Co^{2+} sorption measured in batch experiments with some results obtained by interpretation of diffusion experiments (K_d derived from R parameter of diffusion experiments). The latter results thus respresent sorption on compacted clay samples (ρ_d 1.7 kg dm^{-3}). The good agreement indicates that the two techniques give consistent results. This however may be a misleading conclusion because it has to be kept in mind that the sorption value gained from the diffusion experiments is basically valid for the conditions at the interface between the clay and the solution. For other positions in the clay it may differ according to the specific sorption behaviour of the tracer.

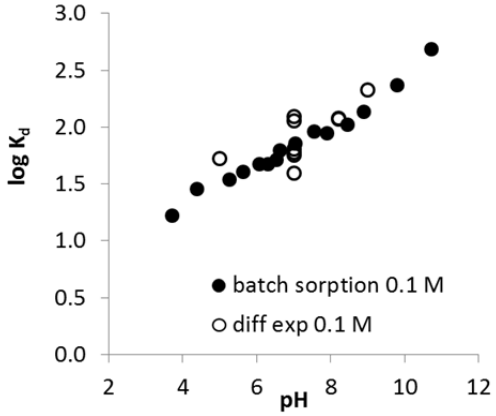

Figure 34 Comparison of the experimental defined K_d values for Sr on illite at IS 0.1 M and the K_d's derived from the fitted capacity factor ηR of the diffusion experiments.

The results for Co^{2+} from the batch sorption experiments at pH 5 clearly indicate non-linear sorption behaviour in the range of Co concentrations relevant for the diffusion experiment. However, the profiles in the diffusion experiments measured for pH 5 suggested that the sorption behaviour would be linear also for lower Co concentrations within the clay area. This is a contradiction for which no explanation is available presently.

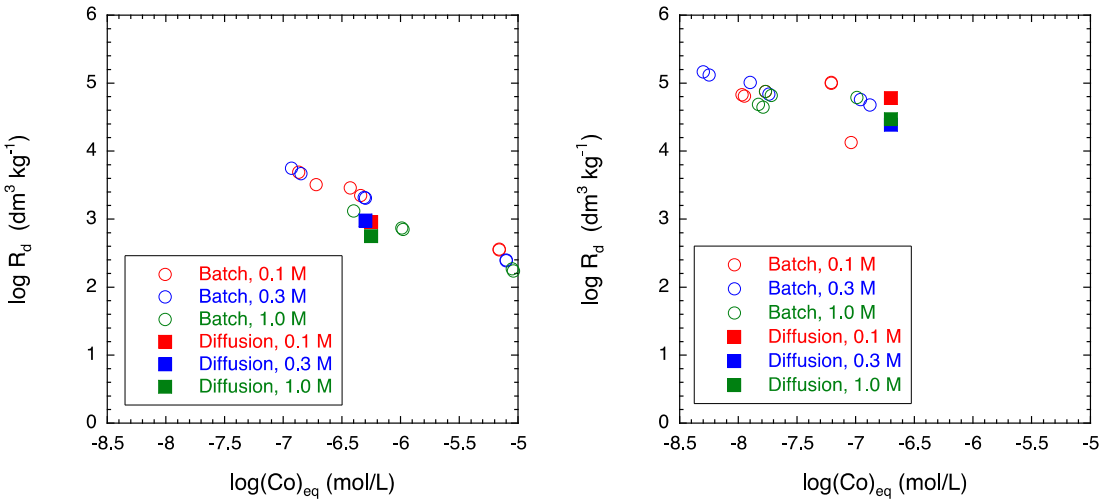

Figure 35 Sorption distribution values (R_d) for $^{60}Co^{2+}$ obtained from batch sorption and in-diffusion measurements. The left-hand plot shows the results for pH 5 and the right-hand plot for pH 9. The background electrolyte was NaClO4.

2.5 Diffusion experiments with illite de Puy

In recent years the diffusive properties of neutral and charged tracers (i.e. anionic and cationic species) in compacted clay minerals (illite, montmorillonite and kaolinite) have been widely investigated (Glaus et al., 2010 and literature therein). It was observed, that the diffusive transport (i.e. the effective diffusion coefficient D_e) for neutral and charged tracers decreases in the order cations > neutral species > anions (Glaus et al., 2007; Van Loon et al, 2007; Wersin et al., 2008). The reduced diffusivity of anionic compared to neutral species is well understood and can be related to a repulsive interaction of anions with the negatively charged clay surfaces leading to a reduced accessibility of the total pore space (anion exclusion). By contrast, cationic species sorbing by cation exchange are able to move through the whole pore space. Although being electrostatically attracted to the negatively charged clay surfaces, cations retain their mobility and the higher effective diffusion coefficient compared to HTO can be related to their enrichment in the interlayer (surface diffusion). Values for D_e were observed to decrease for cationic and increase for anionic tracers with increasing ionic strength (Glaus et al., 2007; 2010), thus indicating that an electrostatic shielding of the surface charge (by an increase in ionic strength) is affecting the diffusion properties of charged solutes.

In the CatClay project, diffusion experiments were designed to determine the diffusive behaviour of cations (Sr, Zn, Co) in clays under different geochemical conditions in order to enlarge the knowledge base. The experiments were

performed in three institutes. PSI-LES and SCK·CEN studied the diffusion of HTO, Sr(II) and Zn(II) in purified Na-illite. PSI-LES studied in addition also Co(II). KIT-INE studied the diffusion of HTO and Cl^- in purified Na-illite and HTO, Cl^- and Sr(II) in 'reduced surface charge' illite.

2.5.1 Diffusion in Na-illite

2.5.1.1 Experimental methods

Different experimental techniques were used by the three institutes (KIT-INE, PSI-LES, SCK-CEN). The majority of the experiments were performed with the classic through-diffusion technique, as shown in Figure 36. In the setup of the through-diffusion method, a clay plug is placed between two reservoirs, a large source reservoir at one side and a smaller target reservoir at the other side. The source reservoir is spiked with a tracer, while the target reservoir initially does not contain tracer. For the through-diffusion experiments, the decrease in concentration in the source reservoir and increase in the target reservoir are monitored. After a few weeks or months (depending on the studied radionuclide), the clay is sliced and measured to obtain the tracer profile in the clay plug. In-diffusion experiments are performed the same way, except that there is no breakthrough in the target reservoir.

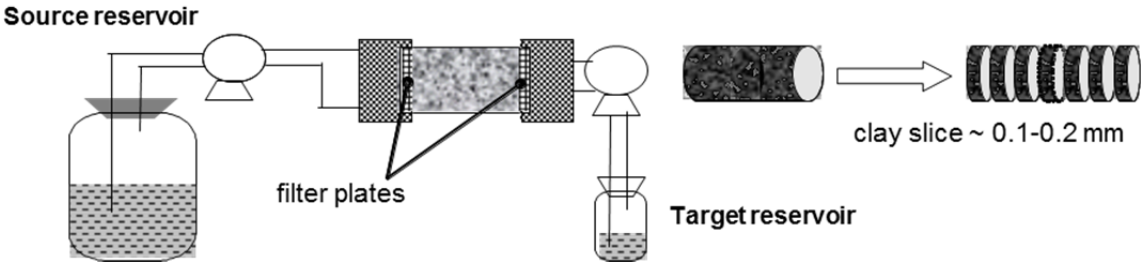

Figure 36 Schematic presentation of the through-diffusion method.

All experiments were performed at a temperature of 22-25°C and the clay was packed at a density of 1700 kg m^{-3} (corresponding to calculated effective illite density in Callovo-Oxfordian Clay). At PSI-LES and KIT-INE, they focused on the effect of the background electrolyte and pH on the diffusion behaviour. At SCK·CEN, pH and CO_2 atmosphere was varied to see how this influenced the diffusion of the cations.

The overall concept of the through-diffusion method is the same for all institutes, but the diffusion cells (material, design, dimensions) and experimental details (volume reservoirs, sampling, preparation and saturation of the clay,…) differ for each institute. These details are described in annex 1. One of the most important differences is the different concept for the interface between the clay and solutions. The diffusion cells of SCK·CEN have static (mostly) stainless steel filter plates, while in case of the experiments performed at KIT-INE, a perforated PEEK plate was used. The solution is continously pumped through flow channels which are in contact with the filter plates. In this case, the diffusion in the filter plates must be taken into account (for cation diffusion). PSI used a variation on this classic through-diffusion technique, namely a diffusion cell with filters which are advectively flushed in order to reduce the diffusive barrier of the filters. SCK·CEN used this design also for a few experiments. In addition, PSI-LES performed their diffusion method with a draining technique at the downstream boundary (annex 1 – Glaus et al., in preparation).

For the strongly sorbing radionuclides, this classic through-diffusion technique was, however, not able to provide good results, due to sorption on the filter plates. At PSI-LES, they developed a **membrane-confined diffusion cell (MCDC)** which avoids the use of porous steel filters and hence eliminates the sorption problem (annex 2). The tests of the prototype cells were carried out using $^{85}Sr^{2+}$. In contrast to the experiments with Opalinus Clay, a mechanical confinement of the compacted illite sample is necessary. Figure 37 shows a schematical view of this diffusion cell. The cell was immersed to a minimum necessary in the source reservoir solution containing the radiotracer under study. The uptake of the radionuclide to the equipment was thereby minimised. A confinement of the clay sample by one or two layers of an organic polymeric membrane with a resulting overall thickness of ~100–200 µm was sufficient to withstand the swelling pressure of the clay sample. Slight deformations of the clay of the order of 0.1–0.2 mm were observed, but taxed as rather unimportant for experiments in which the tracer penetration into the clay is larger than ~1 mm.

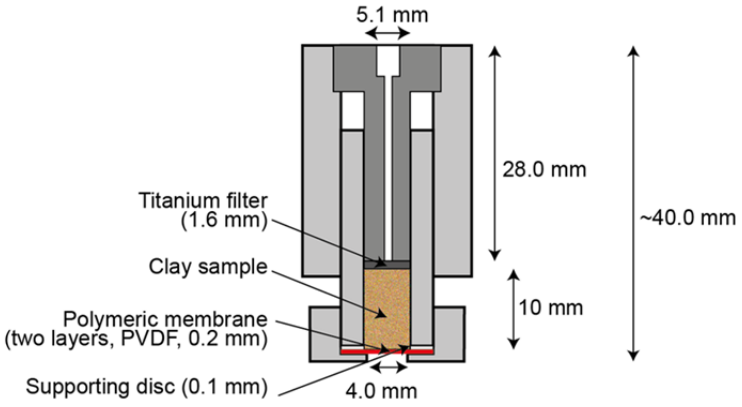

Figure 37 Schematic drawing of the final version of the membrane-confined diffusion cell (MCDC). In contrast to previous versions the supporting slotted titanium disc was left out. An aperture of 4 mm provided sufficient mechanical stability to withstand the swelling pressure of the clay sample. As in former versions, saturation of the clay sample can be realised under advective conditions using a stainless steel plate as a support (not shown). After the in-diffusion phase the sample can be extruded from the holder and sliced using an appropriate end-piece (also not shown).

These different experimental set-ups require also a different modelling approach. The classic through-diffusion (SCK·CEN) can be modelled with a 1-D model, while the perforated PEEK plates (KIT-INE) require a 3-D model. The experimental setup of the MCDC can be described with rotational symmetric 2-D model.

2.5.1.2 Diffusion of reference tracers (HTO, Cl) in Na-illite

HTO diffusion experiments are used as a benchmark between the institutes involved in Catclay, but are also used to check if the packing of the clay plug was performed properly. A deviating diffusion coefficient could point to inhomogeneities in the clay plug (different density,...). Besides, HTO diffusive properties serve as a reference to compare with cation diffusion. HTO diffusion was measured in different set ups and geochemical conditions (pH, pCO_2, ionic strength). At KIT-INE, the diffusion of Cl^- was also studied at different ionic strenghts.

PSI-LES. The results for HTO diffusion were obtained from the linear relation between accumulated activity as a function of time, because the flux data were merely from the steady-state phase of diffusion (Glaus et al., 2012). The best-fit parameters are summarised in Table 19. Uncertainties were calculated according to published procedures (Glaus et al. 2008). As can be seen from these data, the diffusion properties of HTO do not depend on external salinity and pH (details pH not shown). The seeming differences between the various α values have to be treated with caution because an assessment of the uncertainties involved cannot be unambiguously done. It might be possible that the true uncertainties are underestimated by the specified values.

SCK·CEN. Almost all diffusion experiments of Sr and Zn carried out by SCK·CEN, were preceded with HTO through-diffusion. The average values for diffusion parameters α and D_e of the 17 performed experiments are given in Table 19. The diffusion of HTO did not depend on the type of cell (conventional diffusion cell or flushed filter cell) or the chemical conditions of the experiments (different pH, different pCO_2). Results of each experiment are described in Deliverable 2-3. For the conventional diffusion cells, the filters had to be taken into account for the modelling. The data were fitted with the assumption that diffusion in clay and filters is similar in order to decrease the amount of fitting parameters. Indeed, the D_e of HTO in the filter (1.5×10^{-10} m² s^{-1}) is comparable to the D_e in the compacted clay (Table 19). Therefore, only the length of the filters has to be taken into account and added up to the length of the clay plug.

The model provides the best-fit parameters of the apparent diffusion coefficients, D_a and the capacity factor α for HTO in the purified Na-illite. The effective diffusion coefficient, D_e is calculated as the product of both parameters. The average effective diffusion coefficient for HTO in illite packed at a density of 1700 kg m^{-3} is 1.83×10^{-10} m² s^{-1} with a standard deviation of 0.31×10^{-10} m² s^{-1}. This agrees quite well with the average D_e determined by PSI-LES (2.0×10^{-10} m² s^{-1}) with flushed filter diffusion cells and KIT-INE ((1.95×10^{-10} m² s^{-1}). Diffusion parameter values for HTO are independent on the geochemical conditions (pH, pCO_2, ionic strength). The average capacity factor α agrees very well with the theoretical porosity (±0.36) for a clay plug with density 1700 kg m^{-3} (retardation assumed to be 1).

Table 19 Summary of D_e (m^2 s^{-1}) and α (-) values for HTO and ^{36}Cl in Na-illite at a bulk dry density (ρ_{db}) of ~1700 kg m^{-3} together with literature data.

Tracer	NaCl (M)	D_e (x 10^{-10}) (m^2 s^{-1})	α	Performed by
HTO	0.1	1.83±0.31	0.43±0.11	SCK-CEN
	0.1	1.95±0.04	0.53	KIT-INE
	0.1	2.0±0.2	0.43±0.20	PSI
	0.5	1.97±0.05	0.43	KIT-INE
	0.5	2.1±0.2	0.60±0.21	PSI
^{36}Cl	0.1	0.67±0.04	0.18	KIT-INE
	0.1	0.28±0.03[a]	0.12±0.03[a]	Glaus et al. (2010)
	0.5	1.00±0.05	0.25	KIT-INE
	0.5	0.53±0.07[a]	0.18±0.05[a]	Glaus et al. (2010)

[a] ρ_{db} = 1900 kg m^{-3}

KIT-INE. Breakthrough curves for HTO and ^{36}Cl in 0.1 M NaCl, as well as the activity/concentration decrease in the source reservoir, are presented in Figure 38a and b. The data are also representative for the higher ionic strength. For both tracers, a steady state (indicated by a constant flux) is achieved after ~3 days and remained more or less constant to the end of the experiment. In case of ^{36}Cl, the values for the diffusive flux are observed to scatter, which can be related to a low activity in the downstream solution. The results are presented in Table 19. It should be kept in mind, that the activity in the high-concentration reservoir decreased during the course of the experiment to ~91% of the initial concentration in case of HTO (the decrease in case of ^{36}Cl was only 2%). As constant boundary conditions were thus not fulfilled, the diffusion parameters calculated hereby may be inaccurate.

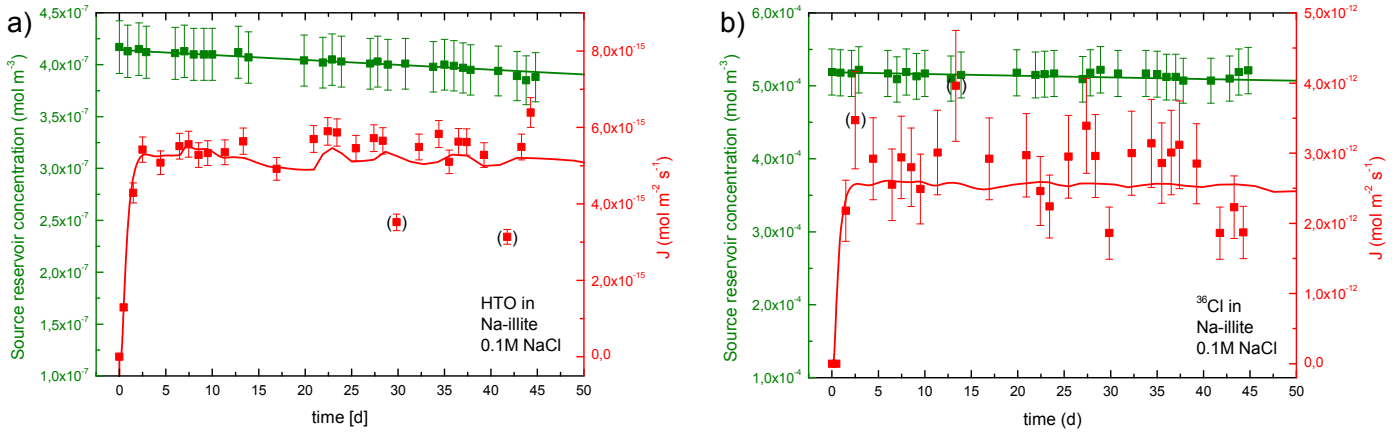

Figure 38 Diffusion of HTO (a) and $^{36}Cl^-$ (b) in compacted Na-illite (ρ_{db}~1700 kg m^{-3}) at pH 5.5 and 0.1 M NaCl as mass flux in the low concentration reservoir (J) and evolution of the source reservoir concentration.

HTO diffusion coefficients and values for α (or the porosity ε, respectively) are similar in 0.1 and 0.5 M NaCl, indicating that an increase in background electrolyte concentrations has no effect on the geometrical properties (tortuosity or constrictivity) on the compacted clay mineral. However, an increase in ionic strength affected the transport parameters in case of ^{36}Cl, where D_e and α are observed to be higher in 0.5 M NaCl. The lower D_e value for Cl compared to HTO can be related to a reduced accessible pore space for anionic tracers (anion accessible porosity ε_{acc}), as anions are repelled from the vicinity of the negatively charged clay surfaces. On the other hand, the increase in D_e at higher ionic strength can be linked to an enhanced electrostatic shielding of this negative surface charge, increasing the fraction of anion accessible pore space (Glaus et al., 2010).

In case of ^{36}Cl, available diffusion coefficients and ε values in the literature are only reported for a higher bulk dry density (ρ_{db}) of ~1900 kg m^{-3}. Consequently, D_e and α are lower compared to the present set of experiments at ρ_{db} ~1700 kg m^{-3}, but are also observed to increase with increasing background electrolyte concentration (Table 19).

2.5.1.3 Diffusion of cations ($^{85}Sr^{2+}$, $^{65}Zn^{2+}$ and $^{60}Co^{2+}$) in Na-illite

Results for Sr diffusion

The diffusion of Sr in Na-illite was studied at different geochemical conditions. At PSI-LES, Sr diffusion was studied at different pH and ionic strength. SCK•CEN performed experiments at different pH and pCO_2 conditions. Ion chromatography measurements showed that the concentrations of stable Sr in the diffusion experiments was of the order of $1x10^{-6}$ M. It can be concluded that this concentration was governed by dissolution of mineral impurities rather than by the stable Sr added by the tracer solution. The measured concentrations were thus in agreement with results obtained from dispersed suspensions of illite (cf. Figure 15). Similar observations can also be stated for the concentrations of Mg^{2+} and Ca^{2+} which were in the micromolar range for Mg and several tenths of micromolar for Ca with some dependence on pH (lower concentrations for pH 9).

PSI-LES. Experimental data of the through-diffusion experiment (performed at 0.01 M $NaClO_4$ and pH 5) using the draining method and fit curves obtained from the best-fit parameter values are shown in Figure 39. The left-hand plot shows the tracer flux measured at the target boundary and the tracer concentration in the source reservoir as a function of time. The right-hand plot shows the tracer profile measured after termination of through-diffusion. Note that this experiment had to be terminated prematurely because of unidentified hydraulic difficulties arising at the target boundary side. However, the tracer flux and concentration decrease advanced sufficiently for a robust evaluation of the diffusion parameters and the results perfectly complement those obtained previously (Glaus et al., 2012, Catclay deliverable 2-1) in the range of background electrolyte concentrations between 0.1 and 1.0 M. Extending this range to lower concentrations enhances (i) the range of intercomparison with the results of batch sorption experiments and (ii) the range for the interpretation of the effects of salinity on the diffusive properties of the tracers under study. Table 20 shows that D_e values drastically increase with decreasing concentration of the background electrolyte. Further pH effects are observed which would not be expected for a pure cation exchange mechanism. The increased R_d values at pH 9 indicate that surface complexation may be partly involved in the sorption of Sr^{2+} under these conditions.

The results of the in-diffusion experiments with the MCDC's are shown in Figure 40 for pH 5 and Figure 41 for pH 9. The best-fit parameter values are summarised in Table 20 together with the previously measured values. Despite the good consistency between the fit curves and the experimental data the resulting errors in D_e and R_d are relatively large because of the uncertainties associated with the filter (or membrane) diffusion properties.

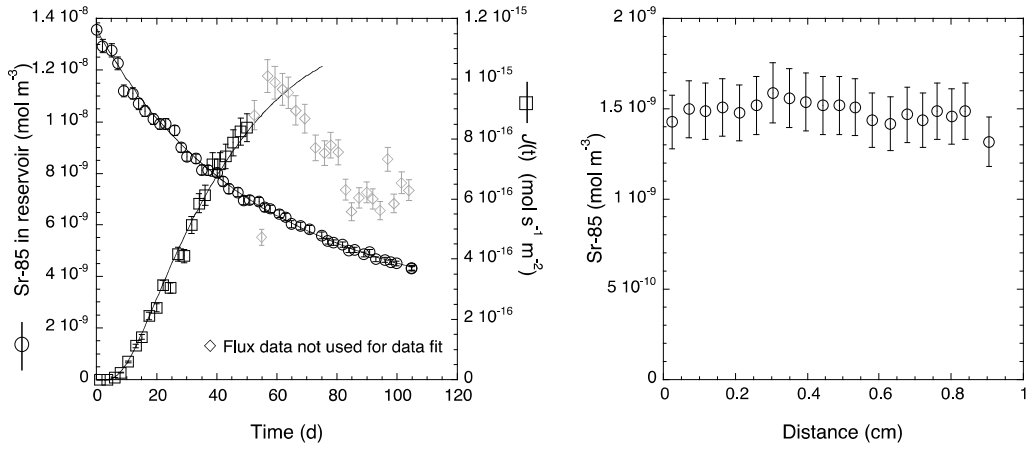

Figure 39 Experimental data and fit curves for best-fit parameter values for through-diffusion of $^{85}Sr^{2+}$ in compacted Na-IdP at pH 5 and $NaClO_4$ concentration of 0.01 M (experiment 13003, 0.01A).

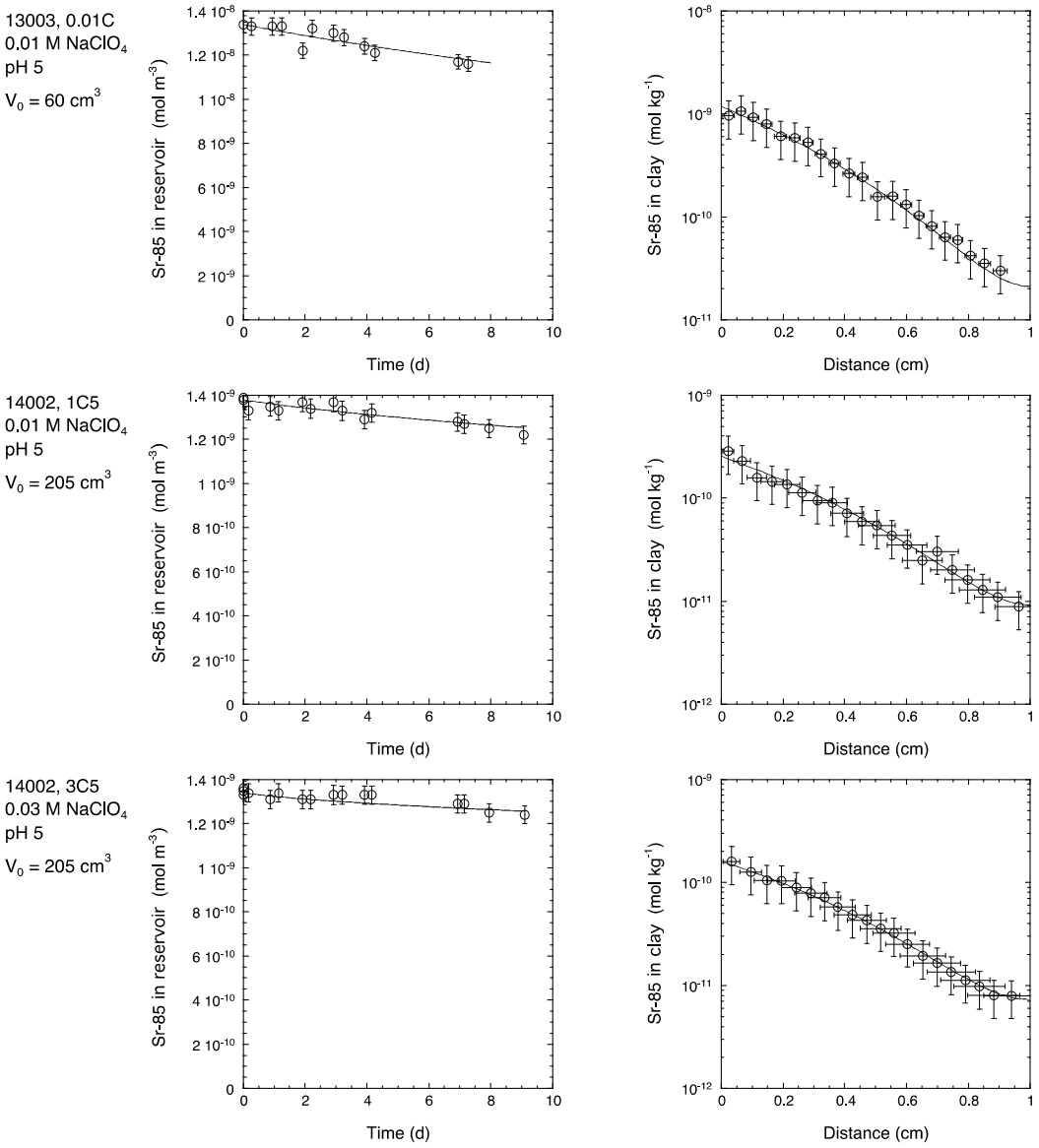

Figure 40 In-diffusion experiments with $^{85}Sr^{2+}$ at pH 5 showing the radiotracer concentration on the left-hand plot and the tracer profile in the clay on the right-hand side. Fit curves were obtained from the best-fit parameter values given in Table 20.

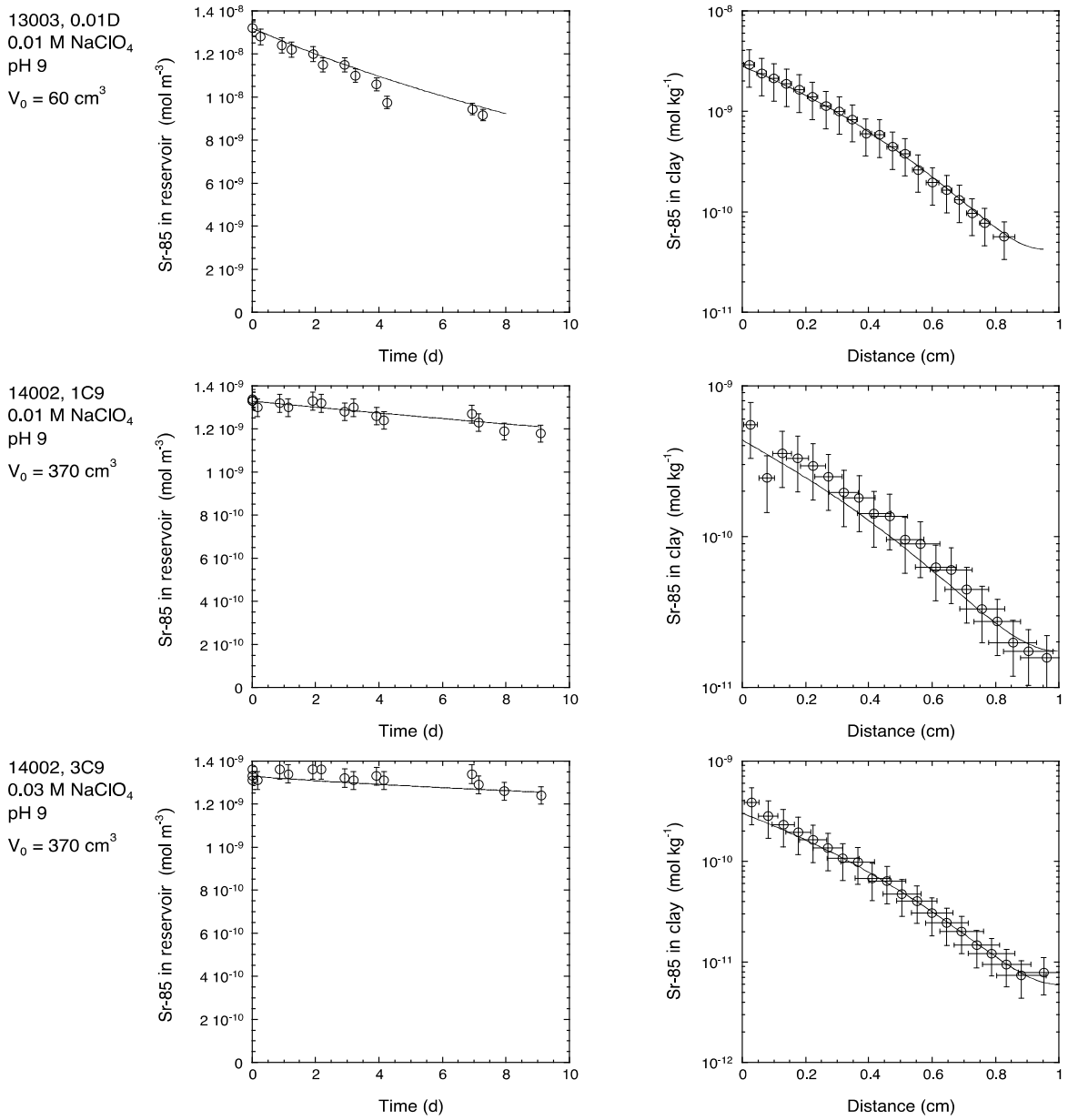

Figure 41 In-diffusion experiments with $^{85}Sr^{2+}$ at pH 9 showing the radiotracer concentration on the left-hand plot and the tracer profile in the clay on the right-hand side. Fit curves were obtained from the best-fit parameter values given in Table 20.

Table 20 Best-fit parameter values for D_e and R_d for in-diffusion of Sr^{2+} in Na-IdP.

Experiment	pH	[$NaClO_4$] (M)	D_e(opt) (m^2 s^{-1})	D_e(min) (m^2 s^{-1})	D_e(max) (m^2 s^{-1})	R_d(opt) (m^3 kg^{-1})	R_d(min) (m^3 kg^{-1})	R_d(max) (m^3 kg^{-1})
13003, 0.01A [a]	5.0 – n.d.	0.01	**1.6×10^{-8}**	1.4×10^{-8}	1.8×10^{-8}	**0.62**	0.55	0.69
13003, 0.01C [b]	5.0 – n.d.	0.01	**9.0×10^{-9}**	n.a.	n.a.	**(0.62)**	n.a.	n.a.
14002, 1C5 [b d]	5.0 – 5.03	0.01	**9.0×10^{-9}**	4.5×10^{-9}	1.4×10^{-8}	**0.38**	0.19	0.57
14002, 3C5 [b d]	5.0 – 5.03	0.03	**4.2×10^{-9}**	2.1×10^{-9}	6.3×10^{-9}	**0.17**	0.08	0.26
11003_2, 1.7G [c]	5.0	0.1	**9.6×10^{-10}**	8.6×10^{-10}	1.1×10^{-9}	**0.047**	0.044	0.049
11003_2, 1.7H [c]	5.0	0.5	**1.6×10^{-10}**	1.4×10^{-10}	1.8×10^{-10}	**0.0061**	0.0052	0.0072
11003_2, 1.7I [c]	5.0	1.0	**1.1×10^{-10}**	0.9×10^{-10}	1.3×10^{-10}	**0.0035**	0.0030	0.0042
13003, 0.01D [b]	9.0 – n.d.	0.01	**3×10^{-8}**			**1.7**		
14002, 1C9 [b d]	9.02 – 8.82	0.01	**9.0×10^{-8}** [e]			**3.5** [e]		
14002, 3C9 [b d]	9.01 – 8.90	0.03	**4.2×10^{-9}**			**0.17**		
11003_2, 1.7K [c]	9.0	0.1	**5.3×10^{-9}**	3.4×10^{-9}	8.0×10^{-9}	**0.48**	0.33	0.68
11003_2, 1.7L [c]	9.0	0.5	**2.4×10^{-10}**	1.7×10^{-10}	3.2×10^{-10}	**0.10**	0.078	0.13
11003_2, 1.7M [c]	9.0	1.0	**1.2×10^{-10}**	9.5×10^{-11}	1.5×10^{-10}	**0.076**	0.063	0.090

[a] Through-diffusion with "drain+scrubber" = pseudo steady-state, Flushed-filter diffusion cells (assuming $D_f = 1.5\times10^{-9}$ m^2 s^{-1})

[b] In-diffusion + reservoir (membrane-confined diffusion cell) = transient state (assuming D_f in a range between 2×10^{-9} and 4×10^{-9} m^2 s^{-1})

[c] Conventional through-diffusion, Flushed-filter diffusion cells (assuming $D_f = 1.5\times10^{-9}$ m^2 s^{-1})

[d] The use of a larger reservoir volume (270 ml instead of 60 ml) resulted in better stability of pH

[e] Diffusion largely dominated by the filter membrane leading to largest parameter uncertainties of this series

SCK·CEN. A series of Sr-diffusion experiments were performed at different pH and different pCO_2. The best-fit parameters are summarised in Table 21. The experimental data and best fits of experiment IdP14 are shown in Figure 42 and are representative for the other experiments. Experiment IdP 14 served as benchmark experiment with PSI-LES. The other experiments are all graphically represented in Van Laer et al. (2014; Deliverable 2-3).

The diffusion of Sr at pH 7 was repeated several times under different experimental conditions (different volume source reservoir, different sampling frequency target reservoir) and seem to give comparable results (Table 21) when the used models adequately reflect the experimental conditions.

The fitted D_a values for the experiments performed under higher pCO_2 conditions (IDP7 and IDP8) showed no difference with D_a under atmospheric conditions (Table 21). The capacity factor α was, however, slightly higher which can be attributed to the higher equilibrium pH (8.2) and not to the higher pCO_2. This also results in higher D_e values compared to the experiments performed at pH7 under atmospheric conditions. Given the prediction that only 5% of the aqueous Sr is assumed to bind with carbonates at pCO_2 0.4% (Figure 16), no measurable effect on the diffusion behavior was expected.

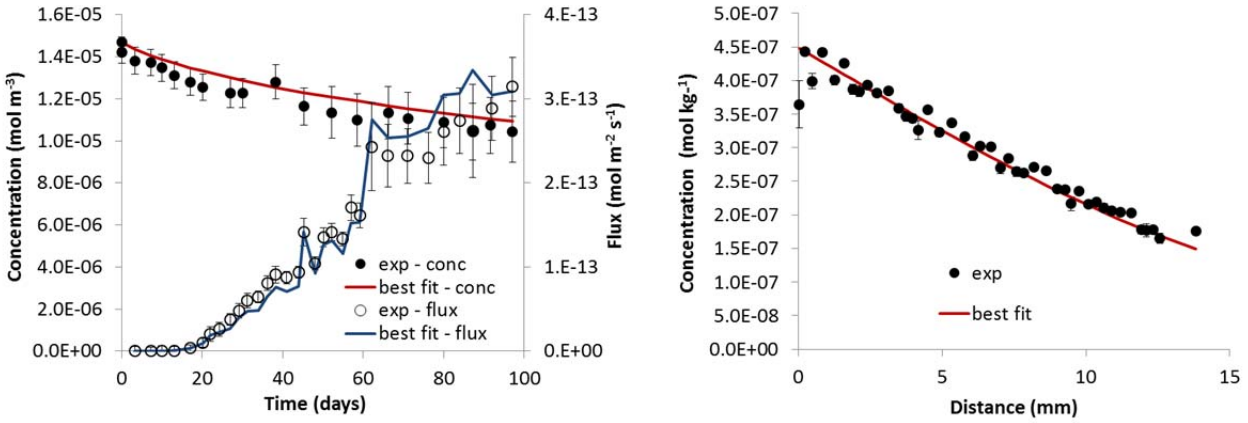

Figure 42 Experimental and best fits of IDP 14 (Through-diffusion Sr - pH 5 – IS 0.1 M – pCO_2 atm). Left-hand plot: concentration decrease source reservoir (left axis) – flux target reservoir (right axis); right-hand plot: concentration profile in the clay plug.

From the experiments under different pH conditions, it is clear that sorption increases (increasing α) with increasing pH. Moreover, the K_d's derived from the fitted α values are very consistent with the experimentally defined K_d's of the batch sorption experiments under the same ionic strength (Table 21). In contrast to the capacity factor, D_a seems to be independent of pH in this pH range. As α increases and D_a remains more or less constant, D_e increases with increasing pH. This trend is in agreement with the observations made by PSI (Table 20). Between pH 5 and 7 the difference is small, but α and D_e values are remarkably higher at pH 8.2 and 9.

Table 21 Diffusion parameters for Sr in Illite du Puy. D_a and α are the fitted parameters (D_e is the product of both parameters). Errors on the fitted D_a and α vary between 1 and 10%.

Experiment	pH	Inorganic carbon	D_a ($m^2\ s^{-1}$)	α(-)	D_e ($m^2\ s^{-1}$)
IDP7 [a]	8.2 ± 0.1	IC 0.4%	1.3×10^{-11}	200	**2.5×10^{-9}**
IDP8	8.2 ± 0.1	IC 0.4%	1.1×10^{-11}	204	**2.3×10^{-9}**
IDP14	5 ± 0.1	atm IC	1.2×10^{-11}	91	**1.1×10^{-9}**
IDP5	7 ± 0.1	atm IC	1.2×10^{-11}	98	**1.2×10^{-9}**
IDP6 [a]	7 ± 0.1	atm IC	1.1×10^{-11}	110	**1.2×10^{-9}**
IDP19 [a]	7 ± 0.1	atm IC	1.2×10^{-11}	103	**1.2×10^{-9}**
IDP18[a]	9 ± 0.1	atm IC	1.1×10^{-11}	364	**3.9×10^{-9}**

[a] fittings only based on the concentration decrease/increase of the source/target reservoir

Results for Co(II) and Zn(II) diffusion

PSI-LES. Representative graphic illustrations of the evolution of concentration in the source reservoir and the tracer concentration profile in the sliced clay segments are given in Figure 43 to Figure 46. The data were taken from experiments 13004.CAT and 13005.CAT. A complete set of data can be found elsewhere (Glaus et al., 2012). Model

curves obtained from the best-fit parameter values are also shown in these plots. The best-fit parameter values are summarised in Table 22 for Co(II) and Table 23 for Zn(II).

For a rough qualitative interpretation, it can be noted that the tracer contents in both clay and solution are of similar order of magnitude irrespective of the concentration of the background electrolyte. Ignoring the concentration effects within the membrane, one may conclude that the R_d values exhibit only a weak dependence of ionic strength, which is in agreement with the expectation that these elements preferentially sorb via surface complex formation. The profiles in the clay, however, show a clear trend of increasing diffusion length with decreasing concentration of the background electrolyte. This implies that D_e values strongly depend on salinity with a trend of increasing D_e values with decreasing salinity. It can further be concluded qualitatively that R_d values strongly depend on pH which again is in agreement with an uptake mechanism by surface complexation. The effect of background electrolyte concentration on the diffusion length – and thus on D_e values – is still effective, even at high pH values.

The general reliability of the data measured at pH 5 is clearly better than of those measured at pH 9. The sensitivity to the variation of the background electrolyte concentration is larger at pH 5, while it may be similar or only slightly larger than the error bars at pH 9. Further a certain loss of tracer to the equipment is observed at pH 9 despite the use of MCDC cells. Typically this loss ranges in the order of 20 to 40 % of the initial tracer concentration (particularly in the case of Zn). Part of the uptake of the tracer by the equipment appears to be a rapid process as indicated by the initial drop of the tracer concentration (typically of the order of 10 to 20 %). Consequently the tracer also gets lost to the equipment by a slower process. This may cause some discrepancy with respect to curve fitting because the fitting procedure does not comprise any uptake of the tracer by the equipment. At pH 5 the observed loss of tracer to the equipment is merely negligible.

Most of the element profiles could be successfully modelled using a constant-R_d approach. This is somewhat surprising in view of the site capacities applied in discrete site modelling, such as the "2SPNE SC/CE" model (Bradbury and Baeyens, 2009b) in which the site density of the so-called strong sites is 2×10^{-3} mol kg^{-1}. The clay profiles of both Co(II) and Zn(II) in experiment series 13001 show that the loading of the clay at the interface between the clay and the solution may undergo saturation. A non-linear behaviour would be expected accordingly. The observation of linear sorption cannot be unambiguously interpreted. One possible hypothesis may be that strong sites are not active or accessible in the experiments with the compacted illite sample. Note that the 2SPNE SC/CE model was calibrated from experiments in which the clay was provided as a homogeneously distributed clay suspension. Alternatively this could be interpreted as a situation in which weaker binding sites present at larger amounts would outcompete the strong binding sites. Because the element loading of the clay in the present experiments does not reach values typical for site densities of weak sites (~4×10^{-2} mol kg^{-1}) such effects cannot be unambiguously interpreted by the experimental data available. Blocking of strong binding sites by competing elements would be a further interpretation. This option is, however, less feasible because the clay has undergone almost the same conditioning procedure (washing with acid and concentrated salt solutions) before compaction as the material used for the calibration of the 2SPNE SC/CE model.

Only in a single case (Co(II) at pH 5, 0.01 M $NaClO_4$, cf. Figure 43) the fit obtained from a constant R_d approach was clearly worse than the one obtained from an isotherm approach. In some other cases (e.g. Zn(II) at pH 5, series 13001, cf. Figure 45) no preference can be given to one of these options. A discrimination is further not feasible in all those cases where only a very few data points could be used for the fitting. This is particularly the case for experiments with Zn(II) at pH 9.

The results of the element analyses by ICP-MS showed a rather homogeneous picture for samples taken from the re-saturation phase and the diffusion experiments (cf. Figure 96 in Annex 3). For some elements no significant differences could be discerned. Examples are Fe, Ni, Cu, Al and Si. It can further be concluded from these measurements that the concentrations were governed by mineral dissolution or re-precipitation in the case of Fe, Ni, Cu, and Zn, whereas the metals were already present as impurities stemming from chemicals or containers in the case of Si and Al. A special case is Co. The concentration of this element in the diffusion experiments is clearly given by its concentration in the tracer stock solution. The values agreed with the specific activity (defined as the ratio of radionuclide per total element content) specified by the producer.

The case of Zn is different. The background concentration of Zn in the tracer stock solution was of a similar order of magnitude as the concentrations added from impurities. Further a significant element concentration decrease between the re-saturation phase and the diffusion experiments with $^{60}Co^{2+}$ could be observed for the experiments at pH 5. This can be interpreted as an uptake of added Zn by the clay.

For a simplified view it can be generally concluded for the transition elements that their concentrations in the pore water and the tracer reservoir remained more or less unchanged during the diffusion experiments. Possible competition effects on the uptake of Zn and Co can thus be roughly viewed as constant and rather similar to those occurring in a batch sorption experiment. In-diffusion of Co(II) and Zn(II) can both be viewed as a concerted process of a tracer species in a high background of the stable element in which the tracer is distributed between the solid and solution phase according to the distribution of the stable species.

A similar picture was also obtained for the earth alkaline elements and K^+ (cf. Figure 97, Annex 3). Although small differences between the results of the re-saturation and the diffusion experiments exist, these are rather caused by the fact that the first were only measured for 0.01 and 0.03 M $NaClO_4$, while the latter also include data in the range between 0.1 and 1.0 M $NaClO_4$. Possible correlations of the element concentrations with the concentrations of the background electrolyte could rather be expected for these elements. For this reason the results are plotted as a function of $NaClO_4$ concentration in Figure 98 (Annex 3). Although there is a certain trend of increasing element concentration with increasing concentration of the background electrolyte in the case of Mg^{2+} and Ca^{2+}, the effects are clearly less than predicted for a pure cation exchange process. A rather quadratic dependence would be the expectation for the exchange of two mono-valent Na^+ against bivalent cations. Almost no dependence of the concentration of K^+ on the background electrolyte concentration could be observed. It has to be noted that the background level concentration of K^+ was effected by addition of this element to the buffered electrolyte solution, while the concentrations of Mg^{2+} and Ca^{2+} were produced by the contact of the clay with the electrolyte solutions.

The experiments from series 13001 and 13004 may give the impression of being replicate measurements. However, a few nuances were done differently in these series. A major difference is the diffusion time: The duration was longer in series 13004 than in series 13001 (details are not explicitly stated in the Tables, but can be taken from left-hand plots in Figure 43 to Figure 46). Another difference is the total element concentration. These were generally larger in series 13001 compared to the experiments in series 13004. While the consistency of the results for Co(II) from both series is rather satisfying in view of the parameter uncertainties, this consistency is given for Zn(II) only for the experiments carried out at pH 5. Larger discrepancies were observed at pH 9. The reason for this discrepancy is not known.

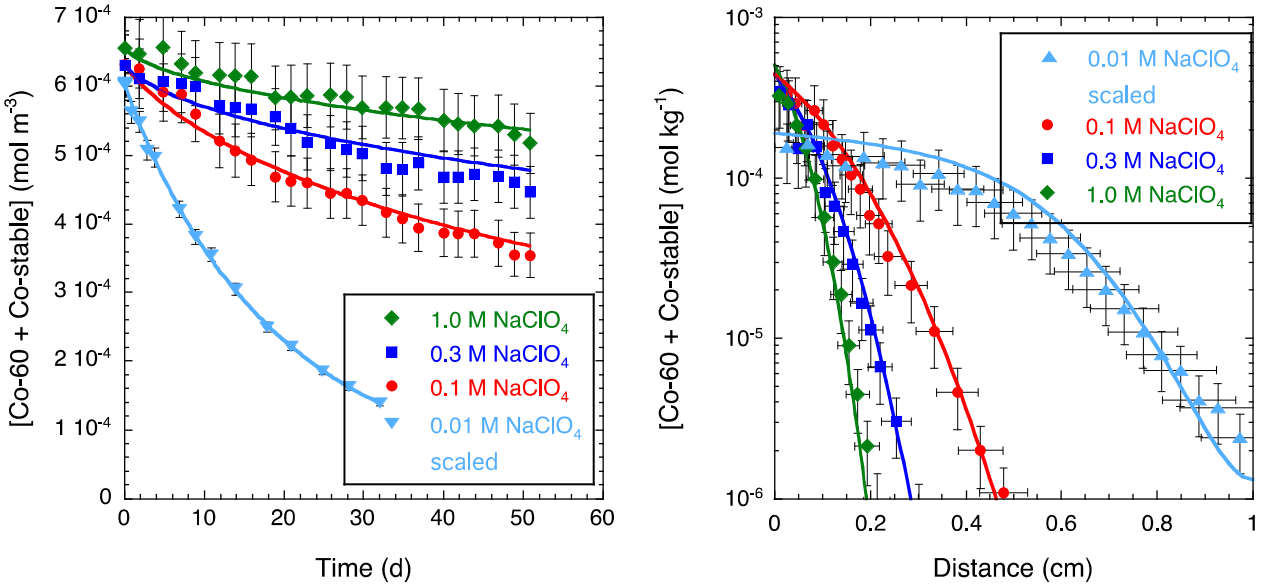

Figure 43 In-diffusion experiments with $^{60}Co^{2+}$ at pH 5 showing the total element concentration (left) and the profile of total element concentration in the clay (right). The initial concentration of the source reservoir data measured at 0.01 M $NaClO_4$ was calculated from the tracer activities using the ratio of stable element to radiotracer in the radiotracer stock solution. Fit curves were obtained from the best-fit parameter values given in Table 22.

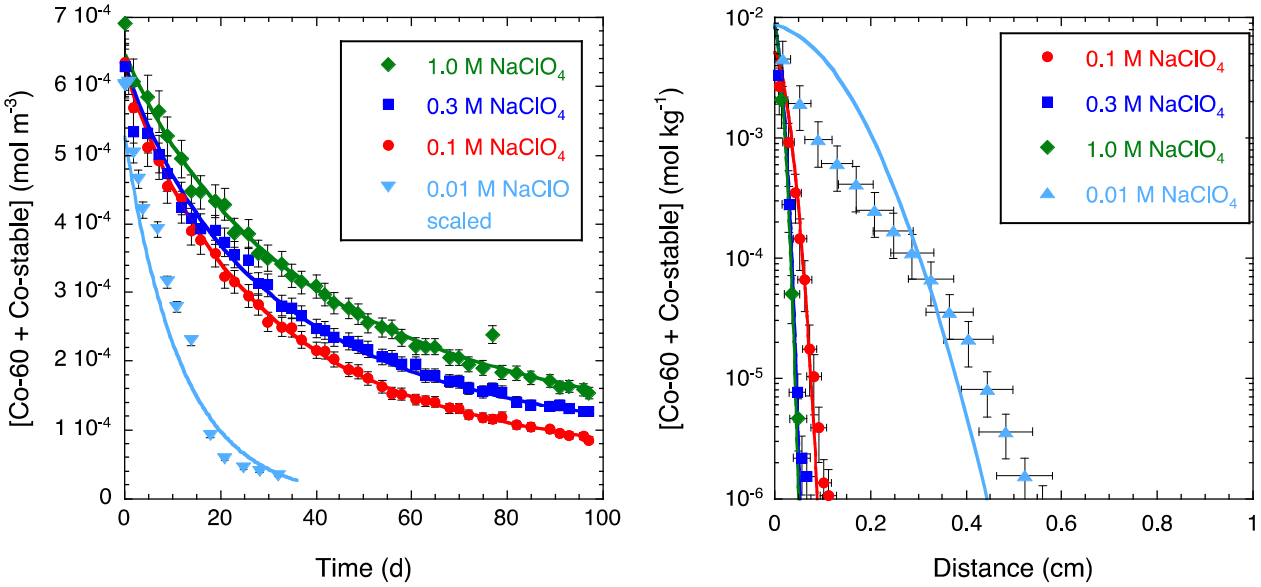

Figure 44 In-diffusion experiments with $^{60}Co^{2+}$ at pH 9 showing the total element concentration (left) and the profile of total element concentration in the clay (right). The initial concentration of the source reservoir data measured at 0.01 M $NaClO_4$ was calculated from the tracer activities using the ratio of stable element to radiotracer in the radiotracer stock solution. Fit curves were obtained from the best-fit parameter values given in Table 22.

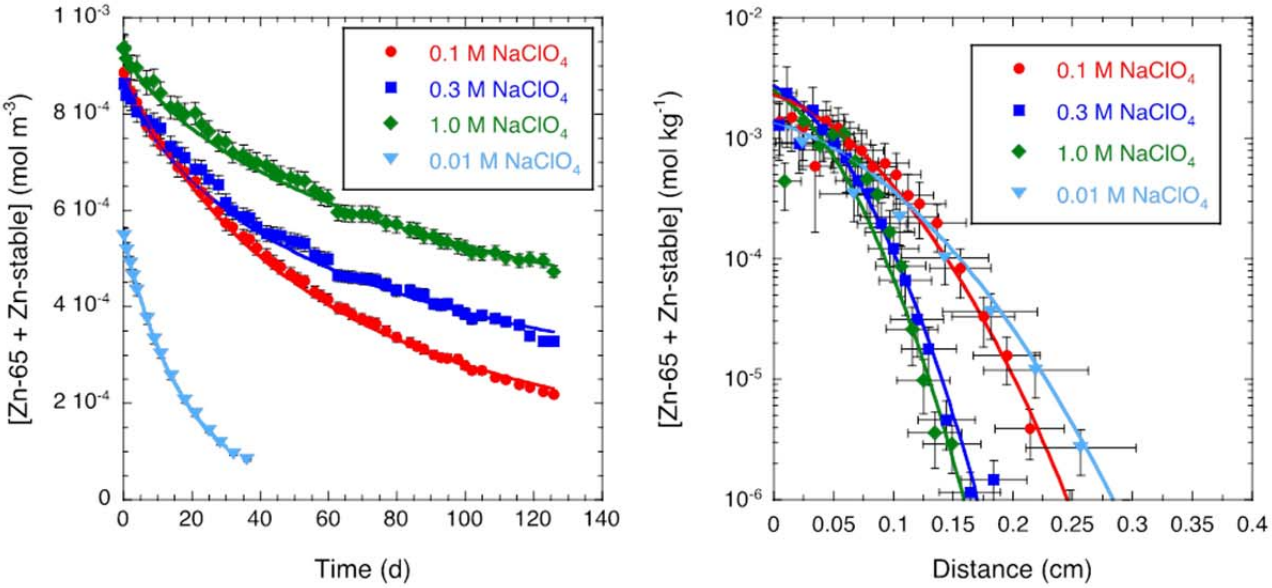

Figure 45 In-diffusion experiments with $^{65}Zn^{2+}$ at pH 5 showing the total element concentration (left) and the profile of total element concentration (right). Fit curves were obtained from the best-fit parameter values given in Table 23.

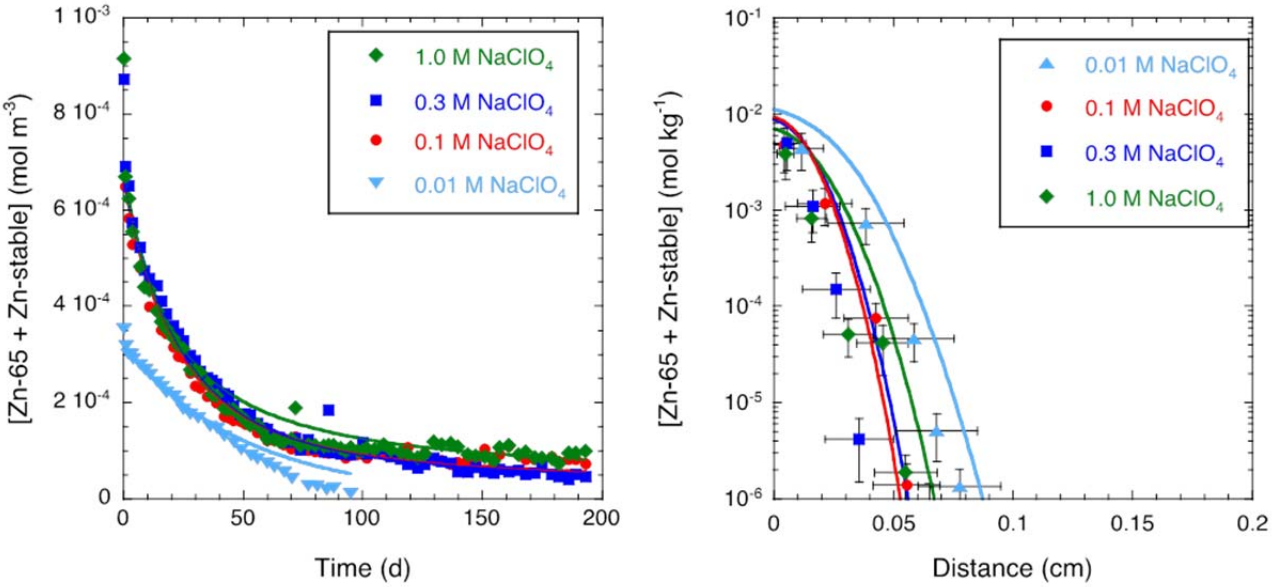

Figure 46 In-diffusion experiments with $^{65}Zn^{2+}$ at pH 9 showing the total element concentration (left) and the profile of total element concentration (right). Fit curves were obtained from the best-fit parameter values given in Table 23.

*Table 22 Best-fit parameter values for D_e and R_d and their ranges of uncertainty (95 % confidence) for in-diffusion of **Co(II)** in Na-IdP. The effective diffusion coefficient for the membrane ($D_{e,filter}$) was also treated as an adjustable parameter within a narrow range.*

Name	pH	[$NaClO_4$] (M)	D_e (opt) ($m^2\ s^{-1}$)	D_e (min) ($m^2\ s^{-1}$)	D_e (max) ($m^2\ s^{-1}$)	R_d (opt) ($m^3\ kg^{-1}$)	R_d (min) ($m^3\ kg^{-1}$)	R_d (max) ($m^3\ kg^{-1}$)	$D_{e,filter}$ ($m^2\ s^{-1}$)
13005, 4A5	4 – 5	0.01	**3.5×10^{-8}**	1.3×10^{-8}	9.1×10^{-8}	**~5 – 14** [a1]	n.a.	n.a.	2.5×10^{-10}
13005, 3A5 [d]	4 – 5	0.01	**9.6×10^{-8}**	5.5×10^{-8}	1.7×10^{-7}	**16 – 38** [a1]	n.a.	n.a.	2.5×10^{-10}
14001, 1A5	5.1	0.01	**1.8×10^{-8}**	1.2×10^{-8}	2.6×10^{-8}	**6.6** [b]	3.6	11.9	3.2×10^{-10}
14001, 3A5	5.0	0.03	**3.5×10^{-9}**	2.0×10^{-9}	5.9×10^{-9}	**2.5** [b]	1.9	3.4	2.4×10^{-10}
13001, 5A2	5.0	0.1	**6.9×10^{-10}**	4.3×10^{-10}	11.0×10^{-10}	**0.90** [b]	0.55	1.47	3.4×10^{-10}
13004, 5D	5.0	0.1	**7.8×10^{-10}**	5.3×10^{-10}	11.5×10^{-10}	**1.62** [b]	1.03	2.54	2.1×10^{-10}
13001, 5B2	5.0	0.3	**3.0×10^{-10}**	2.3×10^{-10}	3.6×10^{-10}	**1.06** [b]	0.87	1.26	1.9×10^{-10}
13004, 5E	5.0	0.3	**1.9×10^{-10}**	1.2×10^{-10}	3.0×10^{-10}	**1.10** [b]	0.63	1.93	2.1×10^{-10}
13001, 5C2	5.0	1.0	**1.1×10^{-10}**	0.95×10^{-10}	1.2×10^{-10}	**0.61** [b]	0.55	0.68	1.9×10^{-10}
13004, 5F	5.0	1.0	**0.84×10^{-10}**	0.48×10^{-10}	1.46×10^{-10}	**1.08** [b]	0.54	2.17	2.1×10^{-10}
13005, 4A9	8 – 9	0.01	**~8.0×10^{-8}** [c]	n.a.	n.a.	**~130** [a2]	n.a.	n.a.	5.6×10^{-10}
13005, 3A9 [d]	8 – 9	0.01	**~1.0×10^{-7}** [c]	n.a.	n.a.	**~200** [a2]	n.a.	n.a.	5.6×10^{-10}
14001, 1A9	9.1	0.01	**1.1×10^{-8}**	4.4×10^{-9}	2.8×10^{-8}	**135** [a2]	53	348	2.3×10^{-9}
14001, 3A9	9.1	0.03	**2.2×10^{-9}**	1.0×10^{-9}	4.7×10^{-9}	**324** [a2]	157	669	4.3×10^{-9}
13001, 9A2	8.9	0.1	**8.3×10^{-10}**	7.4×10^{-12}	9.3×10^{-8}	**60.2** [b]	0.59	6193	2.9×10^{-10}
13004, 9D	9.0	0.1	**5.3×10^{-10}**	4.3×10^{-10}	6.5×10^{-10}	**90** [b]	72	112	3.3×10^{-10}
13001, 9B2	9.0	0.3	**1.0×10^{-10}**	1.1×10^{-11}	9.0×10^{-10}	**23.3** [b]	3.0	181	1.9×10^{-10}
13004, 9E	9.0	0.3	**2.1×10^{-10}**	1.4×10^{-10}	3.0×10^{-10}	**103** [b]	72	147	3.4×10^{-10}
13001, 9C2	9.0	1.0	**1.5×10^{-10}**	1.0×10^{-11}	2.1×10^{-9}	**26.3** [b]	1.49	464	1.9×10^{-10}
13004, 9F	9.0	1.0	**1.7×10^{-10}**	1.0×10^{-10}	2.7×10^{-10}	**93** [b]	59	148	2.2×10^{-10}

[a1] 1-sites isotherm using a site capacity of 2.7×10^{-3} mol kg^{-1} [a2] The parameter uncertainties are extraordinary large in this experiment [b] Data modelled using a constant R_d.

[c] Fit by eye. [d] Diffusion cell equipped with a 3 mm aperture mask. The best-fit parameter values were taken from the corresponding experiment with a 4 mm aperture mask as a blind prediction.

*Table 23 Best-fit parameter values for D_e and R_d and their ranges of uncertainty (95 % confidence) for in-diffusion of **Zn(II)** in Na-IdP. The effective diffusion coefficient for the membrane ($D_{e',filter}$) was also treated as an adjustable parameter within a narrow range.*

Name	pH	[$NaClO_4$] (M)	D_e (opt) ($m^2\ s^{-1}$)	D_e (min) ($m^2\ s^{-1}$)	D_e (max) ($m^2\ s^{-1}$)	R_d (opt) ($m^3\ kg^{-1}$)	R_d (min) ($m^3\ kg^{-1}$)	R_d (max) ($m^3\ kg^{-1}$)	$D_{e,filter}$ ($m^2\ s^{-1}$)
13005, 4B5	4 – 5	0.01	**4.1×10^{-8}**	n.a.[c]	n.a.[c]	**204**[b]	n.a.[c]	n.a.[c]	3.7×10^{-10}
13005, 3B5[d]	4 – 5	0.01	**4.1×10^{-8}**	n.a.[c]	n.a.[c]	**204**[b]	n.a.[c]	n.a.[c]	3.7×10^{-10}
14001, 1B5	5.0	0.01	**9.3×10^{-9}**	8.0×10^{-9}	1.1×10^{-8}	**44**[b]	36	55	4.7×10^{-10}
14001, 3B5	5.0	0.03	**4.6×10^{-9}**	2.2×10^{-10}	1.1×10^{-7}	**49**[b]	2	1420	3.4×10^{-10}
13004, 5G	5.0	0.1	**7.0×10^{-10}**	5.9×10^{-10}	8.3×10^{-10}	**17.5**[b]	14.5	21.0	2.1×10^{-10}
13001, 5B	5.0	0.3	**4.6×10^{-10}**	1.2×10^{-10}	1.8×10^{-9}	**13.5 – 16.9**[a1]	n.a.[c]	n.a.[c]	1.9×10^{-10}
13001, 5B	5.0	0.3	**3.3×10^{-10}**	1.8×10^{-10}	6.1×10^{-9}	**11**[b]	5.7	21.1	1.9×10^{-10}
13004, 5H	5.0	0.3	**1.9×10^{-10}**	1.9×10^{-10}	3.0×10^{-10}	**10.4**[b]	7.1	15.3	2.1×10^{-10}
13001, 5C	5.0	1.0	**8.0×10^{-11}**	n.a.[c]	n.a.[c]	**5.4 – 9.5**[a2]	n.a.[c]	n.a.[c]	1.9×10^{-10}
13001, 5C	5.0	1.0	**8.0×10^{-11}**	n.a.[c]	n.a.[c]	**6**[b]	n.a.[c]	n.a.[c]	1.9×10^{-10}
13004, 5I	5.0	1.0	**1.1×10^{-10}**	0.58×10^{-10}	2.1×10^{-10}	**6.7**[a]	3.7	12.3	1.7×10^{-10}
13005, 4B9	8 – 9	0.01	**9.0×10^{-9}**	n.a.[c]	n.a.[c]	**856 – 977**[a3]	n.a.[c]	n.a.[c]	3.8×10^{-10}
13005, 3B9[d]	8 – 9	0.01	**9.0×10^{-9}**	n.a.[c]	n.a.[c]	**856 – 977**[a3]	n.a.[c]	n.a.[c]	3.8×10^{-10}
14001, 1B9	9.0	0.01	**2.0×10^{-8}**	n.a.[c]	n.a.[c]	**2700 – 4000**[a3]	n.a.[c]	n.a.[c]	6.4×10^{-10}
14001, 3B9	9.0	0.03	**5.0×10^{-9}**	n.a.[c]	n.a.[c]	**1150 – 2000**[a3]	n.a.[c]	n.a.[c]	5.8×10^{-10}
13001, 9A	8.9	0.1	**1.2×10^{-9}**	6.3×10^{-10}	2.2×10^{-9}	**158**[b]	85	295	3.1×10^{-10}
13004, 9G	9	0.1	**1.8×10^{-10}**	1.4×10^{-10}	2.4×10^{-9}	**198**[b]	195	201	6.9×10^{-10}
13001, 9B	9.0	0.3	**4.6×10^{-10}**	2.5×10^{-10}	8.6×10^{-10}	**99**[b]	50	193	3.0×10^{-10}
13004, 9H	9	0.3	**1.7×10^{-10}**	1.4×10^{-10}	2.0×10^{-9}	**343**[b]	342	344	3.8×10^{-10}
13001, 9C	9.0	1.0	**4.8×10^{-10}**	1.7×10^{-10}	1.4×10^{-9}	**270**[b]	97	751	3.6×10^{-10}
13004. 9I	9	1.0	**$(1.0–1.5)\times10^{-10}$**	[e]—	—	**100–250**	—	—	5.0×10^{-10}

[a1] 1-sites isotherm using a site capacity of 1.25×10^{-2} mol kg^{-1} [a2] 1-sites isotherm using a site capacity of 0.55×10^{-2} mol kg^{-1}. [a3] 1-sites isotherm formally applied with no clear justification. [b] Data modelled using a constant R_d. [c] Uncertainties not accessible. [d] Diffusion cell equipped with a 3 mm aperture mask. The best-fit parameter values were taken from the corresponding experiment with a 4 mm aperture mask as a blind prediction. [e] fit by eye

SCK·CEN. The purpose at SCK·CEN was to find out if diffusion of Zn in illite is dependent on pH and/or inorganic carbon. A part of the planned experiments could, however, not be performed due to sorption on the filter plates at higher pH. For pH 5, the conventional diffusion cell with steel filter plates could be used, but at higher pH not anymore. Finally, an alternative set up with a PEEK filter (IDP13) and polypropylene filter (IDP15) could provide results for Zn diffusion in illite at pH 7. The best-fit parameters of the experiments at pH 5 and 7 are summarised in Table 24. Note that the errors on the capacity factor α are quite large compared to the errors obtained for Sr diffusion. This can be explained by the fact that the influence of the capacity factor on the clay profile is much larger for low α (as for Sr) than for high α. Since D_e is the product of D_a and α, this indicates that the error on D_e is also large.

Table 24 Parameters for diffusion of Zn in Illite du Puy. D_a and α are the fitted parameters (D_e is the product of both parameters). Errors on the fitted D_a vary between 1 and 6%; errors on α are given in the table.

Experiment	pH	IS (M)	Inorganic carbon	D_a ($m^2\ s^{-1}$)	α (-)	Error α (%)	**D_e ($m^2\ s^{-1}$)**
IDP9	5±0.1	0.1	no IC	5.5×10^{-14}	1.23×10^{4}	45	**6.8×10^{-10}**
IDP10	5±0.1	0.1	no IC	1.5×10^{-13}	5.27×10^{3}	72	**7.8×10^{-10}**
IDP22	5±0.5	1	atm IC	1.0×10^{-14}	7.99×10^{3}	116	**8.0×10^{-11}**
IDP13	7±0.1	0.1	atm IC	3.1×10^{-14}	1.64×10^{4}	18	**5.1×10^{-10}**
IDP15*	7±0.1	0.1	atm IC	1.4×10^{-14}	1.60×10^{4}	26	**2.2×10^{-10}**

* A leak at the inlet reservoir may have resulted in a discontinuity in the inlet reservoir concentration decrease. Also sorption of the Zn tracer on the tubing resulted in loss of ~ 25% of the mass at the end of the experiment. This sorption has not been taken into account in the modelling.

Figure 47 shows one of the experiments (IDP 10) as an example for the Zn diffusion experiments. From this figure it can be seen that the concentration in the source reservoir decreases very strongly (to a few % of the initial concentration). The two experiments at pH 5 (IDP9 and IDP10) gave different experimental data, although being replicates (identical experimental setup, initial activity, sampling regime). In experiment IDP10 Zn diffused into the clay over a distance of 5 mm (cf. Figure 47), while it only diffused over 3 mm in experiment IDP9. This resulted in different D_a and α (factor of two difference), but the D_e is in agreement.The reasons for this difference are currently unknown. Experiment IDP22 is performed at higher ionic strength in a flushed filter set up. An increase of the IS with a factor 10 caused a decrease of D_e with a factor 10 too. This trend was also observed at PSI (Table 23).

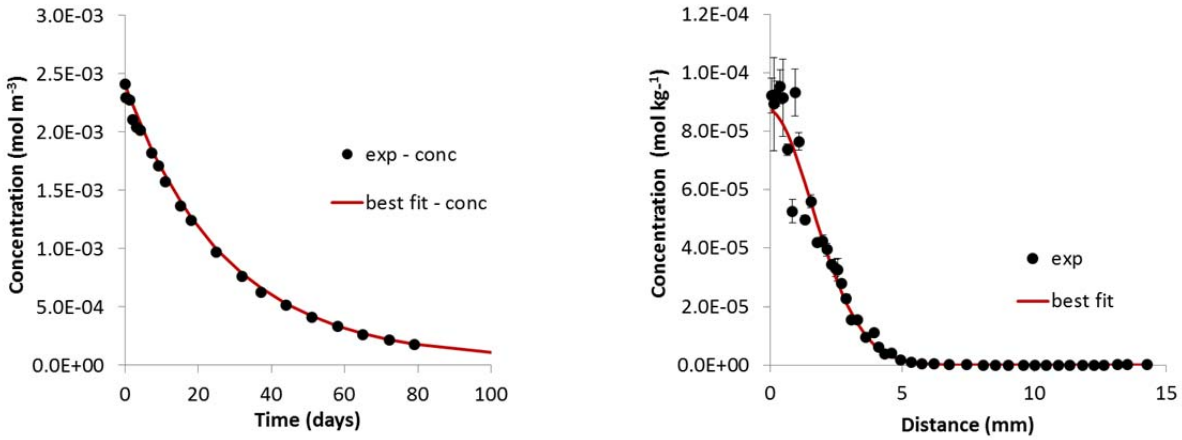

Figure 47 Experimental and best fits of IDP 10 (In-diffusion Zn - pH 5 – IS 0.1 M – no CO_2). Left-hand plot: concentration decrease source reservoir (left axis); right-hand plot: concentration profile in the clay plug.

Experiments IDP13 and IDP15 were both performed at pH 7, but differ in experimental setup: IDP13 was performed with a PEEK filter while IDP15 was performed with a flushed filter diffusion cell with polypropylene filters. The obtained best-fit values should be interpreted carefully since the experimental conditions were not ideal for the two experiments. Due to the small source reservoir in experiment IDP13, the concentration decrease is very steep, which is difficult to fit. In IDP15, the data of the concentration in the source reservoir are biased due to a leak in the system and sorption on the tubing. The concentration profiles in the clay could be fitted well in both experiments, but the concentration decrease in the source reservoirs was overestimated. The α values agree very well and are higher than the α determined for the experiments at pH 5. The corresponding K_d values ($9.4\text{-}9.6\times10^{3}$) are, however, one order of magnitude lower than the K_d values determined in batch sorption experiments (K_d 1.1×10^{5}) at pH 7 and IS 0.1 M. The D_a values vary by a factor two between the two experiments. Additional results are necessary to be able to make a strong conclusion. The MCDC could be an alternative to measure the diffusion at higher pH.

This sorption problem had also consequences for the experiments at different pCO_2 to define the effect of carbonates on the diffusion of Zn. Since the complexation of Zn with carbonates only starts above pH 7 (speciation calculations are shown in Figure 19) at 0.4% CO_2 conditions, it was not possible to perform the experiments at higher pCO_2 conditions with the currently available diffusion technique at SCK·CEN. The hypothesis was that the carbonate complexation at higher pH would result in a lower sorption due to the lower amount of free Zn^{2+} available. However, in the sorption isotherms (Figure 28), this effect could not be observed. Hence, it is expected that there is neither an effect on diffusion.

The main conclusion that can be drawn at this moment, is that the D_e values determined from these experiments are consistently higher than the D_e of HTO (average 1.83×10^{-10} m² s^{-1}), but the effect is less pronounced than for Sr. The first data reveal that diffusion of Zn in illite is faster than expected from the batch K_d values.

2.5.2 Diffusion in reduced surface charge clay minerals

As observed in part 2.5.1 and earlier studies (Glaus et al., 2007; 2010), values for D_e decrease for cationic and increase for anionic tracers with increasing ionic strength. This indicates that an electrostatic shielding of the surface charge (by an increase in ionic strength) is affecting the diffusion properties of charged solutes. An interesting question related to this subject is, how these properties are altered if the negative surface charge is occupied by (i) Cs^+ or (ii) a high selective organic ligand-metal complex such as copper-ethylenediamine $Cu(en)_2^{2+}$. While the former is known to be associated with both the "frayed edges" (FES) and "type II" sites (situated on the permanently charged basal surfaces) (Glaus et al., 2007; Poinssot et al, 1999), the latter was reported to block effectively the planar surface charge in montmorillonites and reduce considerably the access of alkaline-earth metals to these exchange sites (Maes et al., 1978; Maes & Cremers, 1979). Thus, Cs- and $Cu(en)_2^{2+}$ exchanged illites were prepared and used for multi-tracer (HTO, $^{36}Cl^-$ and $^{85}Sr^{2+}$) diffusion studies.

Additionally, a $Cu(en)_2^{2+}$-exchanged montmorillonite was prepared, as effects on charge-reduction on the planar surfaces are expected to be higher for swelling clay minerals (the interlayers of the low-charged montmorillonite are accessible for positively charged solutes (Glaus et al., 2007)). The experiments were performed in two laboratories, i.e. diffusion with Cs-illite (only HTO and $^{36}Cl^-$) was tested at KIT-INE, while the experiments on $Cu(en)_2^{2+}$-exchanged illite and montmorillonite ((HTO, $^{36}Cl^-$ and $^{85}Sr^{2+}$) were performed at PSI-LES.

2.5.2.1 Experimental method

Cs-illite was prepared according to the protocol used for Na-illite. Shortly, 100 g of Na-illite were equilibrated in 1L of 1M CsCl at pH 3.5 for four hours, by which exchangeable Na^+ is replaced by the Cs^+. Hereby, a constant pH is maintained by addition of 5×10^{-2} M Cs-formiate/formic acid buffer. Subsequently the clay is washed with 1 M CsCl (4 times; no buffer added) and dialyzed against MilliQ water, removing excessive CsCl. This dialysis step is repeated until no Cl could be measured in the outer solution (by precipitation of AgCl). A fine grained and homogeneous dry material was obtained by freeze-drying. For $Cu(en)_2^{2+}$-illite preparation, 13.5 mmol $CuSO_4\cdot5H_2O$ were dissolved in 2 L MilliQ water. Subsequently 30 mmol ethylenediamine was added and the mixture stirred for 1h. The solution was transferred in a 2 L Kautex bottle containing 100 g Na-illite (CEC = 225 meq kg^{-1}) and shaken end-over-end overnight. Hereafter, the supernatant was separated and discarded by a gentle centrifugation (2000 rpm for 1h) and the solid was suspended in neutral MilliQ water (pH 7). This procedure was repeated until the solution was colourless. The fine grained material was obtained by freeze drying and sieving (<63µm). In case of montmorillonite the experimental procedure was adapted to the higher CEC of Na-montmorillonite (CEC = 850 meq kg^{-1}): 51.5 mmol Cu(II), 2 L MilliQ water, 112.2 mmol ethylenediamine.

The solids were compacted to a bulk dry density ρ_{db} of ~1700 kg m^{-3}. The diffusion experiments with $Cu(en)_2^{2+}$-illite and -montmorillonite were performed according to published procedures ((Van Loon et al., 2003). However, diffusion cells with advectively flushed filters were used (for details see Glaus et al., 2007; 2010). The samples were pre-equilibrated against 0.1M $NaClO_4$/1×10^{-4} M KCl/5×10^{-3} M MES solutions (pH 5) from both sides. After one month the solutions were replaced against new ones. The new solution in one reservoir was spiked with HTO, ^{36}Cl (both at ~1000 Bq cm^{-3}) and ^{85}Sr (~ 100 Bq cm^{-3}), while the other one contained the background electrolyte solely (representing the high (HCR)- and low-concentration (LCR) reservoir with V_{tot} = 100 and 20 mL, respectively). The solutions at the low-concentration boundary were replaced daily (to keep the concentration of the tracer in this compartment as low as possible), while the high-concentration reservoir remained unchanged and was sampled in time intervals of three or four days. The activities of $A_{85\text{-}Sr}$, $A_{36\text{-}Cl}$ and A_{HTO} (Bq) were measured by γ- (^{85}Sr) and liquid scintillation counting (HTO and $^{36}Cl^-$) and can be calculated respectively according to the following equations:

$$A_{Sr} = \frac{N_{Sr}}{f_{Sr}\cdot 60} \qquad (13)$$

$$A_{Cl} = \frac{N_{tot}^{20-600keV} - A_{Sr} \cdot 60 \cdot f_{Sr}^{20-600keV}}{f_{Cl}^{20-600keV} \cdot 60} \quad (14)$$

$$A_{HTO} = \frac{N_{tot}^{0-20keV} - A_{Cl} \cdot 60 \cdot f_{Cl}^{0-20keV} - A_{Sr} \cdot 60 \cdot f_{Sr}^{0-20keV}}{f_{HTO}^{0-20keV} \cdot 60} \quad (15)$$

where N_{Sr} is the measured activity in counts per minute (cpm), f_{sr} the system dependent efficiency factor for ^{85}Sr for γ-counting, $N_{tot}^{20-600keV}$ and $N_{tot}^{0-20keV}$ the total activities (cpm) determined by LSC in the respective energy windows (0-20 and 20-600 kEv) and $f_{Cl/Sr}^{0-20/20-600keV}$ the system dependent efficiency factor for ^{85}Sr and ^{36}Cl determined in the respective energy windows for liquid scintillation counting. The therein determined activities were corrected for decay.

Experiments on HTO and ^{36}Cl diffusion in Cs-illite (executed by KIT-INE) were performed in 0.1 and 1 M NaCl at pH 5 (addition of 1×10^{-4} M KCl and 1×10^{-2} M MES). The experimental setup and procedure followed the one described in the part of HTO and Cl^- diffusion in Na-illite. However, two modifications were applied: (i) the activities were increased to improve the resolution (~2000 and ~200 Bq cm^{-3} for HTO and ^{36}Cl, respectively) and (ii) the volume of the low-concentration reservoir was increased to V_{tot} = 500 mL, while the solution remained unchanged throughout the experiment. Consequently the concentration of the tracer in this compartment after termination (t~100d) was ~6 % and ~9% of the tracer concentration in the high concentration reservoir for ^{36}Cl and HTO, respectively.

2.5.2.2 Diffusion of HTO, $^{36}Cl^-$ and $^{85}Sr^{2+}$ in reduced surface charge illite

In Figure 48 the results for HTO (a), $^{36}Cl^-$ (b) and $^{85}Sr^{2+}$ (c) diffusion through $Cu(en)_2$-illite, both as flux and evolution of activity in the high concentration reservoir, are depicted. The data are also representative for $Cu(en)_2^{2+}$-montmorillonite. For HTO and $^{36}Cl^-$, a steady state (indicated by a constant flux) is reached fast (~4 and ~8 days for HTO and ^{36}Cl, respectively), while the flux for $^{85}Sr^{2+}$ is still increasing after 32 days. Due to a limited amount of time, the experiments were terminated after this period. The effective diffusion coefficient D_e and the rock capacity factor α were calculated using the Comsol Multiphysics computer code and are presented in Table 25 together with values determined for Na-illite and -montmorillonite.

Table 25 Summary of D_e ($m^2\ s^{-1}$) and α (-) values for HTO, ^{36}Cl and ^{85}Sr in $Cu(en)_2^{2+}$-illite and -montmorillonite at a bulk dry density (ρ_{db}) of 1700 kg m^{-3}, together with literature data for the Na-exchanged clays.

Tracer	$Cu(en)_2^{2+}$-illite		Na-illite		$Cu(en)_2^{2+}$-mnt.		Na-mnt.	
	D_e (10^{-10} $m^2\ s^{-1}$)	α (-)	D_e (10^{-10} $m^2\ s^{-1}$)	α (-)	D_e (10^{-11} $m^2\ s^{-1}$)	α (-)	D_e (10^{-11} $m^2\ s^{-1}$)	α (-)
HTO	1.76±0.19	0.44±0.13	2.0±0.2[a]	0.43±0.20	3.35	0.39	3.1±0.7[b]	0.39[b]
^{36}Cl	0.65±0.09	0.32±0.10	0.67±0.04[a]	0.18[a]	0.98	0.14	0.0072±0.0008[c]	0.019±0.002[c]
^{85}Sr	1.56±0.61	40.9±20.0	9.6[a]	90[a]	9.66±5.50	20.3±15.8	310±220[d]	330±120[d]

[a]: this work ; [b]: total porosity and rescaled D_e (Archie´s law) from (Glaus et al., 2013), ρ_{db} = 1564 kg m^{-3}, salinity 1.0 M $NaClO_4$; [c]: (Glaus et al., 2010); ρ_{db} = 1900 kg m^{-3}, salinity 0.1 M $NaClO_4$; [d]: personal communication M.A. Glaus, recalculated from ρ_{db} = 1600 kg m^{-3}, salinity 0.1 M $NaClO_4$.

For HTO the values for the effective diffusion coefficient and α for both $Cu(en)_2^{2+}$-illite and -montmorillonite are in good agreement with literature data on the Na^+-exchanged clays, indicating that the porosity was not altered by $Cu(en)_2^{2+}$-exchange.

In the case of $Cu(en)_2^{2+}$-montmorillonite D_e as well as the porosity for ^{36}Cl are significantly higher compared to the Na-form, indicating that anions are no longer repelled form the vicinity of the clay surface (note that the data cannot be compared directly due to the higher bulk dry density and higher background electrolyte concentration used by Glaus et al. 2010). However, this effect is not observed in the case of $Cu(en)_2^{2+}$-illite. This dissimilarity can be understood in the context of the different types of pore space available in both clay minerals. While interlayer pores are present in Na-montmorillonite, these are not accessible in illite because of the intercalation of dehydrated K^+-cations. A similar situation is encountered in $Cu(en)_2^{2+}$-montmorillonite as evidenced by X-ray diffraction (Maes et al., 1978). The interlayer spacing is largely collapsed due to intercalation of $Cu(en)_2^{2+}$ complexes and the available porosity can be assumed to exhibit the character of interparticle porosity. The conversion of interlayer porosity to interparticle porosity induced by $Cu(en)_2^{2+}$ has thus a significant effect on anion diffusion in montmorillonite, while the effect of the modification of external surfaces by the presence of $Cu(en)_2^{2+}$ complexes in illite appears to be less.

For cationic ^{85}Sr both D_e and α decrease by $Cu(en)_2^{2+}$-exchange compared to the Na^+-form in case of illite and montmorillonite, pointing thus to the fact that Sr^{2+} enrichment near the charged surfaces (a pre-requisite for the enhanced mass transfer compared to HTO) is reduced due to a local neutralization of the negative surface charge. The diffusive behaviour of Sr^{2+} in the $Cu(en)_2^{2+}$ modified clay minerals is, however, clearly distinct from the one of HTO indicating that charge effects near the interparticle surfaces are still effective.

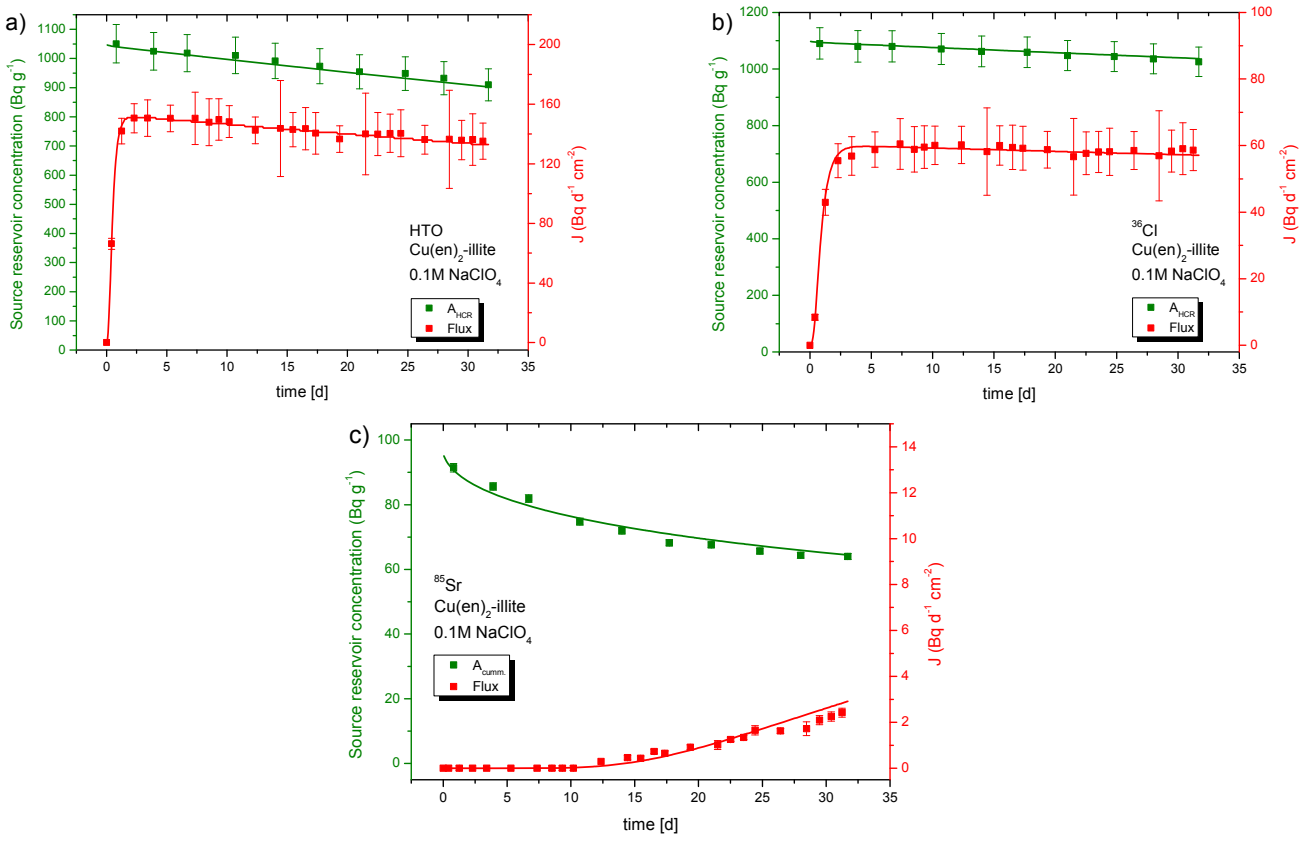

Figure 48 Diffusion of HTO (a) $^{36}Cl^-$ (b) and $^{85}Sr^{2+}$ (c) through compacted $Cu(en)_2$-illite (ρ_{db}~1700 kg m^{-3}; pH 5 and 0.1M $NaClO_4$) as mass flux in the low concentration reservoir (J) and evolution of the source reservoir concentration.

The results for HTO and ^{36}Cl diffusion in Cs^+-exchanged illite at 0.1 and 1.0 M NaCl are shown in Figure 49 (only presented for 1 M NaCl, but similar data are obtained for 0.1 M NaCl). As described in the experimental part, the setup differed compared to the experiments described in §2.5.1 More specifically, (i) the volume at the low-concentration boundary was increased to 500 mL, and (ii) the reservoir solution remained unchanged throughout the experiment. This change might be responsible for the fact that a longer reaction time was needed to reach a steady state compared to the previous experiments (performed with a similar bulk dry density), i.e. steady state conditions are reached after ~20 days for HTO and ~30 days in case of ^{36}Cl.

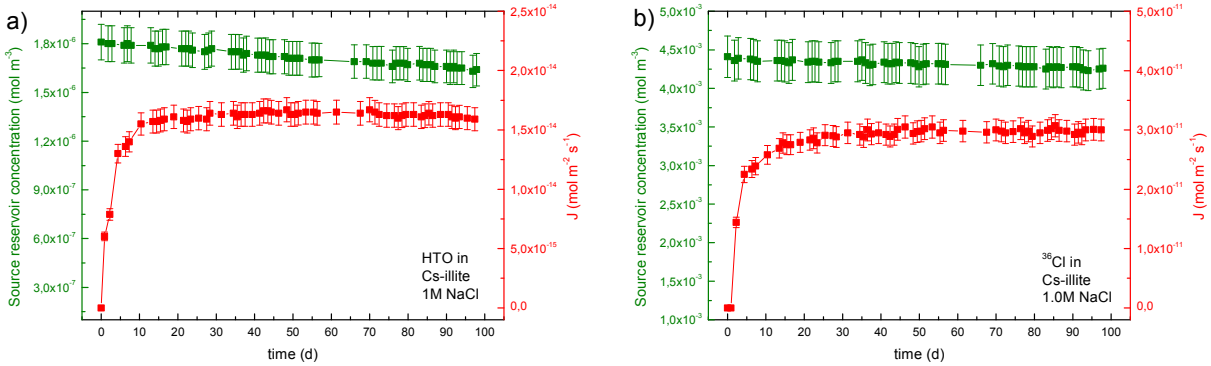

Figure 49 Diffusion of HTO (a) and $^{36}Cl^-$ (b) in compacted Cs-illite (ρ_{db}~1700 kg m^{-3}) at pH 5.5 and 1.0 M NaCl as mass flux in the low concentration reservoir (J) and evolution of the source reservoir concentration.

Values for D_e and α were calculated by linear regression analysis of the data on the total accumulated activity vs. time and are summarised in Table 26 together with the data on Na-illite. Note that by this method the effect of the perforated filter plate (used in the setup by KIT-INE; annex 1) on the diffusion properties is not considered (which leads to significsantly different D_e values in the present results compared with Table 19). Thus, only the relative values in Table 26 can be compared directly. In 0.1 M NaCl, D_e values for HTO in Cs-illite tend to be ~20% smaller than the ones derived for Na-illite, while similar diffusion coefficients are observed for ^{36}Cl in both Cs- and Na-illite. An increase in the background electrolyte concentration leads, as expected, to an increase in D_e in case of ^{36}Cl, while it does not affect the diffusion coefficient in case of HTO. However, the α value for ^{36}Cl in 1 M NaCl was observed to be lower compared to 0.1 M NaCl, which can be related to the higher uncertainties in determining α values by linear regression analysis on the cumulated activity plot. As α is derived from intercept of the cumulated activity vs. time plot, its value is highly dependent on the choice of data points, i.e. if all the data points are chosen, or if the data derived at the end of the experiment, where the constant boundary conditions are violated, are omitted. Therefore, the absolute α values given in Table 26 have to be taken with care and more robust data can be obtained by modelling (results are on the way).

Table 26 Summary of D_e ($m^2\ s^{-1}$) and α (-) values for HTO and ^{36}Cl in Na- and Cs-illite at a bulk dry density (ρ_{db}) of ~1700 kg m^{-3}. The values were calculated using an analytical method (Van Loon et al., 2003).

Tracer	NaCl (M)	Na-illite		Cs-illite	
		D_e (10^{-10} $m^2\ s^{-1}$)	α (-)	D_e (10^{-10} $m^2\ s^{-1}$)	α (-)
HTO	0.1	1.36±0.08	0.56	1.12±0.07	0.35
	1.0	1.41±0.09[a]	0.42[a]	1.14±0.07	0.70
^{36}Cl	0.1	0.55±0.03	0.22	0.60±0.04	0.29
	1.0	0.80±0.05[a]	0.67[a]	0.76±0.05	0.13

[a]: salinity 0.5 M NaCl

Keeping these uncertainties in mind, the comparison between Na- and Cs-illite indicates that Cs-exchange does not alter the diffusion properties of anionic tracers. However, this result may also be due to a leaching of Cs^+ from the solid during the course of the experiments. Poinssot et al. (1999) reported that Cs uptake on Na-illite takes place mainly at two different sites, "frayed edges" (FES) and "type II" sites with sites capacities of 0.55 and 35 meq·kg^{-1} (which is approx. 28% of the available exchange capacity of Na-illite used in their work). Analysis of the outside solution after termination of the diffusion experiments showed that 23 mmol kg^{-1} were released from the clay, which is ~65% of Cs^+ associated with the solid. This release of Cs^+ is in line with the low selectivity coefficient for the cation exchange reaction of Cs on a Na-illite for the "type II" sorption sites $\log K_C^{II}_{Na}^{Ca}$= 3.60±0.2 (a higher selectivity coefficient is reported for the FES ($\log K_C^{FES}_{Na}^{Ca}$= 6.95±0.2), however, the capacity for this sorption site is three orders of magnitude lower compared to the former one).

Thus, a neutralization of the negative surface charge associated with the edges and permanently charged basal surfaces is not fully achieved within the present experiments, as Cs^+, initially associated with illite, is released into solution by (most likely) Na^+/K^+ exchange. Thus a negative charge situated on the external surfaces is still present, affecting/decreasing the transport of ^{36}Cl in comparison to neutral HTO. As the present experiments were performed in 0.1 M NaCl (also 1×10^{-4} M KCl were added to account for K^+ release by partial clay dissolution), a change in background electrolyte (solely CsCl) may avoid the observed Cs^+ release.

2.6 Discussion and conclusions: speciation – diffusion model for cations in illite

2.6.1 Dependence of D_e and sorption properties on geochemical conditions

In order to define the underlying mechanisms of cation diffusion in compacted clays, a series of sorption and diffusion experiments were performed at various geochemical conditions (CO_2, pH, external salinity).

Effect of carbonate conditions. According to the speciation calculations in §2.3.2, Sr and Zn can form carbonate complexes at higher pCO_2 conditions. At the studied conditions (0.4% CO_2, 16 mM $NaHCO_3$, pH 8.2), however, only 5% of Sr would complex with carbonates, while 25% Zn could form complexes. At higher pCO_2 pressures, the fraction of carbonate complexes increases, but these conditions are not relevant anymore for the geological disposal concept. In case of carbonate complexation, it was expected that sorption would be lower due to less available free metal ion. However, the sorption of Zn was hardly affected by the higher CO_2 pressure (§2.4.4.2). For the diffusion experiments, we could only perform experiments at higher CO_2 pressure with Sr and not with Zn, since the higher pCO_2 results also in a higher pH. There is not yet a suitable diffusion technique to perform the diffusion experiments at higher pH for Zn (sorption problems of Zn on the filter and cell materials). Finally, we observed a slightly higher diffusion coefficient for

Sr at higher pCO_2, but the higher equilibrium pH (8.2 compared to 7) at these pCO_2 conditions is a more plausible explanation for this observation. For Zn, we assume that the diffusion will not be influenced largely by higher pCO_2 conditions, based on the very small effect of pCO_2 observed in the sorption experiments.

Effect of pH. From the sorption edges, it is clear that strontium mainly binds via ion exchange. However, sorption of Sr on illite increases slightly at higher pH, which indicates that Sr will partly bind via surface complexation too. The larger sorption at higher pH was also observed in the diffusion experiments (higher α at higher pH). Also the effective diffusion coefficients increased with an increasing pH (factor 2 to 10 between pH 5 and 9).

For Zn and Co, the sorption experiments revealed that surface complexation is the dominant mechanism. This was also observed in the diffusion experiments. The R_d values for Zn and Co showed a strong dependence of pH, again confirming the surface complexation as sorption mechanism. There was, however, no clear effect observed for the effective diffusion coefficient.

Effect of external salinity. The dependence of best-fit parameter values for D_e and R_d as a function of the $NaClO_4$ concentration in the contacting solution is shown in Figure 50 for Co(II), Figure 51 for Zn(II) and Figure 52 for Sr^{2+}. The error bars and the existing discrepancies in the data obtained from series 13001 and 13004 make an unambiguous discussion difficult. However a few conclusions relevant in view of the overall direction of the Catclay project may be drawn irrespective of these uncertainties.

As a very simple but important appraisal D_e values depend significantly on the background electrolyte concentration in the contacting solution. They increase for the three elements tested with decreasing salinity. The fact that D_e values at the lowest salinity exceed the D_e values of water tracers (D_e for tritiated water is of the order of 2×10^{-10} m^2 s^{-1} (Glaus et al., 2012) by several orders of magnitude, rules out a simple diffusion model in which the effective diffusion coefficient for a given element is determined by its diffusion coefficient in bulk water and a species-independent geometry factor. Only in restricted ranges of the parameter space, such a model is near reality. An example for this would be Zn diffusion at pH 9 in the presence of rather saline solutions where D_e values are slightly exceeding a value of 1×10^{-10} m^2 s^{-1}. The D_e for Zn(II) diffusion in illite would be ~6×10^{-11} m^2 s^{-1} as expected from the ratio of the diffusion coefficients in bulk water for Zn and HTO and assuming the same geometry factors.

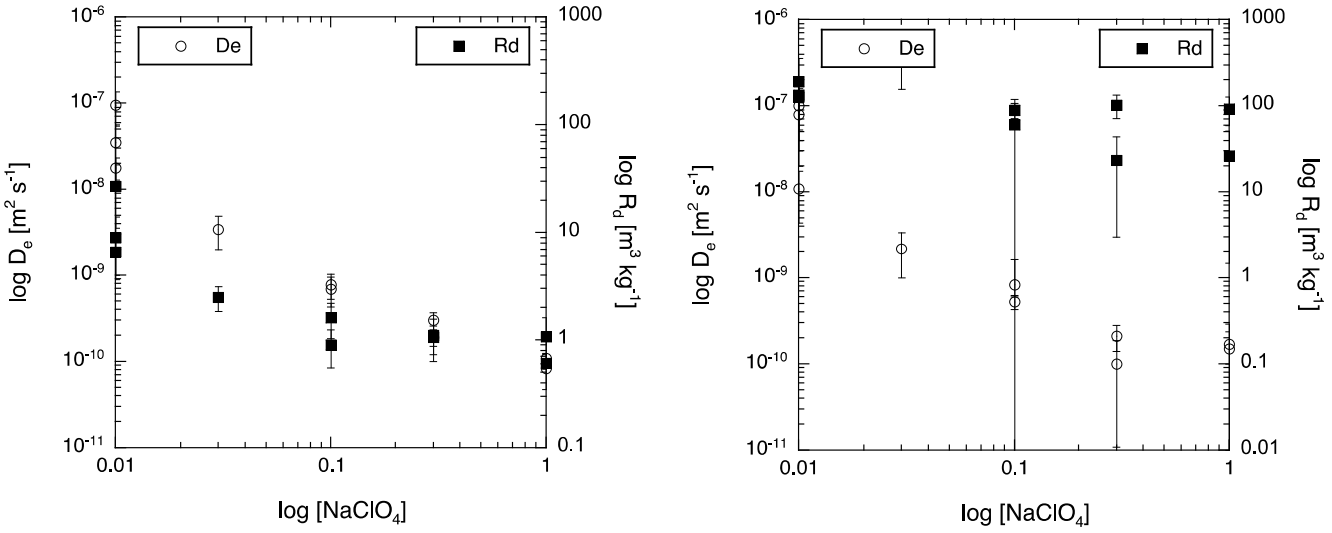

Figure 50 Dependence of D_e and R_d for $^{60}Co^{2+}$ on the $NaClO_4$ concentration in the contacting solution for the experiments at pH 5 (left-hand plot) and the experiments at pH 9 (right-hand plot).

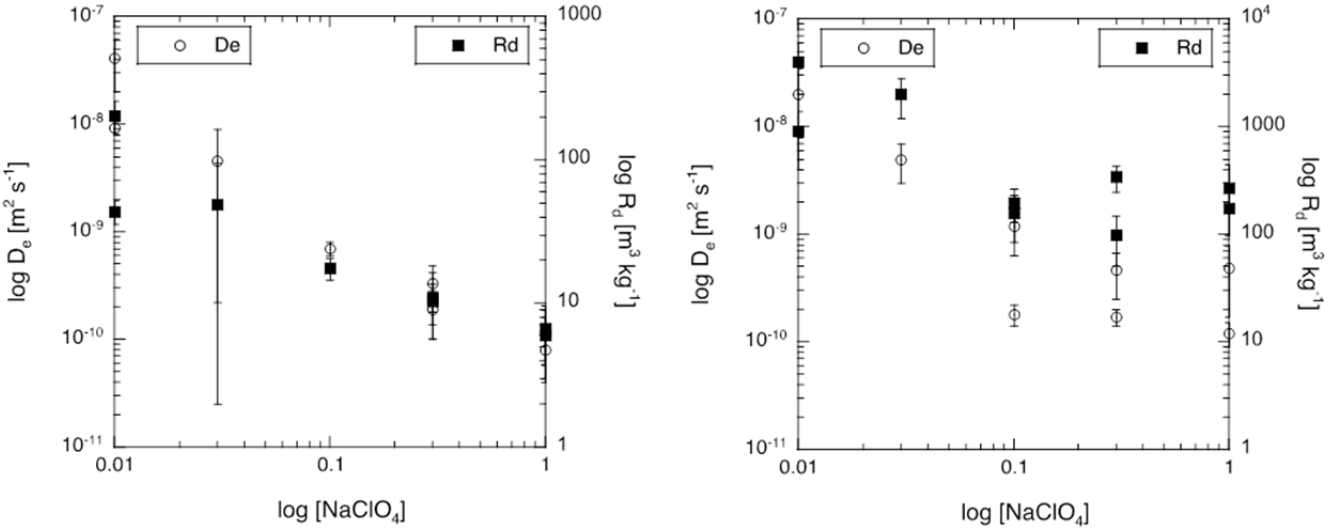

Figure 51 Dependence of D_e and R_d for $^{65}Zn^{2+}$ on the $NaClO_4$ concentration in the contacting solution for the experiments at pH 5 (left-hand plot) and the experiments at pH 9 (right-hand plot).

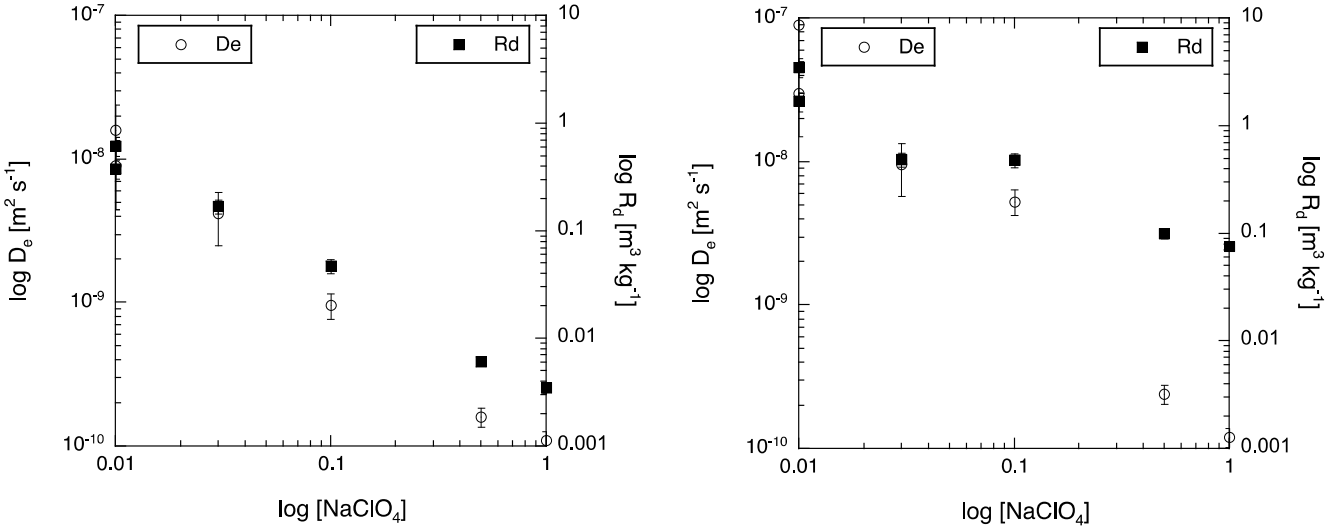

Figure 52 Dependence of D_e and R_d for $^{85}Sr^{2+}$ on the $NaClO_4$ concentration in the contacting solution for the experiments at pH 5 (left-hand plot) and the experiments at pH 9 (right-hand plot).

At the same time a model in which the entire amount of surface species contributes to the diffusive flux can also be ruled out. Such a situation was found to be applicable for the diffusion of Na^+ and Sr^{2+} in compacted montmorillonite (Glaus et al., 2007). The D_e values in those cases were directly proportional to R_d. This was well reflected in the quadratic dependence of R_d values and thus also of the D_e values on salinity for the bi-valent Sr^{2+}, while this dependence was linear in the case of the mono-valent Na^+. The present data measured at the two pH values (comparison between left-hand and right-hand plots) show much higher R_d values at pH 9 than at pH 5, while the D_e values are of similar order of magnitude. A proportional increase in D_e values with R_d values would be expected for this comparison for the situation of a full mobility of surface species being applicable.

A refined modelling approach in which the observed diffusive flux, and thus the D_e values, are viewed as the sum of two parallel fluxes of an aqueous phase species and a mobile surface species has been presented by Gimmi and Kosakowski (2011). In this model D_e values of a given element are normalised using D_e values of tritiated water (D_0^{HTO}) as a reference in order to account for the different mobilities of different elements in bulk water. The normalised effective diffusion coefficient (D_{erw}, –) is defined as:

$$D_{erw} = \frac{D_e D_0^{HTO}}{D_0 D_e^{HTO}} \qquad (16)$$

where D_0 values denote the diffusion coefficients in bulk water. As a working hypothesis it is postulated in that work that D_{erw} values can be expressed as function of R_d and a relative surface mobility, μ_s ($\mu_s = D_{s0}/D_0$, with D_{s0} being an intrinsic surface diffusion coefficient on a flat surface) according to:

$$D_{erw} = 1 + R_d \frac{\rho_{bd}}{\varepsilon} \mu_s = 1 + \kappa \mu_s \qquad (17)$$

with κ defined as a capacity factor similar to α ($\alpha = \varepsilon + R_d \rho_{bd}$) describing the enrichment of the element under consideration on the surface compared to its concentration in the aqueous phase.

Graphic representations of the experimental data for Co(II), Zn(II) and Sr^{2+} are shown in Figure 53 to Figure 55. The plots for Zn(II) and Sr^{2+} contain also data measured at SCK·CEN (Van Laer et al., 2014). It has to be noted that the data measured at SCK·CEN are characterised by a huge loss of element from solution leading probably to a bias in the best-fit parameter values. However, the comparability of the data is not enough to draw unambiguously such a conslusion. The overall picture of the data intercomparison is, however, satisfying because the two research groups used different experimental equipment to measure these data. While most of the data were measured using MCDC's at PSI, most of the measurements at SCK·CEN were done using conventional diffusion cells. The two approaches thus do not only differ in terms of the interface between the clay and the solution, but also in terms of the ratio of binding sites on the clay to the amount of tracer in solution.

As can be seen from Figure 53 to Figure 55 the agreement of the experimental data with the parallel-flux model is in general poor for Co(II) and Zn(II). Only in the case of the Sr^{2+} data at pH 5 a satisfying picture was obtained. The general

disagreement can be interpreted in the sense that the model of Gimmi and Kosakowski (2011) assumes the presence of two species only. This may not be an adequate assumption for the elements tested in this study. According to the 2SPNE CE/SC model (Bradbury and Baeyens, 2009b) it may well be assumed that the surface species may comprise species in the cation exchange and in different types of surface complexing sites. It is further a reasonable assumption that these species may have different relative surface mobilities owing to the different manner of chemical bonding. Such a case has been proposed formally by Gimmi and Kosakowski (2011), but not applied to the experimental data.

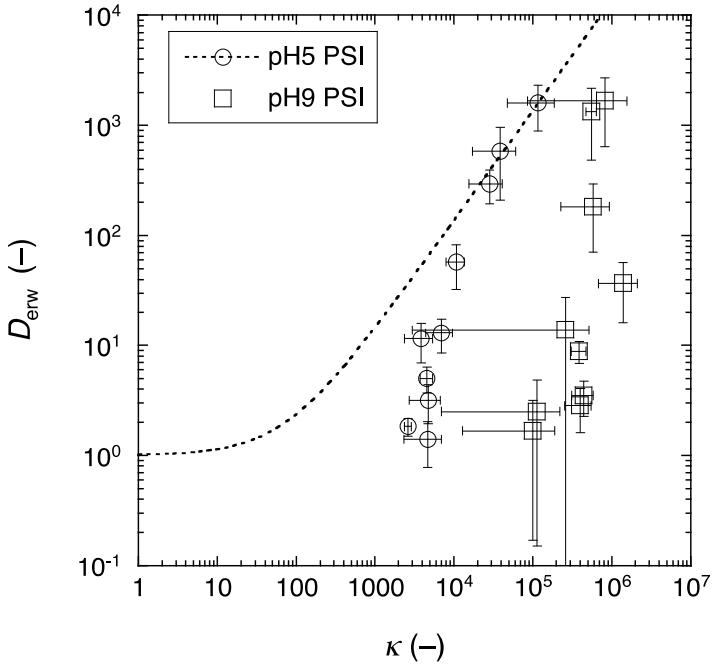

Figure 53 Normalised effective diffusion coefficients plotted as a function of capacity factors (cf. equation 17 for Co(II).The dotted line is a fit curve according to the model of Gimmi and Kosakowski (2011) for the data at pH 5.

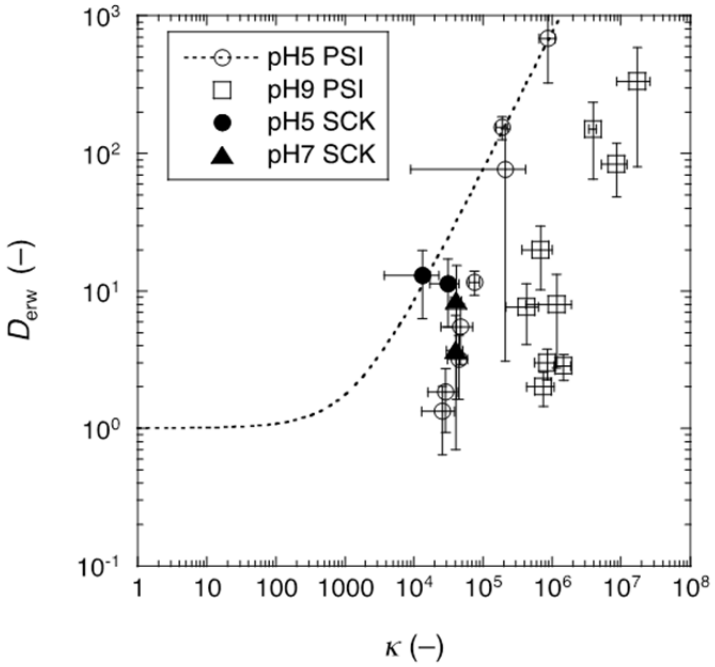

Figure 54 Normalised effective diffusion coefficients plotted as a function of capacity factors (cf. equation 17) for Zn(II). The dotted line is a fit curve according to the model of Gimmi and Kosakowski (2011) for the PSI data at pH 5. The SCK data were taken from Van Laer et al. (2014).

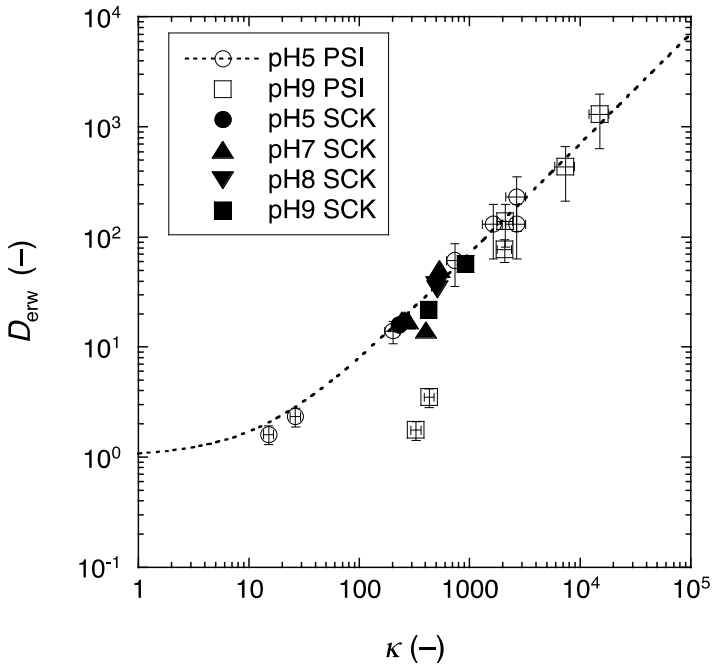

Figure 55 Normalised effective diffusion coefficients plotted as a function of capacity factors (cf. equation 17) for Sr(II). The dotted line is a fit curve according to the model of Gimmi and Kosakowski (2011) for the PSI data at pH 5. The SCK data were taken from Van Laer et al. (2014).

In the following a contribution of cation exchange species to the diffusive flux is considered according to the observed dependence on the concentration of the background electrolyte. For the present consideration it is not differentiated where these species are exactly located (e.g. cation exchange sites versus Donnan layer), they are simply assumed to exhibit a significant relative surface mobility. If their contribution in speciation is of minor importance compared to other surface complexes, a weaker dependence of R_d than of D_e is expected to be observed for given changes in salinity. However the formation of such minor species may not be described correctly in a thermodynamic speciation model for the simple reason that they are not important in speciation and that a possible bias in their thermodynamic data does not lead to inconsistencies between model and data.

In view of such uncertainties an alternative strategic direction would be to obtain information on minor mobile surface species directly from diffusion experiments. A feasible option would be to use the Sr data at pH 5 for establishing a master curve for the case of fully mobile surface species and assume that mobile Co(II) and Zn(II) surface species have the same mobility as Sr^{2+}. Under these assumptions it is possible to assess the amount of mobile surface species as indicated by the arrows in Figure 56 from the measured D_{erw} values. For the element under consideration a "reduced κ for mobile species" κ', can be derived by shifting the data on a constant D_{erw} line to the left until it meets the master curve. The new κ' value read out can be used to calculate a R_d value valid for mobile species only.

The proposition of a "reduced κ for mobile species" has a rather hypothetical character. It is, however, supported to a large degree by the qualitative trends generally observed in the experimental data. The length of the arrows, which are inversely proportional to the mole fraction of mobile surface species, increase with increasing ionic strength and increasing pH. They further increase in the order of elements Sr -> Co ->Zn corresponding to the trend of these ions to form hydrolysed species (acidity of metal cations). It further confirms the hypothesis that binding mechanism of Sr^{2+} on illite is almost pure cation exchange at low pH, whereas an increasing contribution of specific surface complexes becomes noticeable at higher pH (Bradbury and Baeyens, 2005a).

The present interpretation choses thus a different pull compared to the one of Gimmi and Kosakowski (2011) with respect to the ambiguity of κ and μ_s in equation 17. These quantities appear as a product that can be triggered by both of them. Gimmi and Kosakowski (2011) fixed κ based on known R_d values and adjusted μ_s resulting in a broad variety of μ_s values for different elements. The present approach goes the other way around. It is not intelligible why surface-mobile species of Sr, Co and Zn would have different mobilities. Accordingly μ_s is fixed and R_d is adapted in the sense that the "reduced R_d" represents the quantity of mobile surface species only. As a matter of fact the correction factors applied to κ can be compared to theoretical calculations using thermodynamic surface speciation models. A consistency between the two approaches can, however, not be expected a priori because the present interpretation is based on the results from compacted clay systems while the thermodynamic speciation models are calibrated from results obtained in disperse clay suspensions. This may particularly apply for the illite system where the charged surfaces in the latter systems are exposed to a merely infinite solution while they are in vicinity to other surfaces in the

compacted system. For smectite clays such as montmorillonite the difference between these two states may be less because of the existence of hydrated interlayer pores in both systems.

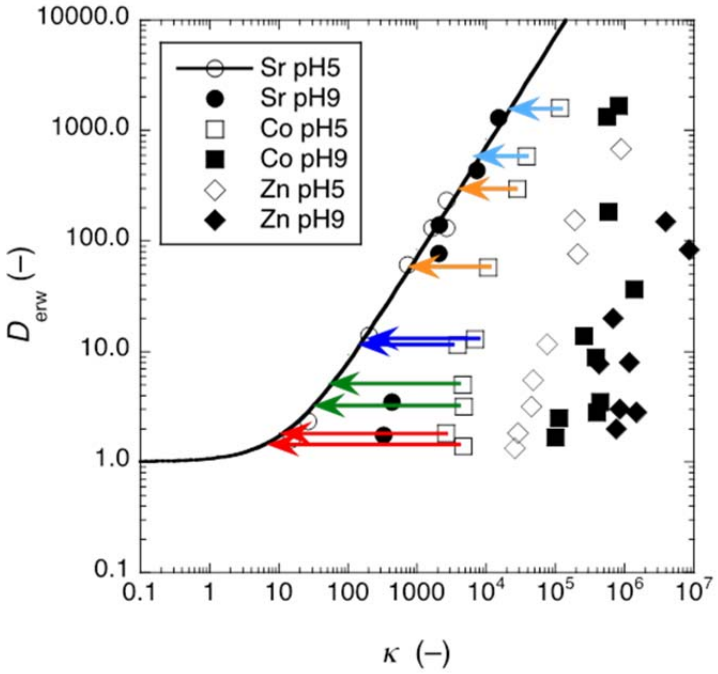

Figure 56 Determination of "reduced κ" (= κ') values for the Co data at pH 5 using the fit curve for $^{85}Sr^{2+}$ at pH 5 (μs = 0.08) as the master curve for mobile species. The colours of the arrows represent the different concentrations of $NaClO_4$ (0.01 M: light blue, 0.03 M: brown, 0.1 M: dark blue, 0.3 M: green, 1.0 M: red).

2.6.2 Refining the model

Gimmi and Kosakowski (2011) attribute the enhanced diffusion of cations in clays to 'surface' diffusion of sorbed species in general. As shown in the previous section, the results are encouraging for Sr^{2+}, but less so for Co^{2+} and Zn^{2+}, which is undoubtedly related to different sorption mechanisms for these cations. The three cations are more or less equally sorbed on the planar sites, but strong sorption of Co^{2+} and Zn^{2+} on specific sites of clay minerals endows these cations with higher distribution coefficients than Sr^{2+}. If diffusion is simply related to the overall distribution coefficient as Gimmi and Kosakowski propose, diffusion will be higher when sorption is stronger. But, the observed diffusion enhancement in illite is essentially the same for these three cations.

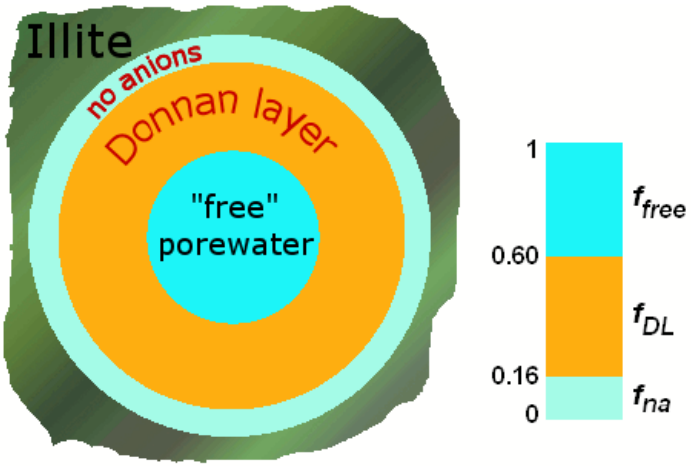

Figure 57 Subdivision of the pore space in illite in fractions of free, uncharged pore water, a Donnan layer with averaged concentrations which neutralize the illite charge, and a limiting-approach distance devoid of anions.

Sorption on the planar sites is mostly electrostatic and similar for these divalent cations. Accordingly, it can be expected that the diffusion enhancement is located in the electrostatic double layer (EDL) on the clay surface, where concentration increases will magnify a concentration gradient and thus increase the driving force for diffusion (Ochs et al., 1998, 2001, Appelo and Wersin, 2007). Similarly, the smaller diffusion coefficient of anions in clays is readily explained by the concentration decrease in the EDL. A simple model structure that subdivides the clay pore in three domains is illustrated in Figure 57.

The concentrations in the EDL can be found by integrating the Boltzmann equation (Ochs et al., 1998; Parkhurst and Appelo, 2013), or, computationally faster and giving very much the same results, by averaging in a Donnan volume (Appelo and Wersin, 2007). The thickness of the Donnan layer can be set to 2 Debye lengths, which gives, for NaCl solutions, the same anion-free distance as the Gouy-Chapman equation for a planar surface (Tournassat and Appelo, 2011):

$$d_{DL} = 2\sqrt{\frac{e_r e_0 \ \mathrm{R}\, T}{2 \ \mathrm{F}^2\, 1000 I}} \qquad (18)$$

where d_{DL} is the thickness of the Donnan layer (m), $\varepsilon_r\varepsilon_0$ is the dielectric permittivity of water (taken to be pure water, $e_r e_0$ = 6.94×10^{-10} Farad m^{-1} at 25°C), R is the gas constant (8.314 J K^{-1} mol^{-1}), T is the temperature (K), F is the Faraday (96485 C eq^{-1}), and I is the ionic strength of the free pore water (-). The minimal approach distance of anions may be in the order of 0.2 nm. The thickness of the free pore water layer then follows by difference of the pore radius or the planar pore width and the sum of the minimal approach distance and the Donnan layer thickness. The fractions f_{free} and f_{DL} of free and EDL water can be calculated for an average pore radius that is given by the bulk density, the crystallographic properties of the clay, and the cation exchange capacity (*CEC*) (Appelo, 2013).

The concentration of an ion in the Donnan layer is obtained by combining charge balance with Boltzmann-type concentration dependence. The charge of the Donnan layer neutralizes the surface charge:

$$\sum z_i m_{DL,i} = \sigma_0 \qquad (19)$$

where z is the charge number (-), $m_{DL,i}$ is the concentration in the Donnan layer (mol/kgw) and σ_0 is the charge of the clay (eq kgw^{-1}). Here, kgw stands for kg of (total) pore water. The Boltzmann equation is:

$$m_{DL,i} = m_{free,i} \exp\left(\frac{-z_i \mathrm{F} \psi_{DL}}{\mathrm{R}T}\right) \qquad (20)$$

where $m_{free,i}$ is the concentration in free pore water (mol kgw^{-1}) and ψ_{DL} is the potential in the Donnan layer (V). ψ_{DL} can be calculated for given concentrations of m_{free} and σ_0.

The concentration decrease of anions in the Donnan layer can be expressed as anion-accessible porosity:

$$\varepsilon_{an} = \varepsilon_{tot}\left(f_{free} + f_{DL}\frac{m_{DL,i}}{m_{free,i}}\right) \qquad (21)$$

where ε_{an} and ε_{tot} are the anion-accessible and the total (water-filled) porosity, respectively. The capacity factors for anions from diffusion experiments are the same as the anion-accessible porosities.

The thickness of the EDL decreases with increasing ionic strength (eqn (18)). In other words, f_{DL} decreases and f_{free} increases when the concentrations in the free solution increase. Hence, the anion-accessible porosity increases with the ionic strength of the free solution towards the total porosity.

Figure 58 illustrates this for illite compacted to a bulk density of 1700 kg m^{-3}. The capacity factors found in diffusion experiments at PSI and KIT-INE (Table 19) follow the same trend.

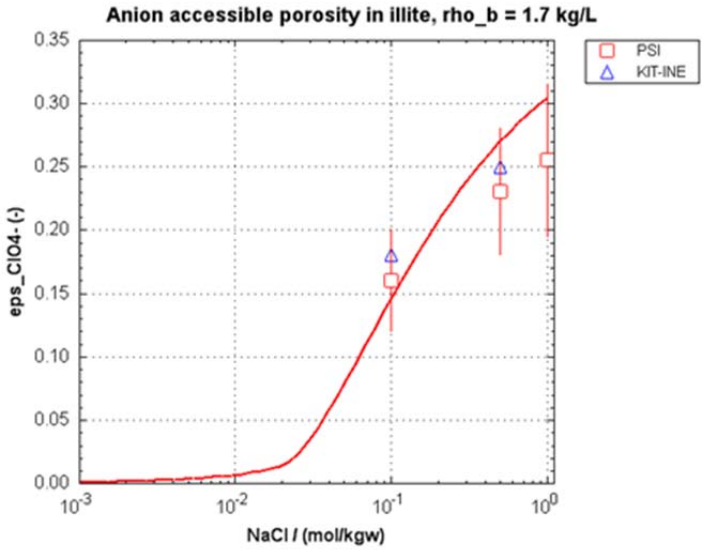

Figure 58 Calculated anion-accessible porosity in illite as a function of the NaCl or $NaClO_4$ concentration and measured porosities in diffusion experiments by PSI and KIT-INE. See Appelo (2013) for details of the calculation.

2.6.3 Estimating diffusion coefficients in clay by the EDL model

The fluxes in free pore water and the Donnan layer are:

$$J_{free,i} = -f_{free}\,\varepsilon_{tot}\,\frac{D_{w,i}}{G_i}\,\frac{\mathrm{d}c_i}{\mathrm{d}x} \qquad (22)$$

$$J_{\mathrm{DL},i} = -f_{\mathrm{DL}}\,\varepsilon_{tot}\,\frac{D_{w,i}}{G_i}\,\frac{c_{\mathrm{DL},i}}{c_i}\,\frac{\mathrm{d}c_i}{\mathrm{d}x} \qquad (23)$$

where J is the flux (mol m^{-2} s^{-1}), G_i is the geometrical factor (-), D_w is the tracer diffusion coefficient in bulk water (m^2 s^{-1}), c is the concentration (mol m^{-3}), and x is distance (m). It is assumed that m, expressed in mol kgw^{-1} in the previous sections, is numerically equal to c mol dm^{-3}.

Taken together, the steady state diffusive flux becomes:

$$J_i = -\frac{\varepsilon_{tot}}{G_i}\left(f_{free} + f_{DL}\,\frac{c_{DL,i}}{c_i}\,\frac{\eta_{\mathrm{H_2O}}}{\eta_{DL}}\right)D_{w,i}\,\frac{\mathrm{d}c_i}{\mathrm{d}x} \qquad (24)$$

where η_{H_2O}/η_{DDL} is the viscosity ratio of free pore water and DDL water.

This equation can be compared with the effective diffusion coefficient that is obtained from a diffusion experiment:

$$J_i = -D_{e,i}\,\frac{\mathrm{d}c_i}{\mathrm{d}x} \qquad (25)$$

Thus, setting $\eta_{DL} = \eta_{H_2O}$ we have

$$\frac{\varepsilon_{tot}}{G_i}\left(f_{free} + f_{DL}\,\frac{c_{DL,i}}{c_i}\right)D_{w,i} = D_{e(\mathrm{model}),i} \qquad (26)$$

With G_i taken from HTO and equal for all cations, the resulting $D_{e(model),\,i}$ is compared with the experimental numbers in Figure 59.

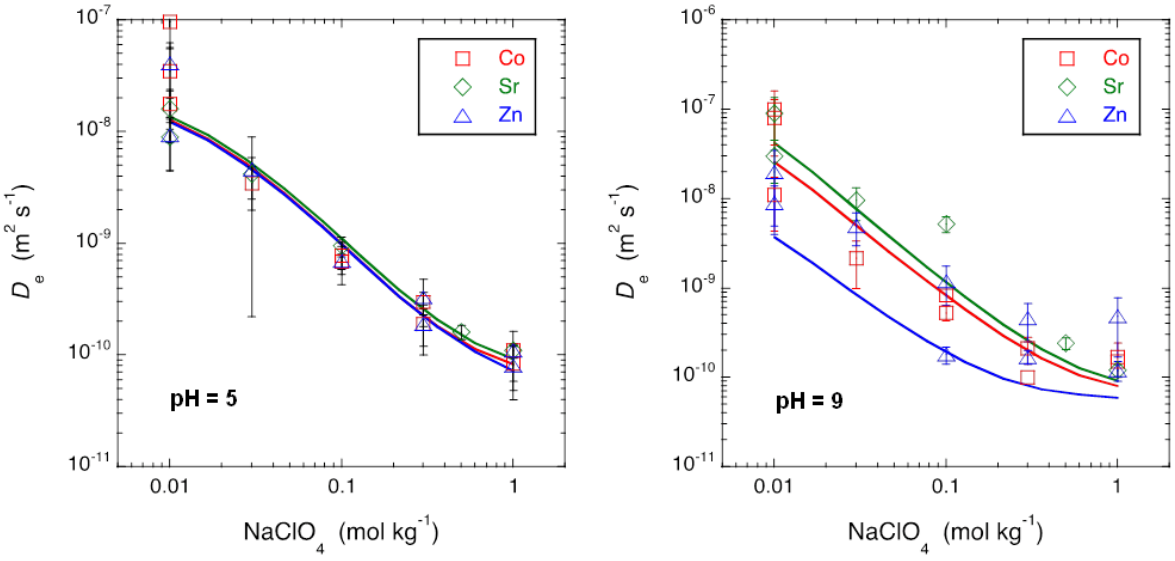

Figure 59 Effective diffusion coefficients of Co^{2+}, Sr^{2+} and Zn^{2+} in illite at pH's of 5 and 9 as a function of the $NaClO_4^-$ concentration. Lines are calculated by the model, data points are from experiment.

Figure 59 shows that the effective diffusion coefficients for the three cations vary in identical manner with the $NaClO_4$ concentration at pH = 5, while they appear to differ somewhat at pH = 9. In the model, the difference at pH = 9 is due to hydroxyl-complexes in solution which reduce the charge of the cation, and thus, also moderate the concentration-increase in the EDL. The hydroxyl complexation increases in the order $Sr^{2+} < Co^{2+} < Zn^{2+}$. At ionic strength above about 5 M, the EDL is so small that only 'free' pore water is present, and the diffusion coefficient of the cations then becomes the one in water divided by the geometrical factor for HTO (G). The diffusion coefficient of anions shows the opposite trend with ionic strength, *cf* eq 26 and Table 19.

The slope of the diffusion coefficient with ionic strength is affected by other cations in solution, which are released by the illite. However, the trend will remain the same in the range of 0.05 - 1 ionic strength and probably be conform the data shown in Figure 59. Thus, we can conclude that surface diffusion of strongly sorbed species on specific sites is absent, because the data show that the effective diffusion coefficients of Sr^{2+}, Co^{2+} and Zn^{2+} are the same although their distribution coefficients are markedly different. But then, the term 'surface diffusion' is inadequate for describing the increase of the diffusion coefficient with decreasing ionic strength of the solution. Physically, the diffusion enhancement occurs in the EDL, which can be negligible at ionic strengths above 5 M, but occupy the whole pore at low ionic strength. The 'surface diffusion' will disappear when the EDL vanishes at high ionic strength, or when the surface charge is zero. Accordingly, the term surface diffusion in clays should be abandoned and replaced by diffusion in the electrostatic double layer or, shortly, EDL diffusion. (But note that interlayer diffusion in swelling clay minerals can be significant.)

3. Clayrock systems

Three possible host rock clays were studied in the CatClay project: Opalinus Clay (Switzerland) studied by PSI-LES, Callovo-Oxfordian Clay (France) studied by CEA and Boom Clay (Belgium) studied by SCK·CEN.

3.1 Opalinus Clay

3.1.1 Experimental procedures and modelling methods

3.1.1.1 Sorption experiments

Opalinus Clay (OPA) was ground in a ball mill and sieved. The <63 μm fraction was used in the experiments. 10 g of OPA powder were put in a dialysis bag and 100 mL of artificial pore water (Type A1, see Table 30) was added. Two such dialysis bags were placed in a 2 L polyethylene bottle filled with synthetic pore water and then shaken for 24 hours. After this time the solution was replaced by a fresh one and the samples were again equililbrated for 24 hours. This procedure was repeated four times. After the last equilibration step, the bags were opened and the OPA suspension was poured in a 100 ml bottle. Equilibrated artificial pore water was added in order to give a suspension having an OPA concentration of ca. 100 g L^{-1}. The exact dry weight was determined by drying a known amount of the suspension at 105 °C untill a constant weight was reached. The dry weight was corrected for the presence of salts. The equilibrated synthetic pore water from the last equilibration step was stored and used to prepare the Co(II) and Zn(II) solutions for measuring a sorption isotherm. The composition of the Co(II) and Zn(II) solutions are given in Table 27 and Table 28, respectively. 35 mL of solution were placed in a centrifuge tube and 5 mL OPA-suspension were added. The mixtures were shaken end-over-end for 7 days and hereafter centrifugated at 90 000 g for 30 minutes. The activity of the ^{60}Co or ^{65}Zn in the supernatant was measured by γ-counting (Minaxi-c, Autogamma 5000 series, Packard). The amount of metal sorbed was calculated from the initial and final concentration of the metal in solution.

Table 27 Composition of the Co(II) solutions used in the sorption experiments.

Solution	Stable Co added as $CoCl_2$ (M)	Stable Co added with ^{60}Co Tracer (M)	Total Co (M)
1	$1x10^{-3}$	$1.34x10^{-6}$	$1.00x10^{-3}$
2	$3x10^{-4}$	$1.34x10^{-6}$	$3.01x10^{-4}$
3	$1x10^{-4}$	$1.34x10^{-6}$	$1.01x10^{-4}$
4	$3x10^{-5}$	$1.34x10^{-6}$	$3.13x10^{-5}$
5	$1x10^{-5}$	$1.34x10^{-6}$	$1.01x10^{-5}$
6	$3x10^{-6}$	$1.34x10^{-6}$	$4.34x10^{-6}$
7	0 M	$1.34x10^{-6}$	$1.34x10^{-6}$
8	0 M	$4.02x10^{-7}$	$4.02x10^{-7}$

Table 28 Composition of the Zn(II) solutions used in the sorption experiments

Solution	Stable Zn added as $ZnCl_2$ (M)	Stable Zn added with ^{65}Zn Tracer (M)	Total Zn (M)
1	$1x10^{-4}$ M	$1.63x10^{-7}$ M	$1.00x10^{-4}$ M
2	$3x10^{-5}$ M	$1.63x10^{-7}$ M	$3.01x10^{-5}$ M
3	$1x10^{-5}$ M	$1.63x10^{-7}$ M	$1.01x10^{-5}$ M
4	$3x10^{-6}$ M	$1.63x10^{-7}$ M	$3.16x10^{-6}$ M
5	$1x10^{-6}$ M	$1.63x10^{-7}$ M	$1.16x10^{-6}$ M
6	$3x10^{-7}$M	$1.63x10^{-7}$ M	$4.63x10^{-7}$ M
7	0 M	$1.63x10^{-7}$ M	$1.63x10^{-7}$ M

3.1.1.2 Diffusion experiments

The clay samples used were from the Mont Terri Underground Research Laboratory in Switzerland. An average mineral composition is given in Table 29. Small cores were drilled parallel to the bedding using a diamond drill bit, and embedded in epoxy resin. One side of the sample was free of resin. The samples were equilibrated with synthetic pore waters having a different NaCl concentration (see Table 30). After 6 months of pre-equilibration, the samples were contacted with a solution containing ^{60}Co(II) and ^{65}Zn(II). The activity concentration of each tracer was 1200 Bq mL^{-1}. The

concentration of ^{60}Co was 4.2×10^{-10} M and 5.5×10^{-11} M for ^{65}Zn. Besides active tracers, there was also a certain amount of inactive tracer present. The concentration of stable Co was 5.1×10^{-6} M and that of stable Zn was 4.3×10^{-7} M. After 16.8 days of in-diffusion, the spatial distribution of both tracers (^{60}Co and ^{65}Zn) was measured. To this end, thin layers of clay were removed using a modified version of the abrasive technique (Van Loon and Eikenberg, 2005) described by Van Loon and Müller (2014). A stripe of SiC abrasive paper (P800 and P400; 1cm x 7 cm; Siawatt fc, SIA Abrasives, Switzerland) was fixed on a special holder. The sample was placed in a sample holder and moved 2 times 5 cm back and forth along the abrasive paper. The grinding swarf containing the radionuclides was measured using γ-spectrometry. The thickness of the removed layer was determined by measuring the length of the sample before and after each grinding step with a micrometer (Mitutoyo, Japan). The average thickness of the removed layers was ca. 135 μm. Twenty layers were removed resulting in a total removed clay thickness of circa 2500 μm.

Table 29 Reference mineralogy for Opalinus clay from Mont Terri (Nagra, 2002b).

Minerals	**Mont Terri OPA** (wt. %)
Calcite	13 ± 8
Dolomite/Ankerite	n.d.
Siderite	3 ± 1.8
Quartz	14 ± 4
Albit	1 ± 1.0
K-Feldspar	1 ± 1.6
Pyrite	1.1 ± 0.5
Phyllosilicates	66 ± 11
Illite	23 ± 2
Illite/Smectite mixed layer	11 ± 2
Kaolinite	22 ± 2
Chlorite	10 ± 2
Organic Carbon	0.8 ± 00.5
CEC ($meq \cdot kg^{-1}$)	95

n.d.: not detectable

Table 30 Composition of the different porewaters used to study the effect of ionic strength (IS) on the diffusion of HTO, $^{22}Na^+$ and $^{36}Cl^-$ in Opalinus Clay.

Element	**OPA (A1) [M]**	**OPA (A1 without NaCl) [M]**	**OPA (A1 + 40 g L^{-1} NaCl) [M]**
Na	2.40×10^{-1}	2.86×10^{-2}	9.24×10^{-1}
K	1.61×10^{-3}	1.61×10^{-3}	1.61×10^{-3}
Mg	1.69×10^{-2}	1.69×10^{-2}	1.69×10^{-2}
Ca	2.58×10^{-2}	2.58×10^{-2}	2.58×10^{-2}
Sr	5.05×10^{-4}	5.05×10^{-4}	5.05×10^{-4}
Cl	3.00×10^{-1}	8.82×10^{-2}	9.84×10^{-1}
SO_4	1.41×10^{-4}	1.41×10^{-4}	1.41×10^{-4}
CO_3/HCO_3	4.76×10^{-4}	4.76×10^{-4}	4.76×10^{-4}
pH	7.9	7.9	7.9
Σ Cations[a]	3.28×10^{-1}	1.17×10^{-1}	1.01×10^{0}
Σ Anions[a]	3.28×10^{-1}	1.17×10^{-1}	1.01×10^{0}
Ionic strength	0.39	0.17	1.07

A1: Opalinus Clay water Type A1 (Pearson 1998).

[a] given in eq L^{-1} (N)

3.1.1.3 Modelling of the in-diffusion data

Single species model

The approach used to model the in-diffusion data (one-dimensional diffusion of a single species from a single reservoir with decreasing source concentration, semi-infinite case) has been described in detail in Van Loon and Eikenberg (2005). The analytical expression is:

$$c_{ri} = \frac{\alpha}{\rho_b} c_0 \exp\left[\alpha \frac{x}{H_f} + \frac{D_e \alpha}{H_f^2} t\right] \cdot \operatorname{erfc}\left(\frac{x}{2\sqrt{D_e t/\alpha}} + \frac{\sqrt{D_e \alpha t}}{H_f}\right) \qquad (27)$$

where:

α	=	rock capacity factor (defined as $\alpha = \varepsilon + \rho_b.K_d$, where ε = porosity)
K_d	=	sorption coefficient [m^3 kg^{-1}]
ρ_b	=	bulk dry density [kg m^{-3}]
c_0	=	initial concentration of the radionuclide in the source solution [mol m^{-3}]
t	=	time [s]
D_e	=	effective diffusion coefficient [m^2 s^{-1}]
x	=	diffusion distance [m]
R_d	=	retardation factor [-]
H_f	=	height of source solution [m]
erfc(z)	=	complementary error function of argument z

The experimental data were fitted using equation 19. Both D_e and K_d (or α) were adapted until an optimal fit was obtained. The quality of the fit was judged by eye. Beside an optimal fit, also a lower and an upper bound were determined.

Multicomponent diffusion model

The multicomponent diffusion model (Appelo and Wersin, 2007) implemented in Phreeqc3 has been described in detail by Appelo et al. (2010). The sorption model developed by Bradbury and Baeyens (2009a) for the sorption of metals on illite was implemented in this model. Both surface complexation sites and cation exchange sites were used. The surface complexation sites (strong sites: Xpa_sOH and weak sites: Xpa_wOH) were made electrically neutral so that electrostatics have not effect on these sites. The ion exchange sites (planar sites: Su_-) are electrically charged and create an electrical diffuse layer (EDL) in the pore. This EDL is necessary for modeling diffusion differences of anions and cations in the (partly) charged pores. Not all surface sites (Su_-) are occupied by cations. The charge of the empty sites is compensated by cations present in the EDL. The volume of the EDL is approximated by a Donnan volume. The concentration of cations in the Donnan layer is related to the concentration in the free pore water by the Boltzmann equation. The potential in the Boltzmann equation represents a single average Donnan potential that can be calculated assuming that the surface charge is compensated by the cations in this Donnan volume (Appelo and Wersin, 2007).

A key assumption in the multicomponent diffusion model is the fact that "sorbed" cations that are located in the EDL or in the interlayer, are mobile and contribute to the diffusive flux: $M^{n+} + nS\_- = MS\_n$. Sorbed cations that are not located in the EDL or interlayer, are assumed to be immobile. These cations are sorbed via surface complexation on the strong (S^sOH) and weak (S^wOH) broken bond sites located mainly along the edges of the clay platelets: $\equiv S^sOH + M^{n+} \Leftrightarrow \equiv S^sOM^{(n-1)+}$ and $\equiv S^wOH + M^{n+} \Leftrightarrow \equiv S^wOM^{(n-1)+}$. The same model parameters as described in Appelo et al. (2010) were used.

3.1.2 Results and discussion

3.1.2.1 Sorption experiments

The sorption isotherms measured for Co(II) and Zn(II) are shown in Figure 60, together with a sorption isotherm for Co(II) measured by Bradbury and Baeyens (2011) for a slightly lower pH value of 7.3. There is a very good agreement between the two sets of Co-data. It can also be observed that Zn(II) sorbs much stronger on OPA than Co(II).

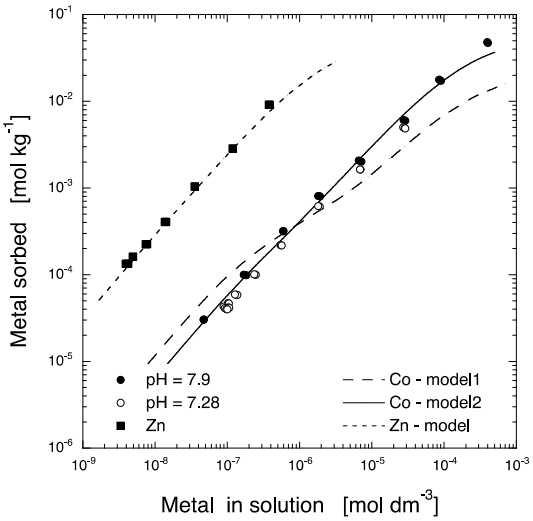

Figure 60 Sorption isotherms fo Co(II) and Zn(II) on OPA measured in a synthetic pore water at pH 7.8. The filled symbols represent data measured in this work. Open symbols represent measurements from Bradbury and Baeyens (2011).

The sorption isotherms were modelled using the sorption model described in Baeyens and Bradbury (2011), implemented in Phreeqc3 (Parkhurst and Appelo, 2013). Information on the reactions and site densities can be found in Table 31, Table 32 and Table 33. In a first trial, we used the site densities as calculated from the site density in illite (Table 33) and the fraction of illite and illite/smectite in OPA (0.34, Table 29). This resulted in a strong site density of 6.8×10^{-4} mol kg^{-1} and a weak site density of 1.36×10^{-2} mol kg^{-1} in OPA. Using these site densities and the interaction constants summarised in Table 32, the measured isotherm could be reproduced only moderately good (Figure 60; Co - model 1). Only when the concentration of strong sites was reduced to 1×10^{-5} mol kg^{-1} or lower and the amount of weak sites increased to 4.0×10^{-2} mol kg^{-1}, the modelled and measured isotherms were in good agreement (Figure 60; Co - model 2). In case of Zn(II), no interaction constants are known so far. We therefore assumed that the sorption of Zn(II) took place at the same sorption sites and adjusted the constants (Table 32) so that the modelled and experimental sorption isotherms were in agreement (Figure 60; Zn - model). The same site densities were taken as for Co(II), i.e. 1×10^{-5} mol kg^{-1} for the strong sites and 4.0×10^{-2} mol kg^{-1} for the weak sites. The same sorption model will be used for modelling the diffusion profiles of Co(II) and Zn(II) in OPA.

Table 31 Overview of the ion exchange reactions for Co(II) and Zn(II) and the corresponding selectivity coefficients on illite used in the sorption model for OPA.

Cation exchange reaction	Selectivity coefficient ($\log K_c$)	Reference
$2Na-clay + Co^{2+} \Leftrightarrow Co-clay + 2Na^{+}$	1.3	Baeyens and Bradbury (2011)
$2Na-clay + Zn^{2+} \Leftrightarrow Zn-clay + 2Na^{+}$	1.3	This work

Table 32 Overview of the surface complexation reactions and their corresponding constants for the sorption of Co(II) and Zn(II) on illite used to model the sorption on OPA.

Surface complexation reaction	Surface complexation (logK)	Reference
$\equiv S^sOH + Co^{2+} \Leftrightarrow \equiv S^sOCo^+ + H^+$	0.0	Baeyens and Bradbury (2011)
$\equiv S^sOH + Co^{2+} + H_2O \Leftrightarrow \equiv S^sOCoOH^0 + 2H^+$	-7.0	Baeyens and Bradbury (2011)
$\equiv S^sOH + Co^{2+} + 2H_2O \Leftrightarrow \equiv S^sOCo(OH)_2^- + 3H^+$	-16.5	Baeyens and Bradbury (2011)
$\equiv S^{w1}OH + Co^{2+} \Leftrightarrow \equiv S^{w1}OCo^+ + H^+$	-1.8	Baeyens and Bradbury (2011)
$\equiv S^sOH + Zn^{2+} \Leftrightarrow \equiv S^sOZn^+ + H^+$	0.86	This work
$\equiv S^sOH + Zn^{2+} + H_2O \Leftrightarrow \equiv S^sOZnOH^0 + 2H^+$	-5.73	This work
$\equiv S^sOH + Zn^{2+} + 2H_2O \Leftrightarrow \equiv S^sOZn(OH)_2^- + 3H^+$	-15.27	This work
$\equiv S^{w1}OH + Zn^{2+} \Leftrightarrow \equiv S^{w1}OZn^+ + H^+$	0.2	This work

Table 33 Overview of the surface complexation reactions and their corresponding constants for the sorption of Co(II) and Zn(II) on illite used to model the sorption on OPA with phreeqc.

Edge sites	[1,3]site capacity (mol kg^{-1})	[2]site capacity (mol kg^{-1})
$\equiv S^sOH$	6.80×10^{-4}	1.0×10^{-5}
$\equiv S^{w1}OH$	1.36×10^{-2}	4.0×10^{-2}
$\equiv S^{w2}OH$	1.36×10^{-2}	4.0×10^{-2}

Protolysis reaction	logK	[3]logK	logK
	$\equiv S^sOH$	$\equiv S^{w1}OH$	$\equiv S^{w2}OH$
$\equiv SOH + H^+ \Leftrightarrow \equiv SOH_2^+$	4.0	4.0	8.5
$\equiv SOH \Leftrightarrow \equiv SO^- + H^+$	-6.2	-6.2	-10.5

[1] Bradbury and Baeyens (2011)
[2] this work
[3] weak sites were not necessary for modelling the sorption

3.1.2.2 Diffusion experiments

Single species modeling

The concentration of the tracers in the reservoirs did not change significantly during the 17 days of in-diffusion (data not shown). The mass transfer from the solution into the small sample was too low to cause a measurable concentration change in solution. Profiles of Zn and Co in the different OPA samples are given in Figure 61. It is obvious that the sorption of ^{65}Zn(II) on OPA is stronger than the sorption of ^{60}Co(II) resulting in a more shallow diffusion profile for ^{65}Zn(II). It can further be observed that the higher the ionic strength of the pore water in contact with the solid, the more shallow the diffusion profiles, both for ^{60}Co(II) and ^{65}Zn(II). Such a behaviour is typical for sorption enhanced diffusion (Glaus et al., 2007; Appelo et al., 2010; Gimmi et al., 2011), i.e. the sorbed Co and Zn – or at least a part of it – seems to be mobile.

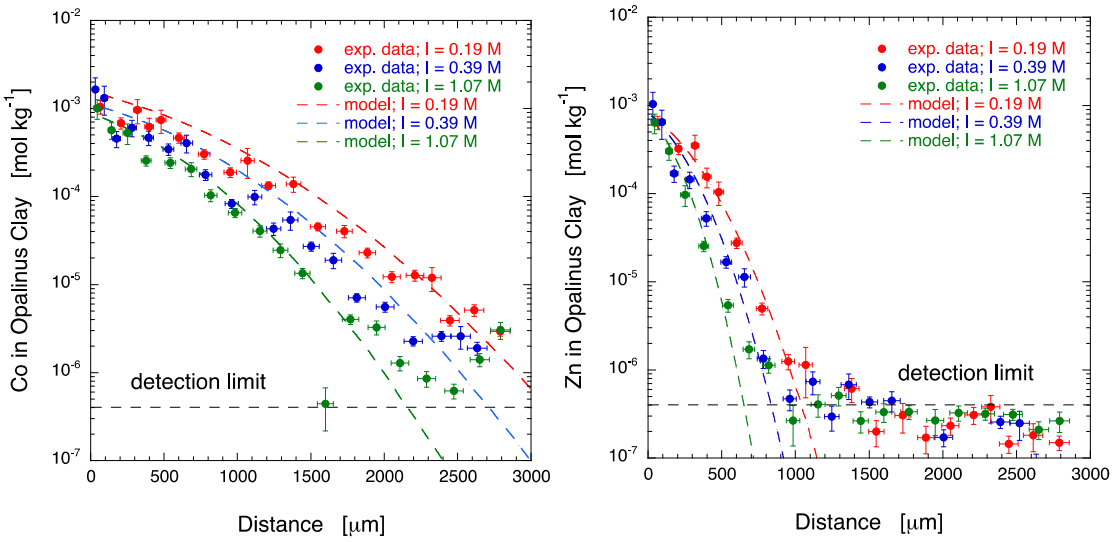

Figure 61 Diffusion profiles for Co(II) (left) and Zn(II) (right) in Opalinus Clay as a function of the ionic strength of the pore solution. Symbols represent experimental data, dashed lines are calculated by the single species model.

An extensive modelling exercise was performed in order to explain the observed phenomena. In a first phase, we used a simple aqueous pore diffusion model as described in Van Loon and Eikenberg (2005). The sorption coefficient (K_d) and the effective diffusion coefficient (D_e) were varied in order to fit the experimental data. An overview of the parameters (best fit, upper and lower bound) used to model all data is given in Table 34 and Table 35 for Co(II) and Zn(II), respectively. The experimental and modelled diffusion profiles (only the best fits) are given in Figure 61. As can be seen, all experimental data can be described satisfactorily by this simple model. The data for Co(II) clearly show the effect of ionic strength: at low ionic strength the sorption value and the effective diffusion coefficient are higher whereas at high ionic strength, the opposite can be observed. In the case of ^{65}Zn(II) this is less obvious. It can further be observed that the sorption of Zn(II) is higher, indicated by the higher sorption coefficient. The use of a single sorption coefficient (K_d) indicates that the sorption of both ^{60}Co(II) and ^{65}Zn(II) is linear, i.e. the K_d value does not change with concentration. This means that only one sorption site is involved in the sorption process. This, however, is in contradiction with sorption results published by Bradbury and Baeyens (2011), showing two sorption sites present in the illite fraction in OPA being responsible for the sorption of metals. As will be shown later, the difference can be explained by assuming that in the intact system, one of the sites (i.e. the strong site) is blocked by a competing metal such as Fe(II) and/or Mn(II). Both metals are present in a concentration range of ca. 10^{-5} – 10^{-6} M in Opalinus pore water (Bossart, 1998). Another explanation might be the fact that crushing the rock creates new sorption sites that will be observed in experiments using this crushed rock, but not in experiments using the intact rock.

When comparing the K_d value derived from the diffusion experiments with those measured in batch sorption experiments, it is obvious that the sorption on the intact rock is lower than on the crushed rock (Figure 62). In the case of Co(II), the difference is a factor of 2. For Zn(II), the sorption on intact OPA is one order of magnitude less than on crushed OPA.

Table 34 Overview of the effective diffusion coefficients (D_e) and sorption values (K_d) derived from the in-diffusion profiles for ^{60}Co in OPA for different ionic strength values of the external solution, using the Single Species Model.

Ionic strength (M)	Curve	D_e ($m^2\ s^{-1}$)	K_d ($ml\ g^{-1}$)
0.39	best fit	7.0×10^{-11}	180
	upper bound	1.1×10^{-10}	250
	lower bound	4.0×10^{-11}	110
0.17	best fit	1.2×10^{-10}	220
	upper bound	1.8×10^{-10}	300
	lower bound	8.0×10^{-11}	150
1.07	best fit	4.0×10^{-11}	130
	upper bound	5.5×10^{-11}	170
	lower bound	2.5×10^{-11}	90

Table 35 Overview of the effective diffusion coefficients (D_e) and sorption values (K_d) derived from the in-diffusion profiles for ^{65}Zn in OPA for different ionic strength values of the external solution, using the Single Species Model.

Ionic strength (M)	Curve	D_e ($m^2\ s^{-1}$)	K_d ($ml\ g^{-1}$)
0.39	best fit	9.0×10^{-11}	2000
	upper bound	1.4×10^{-10}	2500
	lower bound	5.0×10^{-11}	1500
0.17	best fit	1.4×10^{-10}	2000
	upper bound	1.8×10^{-10}	2200
	lower bound	1.0×10^{-10}	1800
1.07	best fit	5.0×10^{-11}	1800
	upper bound	7.0×10^{-11}	2100
	lower bound	3.0×10^{-11}	1500

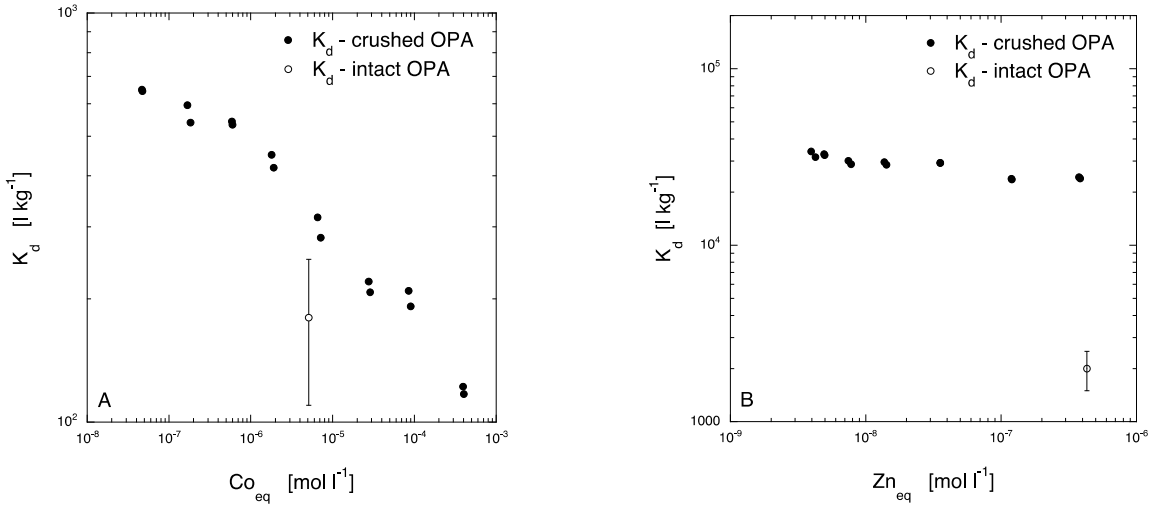

Figure 62 Comparsion between sorption of Co(II) (left) and Zn(II) (right) measured on crushed Opalinus Clay (filled symbols, isotherm) and sorption derived from the diffusion experiment on intact Opalinus Clay (open symbols).

Multicomponent diffusion

In a second phase, we used a multicomponent diffusion model implemented in Phreeqc3 (Appelo and Wersin, 2007; Appelo et al., 2010). The sorption model developed by Bradbury and Baeyens (2009a) for the sorption of metals on

illite was also implemented in the model. The concentration of sorption sites are summarised in Table 33. The interaction constants for ^{60}Co(II) were taken from Bradbury and Baeyens (2011). The interaction constants for ^{65}Zn(II) were estimated from the sorption isotherm discussed in §3.1.2.1.

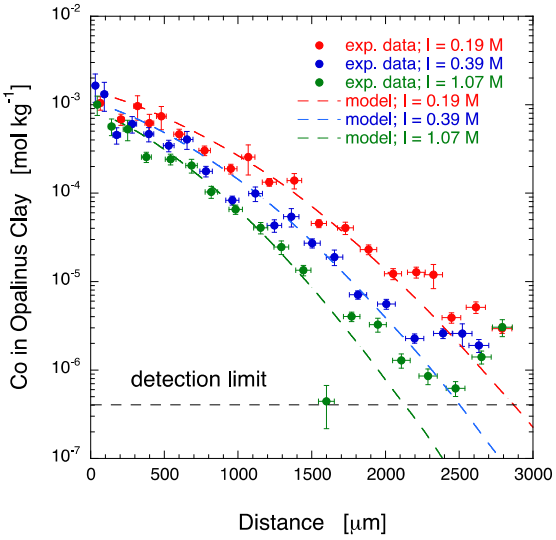

Figure 63 Measured and modeled diffusion profiles of Co(II) in Opalinus Clay. The dashed curves represent modeling with the multi-component diffusion model (Appelo et al., 2010).

We started with the diffusion of Co(II) in OPA performed with the ordinary synthetic pore water (I = 0.39 M). The diffusion was modeled assuming that there was no Zn(II) present. A first trial with the parameters used to model the sorption isotherm reproduced the measured diffusion profile reasonably good. The contribution of strong sites is only minimal. This observation is in agreement with the simple diffusion model used before, indicating that only one sorption site is involved in the sorption of Co(II). The diffusion profile for Co(II) in OPA in contact with the dilute synthetic pore water (IS = 0.17 M) could also be well reproduced by the model using identical site densities as for the ordinary pore water. The same was observed for the more concentrated pore water (IS = 1.07 M). The model also predicts the more shallow diffusion profile for the OPA in contact with the concentrated pore water and the less shallow profile for the most diluted pore water. The effective diffusion coefficient derived from the multicomponent diffusion modelling was 3.3 x 10^{-11} m^2 s^{-1}.

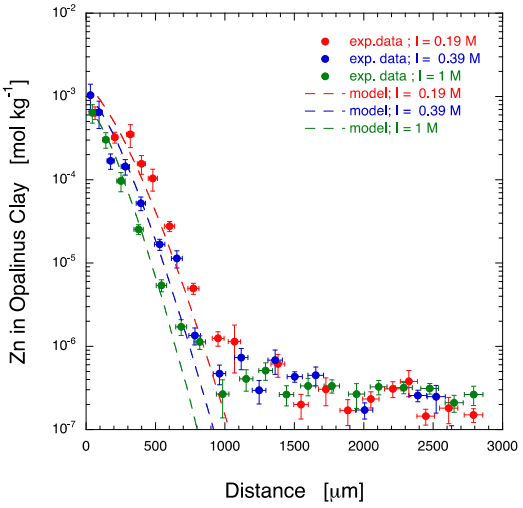

Figure 64 Measured and modelled diffusion profiles of Zn(II) in Opalinus Clay. The dashed curves represent modelling with the multi-component diffusion model (Appelo et al., 2010).

In the case of Zn(II), the situation is different. When using the interaction constants derived from the sorption isotherm (see Table 32) the experimental results could not be reproduced. The calculated diffusion profile is too shallow, i.e. the sorption of Zn(II) on OPA is too high. Only when the constant for the interaction between the weak sites and Zn(II) are lowered from logK = 0.2 to logK = -0.5, a good description of the experimental profile is obtained. However, now the

calculated sorption isotherm no longer matches the measured one. It seems that the sorption on the intact OPA is much lower than the sorption on ground OPA. In the case of Co(II), a similar but weaker effect was observed. The observed difference between intact and crushed OPA can only be explained by the fact that new sorption sites are created by the grounding process. Such an effect was not observed in the case of cations sorbing by ion exchange such as Cs(I), Na(I) or Sr(II) (Van Loon et al., 2005; Van Loon et al., 2009).

Another explanation might be the fact that in a compact system, not all sorption sites are accessible (Montavon et al., 2006). It is also possible that the strong sorption sites are blocked by competing cations such as Mn(II) or Fe(II), or that the pH in the pore water of the intact rock is different from that in the contacting solutions. It was recently shown by Wang et al. (2002) that the protonation-deprotonation (pK) behaviour of surface groups on confined interfaces differs from that on unconfined interfaces. Moreover, it could be shown that as pore size is reduced to nanoscale, the adsorption of ions can vary by more than two orders of magnitude compared to unconfined interfaces. Which process explains the observed differences between sorption in confined and unconfined systems is not clear at the moment. Because confined interfaces are not readily accessible, it is almost impossible to directly study effects of confinement on physico-chemical properties such as acidity of surface groups. Model systems such as reverse micelles are therefore used to understand pH in confined spaces (Crans and Levinger, 2012). Albuquerque and Calzaferri (2007) used dye-loaded zeolites and were able to show that - based on the spectroscopic properties of the encapsulated dyes - the pH inside a zeolite could be as low as ca. 3.5.

The effect of ionic strength on the diffusion profiles are matched by the model. The effect can be explained by the dependence of the concentration of cations in the DDL on the ionic strength. The higher the ionic strength, the lower the concentration of cations present in the DDL. As a consequence the concentration gradient in the DDL becomes less as well as the diffusive flux. At low ionic strength values the opposite effect can be observed. The effective diffusion coefficient derived from the multicomponent diffusion modelling was 3.8×10^{-11} m^2 s^{-1}. This value is similar to the value observed for Co(II), in agreement with the similar values of the diffusion coefficient of both cations in water ($D_{Co} = 6.99 \times 10^{-9}$ m^2 s^{-1}; $D_{Zn} = 7.15 \times 10^{-9}$ m^2 s^{-1}; Li and Gregory, 1974).

3.1.3 Conclusions for Opalinus

Diffusion of Co(II) and Zn(II) in OPA was studied under different chemical compositions of the pore water in contact with the clayrock. It could be shown that the composition of the pore water has a small but significant effect on diffusion. The lower the ionic strength, the higher the penetration depth of the tracer. This is in agreement with the expected behaviour when surface diffusion takes place.

Because the sorption of Zn(II) is larger than Co(II), the former shows more shallow diffusion profiles. Sorption on crushed OPA was shown to be higher than sorption on intact OPA, the difference being as large as up to one order of magnitude in the case of Zn(II). The reason for this discrepancy is still unresolved and needs further investigations. A plausible explanation could be the fact that relatively high concentrations of trace metals such as Fe(II) and Mn(II) in the pore water of the intact systems effectively block the strong sites and thus compete with the sorption of radionuclides. Another explanation might be the fact that new sorption sites are created by crushing the rock. These new sites will not be observed in the intact rock but can be detected in the crushed systems.

3.2 Callovo-Oxfordian clayrock

3.2.1 Experimental procedures

3.2.1.1 Sample origin and sample preparation

The rock core was collected from the borehole OHZ1705, argon-drilled downwards in the Meuse/Haute Marne Underground Laboratory, at a depth where the mineralogy corresponds to silty and calcareous claystones, containing 35-65% of clay minerals (with 27-38% of mixed layer illite/smectite), 15-28% of carbonates, 21-31% of quartz, and accessory minerals (Gaucher et al., 2004). The grain and bulk dry densities of nearest samples were estimated to 2.7023±0.0016 g cm^{-3} and 2.19±0.2 g cm^{-3} (respectively) (Savoye et al., 2010). The cation exchange capacity was estimated to 13 meq/100g (Gaucher et al., 2004). Just after the drilling, the core was inserted into two air-tight aluminum foils filled with nitrogen until their opening into a N_2 glove box (O_2 < 5 ppmv) in the laboratory. Afterwards, 22 samples were sliced from the core under anoxic conditions, using a diamond wire saw (no lubricating fluid was used) into 1-cm-thick piece. Then twenty were cut as disks (ϕ = 38 mm and ϕ = 18.75 mm) for the different types of diffusion experiments and two were powdered for the batch experiments (particle size < 63 µm).

3.2.1.2 Synthetic pore water composition

Four types of synthetic solutions were prepared with ultrapure deionised water (18.2 MΩ cm) and commercial salts (American Chemical Society (ACS) reagent grade or higher quality and purity salts) in order to investigate either the effect of the ionic strength or the effect of the partial pressure of CO_2 on the diffusive behaviour of the tested cations. Their recipes are given in Table 36 and were calculated so as to be in equilibrium with calcite, dolomite and celestite.

Table 36 Chemical composition of the four synthetic pore-water solutions.

	Equilibrated Pore-water solution	Medium IS Pore-water solution	High IS Pore-water solution	320-ppm-CO_2 Pore-water solution
Ionic strength, mEq/L	85	330	590	85
pCO_2	$10^{-2.4}$ atm	$10^{-2.4}$ atm	$10^{-2.4}$ atm	$10^{-3.5}$ atm
pH	7.4	7.4	7.4	8.1
$[Na^+]$, mM	50.8	301.1	546.00	51.6
$[K^+]$, mM	1.0	1.0	0.95	1.7
$[Ca^{++}]$, mM	6.2	6.0	8.0	2.6
$[Mg^{++}]$, mM	4.3	4.1	5.2	2.3
$[Sr^{++}]$, mM	0.2	0.35	0.55	0.19
$[Cl^-]$, mM	41.0	290.0	540.9	41.0
$[SO_4^{--}]$, mM	15.0	15.0	15.0	11.0
$[HCO_3^-]$, mM	2.0	2.5	2.3	0.7

3.2.1.3 Sorption experiments

The sorption and the desorption behaviour of strontium and zinc were investigated by means of batch experiments. For the study of strontium, about 1 g of argillite powder was put into 10 mL centrifugation tube. The synthetic pore-waters (excluding the 320-ppm-CO_2 one) were added to the tubes with a water/rock (W/R) ratio of 10 mL g^{-1}. For zinc, the water/rock (W/R) ratio is equal to about 42 for 0.5 g of argillite and all the types of synthetic solutions were tested (including the 320-ppm-CO_2 one). According to the Descostes and Tevissen (2004)'s protocol, the equilibration phase was started by a first step of 72 h equilibration followed by two rinsings, and lasting one week each. After equilibration, for strontium, either ^{85}Sr (#CERCA SR85ELSB50, France) or ^{90}Sr (LMRI, France) was added to fresh solutions and for zinc, ^{65}Zn (#CERCA ZN65ELSB45, France) was added with variable concentration of stable zinc to reach a range of total zinc varying from 10^{-5} to 10^{-7} M. Two duplicates were used for each concentration. Blank experiments (same protocol used but without rock sample) did not reveal any sorption for each of the tracers. All the experiments were carried out in an oxygen-depleted (< 5 ppm O2) glove boxes either with a 99.6% N_2/0.4% CO_2 atmosphere or with a 99.968% N_2/0.032% CO_2 atmosphere and operated at ambient temperature (21 ± 1 °C). The reversibility of Sr and Zn sorption was evaluated with a desorption test. For that purpose, at the end of the sorption test, the supernatant was removed after centrifugation and fresh synthetic porewater was added in order to adjust the W/R ratios. The rock samples were resuspended with a vortex shaker. After a time equal to the sorption tests, the tubes were centrifuged and the supernatant filtered before counting.

Before sampling, tubes were centrifuged at 96 000 g for 45 min. An aliquot of supernatant was then withdrawn, weighted and analysed either by gamma counting (Packard 1480 WIZARD, USA) for ^{65}Zn or ^{85}Sr or by liquid scintillation (Tricarb 2500, Canberra-Packard, USA) using Ultima Gold XR (Canberra-Packard) as scintillation cocktail for ^{90}Sr. Moreover, the total zinc concentration was determined at the end of the experiments by means of an ICP-MS (Varian 810-MS) because of the role played by the zinc natural background.

3.2.1.4 Diffusion experiments

Two types of setup were used in this study, depending on whether the tracers are radioactive or not. Figure 65 (left) schematically represents the diffusion cells used with radio-tracers. The through-diffusion cells comprise two reservoirs in polypropylene (up and downstream: 175 and 130 mL, respectively), a polypropylene sample holder, two perforated plates in polyetheretherketone (PEEK), and the whole being pasted with glue and screwed together (see Descostes et al., 2008, Savoye et al., 2012b for details). Each part of the diffusion cell was beforehand cleaned with HNO_3 (1%) and water, and then dried. All the preparation of the diffusion cells was made in a glove box (O_2 < 5 ppm). All the diffusion experiments were carried out in a glove box with a 99.6% N_2/0.4% CO_2 gas mixture and operated at ambient temperature (21 ± 1 °C). Figure 65 (right) shows the diffusion cell used with non-radioactive tracers. These cells were made of PEEK to limit the sorption onto the material, especially for europium. This reason also led us to choose PEEK grids instead of PEEK filters, because grids exhibited less reactive surface than filters. Each part of the diffusion cell was previously cleaned successively with HNO_3, water, and ethanol and dried. All the experiments with this type of cell

were carried out in an oxygen-depleted (< 5 ppm O_2) glove boxes either with a 99.6% N2/0.4% CO_2 atmosphere or with a 99.968% N_2/0.032% CO_2 atmosphere and operated at ambient temperature (21 ± 1 °C).

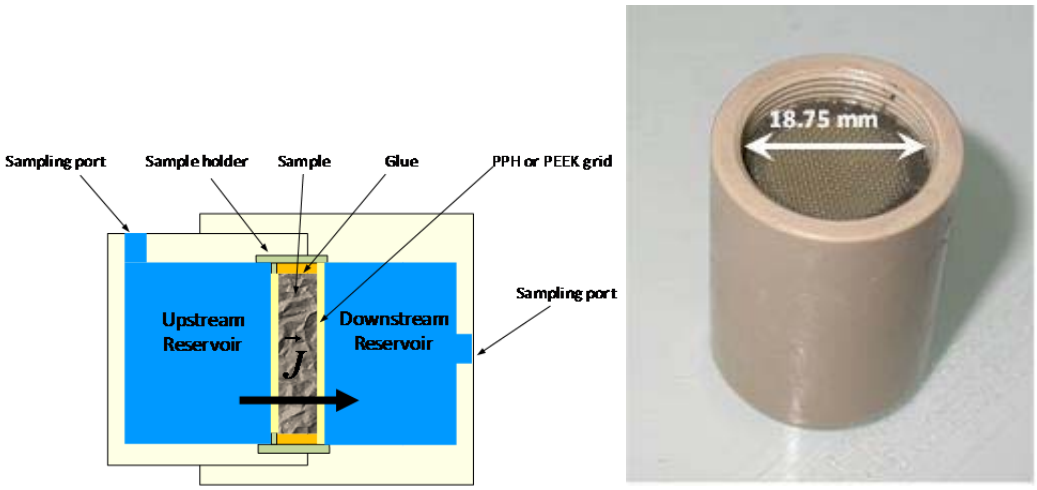

Figure 65 Schematic representation of the through-diffusion cell used with radiotracers (left). The micro-cell used for the in-diffusion experiment (right) (Frasca et al., 2012).

The rock disks of the diffusion cells were equilibrated more than 3 months until 6 months with synthetic water solutions of a composition shown in Table 36.

Through-diffusion cells

For the through-diffusion cell type, successive diffusion experiments were carried out. The synthetic solutions used for the equilibration step were replaced by fresh ones and, solutions in the upstream reservoir were then spiked with HTO, and $^{36}Cl^-$. Up and downstream reservoirs were periodically sampled, and the solution volume taken was replaced in each compartment either by the radio-labelled solutions or by the synthetic waters. After completion of the first through-diffusion stage, an out-diffusion procedure was applied. The solutions in both reservoirs were fully replaced by synthetic solutions without tracer to induce HTO and $^{36}Cl^-$ to diffuse out of the rock samples. At selected time intervals, the activity in the solutions was measured for monitoring the activity rate at which the tracers came out of the samples. A second through-diffusion stage was then performed by replacing the solution in the upstream reservoir by synthetic solutions containing ^{85}Sr (#CERCA SR85ELSB50, France), while in the downstream reservoir, tracer-free synthetic water solution was used. After 240 days of strontium-85 through-diffusion stage, a new out-diffusion procedure was carried out for 150 days to study the reversibility behaviour of ^{85}Sr diffusing out of the rock sample.

Therefore, an in-diffusion protocol was applied for studying the diffusion of Zn and Eu, by replacing the solutions in cells by synthetic solutions containing (i) ^{65}Zn (#CERCA ZN65ELSB45, France) + $ZnCl_2$ at a concentration of 10^{-5} M in the upstream reservoir and (ii) ^{152}Eu (#CERCA EU152ELSB50, France) + $EuCl_3$ at a concentration of 10^{-6} M in the downstream reservoir. After 90 days of Zn and Eu diffusion, the cells were dismantled by removing the sample holder. They were then roughly dried overnight in the dried atmosphere of the glove box, and afterwards in an oven at 60°C, out of the glove box, for 3 days under a vacuum of about 600 mbar. Then, the abrasive peeling technique developed by Van Loon and Eikenberg (2005) for Opalinus Clay, was applied to the rock samples, previously extracted from the sample holder and the glue. This technique enables the abrasion of a sample layer, thickness of which can vary from 10 µm to 250 µm depending of the abrasion duration and the type of the grit grinding paper used (from P220 to P80). The choice of the thickness is directly related to the distance to the disk surface previously in contact with the upstream reservoir solution. That means that the closer to the disk surface the layer, the higher the specific ^{65}Zn or ^{152}Eu activity and the smaller the thickness.

Note that, in addition to the three diffusion cells on which successive diffusion experiments were carried out with HTO/^{36}Cl, ^{85}Sr and ^{65}Zn and ^{152}Eu, two new cells were setup for launching in-diffusion experiments with ^{65}Zn and $ZnCl_2$ at a concentration of 10^{-6} M and ^{152}Eu + [$EuCl_3$]=9 10^{-7}M. These two experiments are still on-going.

The activities for HTO and ^{36}Cl were counted by α–β liquid scintillation (Packard TRICARB 2500, USA) and by γ counter (Packard 1480 WIZARD, USA) in the case of ^{85}Sr, ^{65}Zn and ^{152}Eu. The counting efficiency for each tracer was measured using synthetic water with known amounts of radioactivities. Background measurements were performed in a similar way using synthetic water without radiotracers. HTO, ^{36}Cl, ^{85}Sr, ^{65}Zn and ^{152}Eu data were corrected for radioactive decay with respect to the tracer injection time.

Micro-diffusion cells

After the equilibration stage, an in-diffusion stage was performed by introducing the cell in a bottle filled with synthetic solutions in which Zn or Eu was added at the concentrations given in Table 37. The bottles devoted to blank tests were only filled with the corresponding synthetic solution. Regular samplings were carried out for monitoring the tracer concentration evolution (i.e. 0.1 mL) for the duration given in the Table 37. The Eu and Zn concentrations were analysed by ICP-MS (Varian 810-MS) with an accuracy of about 5%. At the end of the diffusion stage, the cells were dismantled and the rock samples were dried in the anhydrous atmosphere of an O_2-depleted glove box for 3 days, thus, embedded in epoxy resin, and cut in two equal parts along the axis of the cylinder and these parts were polished and a Zn- or Eu- rock profiles were acquired by means of the Laser Induced Breakdown Spectroscopy (Libs) microprobe technique (Altmann et al., 2012; Jacquier et al., 2013). Because zinc was a new species analysed by µLibs, a calibration of the Zn µLibs signal was required so that the abrasive peeling technique was applied to the rock sample for acquiring a quantitative Zn profile. For that purpose, after its grinding, the abraded material was transferred in a 10 mL PPCO tube (Nalgene, USA) and put in contact with an acidic solution (2% of HNO_3, pH ~0.5) for extracting the sorbed zinc. Suspensions were shaken end-over-end for one week. Phase separation was carried out by centrifugation (1 hour at 96 000 g). The clear supernatant solutions were filtered at 0.2 µm and analysed for Zn by ICP-MS (Varian Inc, Australia) with a 5% uncertainty.

Table 37 Overview of the tracers used, their concentration and the duration of the experiments with micro-cells

	Sample	PCO_2 (atm)	Initial concen-tration tracer (M)	Duration diffusion experiment (days)
1st series Zn	Cell Zn1	$10^{-2.4}$	$3\ 10^{-6}$	37
	Cell Zn2	$10^{-2.4}$	$8\ 10^{-6}$	37
	Cell Zn3	$10^{-2.4}$	$4\ 10^{-5}$	37
	Cell Zn4	$10^{-2.4}$	$1\ 10^{-4}$	37
	Cell Zn5 ⇔ Blank	$10^{-2.4}$	$3\ 10^{-6}$	37
2nd series Zn	Cell Zn6	$10^{-2.4}$	10^{-5}	400
	Cell Zn7	$10^{-3.5}$	10^{-5}	400
1st Series Eu	Cell Eu1	$10^{-2.4}$	$5\ 10^{-6}$	55
	Cell Eu2	$10^{-2.4}$	10^{-5}	55
	Cell Eu3 ⇔ Blank	$10^{-2.4}$	$5\ 10^{-6}$	55
2nd Series Eu,	Cell Eu4	$10^{-2.4}$	10^{-6}	270
not *yet*	Cell Eu5	$10^{-2.4}$	10^{-6}	Still ongoing
analysed with	Cell Eu6	$10^{-3.5}$	10^{-6}	270
µLibs	Cell Eu7	$10^{-3.5}$	10^{-6}	Still ongoing

Diffusion data analyses

A planar diffusion is considered, expressed by the second Fick's law:

$$\frac{\partial}{\partial t}(\theta_{acc} C + \rho_d S) = D_e \frac{\partial^2 C}{\partial x^2} \qquad (28)$$

where C is the tracer concentration (mol m^{-3} or Bq m^{-3}), θ_{acc} is the porosity accessible to the tracer(-), ρ_d the bulk dry density of the diffusion sample (kg m^{-3}), S the amount of tracer adsorbed on the solid phase (mol kg^{-1}) and D_e the effective diffusion coefficient (m^2 s^{-1}). For the through diffusion problem, only the initial conditions are given, because the boundary conditions in our case can evolve freely. For HTO, ^{36}Cl and ^{85}Sr (when considering a K_d approach), fully analytical solutions for through-diffusion and reservoir-depletion studies are obtained in the Laplace space, which are subsequently numerically inverted to provide the solution in time (Moridis, 1998). For the out-diffusion stage equation 20 has to be solved with the corresponding boundary conditions: C(0,t) = C(L,t) = 0, t>0. Assuming that the concentration gradient across the sample is linear when the through-diffusion stage reaches the steady-state, the concentration profile that gives the initial conditions for out-diffusion, is

$$C(x) = C_0\left(1 - \frac{x}{L}\right) \qquad (29)$$

According to Jakob et al. (1999), the total activity (Bq) diffused out of the sample at the two boundaries is given by:

$$A(0,t) = 2 \cdot C_0 \cdot S \cdot \alpha \cdot L\left[\frac{1}{6} - \sum_{n=1}^{\infty} \frac{1}{\pi^2 n^2} e^{-\left(\frac{n\cdot\pi}{L}\right)^2 \frac{D_e}{\alpha} t}\right]$$ at x = 0, and

$$A(L,t) = 2 \cdot C_0 \cdot S \cdot \alpha \cdot L\left[\frac{1}{12} + \sum_{n=1}^{\infty} \frac{(-1)^n}{\pi^2 n^2} \cdot e^{-\left(\frac{n\cdot\pi}{L}\right)^2 \frac{D_e}{\alpha} t}\right]$$ at x = L,

where S is the surface of the rock sample (m^2). Moreover, a numerical approach was also applied by using a coupled chemistry-transport code, Phreeqc, for describing the through- and out-diffusion stages of strontium. Details of the approach are given in Savoye et al. (2012) for caesium.

For modelling the in-diffusion data, a single reservoir method with decreasing source concentration for a semi-infinite case was used having the following analytical solution for the appropriate initial and boundary conditions (Shackelford, 1991):

$$\frac{C(x,t)}{C_0} = \exp\left[\frac{\alpha x}{H_f} + \frac{\alpha D_e t}{H_f^{\,2}}\right] \times erfc\left(\frac{x}{2\sqrt{D_e t/\alpha}} + \frac{\sqrt{D_e \alpha t}}{H_f}\right) \qquad (30)$$

where c(x,t) is the concentration of the tracer in the pore water of the rock at distance x after time t (Bq m^{-3} or mol m^{-3}), H_f is the length of upstream reservoir (m), α is the rock capacity factor determined for zinc or europium and erfc(z) is the complementary error function of argument z. In addition, a numerical approach was also tested by using a coupled chemistry-transport code, Phreeqc for describing the in-diffusion of zinc.

3.2.2 Results and Dicussion

3.2.2.1 Sorption experiments

Strontium

Figure 66 shows the kinetics of the strontium sorption extent determined either with ^{85}Sr or ^{90}Sr for the three synthetic solutions with different ionic strength. The increase of the Na concentration clearly induced a decrease of the strontium sorption extent, independently of the radiotracers used. Moreover, the stability of the K_d values over time suggests that under these batch conditions, i.e. relatively high water/rock ratio, only the fast ion exchange phenomenon would be responsible for the sorption. This statement was also confirmed by the desorption experiments carried out with the two series of batch (^{85}Sr and ^{90} Sr), showing a complete reversibility of the sorption (not shown here).

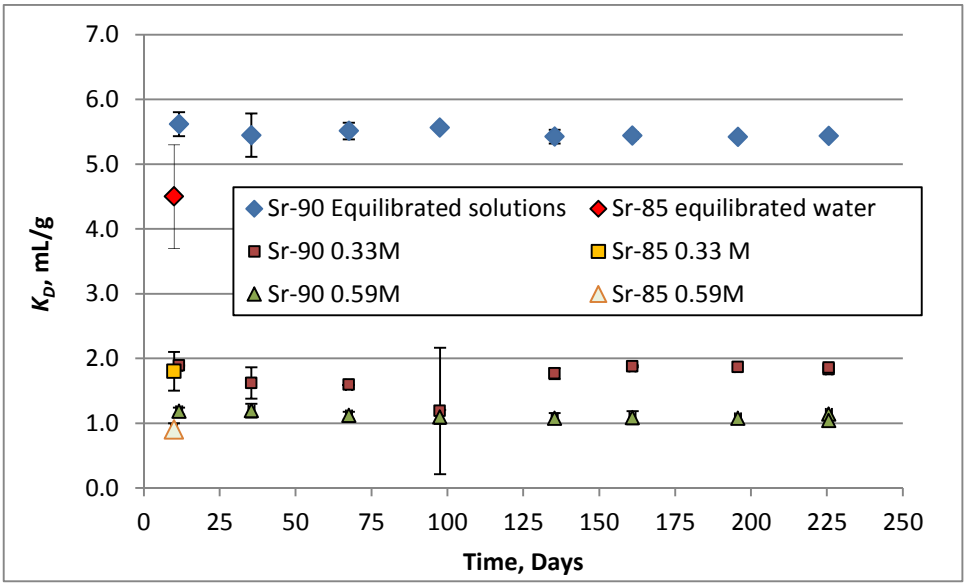

Figure 66 Evolution of the K_d values for ^{90}Sr and ^{85}Sr as a function of time. Error bars correspond to the duplicates.

Zinc

Before presenting batch results, we calculated the Zn speciation in solution for the three ionic strengths by means of Phreeqc code, the Andra's database and Zn data from Tertre et al. (2008) (Figure 67). The speciation distribution shows that Zn^{2+} is the dominant species, independently of the IS, with more than 66% at 85 mEq/L to 83% at 580 mEq/L, followed by $ZnCO_3$ (from 2% to 7%). When the ionic srength increases, the proportion of $ZnCO_3$ decreases while that of the Cl complexes increases. Regarding the solubility limit towards the $ZnCO_3$(s), the values are equal to 1.2, 2.4, 2.8 and 4.10^{-5} M, when increasing the pCO_2 and the ionic strength.

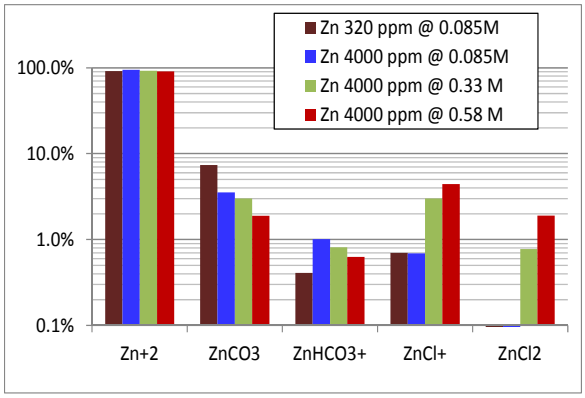

Figure 67 Speciation of Zn in solution for different values of pCO_2 and ionic strength.

As shown in Figure 68, the picture for the zinc sorption is more complicated than for strontium. Indeed, the increase of the sodium concentration in solution has little impact on the K_d values compared to what expected by modelling using the Multi-Site Ion Exchange Model. One can also notice a good reversibility of the sorption phenomenon by means of the desorption experiments.

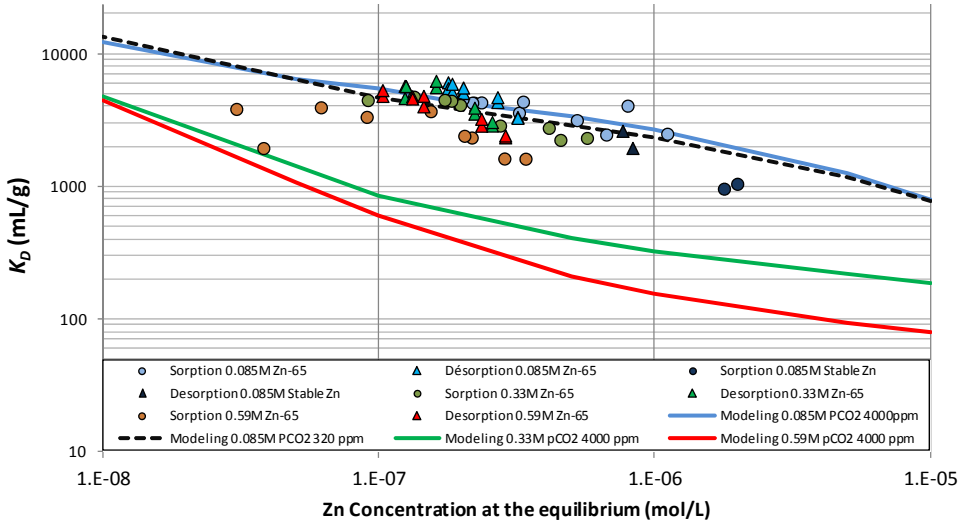

Figure 68 Zn sorption/desorption isotherms for the four types of synthetic solutions with the associated modelling by means of the Multi-Site Ion Exchange Theory (Savoye et al., 2013).

3.2.2.2 Diffusion experiments

Strontium

Figure 69 shows the evolution of ^{85}Sr activity results obtained for the three cells both in the upstream and downstream reservoirs and the associated modelling both with a semi-analytical approach and a numerical one.

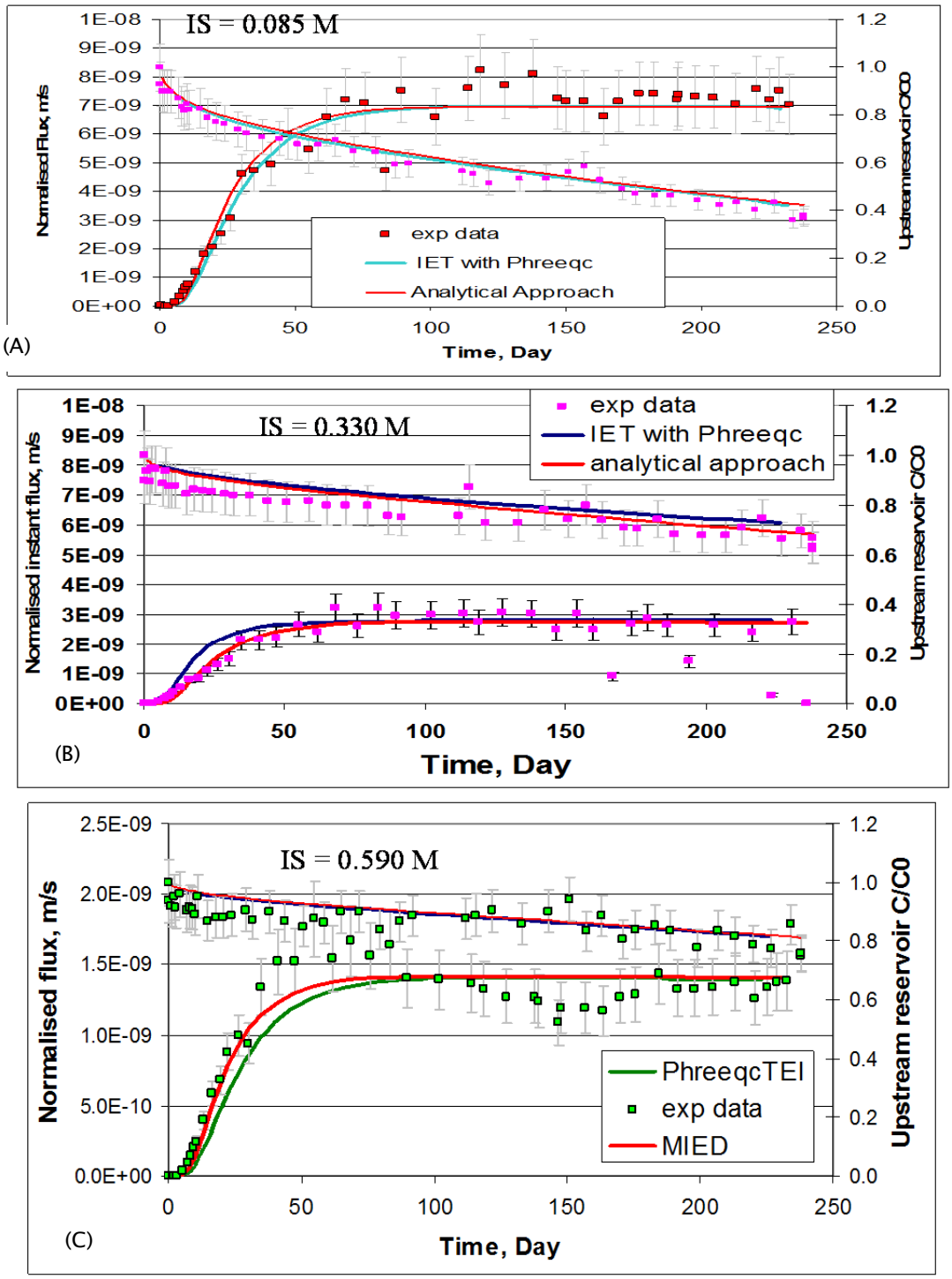

Figure 69 *^{85}Sr activity evolution in the upstream reservoir and ^{85}Sr flux in the downstream reservoir as a function of time in the 0.085 M cell (A), the 0.330M cell (B) and the 0.590 M cell (C). The modelling by an analytical approach is entitled "MIED" and by a numerical approach with the multi-site ion exchange model.*

We can notice that the increase of the ionic strength led to a less pronounced activity decrease in the upstream reservoir, while the associated flux decreases in the downstream reservoir. Moreover, the two modelling approaches are very consistent each other reproduce the experimental data well. The diffusive parameters used are reported in Table 38 with, for comparison, the K_d values estimated from batch experiments with ^{85}Sr. When the ionic strength increases, the effective diffusion coefficient values show a decrease with the same extent as the decrease of the K_d values, in accordance with what expected when considering the role played by the surface diffusion phenomenon. Moreover, a good consistency can be observed for the K_d values estimated either by diffusion or by batch.

Table 38 Effective diffusion coefficients, distribution ratios from the diffusion and batch experiments for Sr.

Ionic Strength (mEq/L)	D_e (^{85}Sr) x 10^{11} (m^2 s^{-1})	D_a(^{85}Sr) x 10^{12} (m^2 s^{-1})	K_d (mL g^{-1})	K_d (batch) sorption (L kg^{-1})	K_d (batch) desorption (L kg^{-1})
85	5.2	4.7	5.0	4.5±0.8	4.2±0.7
330	2.4	5.5	1.9	1.8±0.3	1.7±0.8
590	1.35	7	0.75	0.9±0.1	1.2±0.1

The results of the out-diffusion experiments are reported in Figure 70 with the associated modelling using diffusive parameters determined from the through-diffusion stage (Table 38).

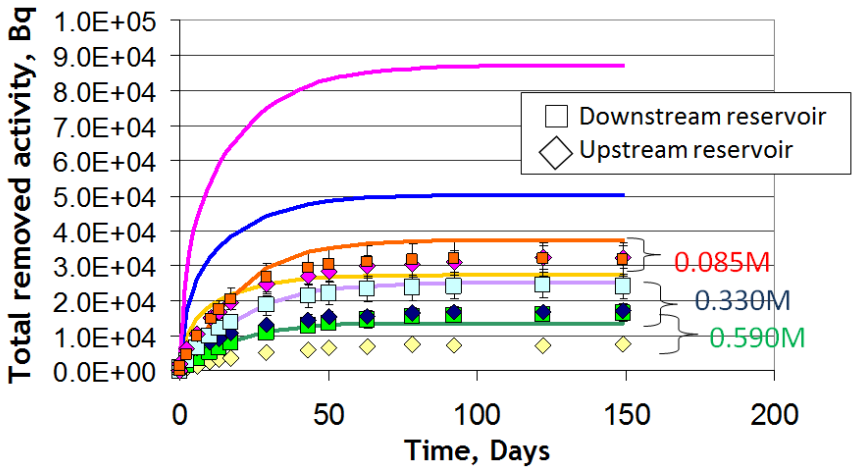

Figure 70 Evolution of the ^{85}Sr activity in the up-and downstream reservoirs of the three cells during the out-diffusion stage. Curves were modelled by means of analytical approach using the diffusive parameters determined from through-diffusion experiments and given in Table 38.

While the modelling reproduces the activity evolution in the downstream reservoir relatively well, it strongly overestimates the activity measured in the upstream reservoir with a more pronounced tendency for the cell with the lowest ionic strength. The origin of this discrepancy could be explained by the occurrence of some processes with slower kinetics than cation exchange, such as the isotopic exchange of ^{85}Sr on Sr-bearing minerals or precipitation of celestite. This is this unexpected discrepancy which has motivated us to launch the long-term batch experiment series with ^{90}Sr. However, as already mentioned above, very stable K_d values were determined throughout the duration of the sorption and desorption experiments with ^{90}Sr, i.e. more than 300 days, suggesting that the quite high water/rock ratio used for batch could have prevented or limited the occurrence of the phenomenon observed within the more compacted system for diffusion.

Zinc

Micro-cells with non radioactive tracer

Figure 71 shows the evolution of the Zn concentration in solution for four cells of the first series. No measurement was carried out for the cell with the highest concentration at 10^{-4} M, because precipitates were observed in the solution, suggesting a Zn oversaturation towards smithsonite.

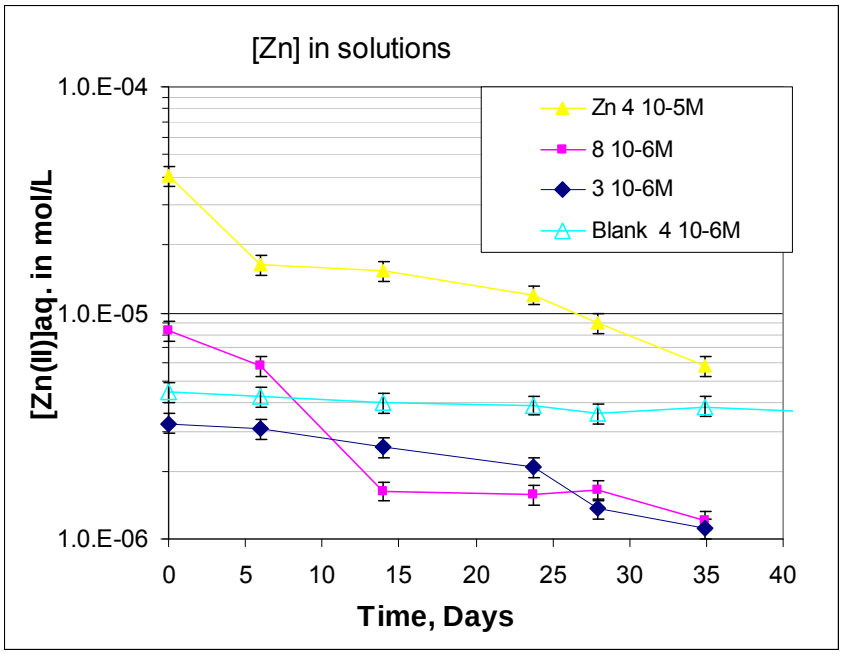

Figure 71 Evolution of the Zn concentration in solution during the diffusion-step.

The stability of the Zn concentration for the blank cell suggests that no or less sorption occurred onto the material, and no precipitation took place. The other cells exhibit a regular decrease consistent with a diffusion process, even though data were quite scattered. The zinc distribution relative to the two solution contact surfaces was determined by µLibs element mapping. A clear diffusion profile can be observed, especially in Figure 72, with high contents near the edges and lower content inside. It is noteworthy that some hot-spots of Zn exist in the middle of the sample, revealing the occurrence of some Zn-rich minerals.

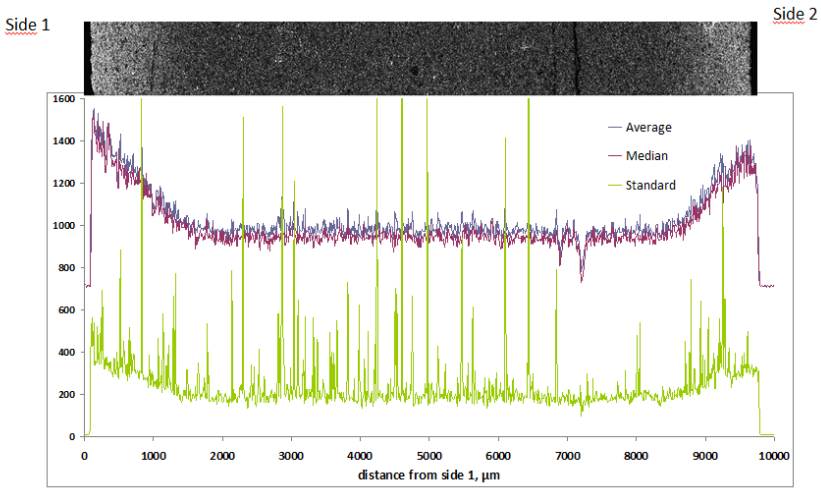

Figure 72 Profile of the averaged and median Zn signals with the corresponding standard deviation.

The Zn rock profile was also acquired by means of the abrasive peeling technique on the same part studied by µLibs. A comparison of the two data sets is given in Figure 73. The calibration indicates that a signal intensity of 1300 corresponds to a Zn concentration of 3.0 µmol g^{-1} of rock. The natural Zn background can be evidenced in the center of the sample, with a content of about 0.5 µmol g^{-1} of rock.

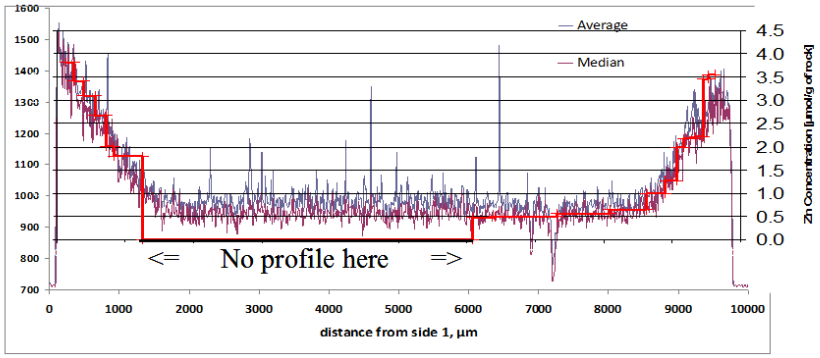

Figure 73 Comparison of the Zn profile obtained by µLibs (blue and purple curves) and by abrasive-peeling (red curve).

Some simulations were carried out to reproduce Zn experimental data derived from the cell with $[Zn(II)]_{ini}$=4 10^{-5} mol L^{-1} (Figure 74). The analytical approaches led to best fits with a K_d = 380 or 300, K_d = 540 L kg^{-1}, and a D_e = 5 10^{-11} or 7 10^{-11} m^2 s^{-1}, considering respectively no solubility control of Zn in solution or a solubility control.

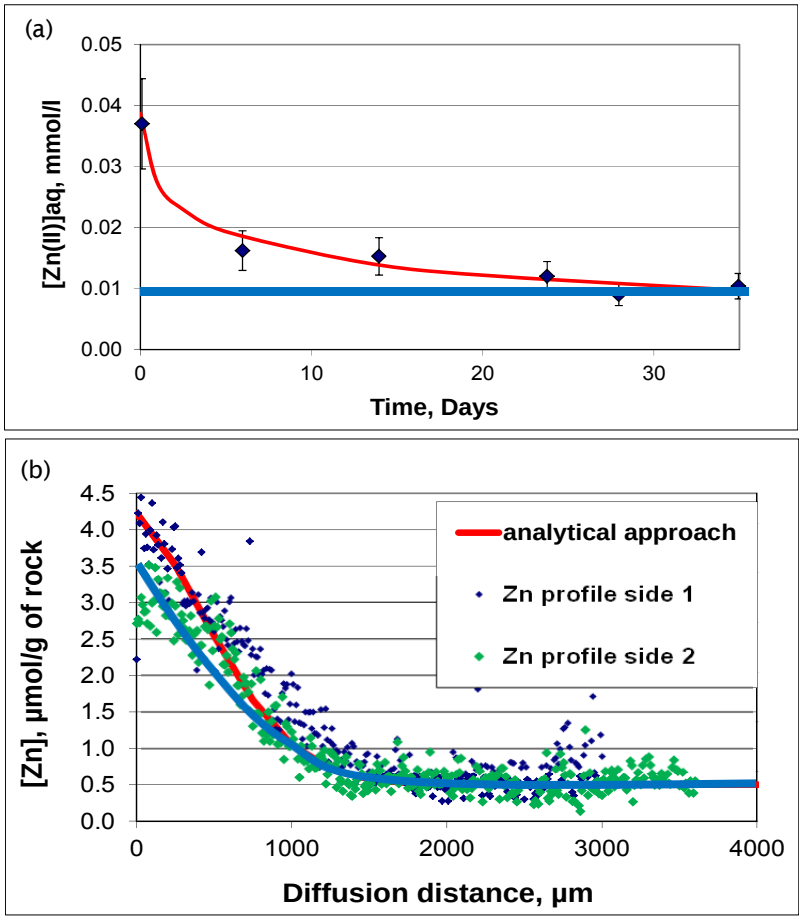

Figure 74 Comparison of the Zn experimental data from the cell with [Zn(II)]ini=4 10-5 mol L-1 with modelling in (a) the reservoir and (b) the rock profile assuming in blue a solubility control and in red no solubility control.

In order to test the sensitivity of the µLibs technique, the sample having underwent in-diffusion of Zn at a lower concentration, i.e. 8 10^{-6} M, was also investigated by the same technique. A global pattern looking like a diffusion profile slightly emerges from the noisy natural background, making difficult the use of such data (not shown). However, this profile was obtained after only 37 days of diffusion, meaning that longer duration will lead to better profiles. The results obtained from the second series of experiments were reported in Figure 75.

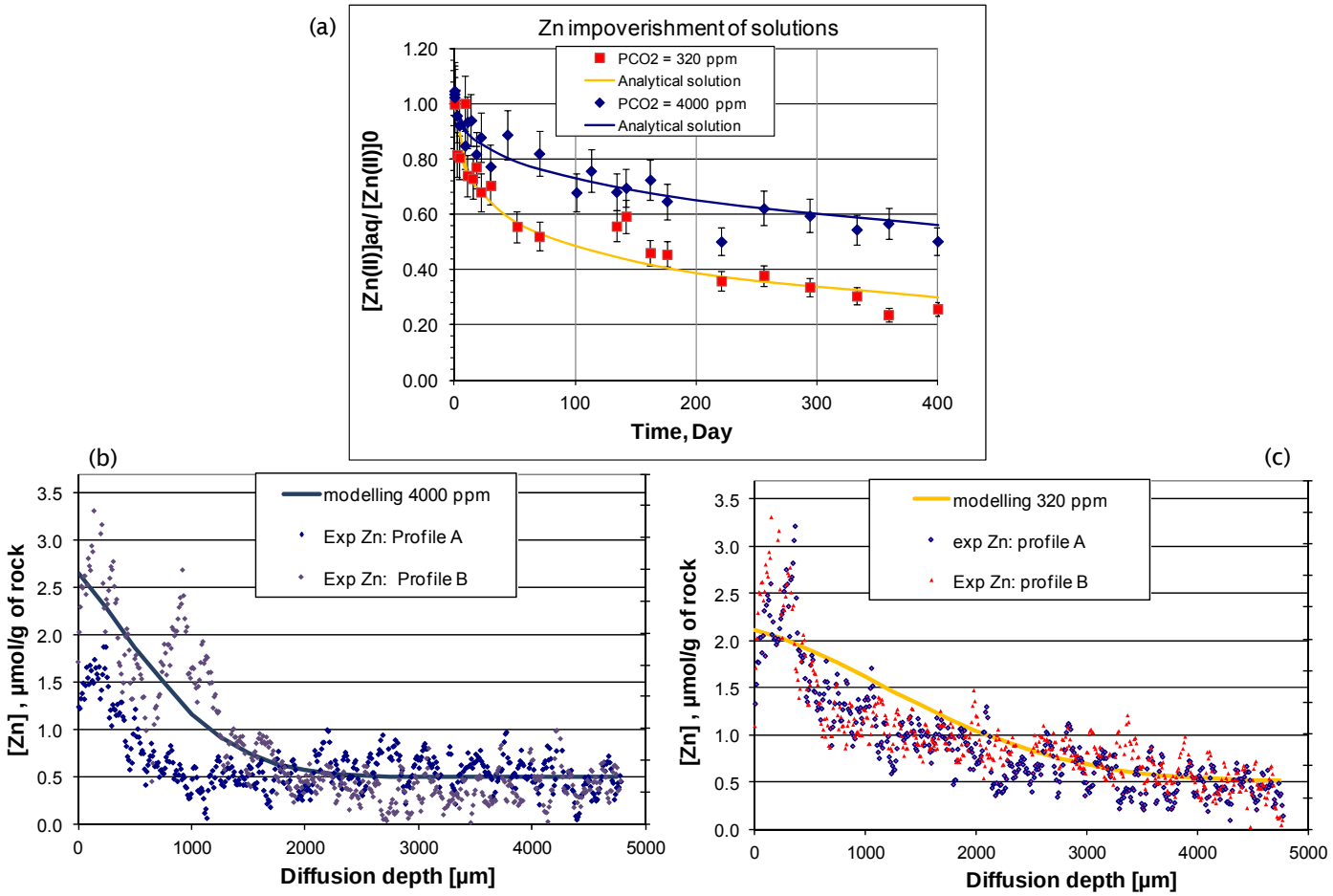

Figure 75 Comparison of the Zn experimental data from the cells with [Zn(II)]ini=10^{-5} M with modelling in (a) the reservoir, (b) the rock profile for the cell under 320 ppm of CO_2 and (c) the rock profile for the cell under 4000 ppm of CO_2.

Only preliminary simulations with an analytical approach were performed for reproducing the experimental data of this second series. As shown in the Figure 75b and especially in Figure 75c, the Zn rock profile acquired from µLibs on these two cells is so noisy that the constraint on modelling is weak, leading to poorly reliable diffusive parameters, all the more so as the zinc sorption is not linear (Figure 68). Therefore, sensitivity analyses using both analytical and numerical approaches are required.

Table 39 Effective diffusion coefficients and distribution ratios from the diffusion experiments for zinc with µ-cells.

Series	pCO_2	D_e (Zn) x 10^{11} (m^2 s^{-1})	K_d, (L kg^{-1})	D_a (Zn) x 10^{14}, (m^2 s^{-1})
1	4000 ppm	7 or 5	300 or 380	11 or 6
2	320 ppm	3.5	580	3
2	4000 ppm	2	380	2

Through-diffusion cells with radioactive tracer

Figure 76 shows the evolution of the ^{65}Zn activity in solutions during the in-diffusion experiments. One can notice a very sharp drop of the activity for the cell with an ionic strength of 85 mEq/L and an initial Zn concentration of 10^{-5} M, while the two cells with the highest IS exhibit a similar behaviour. Note that the activity of all the blank solutions remains stable over time at *ca* 100±5%.

The ^{65}Zn rock profiles acquired by means of the abrasive peeling method are reported in Figure 77.

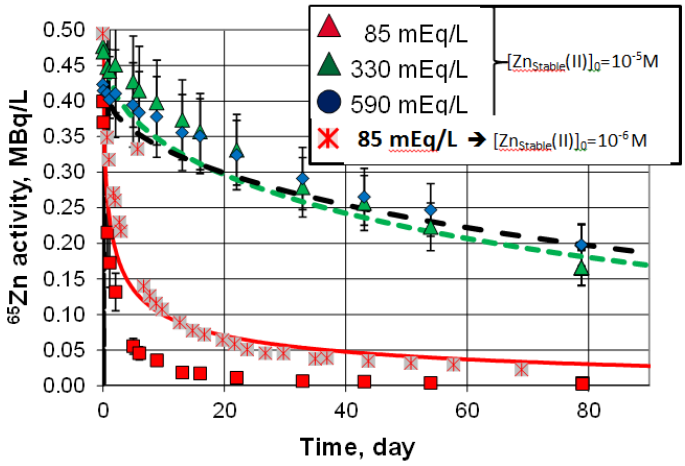

Figure 76 Evolution of the ^{65}Zn activity in solution as a function of time for the four cells with the associated modelling curves using an analytical approach and the diffusive parameters given in Table 40.

For the cell with the equilibrated pore-water (85 mEq/L), an unexpected behaviour was observed, since a too small activity was recovered in rock profile compared to the very sharp decrease in solution. Some processes such as precipitation within the reservoir are suspected, even though the speciation calculations with Phreeqc revealed that the precipitation of the Smithsonite ($ZnCO_3$) was reached for Zn concentration higher than 4 x 10^{-5}M. This led us to launch a new in-diffusion experiment with a lower initial Zn concentration (10^{-6} M) for which only the activity monitoring in solution is available for the moment and seems to give more consistent results (Figure 77).

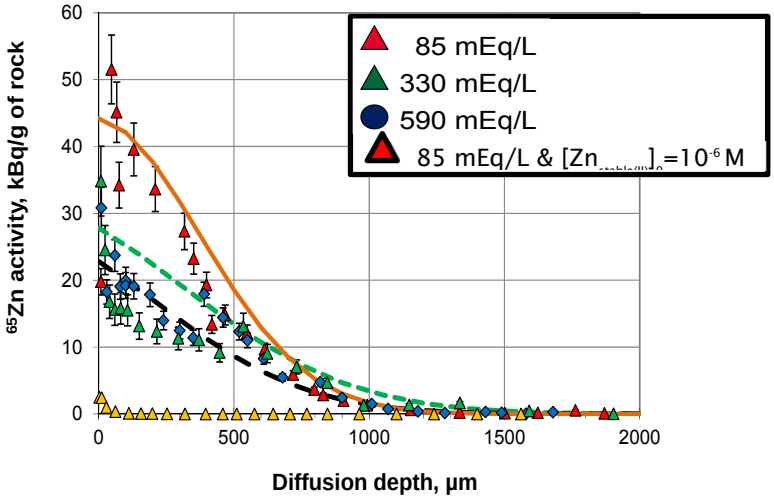

Figure 77 ^{65}Zn rock profile acquired on the four cells and the associated modelled curves.

The diffusive parameters used for the analytical approach are reported in Table 40. A strong drop of the K_d and D_e values can be noticed when the ionic strength increases. It is noteworthy that the K_d values estimated from the cells with the highest ionic strengths are in the same range as what the Multi-Site ion Exchange Model estimated for Zn concentration varying from 10^{-5} to 5 x 10^{-6} M (see the modelled curves in Figure 68).

Table 40 Effective diffusion coefficient, distribution coefficient determined for ^{65}Zn.

Ionic strength (mEq/L)	PCO_2 (ppm)	$[Zn_{Stable}(II)]_0$ (M)	D_e (^{85}Sr) x 10^{11} ($m^2\ s^{-1}$)	K_d, (L kg^{-1})	D_a (^{85}Sr) x 10^{14} ($m^2\ s^{-1}$)
85	4000	10^{-5}	impossible	impossible	impossible
85	4000	10^{-6}	4[a]	2300[a]	1
330	4000	10^{-5}	0.9	153	3
590	4000	10^{-5}	0.5	114	2

[a] diffusive parameters determined only from the activity monitoring in solution

Preliminary simulations were carried out with a numerical approach which takes into account the speciation, the concentration of competitors and which is based on the Multi-Site Ion exchange model (Figure 78). Simulations roughly matched these experimental data (in solution and rock profile).

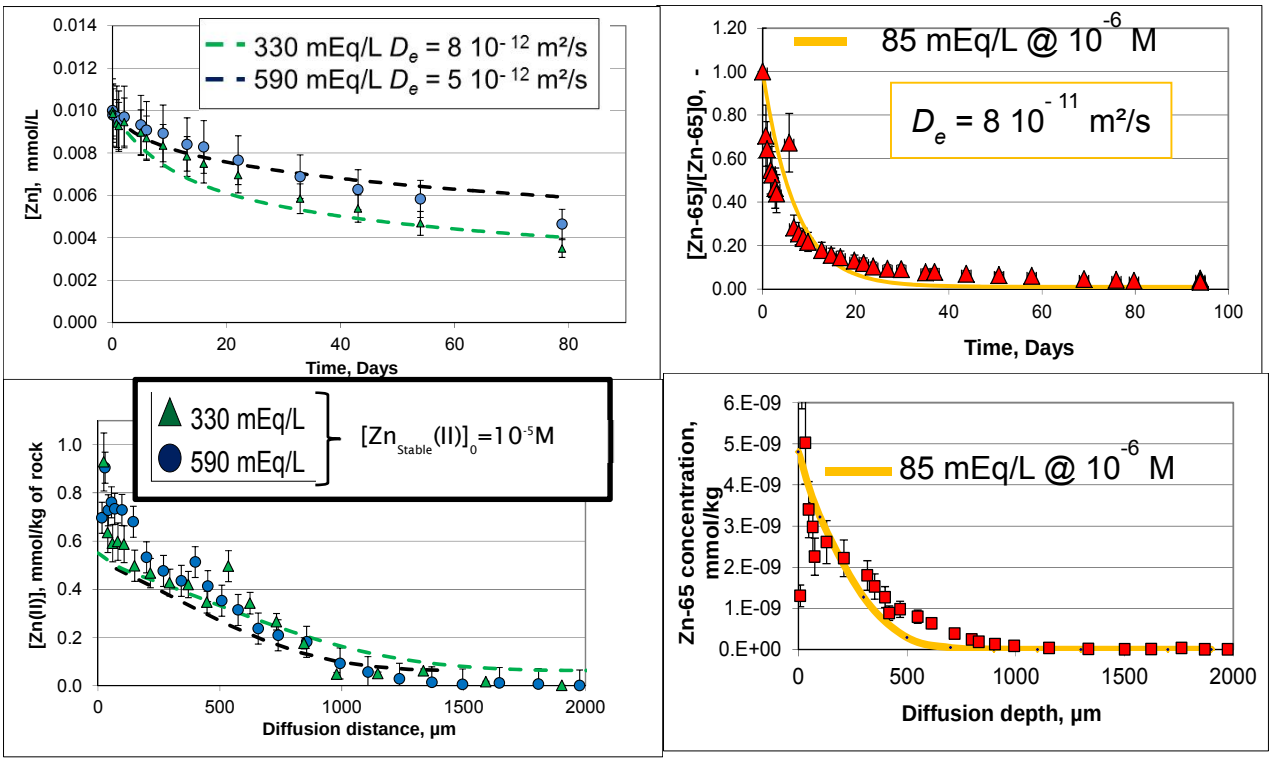

Figure 78 Reproduction Ion Exchange Theory (Figure 78). Only simulations of the experimental data using the Multi-Site Ion Exchange Model.

<u>Europium</u>

Micro-cells with non radioactive tracer

Figure 79 shows the evolution of the Eu concentration in solution as a function of time for the first series of µcells. The blank shows a decrease that can originate either from a sorption process onto the material or from a precipitation of some Eu-bearing minerals towards which Eu is oversaturated, such as Eu(OH)(CO_3) and Eu(CO_3)$_3$s with solubility limits of ca 6 10^{-7} M. However, the behaviour of the cell with highest [Eu(III)], i.e. a plateau at about 3 x 10^{-6} M, suggests that the kinetics of mineral precipitation would be too slow with respect to the duration of the experiments (55 days). Note that the highest concentration was chosen to reproduce the experimental conditions of Menut et al. (2006) (same initial concentration, same duration) who found a very low sorption of Eu associated to a high penetration depth.

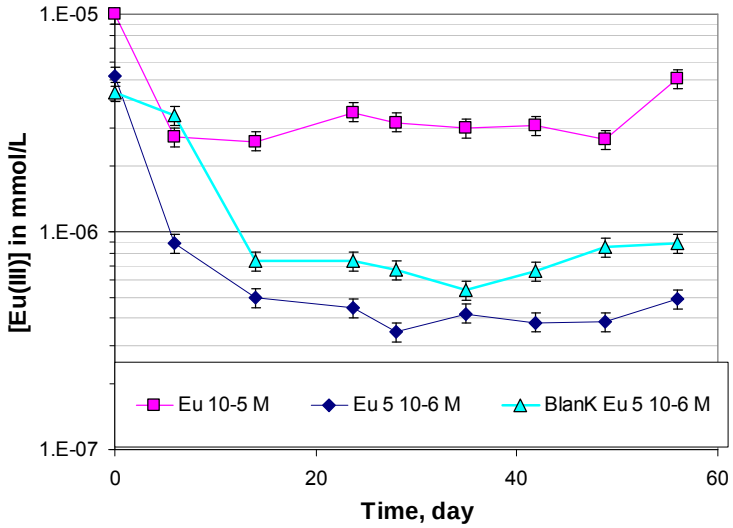

Figure 79 Evolution of the Eu concentration in solution during the diffusion-step.

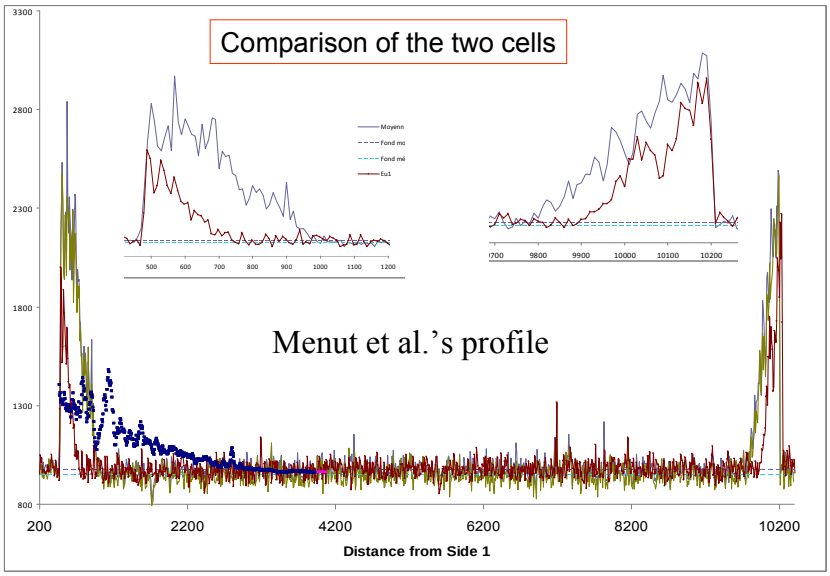

Figure 80 Comparison of the Eu profiles acquired by µlibs on the samples with [Eu(III)]ini=5 x 10^{-6} M brown curves) and [Eu(III)]ini= 10^{-5} M (green curves) with the Menut et al.'s data (blue curve).

The Eu profiles obtained by µLibs were reported in Figure 80. The signal intensity was higher for the cell with the highest initial concentration in agreement with the data acquired in solution. Moreover, the comparison with Menut et al.' s data indicates that the penetration depths remain clearly smaller than that previously determined by Menut et al. (2006) while the signal intensity logically exhibits an opposite tendency. These new results tend to demonstrate that the previous experiment by Menut et al. (2006) was likely affected by an experimental artifact. Indeed, the unloading of the unconstrained sample they used, had likely enabled the enhancement of the diffusion of Eu. The 2nd series of Eu in-diffusion is still ongoing.

Diffusion cells with radioactive tracer

Figure 81 shows the experimental data derived from the four in-diffusion experiments carried out with radioactive Eu(III). The evolution of blank activity as a function of time shows that (i) there is no significant precipitation of Eu-bearing minerals for the 80 days of the experiments, and (ii) the sorption onto the materials remains low, i.e., less than 20%, for this species known to be easily retained. Moreover, the effect of the ionic strength is only noticeable from the rock profiles, especially from the log-scale figure (excluding the preliminary data from the new cell). Indeed, while the Eu rock profiles of the cells 330 and 580 mEq/L are very similar, the one from the 85 mEq/L differentiates from the two others, 200 to 300 µm from the reservoir, when the activity remains almost constant before its decrease so that the penetration depth of ^{152}Eu is more important. This distinct behaviour could be explained by the speciation of europium in solution.

Figure 82 shows the distribution of the main Eu species for the three studied ionic strengths. While $Eu(CO_3)^+$ and $EU(CO_3)^{2-}$ remain the dominant species independently of the ionic strength (60% and *ca* 20% of the total Eu, resp.), the

diagram reveals some discrepancies for the other species as a function of the ionic strength (IS). In the solution with the lowest IS, while the percentage of Eu^{3+} is lower than for the other solutions, one can notice the occurrence at a significant level, of a negatively-charged species $(Eu(SO_4)^{2-}$, capable of diffusing without any uptake process. Therefore, one cannot exclude that the particular pattern of the rock profile can be due to the diffusion in depth of this species. Anyway, this discussion clearly demonstrates the complexity of the europium case, for which the technique we used can only draw a macroscopic picture of its diffusion through the Callovo-Oxfordian mudstones.

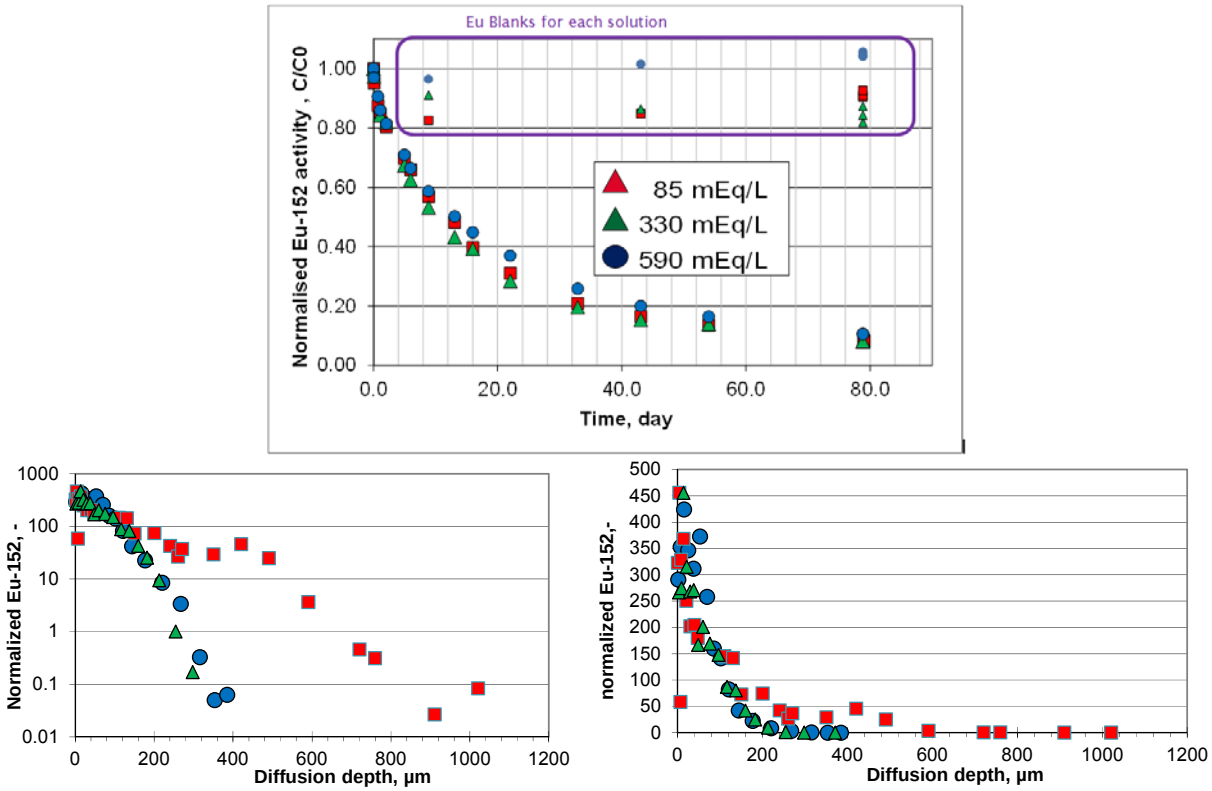

Figure 81 (Top) Evolution of the ^{152}Eu activity in solution of the reservoirs and the blanks as a function of time for the four cells, ^{152}Eu Rock profiles acquired in the three first cells (right) in log scale and (left) in linear scale. The activity in kBq/g of rock was normalized by the initial activity of ^{152}Eu in solution (kBq/mL of solution).

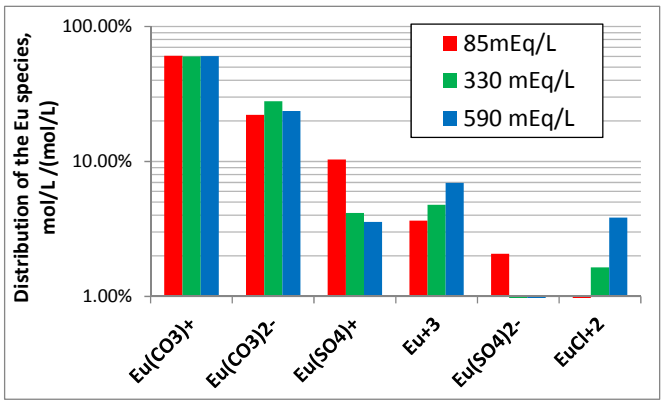

Figure 82 Distribution of the main Eu species present in solution for Eu total concentration varying from 10^{-8} M to 10^{-6} M calculated by means of the Phreeqc code.

- As a first modelling attempt, even though the europium sorption is not linear and the europium speciation in solution is quite complicated (see above), we have used the in-diffusion analytical solution with a fixed K_d value for capturing some tendencies with this species. For the first series of the µ-cells, we assume that some Eu-bearing minerals impose the Eu concentration to a stable value. The simulations are reported in Figure 83 with the associated diffusion parameters summarized in Table 41. The K_d values are quite low compared to the batch literature data on COX, from which K_s values are always higher than 10 000 L kg^{-1} (Andra, 2005).

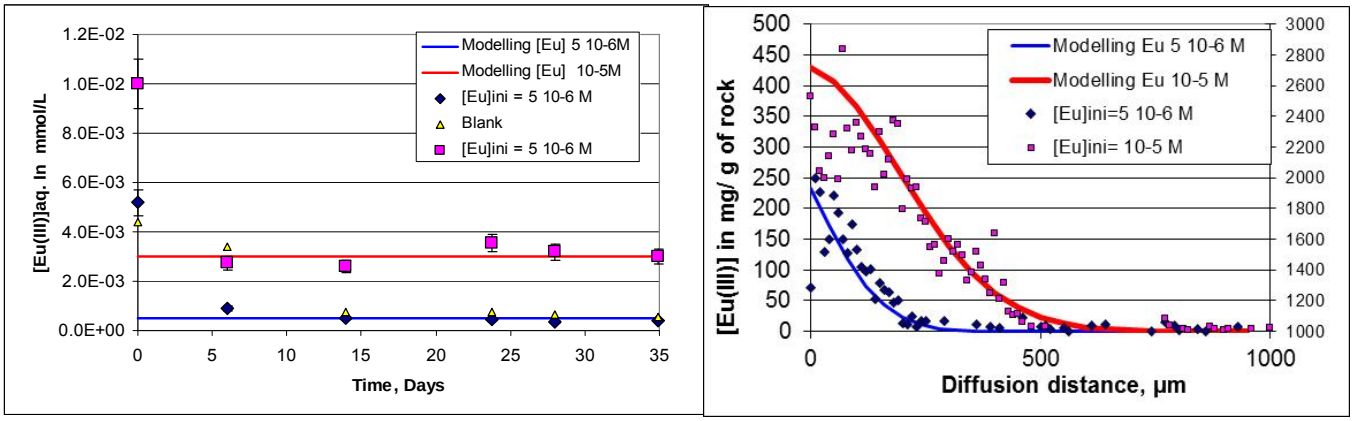

Figure 83 Comparison of the experimental Eu data from the cells with [Eu(III)]ini= 5 x 10^{-6} M (blue curves) and [Eu(III)]ini= 10^{-5} M (red curves) with modeling in the reservoir (left) and the rock profile (right).

Table 41 Summary of the diffusive parameters used for the modelling of the µLibs µ-cells.

		D_e x 10^{11} (m^2 s^{-1})	K_d (L kg^{-1})	D_a x 10^{15} (m^2 s^{-1})
Cell with $[Eu(III)]_{ini}$= 5 x 10^{-6} M	Eu-mineral control	1.1	3000	2
Cell with $[Eu(III)]_{ini}$= 10^{-5} M	Eu-mineral control	1.5	1000	7

Figure 84 shows the comparison of the simulations using the diffusive parameters given in Table 42 with the experimental data acquired in the three through-diffusion cells with variable ionic strengths. For these simulations, we assumed that the sorption did not evolve with the ionic strength because of the strong bound of the Eu sorption. However, under this assumption, the only solution for reproducing the whole Eu rock profile of the 85mEq/L one is to increase the D_e value. However, in this case, the data of the first 100 µm of the rock are clearly underestimated by the modelling, indicating that the Eu diffusion should be the sum of the diffusive contribution of the different Eu species, described in Figure 82. Therefore, we can also use the same D_e value for the three ionic strengths when excluding the tail of the 85 mEq/L rock profile.

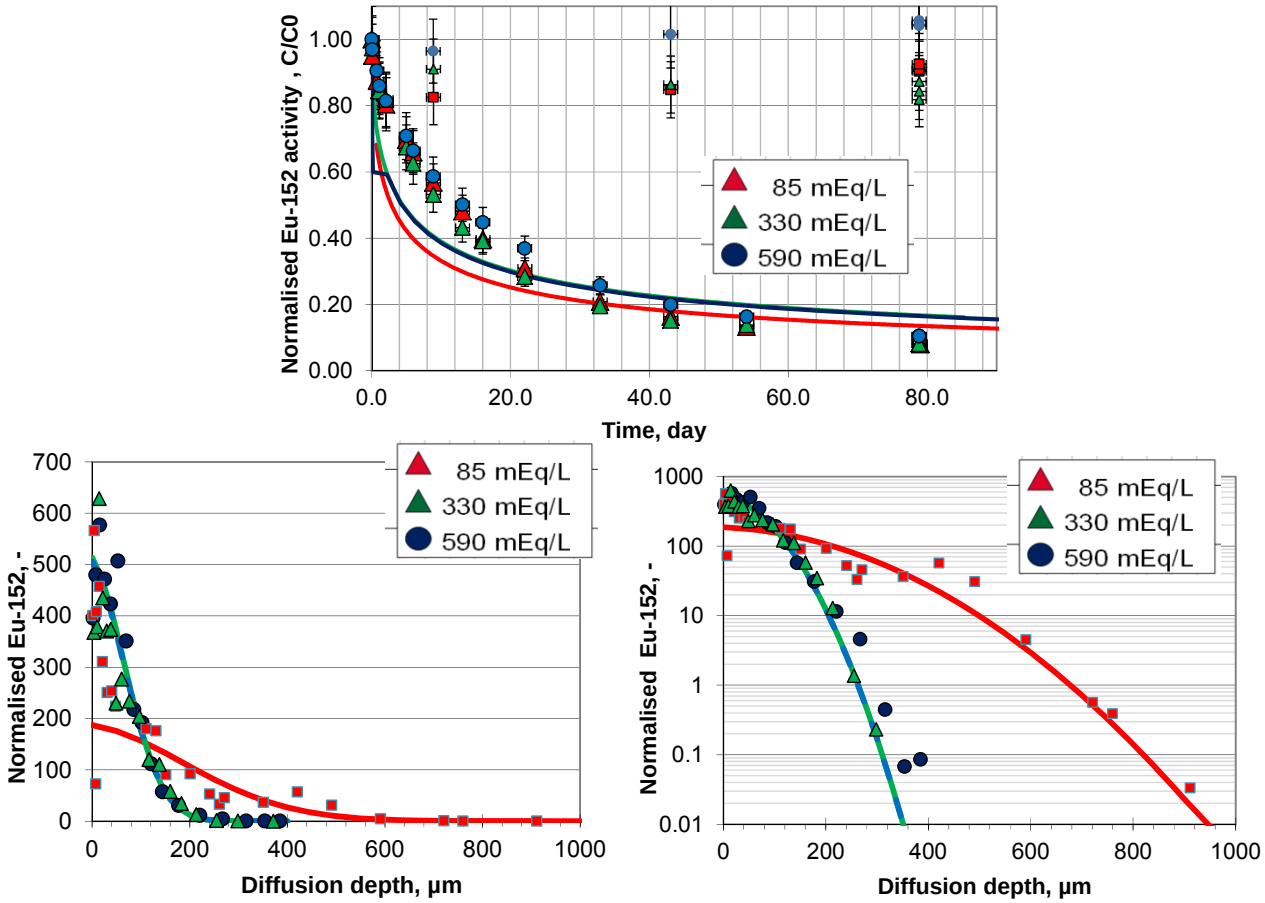

Figure 84 ^{152}Eu activity evolution in solution (at the top) and in the rock profile (at the bottom), and the associated modelled curves.

Table 42 Summary of the diffusive parameters used for the modelling the radioactive ^{152}Eu cells

Cells	[Eu(III)] @79 days	D_e x 10^{11} (m^2 s^{-1})	K_d (L kg^{-1})	D_ax 10^{15} (m^2 s^{-1})
85 mEq/L	8 x10^{-8} M	1.1 or 0.3	1400 or 3100	4 or 0.4
330 mEq/L	8 x10^{-8} M	0.3	3100	0.4
580 mEq/L	1 x10^{-7} M	0.3	3100	0.4

Lastly, one can also notice the bad fits of all the data in solution, which could be explained by the linear sorption model used in the analytical approach which is not able to reproduce the first 60 days of the experiments.

A comparison of the diffusion data acquired in the current study with the literature ones is given in Figure 85. The decrease of the D_a values could be linked to the improvement of the experimental protocols (better mechanical constraints, …). However, the extent of the sorption remains lower than that measured by sorption measurements (K_d batch = 10 000 to 20 000 L kg^{-1} at[Eu(III)]eq from 10^{-7} to 10^{-8} M, Dagnelie personal communication).

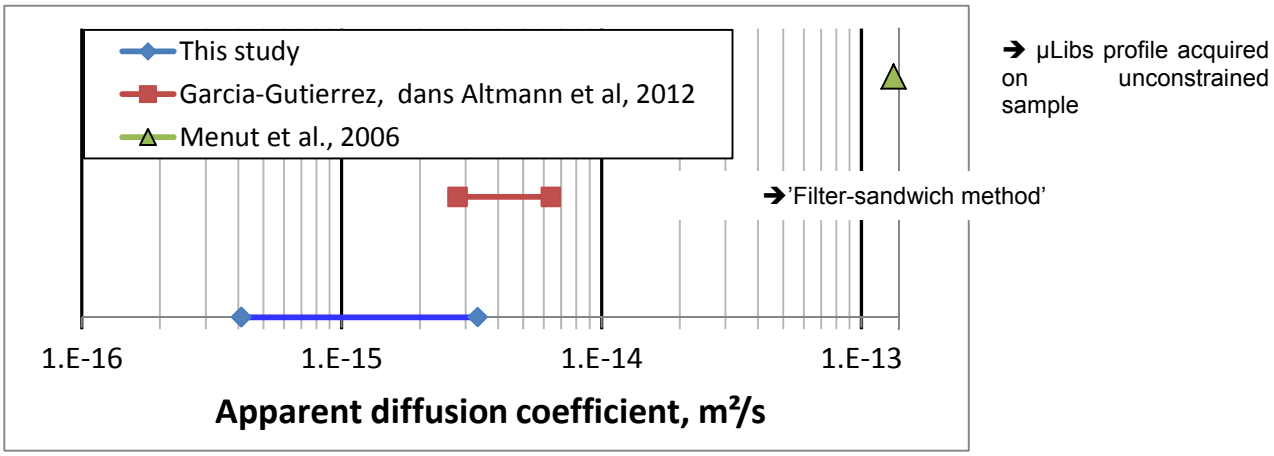

Figure 85 Comparison of the apparent diffusion coefficient values obtained for Eu in the current study with the literature data.

3.2.2.3 Discussion for Callovo-Oxfordian Clay

All the results obtained from the diffusion experiments with the three ionic strengths are compared in Figure 86. They reveal that the ionic strength (IS) would impact the diffusivity of Sr and Zn, in parallel to the sorption extent. At a IS of 85 mEq/L, we observe an enhancement of their diffusion with an extent of the same order of magnitude, while at the highest IS, their diffusivity becomes very close to that of the water tracer, HTO. Only Eu seems not to be influenced by the change of the physic-chemical conditions.

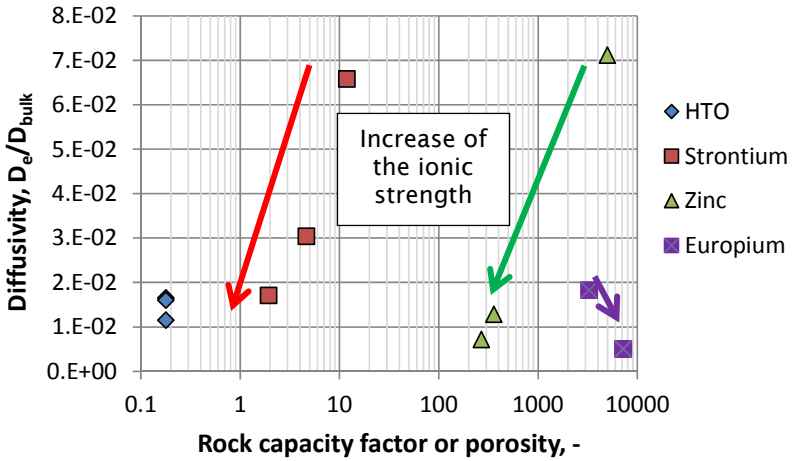

Figure 86 Evolution of the diffusivity as a function of the rock capacity factor or porosity for HTO, strontium, zinc and europium with the increase of the ionic strength.

In literature, Molera and Eriksen (2002) proposed a model for accounting for the diffusion enhancement of some cationic species by means of relationships between the D_e and the K_d:

$D_e(cat)_{exp} = D_e(cat)_{th} \times (1 + m^f . \rho_d \times K_D)$

Where $D_e(cat)_{th} = D_0(cat)/D_0(HTO) \times D_e(HTO)_{exp}$ and m^f denotes the mobile fraction of sorbed strontium.

Figure 87 shows the results of the applications of this relationship using for the calculations the theorical D_e, m^f equal to 27%, 0.07% and 0% for Sr, Zn or Eu (resp.). Such approach clearly failed to reproduce Eu behavior, in accordance with what expected from its strong sorption, while for Sr and Zn, a relatively good agreement was achieved. In these cases, the mobile fraction is almost 1000 times lower for Zn than for Sr, evidencing the distinct contribution of the ion exchange phenomenon in diffusion.

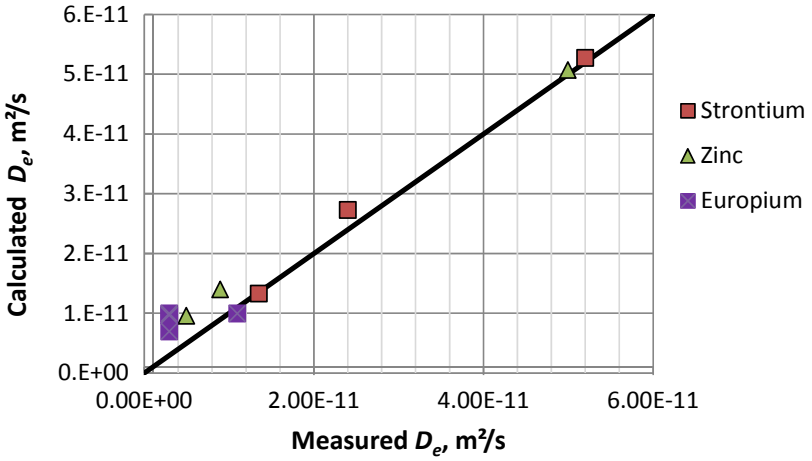

Figure 87 D_e calculated by means of the surface diffusion and Molera and Eriksen's models as a function of the measured D_e for the three studied cations

3.2.3 Conclusions for Callovo-Oxfordian Clayrock

We investigated in this study, the sorption/diffusion in the Callovo-Oxfordian claystones of three cations covering a representative range of cation categories taken into consideration in the performance assessment, from a moderately sorbing cation, Sr, to strongly sorbing cations, one divalent, Zn, and one trivalent, Eu. The impact on diffusion and sorption of the ionic strength and the partial pressure of CO_2 was estimated by means of batch and diffusion experiments. Note that for strongly sorbing cations, such as Zn and Eu, specific approaches were used, and in some cases, developed for improving the reliability of the data acquired.

The batch and through-diffusion experiments carried out with Sr led to a consistent picture for the three ionic strengths explored. Numerical modelling based on the multi-ion exchange model succeeded in well reproducing of these experimental data, using D_e values varying from 5.2 to 1.35 x 10^{-11} m²/s when the IS increases from 85 to 580 mEq/L. On the other hand, the results derived from the out-diffusion experiments clearly show some inconsistencies with the through-diffusion ones, suggesting that some processes could have taken place for retaining Sr during these long experiments (150 days + 240 days). These processes with slower kinetics than the ion exchange are thought to be either isotopic exchange of ^{85}Sr or incorporation of ^{85}Sr into some Sr-bearing minerals. However, long-term batch experiments (300 days) failed to evidence these processes, likely due to the too high water/rock ratio compared to those of the compacted system.

The picture appears more complicated for Zn. For example, its more complex chemistry (complexation, solubility limits, etc...) made its study, especially by µLibs, more tricky, because the Zn initial concentration has to be chosen high enough for acquiring a good µLibs signal and not too high for avoiding any Zn-bearing mineral precipitation. However, first Zn acquisitions by µLibs sound promising. Moreover, all the data obtained by batch experiments are weakly impacted by the change of the experimental conditions (ionic strength, pCO_2), which is unexpected regarding what was estimated by modelling. On the other hand, in-diffusion experiments allowed us to acquire data clearly influenced by the change of the ion strength. And first numerical modellings succeeded in reproducing these data, using D_e values decreasing when the IS increases.

For Eu, some rough tendencies emerge from the data acquired from the first in-diffusion experiments. The extent of Eu sorption estimated by a simple analytical model seems to be slightly lower than what was previously measured from batch experiments but not impacted by the IS change. Dedicated batch experiments should confirm this trend. Regarding the effective diffusion coefficient, the three in-diffusion experiments carried out with equilibrated water led to consistent values of about 0.3 x 10^{-11} m²/s. However, the non-uniform shape of the rock profile derived from one of these cells, using radioactive Eu, suggests that the diffusion process is much more complicated, likely involving the contribution of several Eu species. And among these species, some Eu anionic complexes, occurring in larger amount in the low IS solution, could be responsible for the larger penetration depth than those of the cells with high IS. Finally, it seems that Eu diffusion would be more governed by its chemistry in solution than by some surface diffusion processes. And we hope that the results acquired from the four long-term diffusion experiments (~ 400 days) that are still on-going will strengthen this tendency.

Lastly, the diffusion of Sr, and to a lesser extent, zinc, studying under various experimental conditions, can be described by classical diffusion surface formalisms given in literature. In this case, the extent of the cation diffusion coefficient is clearly correlated to the extent of its sorption.

3.3 Boom Clay

The mineralogical composition of Boom Clay is given in Table 43. The clay mineralogy is dominated by illite, smectite, illite/smectite interstratifications, and kaolinite.

Table 43 Mineralogical composition of Boom Clay (reported in Honty & De Craen., 2012).

	Min (%)	Max (%)	Average (%)
Quartz	21	61	41
K-feldspar	4	10	7
Plagioclase	0.7	4	2.4
Calcite	0	4	2
Siderite	0	0.5	0.25
Dolomite	0	1	0.5
Pyrite	0.5	3	1.8
Anatase	0.4	1	0.7
Apatite	0.1	0.5	0.8
Organic matter	0.5	3.5	2
Kaolinite	2	16	9
Chlorite	1	4	2.5
Smectite	7	24	15.5
Illite	4	18	11
Mixed illite/smectite	7	23	15

The petrophysical and hydraulic parameters of the Boom Clay are summarized in Table 44 (taken from De Craen *et al.* (2004)).

Table 44 Petrophysical and hydraulic parameters of Boom Clay (De Craen et al., 2004).

Parameter	Unity	Value
Bulk density (sat.)	[kg dm-^{3}]	1.9 - 2.1
Average grain density	[kg dm-^{3}]	2.65
Water content	[% dry wt]	19 – 24
Specific surface	[m² g^{-1}]	44
Hydraulic conductivity	[m s^{-1}]	
- Lab experiments		Vert. 1.3-3.4×10^{-12}, Hor. 3.5-7.9×10^{-12}
- *In situ* field testing		Vert. 2.1×10^{-12}, Hor. 4.5×10^{-12}

At the site of Mol, where the underground research facility HADES is located, the porewater in contact (and presumed in equilibrium) with the mineral fabric is mainly a 0.015 M $NaHCO_3$ solution of pH ~ 8.3. The typified inorganic composition of this porewater is referred to as Synthetic Boom Clay Water (SBCW) (De Craen *et al.* (2004)). If porewater is used directly from piezometer sampling, it is referred to as Real Boom Clay Water (RBCW). The most common type of Real Boom Clay Water used throughout the experiments is piezometer water derived from the Experimental Gallery/Bottom Shaft (EG/BS) piezometer. Its composition can be found in De Craen *et al.* (2004). The difference between SBCW and RBCW lies mainly in the presence of dissolved organic carbon in RBCW, whereas in SBCW it is totally absent.

3.3.1 Experimental procedures

3.3.1.1 Sorption experiments

The sorption of Sr on Boom Clay suspensions and on compacted Boom Clay was already studied before (Maes et al., 2009). Since BC water contains natural Sr which is in equilibrium with strontianite, we could not determine a sorption isotherm as the concentration region was limited by the solubility on the one hand and the analytical detection limit on the other hand. Therefore, we performed "single point K_d" experiments.

For the single point K_d measurements with Sr on dispersed Boom Clay, a clay slurry was prepared under anaerobic conditions with a CO_2 atmosphere mimicking in-situ conditions (glove box Ar/0.4% CO_2) by mixing in a polyethylene tube ~3 g of Boom Clay (core: 2001/5 TD19-20 01-31) with ~30 ml Real Boom Clay Water (RBCW, sampled from a

piezometer coded EG/BS installed in the HADES URL, Mol, Belgium) to obtain a S/L ratio of 100 g/L. Then a ^{85}Sr spike solution was prepared by mixing 90 ml of RBCW with 10 ml of the so-called ^{85}Sr mother solution resulting in an activity concentration of ~137 Bq mL^{-1}. In the following, 2 mL of the BC slurry were mixed with 30 ml of the ^{85}Sr spike solution. Thus, the S/L ratio and calculated ^{85}Sr activity concentration in the samples at the beginning of the experiment corresponded to 6.25 g L^{-1} and ~129 Bq mL^{-1}, respectively. Boom Clay also contains natural Sr. Its concentration in Boom Clay porewater was determined by De Craen et al. (2004) to range between 40 and 130 □g L^{-1}. In order to know the precise Sr concentration of the RBCW used for the experiment, it was analysed before starting the batch tests. The measured concentration corresponded to 134 □g L^{-1} (~1.5 x 10^{-6} M). The experiment was performed in triplicate and conducted in an anaerobic glove box (Ar/0.4% CO_2).

For the Sr sorption on thin Boom Clay disks, the through-diffusion set-up was used. A disk of Boom Clay (3.8 cm diameter, 0.2 cm thick and known weight) was loaded in the through-diffusion cell. Both sides of the diffusion cell, equipped with porous stainless steel filters, were connected to a vessel containing 250 mL Real Boom Clay water, spiked with ^{85}Sr (C_0 = 108 Bq mL^{-1}). This water was continuously circulated over the filters being in contact with both sides of the clay disk. The Sr activity in the vessel was measured weekly until a constant Sr activity was reached. The distribution coefficient was calculated from the initial and final activity.

3.3.1.2 Diffusion experiments

The diffusion experiments were carried out using the through diffusion method, as described in 2.5.1.1. More details of the diffusion cells and the filter plates are described in Annex 1.

The migration cells were filled with "undisturbed" clay cores of ±30 mm length (15 mm in case of the flushed filter cell) taken from stainless steel cutting edges at the level of the HADES underground research facility (URF) at Mol, Belgium. Before starting the experiment, the clay plug was equilibrated several days with Real Boom Clay Water (RBCW) before adding tracer to the source reservoir. The in-situ concentration of Sr in RBCW is 1.4×10^{-6} M. The experiments were performed in a glove box with Ar/CO_2 0.4 %.

The *source reservoir* was spiked with a tracer (HTO, ^{85}Sr or ^{65}Zn). The chemical concentrations calculated from the specific activities of the tracers were used to fit the data and not the total concentration (in-situ concentration + added concentration spike) in the solution. The decrease in activity (respectively concentration) was monitored by regularly taking subsamples from the reservoir. Ideally, the activity should not decrease more than 50% in order to have good boundary conditions for modelling. This can be imposed by using a sufficiently large volume of the source reservoir (0.5 l -2.5 l) in the case of sorbing tracers.

For the through-diffusion experiments (HTO and ^{85}Sr), the increase in the *target reservoir* is also monitored. The target reservoir is exchanged at regular time intervals in order to keep the activity/concentration as low as possible. The volume (± 20 ml) was exchanged regularly (e.g., 2-2-3 days regime) in order to avoid a decrease in the flux. In one of the duplicate experiments with ^{85}Sr (further described as experiment 2), a larger target reservoir (150 ml) was used which was not exchanged. Subsamples were taken at the same frequency as experiment 1. The solutions of the source and target reservoir are continuously pumped over or through the filters (depending on the type of diffusion cell) by peristaltic pumps with an average flow rate of a few ml per minute. The duration of the experiment varies from a few weeks for HTO to 7 months for ^{85}Sr. At the end of the experiment, the consolidated clay was cut in slices of 0.5 mm. The moisture content of the clay slices was obtained by measuring the weight before and after drying the clay (at 65°C – at least for 72 hours).

The activity of the subsamples of the source and target reservoir are measured with liquid scintillation counting (Packard/Canberra Tri-Carb 2100TR) for HTO and gamma counting (Packard/Canberra COBRA Quantum) for ^{85}Sr and ^{65}Zn. The tracer activity in the clay slices is measured on the dried samples (no extraction).

Overview experiments

The diffusion experiments with Sr and Zn described below, were preceded with HTO diffusion as a benchmark test. Through-diffusion lasted 2 to 3 weeks and was followed by out-diffusion to remove all HTO from the clay again. The diffusion of Sr in Boom Clay was studied in two replicate experiments (experiments 1 and 2). The electrolyte solution was RBCW (~15 mM $NaHCO_3$, ~100 mg/l DOC, pH 8.5). Both experiments were performed in the same way, except for the volume and changing regime of the target reservoir (as described above).

In addition, the data of the through-diffusion experiments performed in the framework of FUNMIG (Maes *et al.,* 2012) were refit with the most up-to-date model for this type of experiments. The most important difference between these experiments and the ones performed within EC Catclay is the volume of the source reservoir (200 ml vs. 500 ml Catclay experiments), which is expressed in the sharper decrease of the concentration in the source reservoir.

Table 45 Overview of the diffusion experiments in Boom Clay.

Name	Radionuclide	Diameter clay plug (mm)	Volume source reservoir (mL)	Duration (days)
Through-diffusion (exp 1 Catclay)	HTO	31.9	150	35
Through-diffusion (exp 2 Catclay)	HTO	31.1	150	35
Through-diffusion (exp 4 Catclay)[a]	HTO	15	150	14
Through-diffusion (exp 1 Catclay)	^{85}Sr	31.9	500	217
Through-diffusion (exp 2 Catclay)	^{85}Sr	31.1	500	217
Through-diffusion (exp 1 FUNMIG)	^{85}Sr	15	200	185
Through-diffusion (exp 2 FUNMIG)	^{85}Sr	30	200	192
In-diffusion (exp 3 Catclay)	*^{65}Zn*	*31.1*	*200*	*93*
In-diffusion (exp 4 Catclay)[a]	*^{65}Zn*	*15*	*500*	*219*

[a] experiment performed in flushed filter diffusion cell

A first in-diffusion experiment with Zn (here reported as 'experiment 3') was conducted in an early stage of the Catclay project. In this experiment, we found out that Zn sorbs strongly on the stainless steel filter. In the further course of Catclay, a series of different filter materials was tested. Due to the long time needed to find appropriate filter materials, the second experiment was delayed. Finally, a new experiment ('experiment 4') was started in a PEEK diffusion cell with flushed filters in polypropylene. After finishing this experiment, it seemed that at this pH (8.4) sorption cannot be prevented, even not with polypropylene filters. The recovery in the clay and inlet solution was only 12%. The rest is sorbed on the filter and tubing. Moreover, the profile in the clay is too narrow (± 1mm) to make a reliable fit. We can conclude from these experiments that studying the diffusion behaviour of Zn in Boom Clay is not possible with this set-up due to the high pH. A new set-up should be considered, but even the membrane approach (PSI) seems not to work properly at higher pH, due to loss of tracer by sorption on the materials.

Fit procedure

The through-diffusion of HTO and Sr were modelled with the model described in Van Laer et al. (2014) (using the COMSOL Multiphysics® code. The concentration in the source and target (only through-diffusion) reservoirs as function of time, and the tracer profile in the clay at the end of the experiment are used as input data for the fitting of the models. The models have four fit parameters: the apparent diffusion coefficient in the clay (D_a clay), the capacity factor of the clay (α clay), the apparent diffusion coefficient in the filter (D_a filter) and the capacity factor of the filter (α filter). Any combination of these four input parameters can be fitted with any combination of the experimental input data (source, target and profile). The correlation coefficients between the parameters as well as the uncertainties on the fitted parameters are calculated. Fitting occurs by minimization of chi-square.

In most cases the capacity factor of the filter is fixed to the porosity given by the manufacturer (0.31), as the retardation on the filter is expected to be 1. Moreover, since D_a and α are always correlated, a deviation of the α in the filter will be compensated by the value for the D_a of the filter.

3.3.2 Results & Discussion

3.3.2.1 Sorption experiments

The experimentally determined K_d values for the triplicate samples range between 257 and 322 L kg^{-1}, which corresponds to an average K_d value of 293 L kg^{-1} (st. dev= 33, log K_d= ~2.5). On the compacted Boom Clay disk, Sr sorption equilibrium was reached after about 20 days and an average K_d of 318 L kg^{-1} (st. dev. = 3.3) was calculated (Log K_d = 2.5), which matches the distribution coefficients on the dispersed clay systems at low Sr concentrations.

3.3.2.2 Diffusion experiments

Diffusion of HTO in Boom Clay

The diffusion in experiments 1, 2 and 4 with Sr and Zn was preceded by a diffusion experiment with HTO on the same clay plug. The data were fitted under the assumption that diffusion in clay and filters is similar (i.e., filter parameters were not fitted separately but the length of the filters was added to the length of the clay plug). The results are given in Table 46.

Table 46 Diffusion parameters for HTO in Boom Clay.

Exp Method	**D_a ($m^2\ s^{-1}$)**	**α (-)**	**D_e ($m^2\ s^{-1}$)**
Through-diffusion (exp 1 Catclay)	4.1×10^{-10}	0.27	1.1×10^{-10}
Through-diffusion (exp 2 Catclay)	4.1×10^{-10}	0.27	1.1×10^{-10}
Through-diffusion (exp 4 Catclay)	*7.5×10^{-10}*	*0.09*	*6.9×10^{-11}*
Pulse injection (percolation)	2.3×10^{-10}	0.37	8.5×10^{-11}

The duplicate experiments with the conventional diffusion cell gave exactly the same fitted parameter values for D_a, α and hence also D_e. As retardation (R) is assumed to be 1 for HTO, ηR (or α) represents the porosity of the clay. The determined value of 0.27 is lower than the expected porosity (about 40%) and lower than earlier reported values in percolation experiments (average 0.37) (Bruggeman *et al.*, 2014). However, the values determined for D_e are completely in line with earlier determined D_e values (Bruggeman *et al.*, 2014). The parameters D_a and α differ more individually, but since they are correlated, it is better to compare the D_e values. The values determined for the through-diffusion of experiment 4 with the flushed filter diffusion cell deviate more from these values. The α determined is in this case much too low. As described in Van Laer et al. (2014), the model for the flushed filter diffusion cell probably still needs to be improved. The data will be refit when an improved model is available.

Diffusion of Sr in Boom Clay

In the past, Sr migration in Boom Clay was already studied with several different methods: percolation, in-situ, electromigration and through-diffusion experiments. In the framework of Catclay, we performed two through-diffusion experiments in the conventional diffusion cells. The experimental data and best-fit values are presented in Figure 88. The best-fit parameters for the clay are reported in Table 47. The data of the flux in the target reservoir of experiment 2 could not be used for the fitting. The measured activities were too close to the detection limit, which led to high uncertainties.

For fitting the data, the capacity factor α of the filter was fixed to the porosity of the filters as provided by the supplier (0.31). The D_a of Sr in the filter was experimentally determined (annex 1), but since the D_a for used and unused filters may be different (Glaus *et al.,* 2008), it was chosen to fit this parameter. This approach is validated by the experimental observation by means of SEM imaging that the filter after performing the experiment contains numerous clay particles, likely changing the diffusion characteristics. The fits of the Sr profile in the clay agree very well with the experimental datapoints, while the fits of the concentration decrease in the source reservoir were rather good with a small difference in the first period of 100 days. Despite the rather large error bars (due to low activities), the flux in the target reservoir of experiment 1 could be fitted very well. The distribution coefficients K_d, derived from the α when considering a dry bulk density of 1700 kg m^{-3}, amount resp. 510 and 710 L kg^{-1}. This differs a factor of ± 2 with the average K_d of 293 L kg^{-1} experimentally determined in the framework of FUNMIG (Maes *et al.,* 2009). Finally, the parameter D_e, which combines α and D_a, is two orders of magnitue higher than the D_{ea} determined for HTO (± 1×10^{-10} m^2 s^{-1}). The variation between the two experiments is less than 20% (Table 47) and can most probably be explained by the heterogeneity of the Boom Clay, which involves that there is some variation (e.g., in clay mineral content) possible between the different clay plugs.

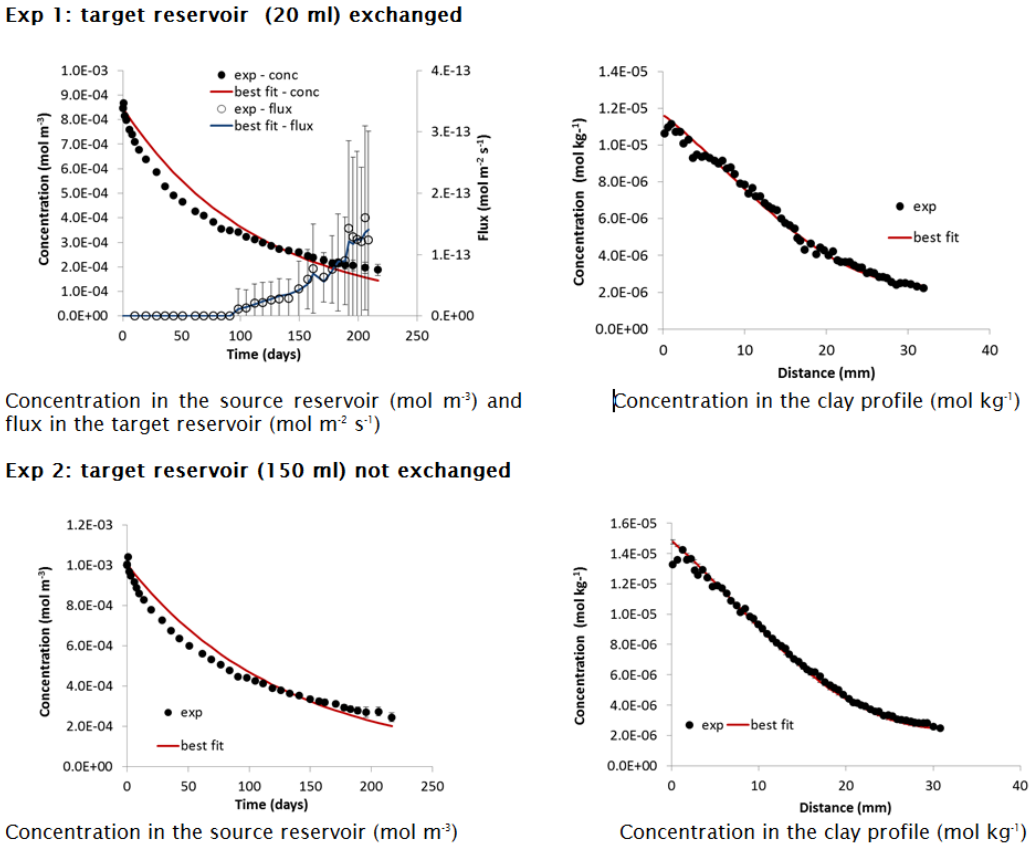

Figure 88 Experimental data and best-fit values for the two through-diffusion experiments performed in the framework of EC Catclay.

Table 47 Fitted diffusion paramaters for the experiments performed in the framework of Catlay and the different methods of studying Sr diffusion in the Boom Clay in the past (Maes et al., 2012). Values between brackets are unreliable.

Exp method	**D_a ($m^2\ s^{-1}$)**	**ηR (-)**	**D_e ($m^2\ s^{-1}$)**
Through-diffusion (exp 1 Catclay)	1.1×10^{-11}	8.7×10^{2}	9.3×10^{-9}
Through-diffusion (exp 2 Catclay)	8.9×10^{-12}	1.20×10^{3}	1.1×10^{-8}
Through-diffusion (exp 1 FUNMIG)	7.4×10^{-12}	6.83×10^{3}	5.0×10^{-8}
Through-diffusion (exp 2 FUNMIG)	7.6×10^{-12}	4.64×10^{3}	3.5×10^{-8}
Electro-migration	7.8×10^{-12}	-	
Percolation	8.9×10^{-12}	*(389)*	
In-situ	6.9×10^{-12}	*(238)*	

The two diffusion experiments performed in the framework of FUNMIG were performed with the same type of diffusion cell, but the volume of the source reservoir was smaller (200 mL). In the framework of Catclay, the data were refit with the most up-to-date model for this through- diffusion experiment (Van Laer et al., 2014) (Figure 89). The determined values of D_a are slightly lower compared to the Catclay experiments, but the biggest difference is observed for α (Table 47). The deduced K_d's (4000 and 2700 L kg^{-1}) are an order of magnitude higher than the experimentally defined K_d (293 L kg^{-1}). The high values for α have as consequence that the values for D_e are also higher (factor 3 to 5) compared to those of the Catclay experiments. This variation cannot only be attributed to the heterogeneity of the clay samples. The sharp decrease in the concentration of the source reservoir (to 10% of the initial concentration after 14 days and finally to even only 2%) makes the uncertainty of the fit higher and is possibly (also) an explanation for the variation.

Experiment 1 FUNMIG (15 mm) **Experiment 2 FUNMIG (30 mm)**

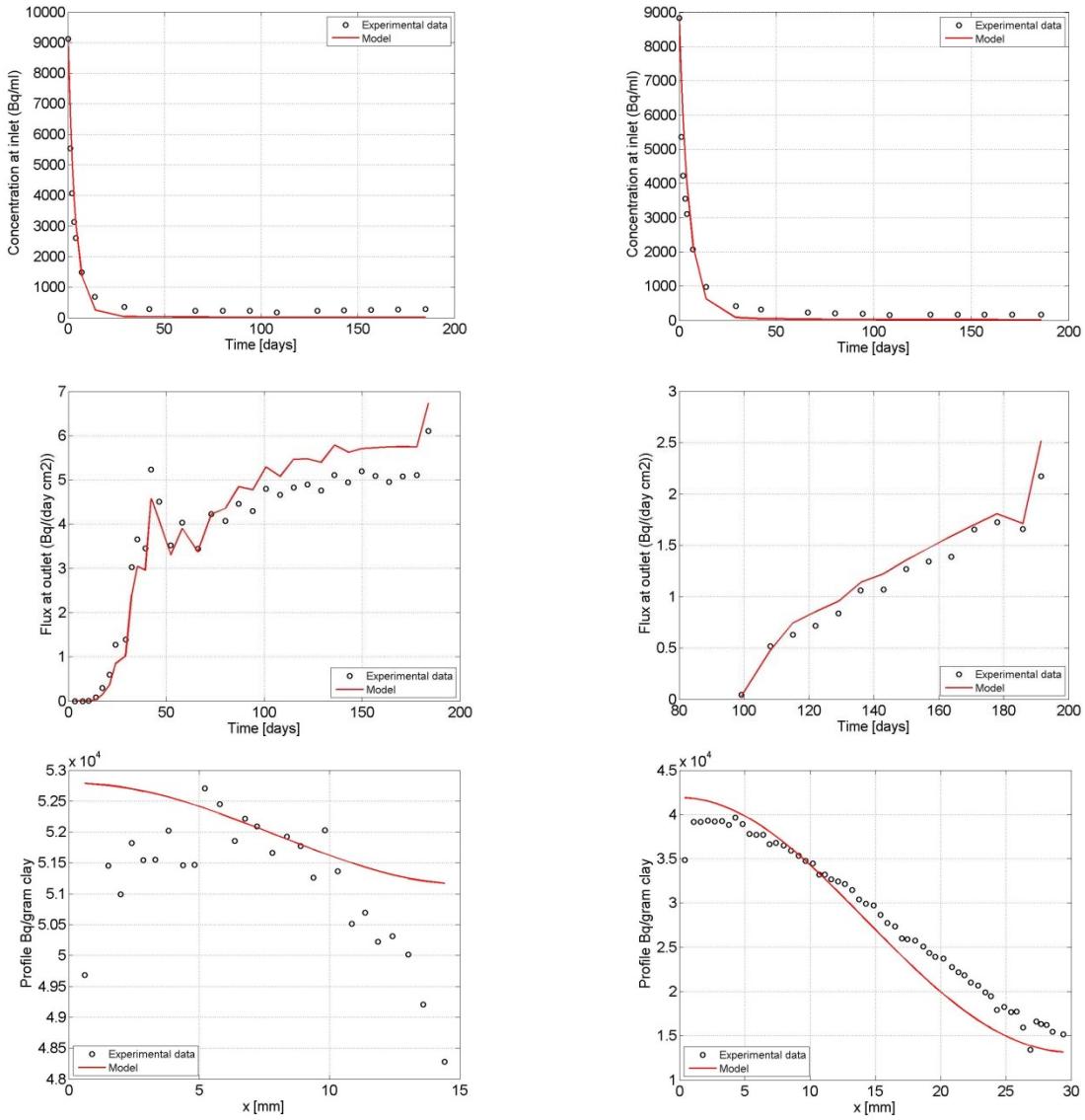

Figure 89 Experimental data and best-fit values for the two through-diffusion experiments performed in the framework of EC FUNMIG. (The Sr profile of experiment 1 is almost a horizontal line. Note that the scale of this graph is very large.)

In Table 47 the D_a determined for the other types of experiments studying the Sr migration in Boom Clay, are also reported. The D_a of the percolation experiment (column migration experiment with advection) is in line with the D_a of the Catclay experiments. Although the value for the α is considered as unreliable (large error), the deduced K_d of 229 L kg^{-1} agrees quite well with the experimentally defined K_d (293 L kg^{-1}). The in-situ experiment gives the lowest D_a and α. Finally, the D_a determined from the electro-migration experiments is slightly lower than the Catclay experiments, but can be considered in the same range. Also here, we have to mention that the heterogeneity of the clay has to be considered when interpreting the values.

3.3.3 Conclusions for Boom Clay

The most important conclusions that can be taken from the performed experiments so far are: (i) the D_a values for Sr diffusion determined with different experimental methods differ by less than a factor 2; (ii) the α values determined in the EC Catclay experiments differ only a factor 2 with the experimentally defined K_d; and (iii) despite the variation in values for the different parameters between the different experimental methods, the overall trend is clear: the effective diffusion coefficient D_e for Sr is at least 2 orders of magnitude higher than the effective diffusion coefficient observed for HTO (± 1×10-10 m^2 s^{-1}). This is a strong indication for double layer-enhanced diffusion.

3.4 General conclusions regarding clayrocks

3.4.1.1 Experimental techniques

- Filter-free experimental techniques to study diffusion of strongly sorbing radionuclides are available for indurated rocks (e.g. OPA, COx). Or the rocks can be used as such, i.e. they can be contacted with a solution without disintegration, or they can be stabilised with a resin (Van Loon and Müller, 2014). The use of a confining filter is not mandatory.
- In the case of plastic clays (e.g. Boom clay), confining filters are mandatory. Interaction of radionuclides with the filters might cause severe problems that make diffusion studies with strongly sorbing radionuclides for such systems very difficult, if not impossible.

3.4.1.2 Observations

- There is a general consensus that surface diffusion (SD) is important in the case of radionuclides (RN) that sorb via cation exchange, CE (e.g. Sr, Cs, Ca, Ba).
- The extent of importance of SD depends on the chemical composition of the pore water that affects the distribution of the cations between free pore water and the interlayer or diffuse double layer (DDL) water.
- Surface diffusion is also important for transition metals that sorb via surface complexation (SC) and cation exchange (e.g. Co, Zn). The contribution of SD for these elements to the overall diffusion is less pronounced than in the case of pure CE-cations because only part of these elements are located in the DDL, depending on the chemical composition of the pore water.
- In the case of tetra- and trivalent actinides, and lanthanides, the importance of surface diffusion is not obvious. A limited dependency of diffusion on the ionic strength of the pore water can be observed. Due to the fact that tri- and tetravalent elements sorb mainly via SC, it can be assumed that SD is not an important issue here. However, it is not clear yet and further research is necessary here.
- A modelling approach including diffusion in a DDL seems to be justifiable (Appelo et al., 2010). However, the amount of data supporting such a model are still limited and a more extensive study on this item should be performed
- The transferability of sorption values obtained on dilute systems (crushed rock material, high liquid-to-solid ratio) to dense systems (intact rock, low water-to-rock ratio) is justified in the case of cations that sorb by CE (e.g. Sr, Cs). For other elements this is still not clear. It seems that the stronger the sorption, the larger the discrepancy between the two systems.
- The role of competing elements that are naturally present in rock material is not clarified and needs further attention.
- It is common practice to apply concepts and thermodynamics that exist for bulk water to situations of confined water (confined water exists in the narrow and charged pores in many clay rocks). This common practice is not justified at all. There is thus an urgent need to have a closer look to the chemistry and thermodynamics in confined pore water systems.

4. General conclusions regarding cation diffusion in clayrich compacted materials

The CatClay (Processes of cation migration in clayrocks) Project, a small-scale focused collaborative EURATOM project[2] had the overall objective of providing a scientifically well grounded answer to the following question: Can the migration of actinides and other strongly sorbing radionuclides in clayrock be predicted by coupling models of (i) their sorption equilibria on representative clay minerals and (ii) the diffusion-driven mass transport of radionuclide sorbed and dissolved species in compacted masses of these clay minerals?

Assuming that speciation models developed for cation sorption on clay materials (illite, clayrock) based on the results of measurements in dispersed material systems are valid for the corresponding compacted material, the Catclay project had the following specific objectives:

- Extending, consolidating and testing against experimental data, theoretical and numerical models for linking the thermodynamic states of *electrostatically interacting cations* (monovalent, bivalent, trivalent) relative to charged clay surfaces with their corresponding diffusion-driven mobility.
- Evaluation of whether or not the above model framework, after inclusion of appropriate representations of surface complexation reactions for Zn^{2+} , Co^{2+} and Eu^{3+} with illite edge sites (based on available literature data, results of specific measurements), is appropriate for modeling diffusion driven transport of these species. The target question is whether or not translational displacement of covalently bound cations is capable of contributing significantly to RN flux, as is the case for electrostatically interacting cations present in the diffuse double layer.
- Determination / modelling of the effects of clay material structure (mineral-porosity-discontinuities, spatial heterogeneity) at the mesoscopic scale (<mm) on diffusion driven transport of strongly sorbing cations.

Because most of the studied cations (Sr, Zn, Co, Eu) have very low transfer characteristics, a major part of the CatClay activities was devoted to developing and applying specific experimental methods needed for acquiring high precision, reliable data. In this sense, new setups have been designed for performing diffusion experiments that are no or less impacted by the presence of filters known to sorb the studied cations and to act as a resistance. For instance, filter-free diffusion techniques are now available for indurated rocks and, for illite, an original diffusion cell confining sample with membrane was successfully tested. Also improved mathematical models were developed which address more close the boundary conditions of the experiments. Moreover, the reliability of new analytical methods, such as the Laser-Induced Breakdown Spectroscopy (LIBS), for acquiring strongly-sorbing cation solid profiles on clay rocks was successfully demonstrated.

In the project, the sorption and the diffusion of Sr^{2+}, Co(II) and Zn(II) were studied with illite and clayrocks (Cox, OPA, BC). Diffusion of the cations in illite was studied under different chemical conditions (pH, ionic strength, carbonate concentrations), diffusion of the cations in the clayrocks was studied only for natural and adapted electrolyte concentrations. Decreasing diffusion rates with increasing background electrolyte concentration were unequivocally demonstrated for all cases. It is thus shown that so-called surface diffusion may be an important migration process also for these strongly sorbing radionuclides depending on the specific chemical conditions of the pore water and the speciation of these elements. Speciation of the element is important as species that interact via ion-exchange (electrostatically) are enriched in the DDL (and IL in case of swelling clays) but still mobile and because of this enrichment the flux increases in this part giving rise to the so-called surface diffusion effect. Species that interact with the surface via surface complexation are immobilised at the surface and will not result in an enhanced flux. Depending on the chemical conditions, both type of species may exist for a given radionuclide.

A modelling approach including diffusion in the diffuse double layer (DDL) promisingly succeeded in reproducing the experimental data under the various conditions. On the other hand, diffusion experiments with Eu(III), only performed through clayrocks, showed that the importance of surface diffusion would be very low. Indeed, no or a limited dependency of diffusion on the ionic strength of the pore water was observed. Finally, it was shown that the transferability of sorption values obtained on dilute systems (crushed rock material, high liquid-to-solid ratio) to dense systems (intact rock, low water-to-rock ratio) was mainly justified in the case of Sr2+, suggesting for the other cations, that the role of the competing elements naturally present in rock material and that can block the strong sites needs further attention.

Moreover, actual 3D geometrical pore size distributions of compacted illite, and in less extent, clayrock samples, were successfully determined by combining TEM and FIB-nt analyses on materials maintained in a water-like saturation state

[2] Grant n° FP7 249624 under Fission 2009 – 1.1.2: Actions in support of the safety case and license applications for geological repositories.

by means of an extensive impregnation step. The resolution limitation of FIB-nt previously described by many authors was resolved and allowed to threshold more than 70% of the total porosity of the sample in compacted illite. Therefore, based on this spatial distribution of pores, first numerical diffusion experiments were carried at the pore scale through virtual illite, enabling a better understanding of how transfer pathways are organized in the porous media.

The CatClay Project allowed a better understanding of the migration of strongly-sorbing tracers through low permeability 'clayrock' formations, increasing confidence in our capacity to demonstrate that the models used to predict radionuclide migration through these rocks are scientifically sound.

5. References

Aertsens, M., Wemaere, I., Wouters, L. (2004). Spatial variability of transport parameters in the Boom Clay. Appl. Clay Sci. 26, 37-45.

Albuquerque, R.Q., Calzaferri, G. (2007). Proton activity inside the channels of zeolite L. Chem. Eur. J. **13**, 8939-8952.

Altmann, S., Tournassat, C., Goutelard, F., Parneix, J-C., Gimmi, T., Maes, N. (2012). Diffusion driven transport in clayrock formations, Appl. Geochem. **27**, 463-478.

ANDRA 2005. Dossier 2005 argile – Tome – Evolution phénoménologique du stockage géologique. Rapport Andra no. C.RP.ADS.04.0025, France, http://www.andra.fr/download/site-principal/document/editions/182.pdf

Appelo, C.A.J., Wersin, P. (2007). Multicomponent diffusion modeling in clay systems with application to the diffusion of tritium, iodide, and sodium in Opalinus Clay. Environ. Sci. Technol. **41**, 5002-5007.

Appelo, C.A.J., Van Loon, L.R., Wersin, P. (2010). Multicomponent diffusion of a suite of tracers (HTO, Cl, Br, I, Na, Sr, Cs) of a single sample of Opalinus Clay, Geochim. Cosmochim Acta **74**,1201-1219.

Appelo, C.A.J., 2013. Analytical solutions for calculating the anion porosity and effective diffusion coefficients in illite. Deliverable 1-7 EC CatClay project, www.catclay.org.

Baes, C.F. and Mesmer, R.E. (1976). The Hydrolysis of Cations. John Wiley & Sons Inc., New York.

Baeyens, B., Bradbury, M. H. (1997). A mechanistic description of Ni and Zn sorption on Na-montmorillonite Part I: Titration and sorption measurements. J. Contam. Hydrology, **27**, 199-222.

Baeyens, B., Bradbury, M.H. (2004). Cation exchange capacity measurements on illite using the sodium and cesium isotope dilution technique: Effects of the index cation, electrolyte concentration and competition: Modeling. Clay Clay Miner. **52**, 421-431.

Bazer-Bachi, F., Tevissen, E., Descostes, M., Grenut, B., Meier, P., Simonnot, M.-O., Sardin, M. (2006). Characterization of iodide retention on Callovo-Oxfordian argillites and its influence on iodide migration. Phys. Chem. Earth **31**, 517-522.

Bazer-Bachi, F., Descostes, M., Tevissen, E., Meier, P., Grenut, B., Simonnot, M.-O., Sardin, M. (2007). Characterization of sulphate sorption on Callovo-Oxfordian argillites by batch, column and through-diffusion experiments. Phys. Chem. Earth **32**, 552-558.

Bethke, C.M. (2008). Geochemical and Biogeochemical Reaction Modeling. Cambridge University Press,Cambridge, UK.

Bossart, P. (1998). Basic geochemical data from water sampling (WS) experiments, Phases 1 and 2. Technical Report TR97-02, Mont Terri, St. Ursanne, Switzerland.

Bourg, I.C., Bourg, A.C.M., Sposito, G. (2003). Modelling diffusion and adsorption in compacted bentonite: a critical review. J. Contam. Hydrol. **61**, 293-302.

Bourg, I., Sposito, G., Bourg, A. (2006). Tracer diffusion in compacted, water-saturated bentonite. Clay Clay Miner. **54**(3), 363–374.

Bradbury, M.H., Baeyens, B. (1997). A mechanistic description of Ni and Zn sorption on Na-montmorillonite Part II: modelling. J. Contam. Hydrol. **27**, 223-248.

Bradbury, M.H., Baeyens, B. (1998). Modeling the sorption of Zn and Ni on Ca-montmorillonite. Geochim. Cosmochim. Acta **63**, 325-336.

Bradbury, M.H., Baeyens, B. (2000). A generalised sorption model for the concentration dependent uptake of caesium by argillaceous rocks. J. Contam. Hydrol. 42, 141–163.

Bradbury, M.H., Baeyens, B. (2005). Experimental and Modelling Investigations on Na-illite: Acid-Base Behaviour and the Sorption of Strontium, Nickel, Europium and Uranyl. PSI Bericht Nr. 05-02, Paul Scherrer Institut, Villigen PSI, Switzerland.

Bradbury, M.H., Baeyens, B. (2005a). Modelling the sorption of Mn(II), Co(II), Ni(II), Zn(II), Cd(II), Eu(III), Am(III), Sn(IV), Th(IV), Np(V) and U(VI) on montmorillonite: Linear free energy relationships and estimates of surface binding constants for some selected heavy metals and actinides. Geochim. Cosmochim. Acta **69**, 875-892.

Bradbury, M.H., Baeyens, B., Geckeis H, Rabung T., (2005). Sorption of Eu(III)/Cm(III) on Ca-montmorillonite and Na-illite. Part 2: Surface complexation modelling. Geochim. Cosmochim. Acta **69**, 5403-5412.

Bradbury, M.H., Baeyens, B. (2009a). Sorption modelling on illite Part I: Titration measurements and the sorption of Ni, Co, Eu and Sn. Geochim. Cosmochim. Acta **73**, 990–1003.

Bradbury, M.H., Baeyens, B. (2009b). Sorption modelling on illite Part II: Actinide sorption and free energy relationships. Geochim. Cosmochim. Acta **73**, 1004–1013.

Bradbury, M.H., Baeyens, B. (2011). Predictive sorption modelling of Ni(II), Co(II), Eu(III), Th(IV) and U(VI) on MX-80 bentonite and Opalinus Clay: a "bottom-up" approach. Appl. Clay Sci. **52**, 27-33.

Bron, F., Jeulin, F. (2004). Modelling a food microstructure by random sets, Image Anal. Stereol. **23**, 33-44.

Brouwer, E., Baeyens, B., Maes, A., Cremers, A., 1983. Cesium and rubidium ion equilibria in illite clay. Journal of Physical Chemistry 87, 1213-1219.

Bruggeman, C., Maes, N., Aertsens, M., De Cannière, P. (2014). Tritiated water retention and migration behaviour in Boom Clay: SFC1 level 5 report: First full Draft – status 2009. Scientific Report SCK·CEN-ER-248, SCK·CEN, Mol, Belgium.

Brunauer, S., Emmett, P.H., Teller, E. (1938). Adsorption of gases in multimolecular layers, J. Am. Chem. Soc. **60**(2), 10.

Churakov, S. Gimmi T. (2011). Up-Scaling of Molecular Diffusion Coefficients in Clays : A Two-Step Approach. J. Phys. Chem. C 115, 6703-6714.

Churakov S. V., Daehn R. (2012). Zinc Adsorption on Clays Inferred from Atomistic Simulations and EXAFS Spectroscopy. Environ. Science. Technol. **46**, 5713−5719.

Cook, R. A., and K. C. Hover (1999). Mercury porosimetry of hardened cement pastes. Cement Concrete Res. **29**, 933-943.

Crank, J. (1975). The Mathematics of Diffusion. Oxford Univ. Press, Oxford, UK.

Crans, D.C., Levinger, N.E. (2012). The conundrum of pH in water nanodroplets: sensing pH in reverse micelle water pools. Accounts Chem. Res. **45**, 1637-1645.

Dähn, R., Scheidegger, A.M., Manceau, A., Schlegel, M., Baeyens, B., Bradbury, M.H., Chateigner, D.L. (2003). Structural evidence for the sorption of Ni(II) atoms on the edges of montmorillonite clay minerals: A polarized X-ray absorption fine structure study. Geochim. Cosmochim Acta **37**,1-15.

Davis, J.A., Kent, D.B. (1990). Surface complexation modeling in aqueous geochemistry, Chapitre 5 dans Mineral-water interface geochemistry, vol. 23 Reviews in Mineralogy, ed. M. Hochella et A White.

De Craen, M., Wang, L., Van Geet, M., Moors, H. (2004). Geochemistry of Boom Clay pore water at the Mol site. Scientific Report SCK·CEN-BLG-990, SCK·CEN, Mol, Belgium.

Delay, F., and Porel, G. (2003). Inverse modelling in the time domain for solving diffusion in a heterogeneous rock matrix, Geophys. Res. Lett. **30**, 1147.

Delay, F., Sardini, P., Porel, G. (2002). Modelling diffusion in a heterogeneous matrix with a time domain Lagrangian method and an inversion procedure, C. R. Geosci., **334**, 967–973.

Delerue, J. F., Perrier, E., Yu, Z.Y., Velde, B. (1999). New algorithms in 3D image analysis and their application to the measurment of a spatialized pore size distribution in soils. Phys. Chem. Earth **24**, 639-644.

Descostes, M., Tevissen, E. (2004). Definition of an equilibration protocol for batch experiments on Callovo-Oxfordian argillite. Earth. 29, 79-90.

Descostes, M., Blin, V., Bazer-Bachi, F., Meier, P., Grenut, B., Radwan, J., Schlegel, M.L., Buschaert, S., Coelho, D., Tevissen, E. (2008). Diffusion of anionic species in Callovo-Oxfordian argillites and Oxfordian limestones (Meuse/Haute-Marne, France). Appl. Geochem. **23**, 655-677.

Diakonov, I.I., Ragnarsdottir, K.V., Tagirov, B.R. (1998). Standard thermodynamic properties and heat capacity equations of rare earth hydroxides:: II. *Ce(III)-, Pr-, Sm-, Eu(III)-, Gd-, Tb-, Dy-, Ho-, Er-, Tm-, Yb-, and Y-hydroxides.* Comparison of thermochemical and solubility data. Chem. Geol. **151**, 327-347.

Diaz, N. (2009.) Modélisation prédictive de la migration des anions par description de la microstructure de la roche : application à l'argilite du Callovo-Oxfordian. PhD thesis, Univ.Paris VI.

Djeran-Maigre, I., Tessier, D., Grunberger, D., Velde, B., Vasseur, G. (1998). Evolution of microstructures and of macroscopic properties of some clays during experimental compaction. Mar. Pet. Geol. **15**, 109-128.

Drugan, W. J., Willis, J.R. (1996). A micromechanics-based nonlocal constitutive equation and estimates of representative volume element size for elastic composites. J. Mech. Phys. Solids **44**, 497-524.

Dzombak, D.A., Morel, F.M.M. (1990). Surface complexation modeling. Hydrous ferric oxide, Wiley, New York.

Fanghanel, T., Weger, H. T., Konnecke, T., Neck, V., Paviet-Hartmann, P. Steinle, E., Kim, J. I. (1998). Thermodynamics of Cm(III) in concentrated electrolyte solutions. Carbonate complexation at constant ionic strength (1 m NaCl). Radiochim. Acta **82**, 47-53.

Frasca, B., Savoye, S., Wittebroodt, C., Leupin, O.X, Descostes, .M., Grenut, B., Etep-Batanken, J., Michelot, J.-L. (2012). Influence of redox conditions on iodide migration through a deep clay formation (Toarcian argillaceous rock, Tournemire, France). Applied. Geochemistry, 27, 2453–2462.

Fripiat, J.J. (1979). Diffusion of HTO, 36Cl-, and 125I- in Opalinus Clay samples from Mont Terri: Effect of confining pressure. Data Handbook for Clay Minerals and Others Non-metallic Minerals, London.

Gabis, V. (1963). Etude minéralogique et géochimique de la série sédimentaire oligocène du Vela. B. Soc. Fr. Mineral CR **86**, 315-354.

Gaboreau, S., Prêt, D., Tinseau, E., Claret, F., Pellegrini, D., Stammose, D. (2011). 15 years of in situ cement-argillite interaction from Tournemire URL: Characterisation of the multi-scale spatial heterogeneities of pore space evolution. Appl. Geochem. 26, 2159-2171.

Gaboreau, S., Lerouge, C., Dewonck, S, Linard, Y., Bourbon, X., Fialips, C.I., Mazurier, D., Prêt, D., Borschneck, D., Montouillout, V., Gaucher, E.C., Claret, F. (2012), In-situ Interaction of Cement Paste and Shotcrete with Claystones in a Deep Disposal Context. Am. J. Sci. **312**, 314-356.

Galli, M., Cugnoni, J., Botsis, J. (2012). Numerical and statistical estimates of the representative volume element of elastoplastic random composites. Eur. J. Mech. A-Solid **33**, 31-38.

Gaucher E., Robelin C., Matray J.-M., Negrel G., Gros Y., Heitz J.-F., Vinsot A., Rebours H., Cassagnanere A., Bouchet A. (2004). ANDRA underground research laboratory: interpretation of the mineralogical and geochemical data acquired in the Callovian-Oxfordian formation by investigative drilling Earth 29, 55-77.

Gimmi, T., Kosakowski, G. (2011). How mobile are sorbed cations in clays and clay rocks? Environ. Sci. Technol. **45**, 1443-1449.

Glaus, M.A., Baeyens, B., Bradbury, M.H., Jakob, A., Van Loon, L.R., Yaroshchuk, A. (2007). Diffusion of $^{22}Na^{+}$ and $^{85}Sr^{2+}$ in montmorillonite: Evidence for interlayer diffusion being the dominant pathway at high compaction. Environ. Sci. Technol. **41**, 478-485.

Glaus, M. A., Frick, S., Rosse, Van Loon, L.R., R. (2010). Comparative study of HTO, $^{22}Na^{+}$ and ^{36}Cl-36^{-} in compacted kaolinite, illite and montmorillonite, Geochim. Cosmochim. Acta, **74**, 1999-2010.

Glaus, M.A., Frick, S., Rossé, R., Van Loon, L. R. (2010). Comparative study of tracer diffusion of HTO, $^{22}Na^{+}$ and $^{36}Cl^{-}$ in compacted kaolinite, illite and montmorillonite. Geochim. Cosmochim. Acta, **74**, 1999-2010.

Glaus, M.A., Frick, S., Jakob, A., Diffusion of moderately and strongly sorbing radionuclides in compacted illite, 2012: Deliverable 2-1 EC CatClay project, www.catclay.org.

Glaus, M.A., Birgersson, M., Karnland, O., Van Loon, L.R. (2013). Seeming Steady-State Uphill Diffusion of $^{22}Na^{+}$ in Compacted Montmorillonite. Environ. Sci.Technol. **47**, 11522-11527.

Glaus, M.A., Aertsens, M., Maes, N., Van Laer, L. & Van Loon, L. (in preparation). Local gradients as a possible source for biased results in through-diffusion experiments. A practical and theoretical approach using $^{85}Sr^{2+}$ diffusion in compacted illite as a case study.

Grambow B., Fattahi M., Montavon G., Moisan C., Giffaut E. (2006). Sorption of Cs, Ni, Pb, Eu(III), Am(III), Cm, Ac(III) Tc(IV), Th, Zr and U(IV) on MX80 bentonite: an experimental approach to asses model uncertainty. Radiochim. Acta **94**, 627-636.

Gu, X., Evans, L.J. (2007). Modelling the adsorption of Cd(II), Cu(II), Ni(II), Pb(II), and Zn(II) onto Fithian illite. J. Colloid Interf. Sci. **307**, 317-325.

Guillaumont, R., Fanghänel, T., Fuger, J., Grenthe, I., Neck, V., Palmer, D.A., Rand, M.H. (2003). Update on the Chemical Thermodynamics of Uranium, Neptunium, Plutonium, Americium and Technetium. Chemical Thermodynamics 5, NEA-OECD. Elsevier, Amsterdam, The Netherlands.

Hassan, M. S., F. Villieras, F. Gaboriaud, and A. Razafitianamaharavo (2006). AFM and low-pressure argon adsorption analysis of geometrical properties of phyllosilicates, J. Colloid Interf. Sci. **296**, 614-623.

Henrion, P.N., Put, M.J., Van Gompel, M. (1991). The influence of compaction on the diffusion of non-sorbed species in Boom Clay. Radioactive Waste Management and the Nuclear Fuel Cycle, **16**, 1-14 .

Honty, M., De Craen, M. (2012). Boom Clay mineralogy - qualitative and quantitative aspects. Status 2012. *Scientific Report SCK·CEN-ER-194, SCK·CEN, Mol, Belgium*.

http://en.wikipedia.org/wiki/Surface_diffusion

Jakob, A., Sarott, F.-A., Spieler, P. (1999). Diffusion and sorption on hardened cement pastes – experiments and modelling results. PSI Bericht 99-05, Paul Scherrer Institut,Villigen, Switzerland. http://www.nagra.ch/documents/database/dokumente/$default/Default%20Folder/Publikationen/NTBs%201994-2000/e_ntb99-06.pdf

Jakob, A., Pfingsten, W., Van Loon, L.R. (2009). Effects of sorption competition on caesium diffusion through compacted argillaceous rock. Geochim. Cosmochim. Acta. **73,** 2441-2456.

Jenkins, R. G., Rao, M.B. (1984). The Effect of Elliptical Pores on Mercury Porosimetry Results. Powder Technol, **38**, 177-180.

Jensenf M. P., Choppin, G.R. (1996). Complexation of Europium(III) by Aqueous Orthosilicic Acid. Radiochim. Acta **72**, 143-150.

Joseph, C., Van Loon, L.R., Jakob, A., Steudtner, R., Schmeide, K., Sachs, S., Bernhard, G. (2013). Diffusion of U(VI) in Opalinus Clay: Influence of temperature and humic acid. Geochim. Cosmochim. Acta **109**, 74-89.

Kalis, E.J.J., Weng, L., Temminghoff, E.J.M., van Riemsdijk, W.H. (2007). Measuring Free Metal Ion Concentrations in Multicomponent Solutions Using the Donnan Membrane Technique. Anal. Chem. **79**, 1555-1563.

Kato, H., Muroi, M., Yamada, N., Ishida, H., Sato, H. (1995). Estimation of Effective Diffusivity in Compacted Bentonite. Mat. Res. Soc. Symp. Proc. **18**, 277-284.

Keller, L. M., Holzer, L., Wepf, R., Gasser, P., Munch, B., Marschall, P. (2011), On the application of focused ion beam nanotomography in characterizing the 3D pore space geometry of Opalinus Clay. Phys. Chem. Earth **36**, 1539-1544.

Keller, L. M., Schuetz, P., Erni, R., Rossell, M.D., Lucas, F., Gasser, P., Holzer, L. (2013), Characterization of multi-scale microstructural features in Opalinus Clay. Micropor. Mesopor. Mat. **170**, 83-94,

Kimura, T., Choppin, G. R. (1994). Luminescence Study on Determination of the Hydration Number of Cm(III). J. Alloy. Compd. **213**, 313-317.

Kimura, T., Choppin, G. R., Kato, Y., Yoshida, Z. (1996). Determination of the hydration number of Cm(III) in various aqueous solutions. Radiochim. Acta **72**, 61-64.

Kozaki T., Fujishima A., Sato S, Ohashi H. (1996). Activation energy for cesium diffusion in compacted sodium montmorillonite. J. Nucl. Sci. Technol. **33**, 522-524.

Kozaki T., Sato H., Fujishima A., Saito N., Sato S, Ohashi H. (1997). Effect of dry density on activation energy for diffusion of strontium in compacted sodium montmorillonite. Mat. Res. Symp. Proc. **465**, 893-900.

Kozaki T., Fujishima A., Sato S., Ohashi H. (1998). Self-diffusion of sodium ions in compacted sodium montmorillonite. Nucl. Technol. **121**, 63-69.

Kraepiel A.M.L., Keller K., Morel F.M.M. (1999). A model for metal adsorption on montmorillonite. J. Colloid Interf. Sci. **210**, 43-54.

Li, Y.-H., Gregory, S. (1974). Diffusion of ions in sea water and in deep-sea sediments. Geochim. Cosmochim. Acta **38**, 703-74.

Luo, Y.-R., Byrne, R. (2001). Yttrium and Rare Earth Element Complexation by Chloride Ions at 25˚C. J. Solution Chem. 2001. **30**, 837-845.

Luo, Y.-R., Byrne, R. (2007). The Influence of Ionic Strength on Yttrium and Rare Earth Element Complexation by Fluoride Ions in $NaClO_4$, $NaNO_3$ and NaCl Solutions at 25 °C. J. Solution Chem., **36**, 673-689.

Maes, A., Peigneur, P., Cremers, A. (1978). Stability of metal uncharged ligand complexes in ion exchangers. Part 2.-The Copper+Ethylenediamine Complex in Montmorillonite and Sulphoric Acid Resin. J. Chem. Soc. Farad. T1 74, 182-189.

Maes, A., Cremers, A. (1979). Stability of metal uncharged ligand complexes in ion exchangers. Part 4.-Hydration effects and stability changes of copper-ethylenediamine complexes in montmorillonite. J. Chem. Soc. Farad. T1 **75**, 513-524.

Maes, A., Cremers, A. 1986. Highly selective ion exchange in clay minerals and zeolites. In: Davies, JA, Hayes, KF, editors. Geochemical processes at mineral surfaces. Washington, DC. Am. Chem. Soc. 254-295.

Maes, N., Salah, S., Jacques, D., Aertsens, M., Van Gompel, M., De Cannière, P., Velitchkova, N., (2008). Retention of Cs in Boom Clay: Comparison of data from batch sorption tests and diffusion experiments on intact clay cores. Phys. Chem. Earth **33**, S149-S155.

Maes, N., Aertsens, M., Salah, S., Jacques, D., Van Gompel, M. (2009). Cs, Sr and Am retention on argillaceous host rocks: comparison of data from batch sorption tests and diffuison experiments. Scientific Report SCK·CEN-ER-98, SCK·CEN, Mol, Belgium.

Maes, N., Salah, S., Bruggeman, C., Aertsens, M., Martens, E., Van Laer, L. (2012). Strontium retention and migration behaviour in Boom Clay. Scientific Report SCK·CEN-ER-197, SCK·CEN, Mol, Belgium.

Majone, M., Papini, M.P., Rolle, E. (1998). Influence of Metal Speciation in Landfill Leachates on Kaolinite Sorption. Water Res. **32**, 882-890.

Marang, L., Reiller, P., Pepe, M., Benedetti, M.F. (2006). Donnan Membrane Approach: From Equilibrium to Dynamic Speciation. Environ. Sci. Technol. **40**, 5496-5501.

Marry V., Turq P., Cartailler T., Levesque D. (2002). Microscopic simulation for structure and dynamics of water and counterions in a monohydrated montmorillonite. J. Chem. Phys. **117**, 3454–3463.

Melkior, T., Yahiaoui, S., Motellier, S., Thoby, D., Tevissen, E. (2005). Cesium sorption and diffusion in Bure mudrock samples. Appl. Clay Sci. **29**, 172-186.

Melkior, T., Yahiaoui, S., Thoby, D., Motellier, S., Barthès, V. (2007). Diffusion coefficients of alkaline cations in Bure mudrock. Phys. Chem. Earth **32**, 453-462.

Menut D., Descostes M., Meier P., Radwan J., Mauchien P., Poinssot C. (2006). Europium migration in argillaceous rocks: On the use of micro Laser-Induced Breakdown Spectroscopy (microLIBS) as a microanalysis tool, *Materials Research Society Symposium Proceedings* 932, 913-918.

Montavon, G., Alhajji, E., Brambow, B. (2006). Study of the interaction of Ni^{2+} and Cs^{+} on MX-80 bentonite; effect of compaction using the "capillary method". *Environ. Sci. Technol.* **40**, 4672-4679.

Molera, M., Eriksen, T. (2002). Diffusion of $^{22}Na+$, $^{85}Sr2+$, $^{134}Cs+$ and $^{57}Co2+$ in bentonite clay compacted to different densities: experiments and modeling. Radiochimica Acta 90, 753–760.

Moridis, G. J. (1998). A set of semi-analytical solutions for parameter estimation in diffusion cell experiments. Report LBNL-41857, Lawrence Berkeley National Laboratory, Berkeley, California.

Muurinen, A., Penttillä-Hiltunen, P., Uusheimo, K. (1989). Diffusion of chloride and uranium in compacted sodium bentonite. Mat. Res. Soc. Symp. Proc. 127, 743-748. Materials Research Society.

Nagra (2002b). Projekt Opalinuston. Synthese der geowissenschaftlichen Untersuchungsergebnisse. Nagra Technical Report NTB 02-03, Wettingen, Switzerland.

Neck, V., Altmaier, M., Lützenkirchen, J., Korthaus, E., Fanghänel, T. (2007). A comprehensive thermodynamic model for the solubility and hydrolysis of Nd(III) and Am(III) in dilute to concentrated NaCl, $MgCl_2$ and $CaCl_2$ solutions. Book of Abstracts of the Migration'07 conference, p. 60.

Ochs M., Boonekamp M., Wanner H., Sato H., Yui M. (1998). A quantitative model for ion diffusion in compacted bentonite. Radiochim. Acta **82**, 437-443

Ochs, M., Lothenbach, B., Wanner, H., Sato, H., Yui, M. (2001). An integrated sorption-diffusion model for the calculation of consistent distribution and diffusion coefficients in compacted bentonite. J. Contam. Hydrol. **47**, 283-296.

OECD (2012) Thermodynamic sorption modeling in support of radioactive waste disposal safety cases. NEA Sorption project Phase III Report. ISBN978.92.64.17781.9. 151p

Parkhurst, D.L., Appelo, C.A.J. (2013). Description of input and examples for PHREEQC version 3 - A computer program for speciation, batch-reaction, one-dimensional transport, and inverse geochemical calculations. U.S. Geological Survey Techniques and Methods, book 6, chap. A43, 497 p., http://pubs.usgs.gov/tm/06/a43/.

Pearson, F.J. (1998). Opalinus Clay Experimental Water: A1 Type, Version 980318. Technical Report TM-44-98-07, Paul Scherrer Institut, Villigen, Switzerland.

Perrin, D.D., Dempsey, B. (1974). Buffers for pH and Metal Ion Control. Chapman and Hall, London.

Plyasunova, N.V., Zhang, Y., Muhammed, M. (1998). Critical evaluation of thermodynamics of complex formation of metal ions in aqueous solutions. V. hydrolysis and hydroxo-complexes of Co^{2+} at 298.15 K. Hydrometallurgy **48**, 153-169.

Poinssot, C., Baeyens, B.,Bradbury, M.H. (1999). Experimental and modelling studies of caesium sorption on illite. Geochim. Cosmochim. Acta **63**, 3217-3227.

Poinssot, C., Baeyens, B.,Bradbury, M.H. (1999). Experimental studies of Cs, Sr, Ni and Eu sorption on Na-illite and the modelling of Cs sorption. PSI Bericht Nr. 99-06, Paul Scherrer Institut, Villigen, Switzerland.

Prêt, D. (2003). Nouvelles méthodes quantitatives de cartographie de la minéralogie et de la porosité dans les matériaux argileux: application aux bentonites compactées des barrières ouvragées. Université de Poitiers, France, Poitiers, 257 p.

Prêt, D., P. Sardini, D. Beaufort, R. Zellagui, and S. Sammartino (2004). Porosity distribution in a clay gouge by image processing of C-14-Polymethylmethacrylate (C-14-PMMA) autoradiographs: Case study of the fault of St. Julien (Basin of Lodeve, France). Appl. Clay Sci. **27**, 107-118.

Prêt, D., S. Sammartino, D. Beaufort, M. Fialin, P. Sardini, P. Cosenza, and A. Meunier (2010). A new method for quantitative petrography based on image processing of chemical element maps: Part II. Semi-quantitative porosity maps superimposed on mineral maps. Am. Mineral. **95**, 1389-1398.

Rabung, T., Pierret, M. C., Bauer, A., Geckeis, H., Bradbury, M. H., Baeyens, B. (2005). Sorption of Eu(III)/Cm(III) on Ca-montmorillonite and Na-illite. Part 1: Batch sorption and time-resolved laser fluorescence spectroscopy experiments. Geochim. Cosmochim. Acta **69**, 5393-5402.

Rajec, P., Macasek, F., Misaelides, P. (1999), Sorption of heavy metals and radionuclides on zeolites and clays, NATO. Adv. Sci. I E-App. **362**, 353-363.

Remy, J. C., Orsini, L. (1976). Utilisation du chlorure de cobaltihexamine pour la détermination simultanée de la capacité d'échange et des bases échangeables dans les sols, Sciences du sol **4**, 269-275.

Robinet JC. And Gaboreau S. (2011) Rapport ANR SIMISOL (Tâche 6.2) Caractérisations multi-échelles de l'illite re-compactée à partir d'observations au Microscope Electronique à Transmission.

Robinet JC. (2012) Caractérisations multi-échelles de l'illite re-compactée à partir d'observations au Microscope Electronique à Transmission, Rapport ANR SIMISOL (Tâche 6.2), Rapport Andra n°CRPASTR120022.

Robinet, J. C., Sardini, P., Coelho, D., Parneix, J.C., Pret, D., Sammartino, S., Boller, E., Altmann, S. (2012). Effects of mineral distribution at mesoscopic scale on solute diffusion in a clay-rich rock: Example of the Callovo-Oxfordian mudstone (Bure, France). Water Resour. Res. *48*, w05554.

Rotenberg B., Marry V., Dufreche JF., Giffaut E., Turq P. (2007). A multi-scale approach to ion diffusion in clays: building a two-state diffusion-reaction scheme from microscopic dynamics. J. Colloid Interf. Sci. **309**, 289-295.

Rotenberg B., Pagonabarraga I., Frenkel D. (2008). Dispersion of charged tracers in charged porous media. Europhys. Lett. **83**, 34004.

Rotenberg, B., Pagonabarraga, I., Frenkel, D. (2010). Coarse-grained simulations of charge, current and flow in heterogeneous media. Faraday discuss. **144**, 223-243.

Sammartino, S., M. Siitari-Kauppi, A. Meunier, P. Sardini, A. Bouchet, and E. Tevissen (2002). An imaging method for the porosity of sedimentary rocks: Adjustment of the PMMA method - Example of a characterization of a calcareous shale. J. Sediment. Res. **72**, 937-943.

Sardini, P., El Albani, A., Pret, D., Gaboreau, S., Siitari-Kauppi, M., Beaufort, D. (2009). Mapping and Quantifying the Clay Aggregate Microporosity in Medium- to Coarse-Grained Sandstones Using the (14)C-PMMA Method, J. Sediment. Res. **79**, 584-592.

Sato H., Ashida T., Kohara Y., Yui M., Sasaki N. (1992). Effect of dry density on diffusion of some radionuclides in compacted sodium bentonite. J. Nucl. Sci. Technol. **29**, 873-882.

Savoye, S., Page, J., Puente, C., Imbert, C., Coelho, D. (2010). A new experimental approach for studying diffusion through an intact and unsaturated medium: A case study with Callovo-Oxfordian argillite. Environ. Sci. Technol. 44, 3698-3704.

Savoye S., Beaucaire C., Fayette A., Herbette M., Coelho D. (2012a). Mobility of Cesium through the Callovo-Oxfordian Claystones under Partially Saturated Conditions. Sci Techno. 46, 2633-2641.

Savoye, S., Frasca, B., Grenut, B., Fayette, A., (2012b) How mobile is iodide in the Callovo–Oxfordian claystones underexperimental conditions close to the in situ ones? Hydrol., 142-143, 82–92

Savoye, S., Lacour, J.L., Fayette, A., Beaucaire, C. (2013) Mobility of zinc through the Callovo-Oxfordian Earth Plane. Sci. 7, 774-777.

Schlegel, M.L., Charlet, L., Manceau, A. (1999a). Sorption of metal ions on clay minerals. II. Mechanism of Co sorption on hectorite at high and low ionic strength and impact on the sorbent stability. J. Colloid Interf. Sci. **220**, 392-405.

Schlegel, M.L., Manceau, A., Chateigner, D. L., Charlet, L. (1999b). Sorption of metal ions on clay minerals : I. Polarized EXAFS evidence for the adsorption of Co on the edges of hectorite particles. J. Colloid Interf. Sci. **215**, 140-158.

Sethian, J. A. (1999). Level Set Methods and Fast Marching Methods, Cambridge.

Shackelford, C.D., 1991. Laboratory diffusion testing for waste disposal – a review. J. Contam. Hydrol. **7**, 177-217.

Soltermann, D., Marques Fernandes, M., Baeyens, B., Miehé-Brendlé J., Dähn, R. (2014). Competitive Fe(II)–Zn(II) Uptake on a Synthetic Montmorillonite. Environ. Sci. Technol. **48**, 190-198.

Spahiu, K., Bruno, J. (1995). A selected thermodynamic database for REE to be used in HLNW performance assessment exercises. SKB Technical Report TR 95-35.

Sposito, G., Prost, R.(1982). Structure of water adsorbed on smectites. Chem. Rev. **82**, 553-573.

Stumm, W., Kummert, R., Sigg, L. (1980). A ligand exchange model for the adsorption of inorganic and organic ligands at hydrous oxide interfaces. Croat. Chem. Acta **53**, 291-312.

Tertre, E., Beaucaire, C. Coreau, N. Juery, A. (2009). Modelling Zn(II) sorption onto clayey sediments using a multi-site ion-exchange model. Appl. Geochem. 24 (2009) 1852.

Thakur, P., Singh, D.K., Choppin, G.R. (2007). Polymerization study of o-Si(OH)4 and complexation with Am(III), Eu(III) and Cm(III). Inorg. Chim. Acta **360**, 3705-3711.

Torstenfelt, B. (1986). Migration of the actinides thorium, protactinium, uranium, neptunium, plutonium and americium in clay. Radiochim. Acta 39, 105-112.

Tournassat, C., Appelo, C.A.J. (2011). Modelling approaches for anion-exclusion in compacted na-bentonite. Geochim. Cosmochim. Acta 75, 3698–3710.

Tournassat, C., Grangeon, S., Leroy, P., Giffaut, E. (2013). Modeling specific pH dependent sorption of divalent metals on montmorillonite surfaces. A review of pitfalls, recent achievements and current challenges. Am. J. Sci. **313**, 395-451.

Van Brackel, F., Heertjes, P.M. (1974). Analysis of diffusion in macroporous media in terms of a porosity, a tortuosity and a constrictivity factor. Int. J. Heat Mass Tran. **17**, 1093-1103.

Van Laer, L., Bruggeman, C., Maes, N., Aertsens, M. (2014). Diffusion of sorbing tracers in compacted clay. Deliverable 2-3 EC CatClay project, www.catclay.org.

Van Loon, L.R., Soler, J.M., Bradbury, M. H. (2003a).J. Contam. Hydrol. **61**, 73-83.

Van Loon, L.R., Soler, J., Jakob, A., Bradbury, M.H. (2003b). Effect of confining pressure on the diffusion of HTO, $^{36}Cl^-$ and $^{125}I^-$ in a layered argillaceous rock (Opalinus Clay): diffusion perpendicular to the fabric. Appl. Geochem. **18**, 1653-1662.

Van Loon, L.R., Baeyens, B., Bradbury, M.H. (2005). Diffusion and Retention of Sodium and Strontium in Opalinus Clay: Comparison of Sorption Data from Batch Sorption and Diffusion Measurements, and Geochemical Calculations. Appl. Geochem. **20**, 2351-2363.

Van Loon, L.R., Eikenberg, J. (2005). A High Resolution Abrasive Method for Determining Diffusion Profiles of Strongly Sorbing Radionuclides in Dense Argillaceous Rocks. Appl. Radiat. Isotopes. **63**, 11-21.

Van Loon, L.R., Glaus, M. A., Müller, W. (2007). Anion exclusion effects in compacted bentonites: Towards a better understanding of anion diffusion. Appl.Geochem. **22**, 2536-2552.

Van Loon, L.R., Baeyens, B., Bradbury, M.H. (2009). The sorption behaviour of caesium on Opalinus Clay: a comparison between intact and crushed material. Appl. Geochem. **24**, 999-1004.

Van Loon, L.R. (2013). Effective diffusion coefficients and porosity values for argillaceous rocks and bentonite: measured and estimated values for the provisional safety analyes for SGT-E2. Nagra Technical Report NTB 12-03, Nagra, Wettingen, Switzerland.

Van Loon, L.R., Müller, W. (2014). A modified version of the combined in-diffusion/abrasive peeling technique for measuring diffusion of strongly sorbing radionuclides in argillaceous rocks: a test study for diffusion of caesium in Opalinus Clay. Appl. Radiat. Isotopes **90**, 197-202.

Van Olphen, H., Vicente, J., Daurelle, J.V., Brossard, G., Blom, A., Douteur, A., Delmotte, Y., Brun, E. (2012). Impact of different confluent fluid stream viscosities on interconnected porous static mixer device. Chem. Eng. Sci. **72**, 172-178.

Van Schaik, J.C., Kemper, W.D., Olsen, S.R., 1966. Contribution of adsorbed cations to diffusion in clay-water systems. Soil Sci. Soc. Am. Proc. 30, 17–22.

Vincent, L., Soille, P. (1991). Watersheds in digital spaces: an efficient algorithm based on immersion simulations. Patt. Anal. Mach. Intell. **13**, 583-598.

Wang, Y., Bryan, C., Xu, H., Pohl, Ph., Yang, Y., Brinker, C.J. (2002). Interface chemistry of nanostructured materials: ion adsoption on mesoporous alumina. J. Colloid Interf. Sci. **254**, 23-30.

Wang, X.K., Rabung, T., Geckeis, H., Panak, P. J., Klenze, R., Fanghanel, T. (2004). Effect of humic acid on the sorption of Cm(III) onto gamma-Al2O3 studied by the time-resolved laser fluorescence spectroscopy. Radiochim. Acta **92**, 691-695.

Wang, L. (2011). A thermochemical data base for phenomenological and safety assessment studies for disposal of radioactive waste in Belgium – Data compilation strategy. SCK·CEN-ER-121.

Washburn, E. W. (1921). The dynamic of capillary flow. Phys. Rev. **17**, 273-283.

Wersin, P., Soler, J. M., Van Loon, L., Eikenberg, J., Baeyens, B., Grolimund, D., Gimmi, T., Dewonck, S. (2008). Diffusion of HTO, Br^-, I^-, Cs^+, $^{85}Sr^{2+}$ and $^{60}Co^{2+}$ in a clay formation: Results and modelling from an in situ experiment in Opalinus Clay. Appl.Geochem. **23**, 678-691.

Woodcock, C. E., Strahler, A. H., Jupp, D.L.B. (1988). The use of variograms in remoute sensing. 2. Real digital images. Remote Sens. Environ. **25**, 349-379.

Wu, T., Amayri, J., Drebert, J., Van Loon, L.R., Reich, T. (2009). Neptunium(V) Sorption and Diffusion in Opalinus Clay. Environ. Sci. Technol. **43**, 6567-6571.

Xu, K., Daian, J.F., Quenard, D. (1997). Multiscale structures to describe porous media .1. Theoretical background and invasion by fluids. Transport Porous Med. **26**, 51-73.

Annex 1: Experimental details diffusion-experiments of each institute

HTO and Cl^- diffusion in Na-IdP at KIT-INE

The experiments at KIT-INE were performed PEEK diffusion cells, with physical dimensions similar to the ones used at PSI-LES and described in Van Loon et al. (2003). In contrast to the latter, stainless steel filters were replaced by perforated PEEK plates and membrane filters (DURAPORE®; 0.54µm; Figure 90). The intention hereby was to omit effects of the filters on the transport properties, while preserving a mechanical stability of the solid (anyhow, a slight swelling of the Na-illite into the open cavities of the supporting PEEK plates was observed in foregoing tests). After compacting the clay material (ρ_{db} ~1700 kg·m^{-3}), the samples were pre-equilibrated against 0.1 and 0.5 M NaCl solutions for one week. To account for K^+ released from partial clay dissolution, KCl was added at 1E-4 M., while the pH was adjusted to 5.5 and kept constant by addition of 1E-2 M MES buffer. Subsequently the solutions on one side (V_{tot} = 500mL) were spiked with HTO and ^{36}Cl (at ~450 and ~20 Bq·cm^{-3}, respectively), while the solution at the other side (containing solely the background electrolyte; V_{tot} = 20mL) was replaced against a new one. The latter reservoir (representing the low-concentration boundary LCR) was changed daily to keep the concentration of the tracer in this compartment as low as possible, while the former solution (representing the high-concentration reservoir HCR) was remained unchanged during the timeline of the experiments. Aliquots from both reservoirs were taken daily and the activities determined by liquid scintillation counting.

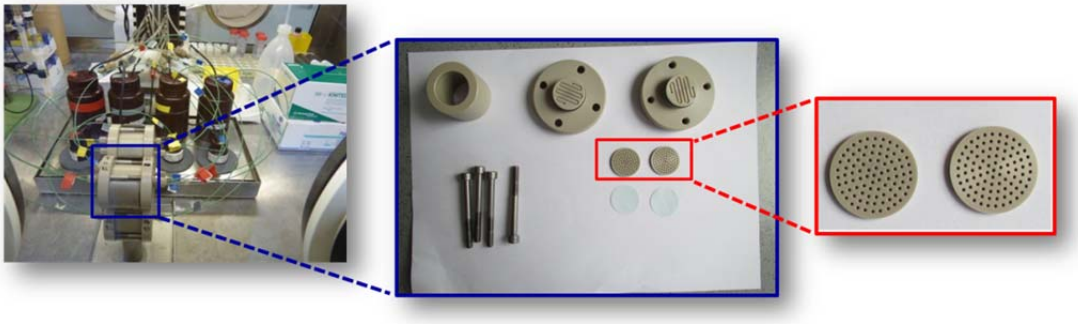

Figure 90 Experimental setup for the diffusion experiments performed by KIT-INE.

From the through diffusion technique described above, the effective diffusion coefficient D_e (in m² s^{-1}) and the rock capacity factor α can be determined, the latter defined as $\alpha = \varepsilon + \rho K_d$ with ε the porosity (-), ρ the bulk dry density (kg m^{-3}) and K_d (L kg^{-1}) the sorption coefficient. For non-sorbing tracers (i.e. HTO and Cl) K_d equals 0 and α = ε. Details on the analytical determination of D_e and α can be found in Van Loon et al. (2003) (for the analytical solution of the through-diffusion problem the reader is referred to the original literature (Crank (1975)). However, these values are only reliable, if the boundary conditions c_{HCR} ~constant and c_{LCR} ~0 are fulfilled throughout the experiment. While the latter is true for the present experimental procedure (as the solution is changed daily), the loss in tracer concentration at the high stream boundary was observed to be ~9% at maximum for HTO, indicating that values for D_e and α may be biased. Therefore, D_e and α were also determined by modelling the experimental data by numerical methods, where the above mentioned restrictions are not applicable (for details see Glaus et al. 2007).

Diffusion HTO, Sr and Zn in Na-IdP at SCK-CEN

Two types of diffusion cells were used to perform these through- and in-diffusion experiments. The majority of the experiments were performed with the so-called conventional diffusion cells with "static filters". At the end of the project, some experiments were performed in "flushed filter" diffusion cells.

Conventional diffusion cells with static filters. The design of these cells was developed more than 20 years ago at SCK·CEN (Henrion *et al.*, 1991) but is adapted to current needs. The whole setup is made from stainless steel. In this design, the clay plug is confined between two porous filter plates at the desired dry bulk density and resaturated (more details below). Both faces of the clay plug are irrigated with solutions which are pumped continuously over the filter plates. Since there is no pressure (or other physical) gradient over the clay plug, the flow of material through the plug is purely diffusive. The diameter of the clay samples in this design is restricted to 38 mm; the thickness can vary, but was 15 mm for all experiments in EC CatClay. This experimental setup requires that the diffusion in the filter has to be taken into account for the modelling. The filters used in these cells are stainless steel filters with a thickness of 2 mm (more details below).

Flushed filter diffusion cells. The design of these cells was developed by PSI (Glaus *et al.,* in preparation) and slightly adapted by SCK·CEN. Two different materials, stainless steel or PEEK (polyether ether ketone), were used for the construction. The main difference with the conventional diffusion cell is that the solution is flushed advectively through

the filter (but without creating a pressure gradient towards the clay). Therefore, in this design the filters do not work as an additional diffusive barrier between the source and target reservoir and the clay. The diameter of the clay plug is smaller compared to the conventional diffusion cell (diameter 20 mm), but the length of the clay plugs in these cells was also 15 mm. For the Sr-diffusion experiments, we used stainless steel filters (thickness 1,57 mm). For the diffusion experiments with Zn, it was necessary to use polypropylene filters and PEEK diffusion cells.

Filters. The majority of the diffusion experiments were performed with stainless steel filters (SIKA-R5 AX; 316L – pore size 10 µm – porosity 31% - manufactured by GKN Sinter metals). The diffusion of HTO and Sr in the filters was experimentally determined with resp. 3 and 4 replicate experiments. The D_e in the unused filter was 1,2 $\times 10^{-10}$ ($\pm$ 2,3 $\times 10^{-11}$) $m^2\ s^{-1}$ for HTO and 4,5 $\times 10^{-11}$ ($\pm$ 3,6 $\times 10^{-12}$) $m^2\ s^{-1}$ for Sr. The D_e in the setup with the clay can, however, be lower due to the infiltration of clay particles into the filter (Glaus *et al.,* 2008).

Due to strong sorption of Zn on the stainless steel filters at pH 7 and higher, it was decided not to use these filters for Zn diffusion experiments at higher pH. All kinds of filter materials were tried out. Hydrophobic materials like PTFE tend not to sorb Zn, but the hydrophobic character is an obstacle for the diffusion/percolation through the filter material. Finally, a polypropylene filter could provide a good compromise for both needs (sorption is limited and permeability is sufficient). These polypropylene were custom-made for our application by Blinex Filter-coat. The filters with diameter 25.4 mm and thickness 2 mm have an average pore size of 25 µm.

Pre-treatment. When circulating $NaClO_4$ electrolyte over a compacted purified Na-illite (Na-IdP) plug, a pH value of 7.4 is recorded. Therefore, for the experiments at pH 7, the clay is used as such. For the experiments at lower or higher pH (5 and 9), the illite is first brought to the desired pH. Initially it was tested to bring the clay to the desired pH by percolating it with buffered solutions, but this method was not successful due to low achieved flow and the pH buffering capacity of the clay. Finally it was chosen to titrate the clay by the following method. A dense suspension of Na-IdP in Milli-Q water (~30-40 g/100 ml) was titrated to the desired pH by adding HCl or NaOH. The suspension was equilibrated during 1 day before freeze drying. Before packing the clay, the clay is brought to a moisture content of 7 to 10% in a desiccator with saturated KNO_3 solution. All clay plugs were compacted at a dry bulk density of 1700 $\pm$ 50 $kg\ m^{-3}$.

Saturation. The clay plugs were saturated with the external solution described below in different ways. The clay plugs in the conventional diffusion cells were saturated by advective percolation at a pressure gradient of 9 bar until at least one pore volume passed the clay. For the flushed filter cells, this would, however, take too much time due to the smaller diameter (lower flux). Therefore, the cells were saturated by vacuum saturation followed by passive saturation. The cells are submerged in the external solution in a dessiccator on which low vacuum is applied to force water into the clay (and air out). To ensure full saturation, the diffusion cells are afterwards saturated passively for minimum 2-3 weeks. This is done by pumping the solution through the filter plates without a pressure gradient, similar to the experimental setup of the through-diffusion experiment.

External solution. The majority of the experiments were performed in $NaClO_4$ 0.1 M + 0.1 mM KCl. In order to ensure pH buffering, appropriate buffers (MES for pH 5, MOPS or TRIS for pH 7 and CHES for pH 9) were added to the external solutions in a concentration of 5×10^{-3} or 10^{-2} M. In the experiments performed at higher pCO_2 (0.4%) conditions, a mixture of $NaClO_4$ (84 mM) and $NaHCO_3$ (16 mM) is used (pH 8.4).

Description experiment. A picture is given in Figure 91. The experiments performed at CO_2 free conditions were performed in a glove box with N_2, the ones at higher pCO_2 in a glove box with Ar/CO_2 0.4 %.

The *source reservoir* is spiked with a tracer (HTO, ^{85}Sr or ^{65}Zn). The chemical concentrations are calculated from the specific activities of the tracers. The decrease in activity (respectively concentration) was monitored by regularly taking subsamples from the reservoir. Ideally, the activity should not decrease more than 50% in order to have good boundary conditions for modelling. This can be imposed by using a sufficiently large volume of the source reservoir (0.5 l -2.5 l) in the case of sorbing tracers.

For the through-diffusion experiments (HTO and ^{85}Sr), the increase in the *target reservoir* is also monitored. The target reservoir is exchanged at regular time intervals in order to keep the activity/concentration as low as possible. The volume ($\pm$ 20 ml) was exchanged regularly (e.g., 2-2-3 days regime) in order to avoid a decrease in the flux.

Figure 91 Picture of the total experimental setup.

The solutions of the source and target reservoir are continuously pumped over or through the filters (depending on the type of diffusion cell) by peristaltic pumps with an average flow rate of a few ml per minute. The duration of the experiment varies from 2 weeks for HTO to 4-5 months for ^{65}Zn. At the end of the experiment, the consolidated clay was cut in slices of 0.1 to 0.5 mm. The moisture content of the clay slices was obtained by measuring the weight before and after drying the clay (at 65°C – at least for 72 hours).

Radio-analytical techniques. The activity of the subsamples of the source and target reservoir are measured with liquid scintillation counting (Packard/Canberra Tri-Carb 2100TR) for HTO and gamma counting (Packard/Canberra COBRA Quantum) for ^{85}Sr and ^{65}Zn. The tracer activity in the clay slices is measured on the dried samples (no extraction).

Diffusion of Sr, Zn and Co in Na-IdP at PSI-LES

The majority of the Sr diffusion experiments ($NaClO_4$ concentrations of 0.1, 0.5 and 1.0 M) were evaluated using the through-diffusion technique. Those results were described in Glaus et al. (2012). It was clear from those experiments that going to lower salinities will cause experimental artefacts related to the inherently large tracer fluxes prevailing under such conditions. Briefly summarised, the main difficulties arising are (i) dominant uncertainties stemming from filter diffusivities and (ii) non-linear responses of increasing tracer concentrations in the target reservoir on the resulting tracer fluxes. Both effects lead to errors in D_e in which the true values are systematically underestimated.

For this reason in-diffusion experiments using MCDC's (annex 2) were carried out and compared with through-diffusion experiments in which a "draining method" was applied to the target reservoir. The details of this technique are described elsewhere (Glaus et al., in preparation). The idea behind is to flush the target side of the diffusion cell with tracer-free electrolyte solution instead of recycling the target solution and exchanging it from time to time. Thereby the tracer concentration at this boundary is almost zero throughout the whole diffusion experiment, viz. it is defined by the pump rate and the diffusive flux. A shark-tooth evolution of the concentration with time, as is the case in traditional through-diffusion experiments, is thereby avoided and the concentration can be approximated to be zero. In order to measure the tracer flux at the target boundary the draining solution is directed over a small separation column filled with a selective ion exchange resin (~2g of Chelex-100 resin, Biorad, Na^+ form). A CHES solution buffered to pH 9 is mixed with the draining solution before entering the Chelex column in order to keep the selectivity for Sr^{2+} over Na^+ at a maximum value. In this way Sr^{2+} is transferred quantitatively to the resin and can be directly measured by γ-counting in such manner.

General methodical aspects of the in-diffusion experiments of $^{60}Co^{2+}$ and $^{65}Zn^{2+}$ with MCDC's and the evaluation of the results are discussed in annex 2. They were carried out at ambient temperature under different conditions regarding pH and ionic strength with $^{60}Co^{2+}$ and $^{65}Zn^{2+}$ tracer, respectively using MCDC's filled with 10 ± 0.5 mm clay. 2 layers of a Durapore® GVWP (Millipore) membrane (polyvinylidene fluoride, PVDF, 0.125 mm thick per layer) were used to separate the compacted clay sample from the tracer source solution. In a few cases (for the lowest concentrations of the background electrolyte), only a single membrane layer was used. The bulk-dry density of Na-IdP-CC was 1700 ±30 kg m^{-3} requiring 347 mg of dry clay for a 10 mm thick clay sample. The total water porosity (ε) was calculated using $\varepsilon = 1 - (\rho_{bd}/\rho_s)$ where ρ_{bd} and ρ_s are the bulk dry and the solid density (kg m^{-3}), respectively. For the experimentally determined ρ_s of 2800 kg m^{-3}, the resulting ε is 0.393 ± 0.011.

The clay was previously conditioned to the pH of the diffusion experiment by adding dilute HNO_3 or NaOH, respectively, and subsequently freeze-drying the resulting suspension. The equilibration time for the pH adjustement was chosen rather short (~1 h) thus not taking into account any slow processes such as the re-equilibration of the clay mineral phases. The tracer solutions contained $NaClO_4$ at variable concentrations (0.01 to 1.0 M), 0.1 mM KCl and 10 mM of an appropriate buffer (MES for pH 5 and CHES for pH 9). The latter concentration was 1 mM of 0.01 M $NaClO_4$ in order not to significantly alter the Na^+ concentration. The clay samples were saturated in an initial phase under advective conditions using an overpressure of ~2 bar. In a second phase equilibration of the clay samples proceeded by passive saturation by immersing the diffusion cells in the contacting solutions for ~30 d. For the present experiments this step was carried out in closed flasks under laboratory atmosphere conditions. For the subsequent tracer diffusion phase, the cells were transferred in a glove box exhibiting an N_2 atmosphere and temperatures of 22 ±2 °C. Diffusion was started by exchanging the saturation solutions by ~60 cm^3 of appropriate tracered electrolyte solutions. The total carbonate concentrations measured in the experiments at pH 9 after the in-diffusion phase was rather negligible (< 2 mM). Note that the stock solution of the $^{60}Co^{2+}$ tracer contained significant amounts of stable Co (~1.3 mM). The experiments were carried out with a minimum of initial tracer activity (100 Bq cm3) in order to keep the concentration of stable Co^{2+} at the lowest possible level. For obtaining adequate count statistics in the γ-scintillation measurements, rather large sample volumes of ~1 cm^3 were required. The sample of the previous measurement was poured back at a time to the tracer reservoir solution after taking the fresh sample ("sample recycling") resulting in a constant volume of the reservoir solution. The resulting error introduced by adding a sample with slightly higher concentration was negligible. This issue was less critical for the Zn tracer solution which contained ~0.15 mM of stable Zn.

After the in-diffusion phase the clay samples were cut into segments with thicknesses of ~0.1 – 1.0 mm. Owing to the small weights of the samples, exact values were determined from the incremental movement of the extruding screw. 10 regular position marks on the outer side helped to determine the exact position of the screw. Wet and dry weights of the segments were measured after cutting and after drying the samples overnight at 60 °C. The recovered amount of dry clay was of the order of 96–97 % of the initial weight. After drying 0.1 M HCl was added to the samples to homogeneise the tracer in the suspension for γ-counting. All results were corrected for tracer decay using the starting date of the experiment as a reference date. Total element concentrations were calculated from the activity data using the initial ratio of the stable isotope to the tracer isotope at the starting date of the experiment.

Annex 2: Membrane-confined diffusion cell (PSI-LES)

For the diffusion measurements foreseen for $^{60}Co^{2+}$ and $^{65}Zn^{2+}$, the new type of MCDC diffusion cell was further developed and tested. The tests of the prototype cells were carried out using $^{85}Sr^{2+}$. In contrast to the experiments with Opalinus Clay, a mechanical confinement of the compacted illite sample is necessary. Figure 37 shows a schematical view of this diffusion cell. The cell was immersed to a minimum necessary in the source reservoir solution containing the radiotracer under study. The uptake of the radionuclide to the equipment was thereby minimised. A confinement of the clay sample by one or two layers of an organic polymeric membrane with a resulting overall thickness of ~100–200 µm was sufficient to withstand the swelling pressure of the clay sample. Slight deformations of the clay of the order of 0.1–0.2 mm were observed, but taxed as rather unimportant for experiments in which the tracer penetration into the clay is larger than ~1 mm.

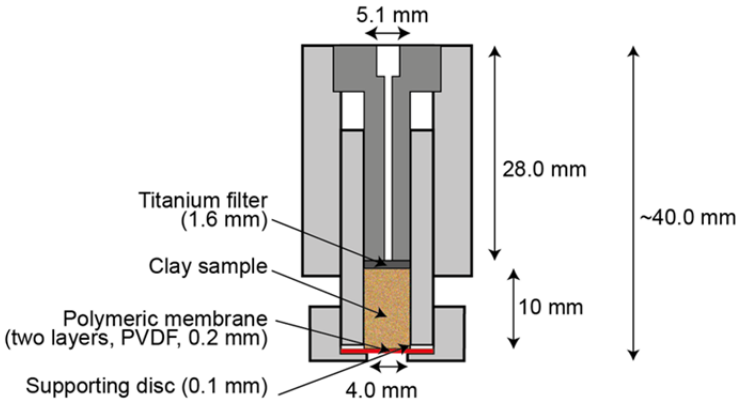

Figure 92 Schematic drawing of the final version of the membrane-confined diffusion cell (MCDC). In contrast to previous versions the supporting slotted titanium disc was left out. An opening of 4 mm provided sufficient mechanical stability to withstand the swelling pressure of the clay sample. As in former versions, saturation of the clay sample can be realised under advective conditions using a stainless steel plate as a support (not shown). After the in-diffusion phase the sample can be extruded from the holder and sliced using an appropriate end-piece (also not shown).

A typical data recording in an in-diffusion experiment with the MCDC comprised the measurement of radionuclide concentration as a function of time in the source reservoir solution accompanied by a few checks of pH and measurement of total inorganic carbon concentration (for experiments carried out at pH 9). After termination of the in-diffusion the clay plug was sliced into segments with thicknesses ranging typically between 0.1 and 1.0 mm. The wet weight of the segments was recorded and its dry weight after drying the samples at 60 °C. Owing to the small dimensions of the MCDC these parameters were less suited to determine the water porosity distribution within a clay sample and the thickness of the segments. The latter quantity was rather determined from the position of the micrometer screw used to protrude the clay from the housings. However the gravimetric data could be used to verify the recovery of clay from the slicing process which was typically better than 95 %. The radionuclide content as a function of the clay distance was subsequently measured and compared to the decrease of the radionuclide concentration in the reservoir solution. The discrepancies in this mass balance were found in most cases to be between 5 and 10 %.

The evaluation of best-fit parameter values for D_e and R_d (effective diffusion coefficient, $m^2\ s^{-1}$, and sorption distribution coefficient, $m^3\ kg^{-1}$, respectively) was performed by numerical methods using a 2-D model with rotational symmetry along the cylindric axis in Comsol Multiphysics® (cf. Figure 93) using the 'Species Transport in Porous Media' model node. The geometrical elements of the model are built from three compartments (clay, membrane, water in the aperture of the cell). Each compartment is assigned with nuclide specific properties, viz. an effective diffusion coefficient and sorption properties defined via a reaction term or a Langmuir sorption isotherm.

The behaviour of the radiotracer in the remaining source reservoir was calculated using a flux integration at the outer boundary of the water element in the cell aperture (represented by the red line in the left-hand plot of Figure 93). For a few cases where the radionuclide distribution comprised the entire clay sample, a further compartment representing the confining filter at the downstream boundary and the adjacent capillary system was also added. This small solution volume acts similar as a solution reservoir at the downstream boundary in through-diffusion. The water in the aperture of the diffusion cell was used as a diffusion volume in modelling because it is not *a priori* clear whether this volume would be homogeneously mixed as the rest of the reservoir solution. Subsequent sensitivity calculations showed that

the assumption with regards to the mixing properties in this volume were less critical. A completely stagnant volume characterised by the diffusion coefficient for bulk water would actually lead to a significant bias in the diffusion results. A ten-fold increase of the diffusion rate typically results in almost the same results as a homogeneously mixed volume. Such an assumption is certainly justified in view of the mechanical stirring in the experiments.

The 2-D geometry in the model was required because of the different diameters of the clay sample and the aperture of the cell. This difference resulted in spherical iso-concentration lines and thus an inhomogeneous concentration distribution in r-direction in the clay sample near the interface between membrane and clay (cf. Figure 94). With increasing distance from the interface these iso-concentration lines became linear in the direction of the radial vector. As shown by the comparison of two apertures in Figure 94, the degree of inhomogeneity increases with decreasing cell aperture. It was not clear from the beginning whether the membrane would withstand the mechanical stress of the swelling clay. For this reason the cells were constructed with apertures varying between 2 and 4 mm. It turned out that the use of 4 mm apertures were sufficient for the degree of clay compaction used in this project. The use of a maximum aperture reduces the inherent uncertainties stemming from the ignorance of a possible anisotropy (in r- and z-direction) of the clay sample caused by an ordered layering of the clay platelets that can be inferred from microscopic pictures.

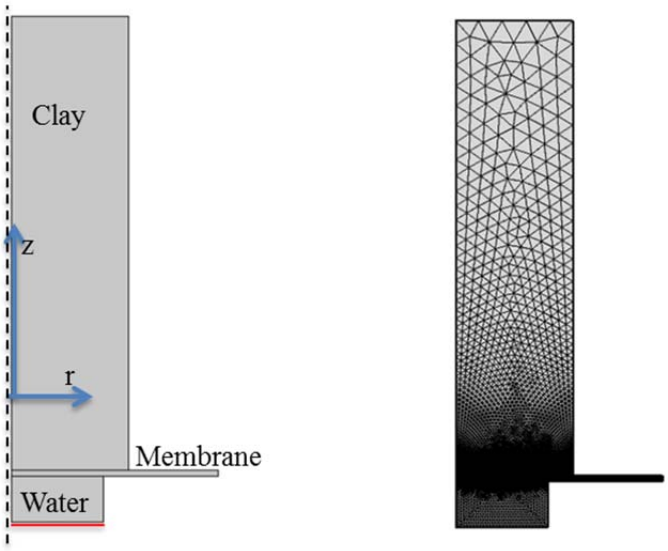

Figure 93 Left-hand plot: 2-D rotation-symmetric geometry of the model used in Comsol Multiphysics comprising the three domains, clay, membrane and water in the aperture of the cell. The rotational symmetry of the cell is represented by the dashed line. The red line shows the calculational boundary used for representing the remaining solution volume of the source reservoir. Right-hand plot: Mesh used for numerical simulations.

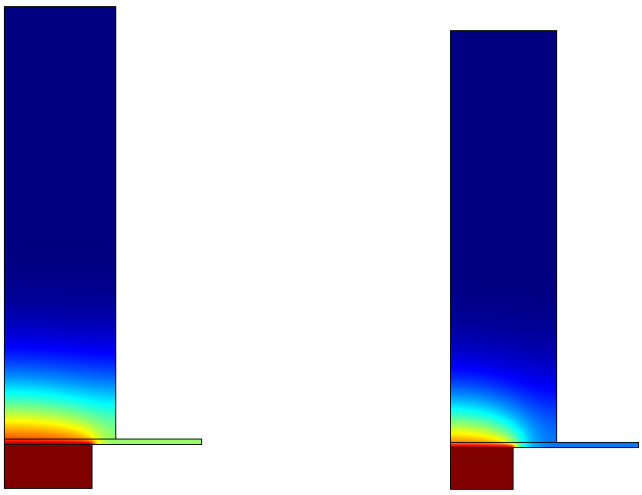

Figure 94 Effect of the width of the cell aperture on the shape of iso-concentration lines (represented by areas of the same colour) as shown by a 4 mm aperture (left-hand plot) compared to a 3 mm aperture (right-hand plot).

A crucial step in the determination of R_d is setting the diffusive properties of the membrane filter. These were measured for a pristine state using the equipment described in Glaus et al. (2008). Using $^{85}Sr^{2+}$ as the test cation a geometry factor (G) of ~2.5 (±30 %) was measured for a total porosity of 0.7 as specified by the supplier. G can be defined as a proportionality factor between D_e, the diffusion coefficient in bulk water (D_0) and the total porosity (ε) according to

$$D_e = \frac{\varepsilon}{G} D_0 \qquad (2.1)$$

It has to be assumed that the filter diffusion properties may be biased in a real situation by the swelling of the clay sample. The filter properties were thus treated as an adjustable parameter in modelling, albeit within a rather narrow range of possible values as given by a relation similar to Archie's law (Archie, 1942):

$$D_{e,filter} = D_0 \, \varepsilon^m \qquad (2.2)$$

where $D_{e,filter}$ is the effective diffusion coefficient of the diffusing species in a porous filter and m an empiric factor often denoted to as the cementation factor. The range of possible values for G was set for using parameter ranges for ε between 0.5 and 0.7 and for m between 2.0 and 2.5. This resulted in a range of possible G factors between ~1.4 and 2.8. Only in a very few cases values outside this range had to be chosen.

Best-fit parameter values for D_e and R_d were chosen by simultaneously fitting (i) the radionuclide concentration in the source reservoir as a function of time and the total radionuclide concentration in the clay. Note that for sorbing elements as used in the present study the radionuclide concentration in the clay pore water is almost insignificant compared to the reservoir concentration during the initial phase of the experiment. The diffusive flux is thus dominated by the tracer concentration gradient in the membrane filter which allows for an almost independent determination of the filter properties to be made from the initial decrease of the radionuclide concentration in the reservoir.

As a consequence of the optimisation of the filter properties, the boundary conditions on the source reservoir side was the amount of radiotracer at time zero only, while the resulting radiotracer mass transfer was used to calculate the boundary concentration at later times. When chosing the measured concentration of the radiotracer in the source reservoir over the whole range of times, these properties would have to be set in advance.

The Comsol model was repeatedly run in a Matlab script which determined the best-fit parameter values by minimisation of the error function. The overall experimental uncertainties were used for weighting the experimental data. In many cases the solution was rather robust with regards to the choice of initial parameter values and the mode of weighting the experimental data. In a number of cases this did not apply. Statistical uncertainties on the best-fit parameter values given on a 95 % confidence interval basis were also determined in this routine. This was possible for those cases in which the parameter correlation was rather low. The detailed discussion of the statistical peculiarities in the individual evaluations will be omitted in the following sections for simplicity. Instead an arbitrarily chosen example of the majority of evaluations will be discussed here in more detail. It can implicitly assumed that this example is rather one of the "nicer cases".

Figure 95 shows the results of an in-diffusion experiment with $^{60}Co^{2+}$ tracer. The blue lines are the model curves for the best-fit parameter values, while the grey lines are the results of 25 parameter combinations randomly generated using a Latin Hypercube Sampling (LHS) algorithm. A reasonable agreement between the scattering of the grey lines and the overall uncertainties of the experimental data (representing 1σ-standard uncertainties) can be observed. The somewhat larger scatter of the grey lines compared to the error bars is thus founded by the differences in statistical definitions (1σ-standard uncertainties versus 95 % confidence intervals). Figure 95 also shows that it is not possible to define the range of uncertainty by an "upper and lower" parameter combination because the LHS lines tend to intersect in the profile plot. This is an intrinsic property of in-diffusion experiments in which a decrease of the tracer concentration in the reservoir solution is observed. The concentration decrease in the source reservoir is directly proportional to D_e and R_d, while the diffusion depth is directly proportional to D_e, but indirectly proportional to R_d. The parameter combinations for which R_d dominates will end with low reservoir concentrations, start with high concentrations in the clay and result in low penetration in the clay. This leads to LHS lines which cross each other in the profile plot.

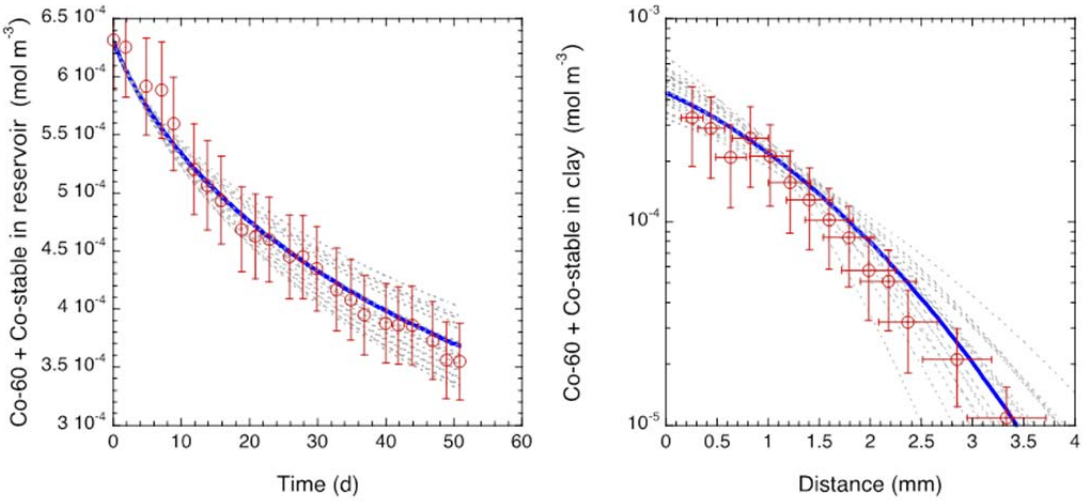

Figure 95 Statistical aspects of the parameter optimisation procedure. The plot shows the fit curve obtained from the best-fit parameter values in blue. The grey lines are the result of 25 parameter combinations stochastically chosen using a Latin Hypercube Sampling algorithm. Note that the error bars represent 1σ standard uncertainties, while the uncertainties from the parameter optimisation procedure cover a 95% confidence interval. Grey lines being outside the experimental uncertainties is thus an intrinsic result of these procedures.

The MCDC was tested using the conditions in which the diffusion of $^{85}Sr^{2+}$ has already been measured using conventional diffusion cells using advectively flushed filters (FFDC), viz. pH 5 and ionic strength of 0.1 M. Whereas the previous experiments (Glaus et al., 2012) were carried out as through-diffusion experiments comprising the steady-state flux phase reached after an experimental duration of ~100 d, the present experiments were stopped after 11 d, in order to obtain results in the transient phase in which the tracer profiles don't almost reach the low concentration target boundary of the clay sample. The results obtained from the steady-state and the transient phase are compared in Table 48. Without an elaborate assessment of the parameter uncertainties involved, it can be stated that the D_e values vary within the usual ranges of uncertainty, while a rather significant difference with respect to α values can be noted between the MCDC and the FFDC cells. Note that the experiments were carried out using the same ratios of dry clay weight to tracer reservoir volume. The reason for this discrepancy has probably to be found in an inhomogeneous distribution of the tracer near the membrane interface.

Table 48 Results for the diffusion of $^{85}Sr^{2+}$ in Na-IdP at pH 5 and ionic strength of 0.1 M using different types of diffusion cells and different durations for experimental observation. Parameter value uncertainties were of the order of 15–20 %.

Cell type	Data evaluation from	Duration (d)	D_e ($m^2\ s^{-1}$)	α (–)
MCDC	Transient phase	11	0.9×10^{-9}	68
FFDC	Transient phase	11	1.2×10^{-9}	100
FFDC	Transient phase	11	1.0×10^{-9}	105
FFDC	Pseudo steady-state phase	110	1.0×10^{-9}	90

Annex 3: Elemental analysis in the aqueous phase of diffusion experiments with compacted Illite du Puy

The following short report summarises the results of element analyses performed in selected aqueous samples from various diffusion experiments in compacted Illite du Puy (acid washed and Na^+-conditioned) carried out at PSI-LES within the scope of the Catclay project. These experiments were carried out at background electrolyte concentrations ($NaClO_4$) varying between 0.01 M and 1.0 M and either at pH 5 or pH 9. Samples were taken from the end of the saturation phase (~1 month of saturation of the clay sample with buffered electrolyte solution) or during/end of the diffusion experiments which varied between 10 days and 3 months.

K^+, Mg^{2+}, Ca^{2+} and Sr^{2+} were measured by high-performance cation-exchange chromatography (Dionex chromatography station, Ionpac CS-12A column) using conductivity detection. Calibration was carried out at least at 3 concentration levels using identical background concentrations of Na^+ for standards and diluted samples in order to avoid possible matrix effects. Most of results were obtained under relatively high background noise levels. For this reason no results can be given for Sr^{2+}, for the other cations the impaired performance of the system only led to higher absolute uncertainties of the results (5-10 % for K^+, 5-20 % for Ca^{2+}, 15-40 % for Mg^{2+}). These had, however, no influence on the qualitative conclusions drawn.

Mn, Co, Ni, Fe, Cu, Zn, Si and Al were measured by ICP-MS (Thermo Fisher) after 1:10 sample dilution in 3 % HNO_3. Calibration was carried out at 5 concentration levels using identical background concentrations of Na^+ for standards and diluted samples in order to avoid possible matrix effects. The overall analytical uncertainties for Ni and Zn were estimated at 15 %, for the other elements at 10 %. These uncertainties do not include non-statistical sources of errors, such as contamination of vials or contamination occurring during the diffusion experiments. In many cases the latter sources of error dominated the overall uncertainty.

Figure 96 shows the ICP-MS results as box plots in which the boxes enclose 50 % of the data with the median given as a solid line. The top and bottom of the box mark the limits of ±25 % of the variable population. The lines extending from the top and bottom of each box mark the minimum and maximum values within the data set that fall within an acceptable range. Outliers are defined as values exceeding the interquartile distance by a factor of 1.5 and are displayed as individual points. It can reasonably be assumed that these outliers are mostly due to non-statistical error sources in ICP-MS. Because no obvious trends could readily be identified for a thermodynamically based dependence of the element concentrations on the concentration of the background electrolyte or kinetically governed effects, all results for the various background electrolyte concentrations and contact times were pooled together in these plots. They were simply grouped as results either measured in samples from the re-saturation phase or from the diffusion experiment and for the two pH values used. Background concentrations measured in the electrolyte solutions before contact with the clay are shown as grey bars and the detection limit of the method as black solid lines.

For some cases no significant difference could be discerned between the results of the re-saturation and the diffusion phase. Examples are Fe, Ni, Cu, Al and Si. According to the height of the grey bars it can further be concluded that the concentrations were governed by mineral dissolution or re-precipitation in the case of Fe, Ni, Cu, and Zn, whereas the metals were already present as impurities stemming from chemicals or containers in the case of Si and Al. A special case is Co. The concentration of this element in the diffusion experiments is clearly given by its concentration in the tracer stock solution. The values agreed with the specific activity (defined as the ratio of radionuclide per total element content) specified by the producer.

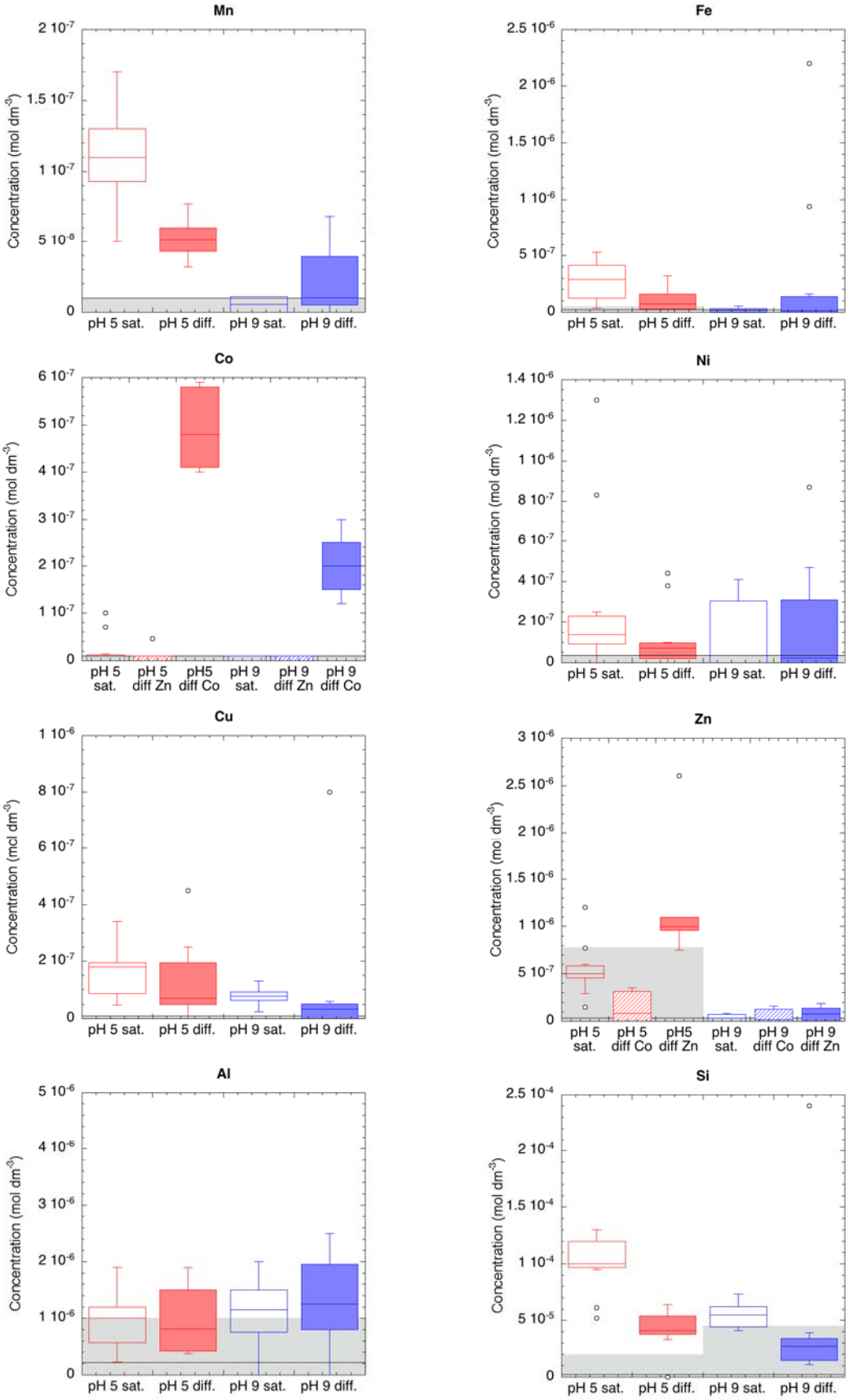

Figure 96 Results of ICP-MS measurements of selected solutions obtained from the re-saturation phase (empty boxes) and the diffusion phase (filled boxes) of the experiments. The grey bars represent values measured in the pure chemicals (electrolyte solutions) and the black lines show the detection limit of the measurement.

The case of Zn is different. The background concentration of Zn in the tracer stock solution was of a similar order of magnitude as the concentrations added from impurities. Further a significant element concentration decrease between the re-saturation phase and the diffusion experiments with $^{60}Co^{2+}$ could be observed for the experiments at pH 5. This can be interpreted as an uptake of added Zn by the clay.

For a simplified view it can be generally concluded for the transition elements that their concentrations in the pore water and the tracer reservoir remained more or less unchanged during the diffusion experiments. Possible competition effects on the uptake of Zn and Co can thus be roughly viewed as constant and rather similar to those occurring in a batch sorption experiment. In-diffusion of Co(II) and Zn(II) can both be viewed as a concerted process of a tracer species in a high background of the stable element in which the tracer is distributed between the solid and solution phase according to the distribution of the stable species.

A similar picture was also obtained for the earth alkaline elements and K^+ (cf. Figure 97). Although small differences between the results of the re-saturation and the diffusion experiments exist, these are rather caused by the fact that the first were only measured for 0.01 and 0.03 M $NaClO_4$, while the latter also include data in the range between 0.1 and 1.0 M $NaClO_4$. Possible correlations of the element concentrations with the concentrations of the background electrolyte could rather be expected for these elements. For this reason the results are plotted as a function of $NaClO_4$ concentration in Figure 98. Although there is a certain trend of increasing element concentration with increasing concentration of the background electrolyte in the case of Mg^{2+} and Ca^{2+}, the effects are clearly less than predicted for a pure cation exchange process. A rather quadratic dependence would be the expectation for the exchange of two monovalent Na^+ against bivalent cations. Almost no dependence of the concentration of K^+ on the background electrolyte concentration could be observed. It has to be noted that the background level concentration of K^+ was effected by addition of this element to the buffered electrolyte solution, while the concentrations of Mg^{2+} and Ca^{2+} were produced by the contact of the clay with the electrolyte solutions.

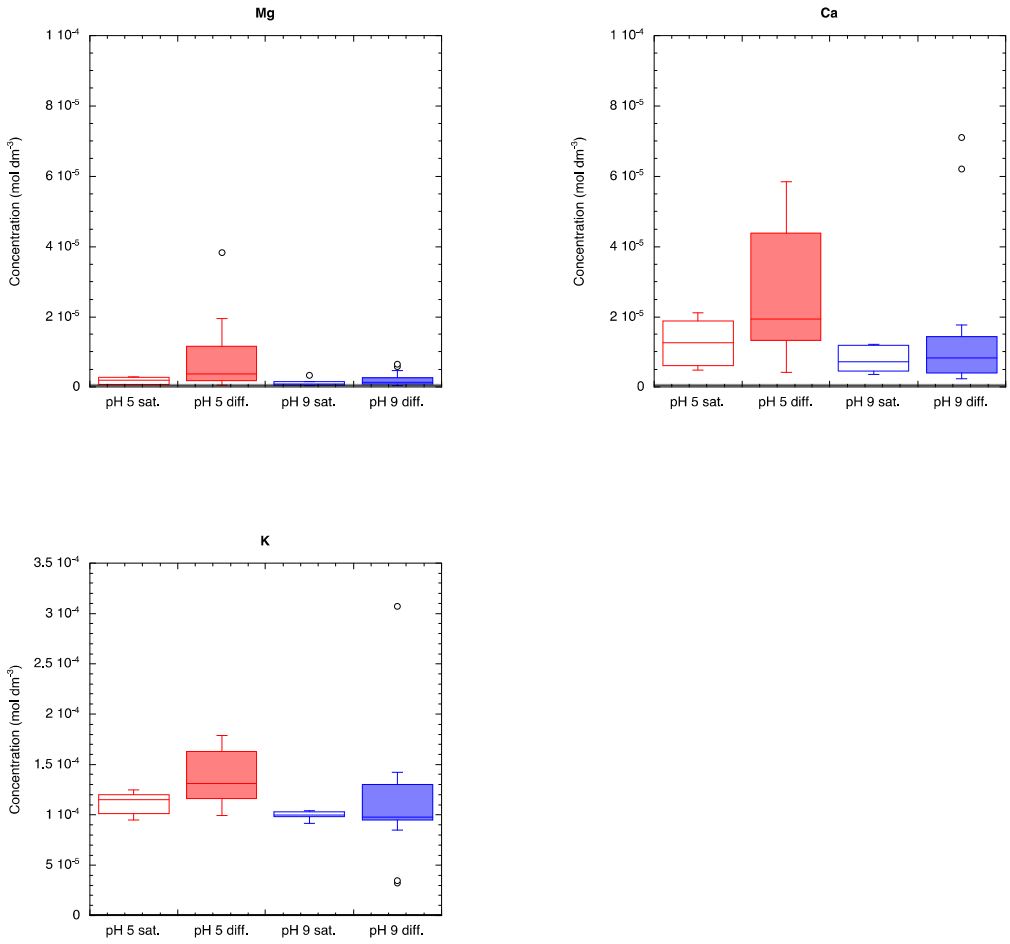

Figure 97 Results of ICP measurements of selected solutions obtained from the re-saturation phase (empty boxes) and the diffusion phase (filled boxes) of the experiments. The grey bars represent values measured in the pure chemicals (electrolyte solutions) and the black lines show the detection limit of the measurement.

As a conclusion for Mg and Ca it can be stated that their concentrations may be governed by clay dissolution and redistribution of the elements to the basal cation-exchange sites to some degree. However, this process is superposed with other redistribution processes which may be for example the formation of solid solutions such as the neo-formation of mixed-metal hydroxo phases (Scheidegger et al., 1997). It can be anticipated that inverse modelling of the experimental data for the identification of the most important process dominating the solution concentrations of these ions may be worth a try, but very difficult in view of the many degrees of freedom involved in such an exercise. A reduction of the thermodynamic equilibrium system to a simple dissolution and cation-exchange process, however, does not seem to be much promising.

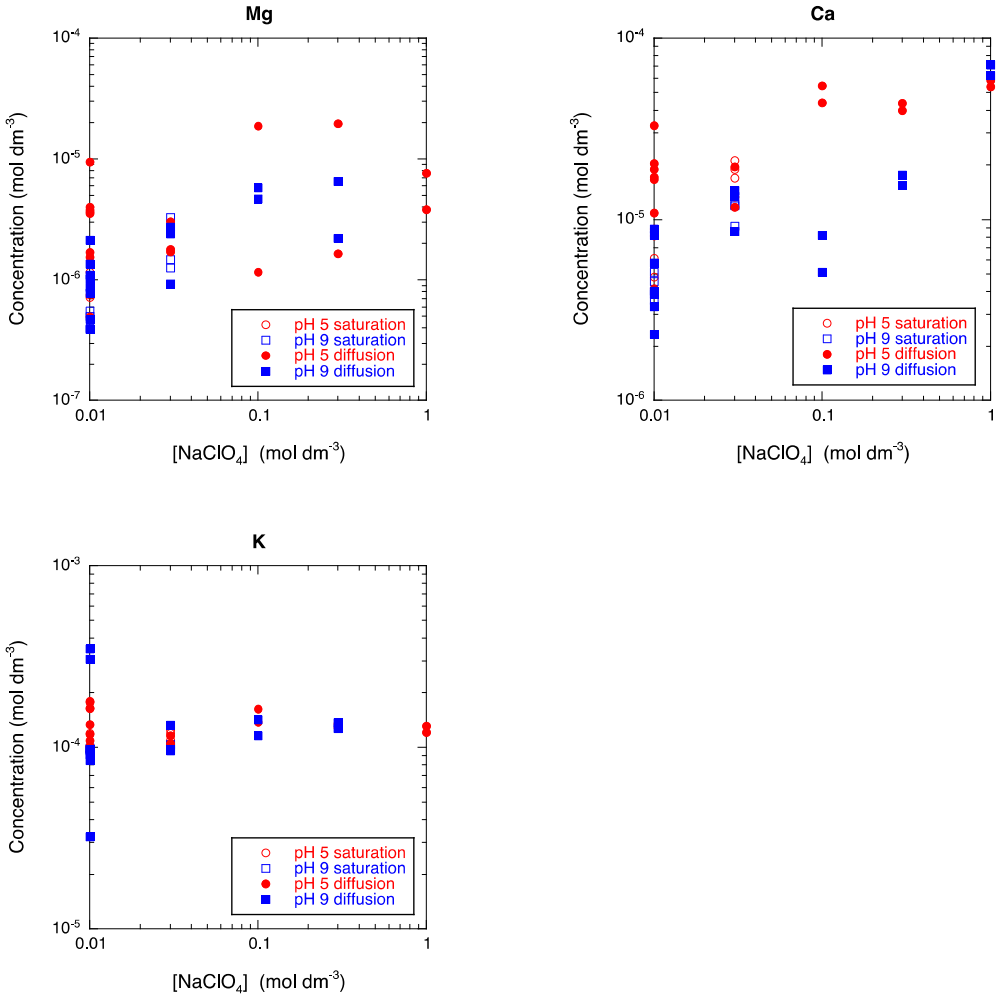

Figure 98 Dependence of the concentrations of Mg^{2+}, Ca^{2+} and K^{+} on the background concentration of $NaClO_4$.

References

SCHEIDEGGER, A.M., LAMBLE, G.M., SPARKS, D.L., 1997. Spectroscopic evidence for the formation of mixed-cation hydroxide phases upon metal sorption on clays and aluminum oxides. Journal of Colloid and Interface Science 186, 118-128.